2013

Framework of damage detection in vehicle-bridge coupled system and application to bridge scour monitoring

Xuan Kong
Louisiana State University and Agricultural and Mechanical College, xkong4@tigers.lsu.edu

FRAMEWORK OF DAMAGE DETECTION IN VEHICLE-BRIDGE COUPLED SYSTEM AND APPLICATION TO BRIDGE SCOUR MONITORING

A Dissertation

Submitted to the Graduate Faculty of the
Louisiana State University and
Agricultural and Mechanical College
in partial fulfillment of the
requirements for the degree of
Doctor of Philosophy

in

The Department of Civil and Environmental Engineering

by
Xuan Kong
B.S., Huazhong University of Science & Technology, 2006
M.S., Tongji University, 2009
May 2013

DEDICATION

To my parents.

ACKNOWLEDGEMENTS

I would like to gratefully thank Dr. Steve C.S. Cai, my advisor, for his continuous and helpful guidance, constant encouragement, and enduring support during my Ph.D. study at LSU, without which this dissertation would never have been accomplished. It has been a wonderful experience to work with such a brilliant mentor and learn from such a knowledgeable and helpful scholar. I deeply appreciate for his guidance of lighting my future both on research and life.

My sincere gratitude also goes to all my committee members for their valuable time and help. More specifically, I appreciate Dr. Ayman Okeil for his wonderful teaching skill and his suggestions on my research; Dr. Michele Barbato for his helpful suggestions and sharing his career experience with me; Dr. Muhammad Wahab for his consistent encouragement and providing job information to me; and Dr. Thomas R Corbitt for his helpful suggestions and comments on my research.

Consistent help from all the members in the research group at Louisiana State University is greatly recognized. My special thanks go to Dr. Wen Xiong, for working together and his contribution to Chapter 6 and invaluable help during my Ph.D. study; Dr. Hui Peng, for consistent encouragement and great help during my dissertation progress; Dr. Menggang Yang, Dr. Yongle Li, Dr. Bin Sun, Dr. Chengming Lan and Dr. Lu Deng for helpful suggestions and help on my research. To all my colleagues: Wei Peng, Junhui Dong, Archana Nair, Miao Xia, Bo Kong, Wei Zhang, Fang Pan, Ye Zhang, Guoji Xu, Fenghong Fan and Jiexuan Hu, thanks a lot for your friendship and lending a helping hand at all times.

The Federal Highway Administration and Louisiana Transportation Research Center (LTRC) for funding the research are fully acknowledged.

Last but not least, I would like to thank my family for their spiritual support. This dissertation would not appear without their consistent encouragement, love, and patience.

TABLE OF CONTENTS

LIST OF TABLES

LIST OF FIGURES

ABSTRACT

Most vibration-based damage identification methods make use of measurements directly from bridge structures with attached sensors. However, the vehicle moving on the bridge can serve as both an active actuator and a response receiver. This dissertation aimed to develop new methodologies to eventually detect bridge damages such as scour using the dynamic response of the vehicle. To reach the final objective, a framework of damage identification was developed first, which gave a guideline on the three crucial steps for damage detection. An optimization method was proposed that combines the Genetic Algorithm (GA) and the First Order (FO) method. It has the advantages of the global and local algorithms and converges faster than the traditional method using any initial values.

Secondly, a new methodology using the transmissibility of vehicle and bridge responses was developed to detect bridge damages. The transmissibility of a simplified vehicle-bridge coupled (VBC) system was analyzed theoretically and numerically to study the feasibility of this method. To obtain the transmissibility, two methods were proposed using two "static" vehicles on the bridge.

Then, a tractor-trailer test system was designed to obtain reliable responses and extract bridge modal properties from the dynamic response of moving vehicles. The test vehicle consists of a tractor and two following trailers. The residual responses of the two trailers were used, which successfully eliminated the roughness and vehicle driving effect and extracted the bridge modal properties. This methodology was applied on a field bridge and revealed a good performance.

Most previous studies of bridge scour focus on the scour causes instead of its consequences. Finally, in this dissertation the developed methodologies were applied to detect scour damage from the response of bridge and/or vehicles. The scour effect on a single pile was studied and methods of scour damage detections were proposed. A monitoring system using fiber optic sensors was designed and tested in the laboratory and is being applied to a field bridge. Finally, the scour effect on the response of the entire bridge and the traveling vehicle was also investigated under the bridge-vehicle-wave interaction, which in turn was used to detect the bridge scour.

CHAPTER 1. INTRODUCTION

This dissertation consists of eight chapters. All chapters, except for the introduction (Chapter 1) and conclusion (Chapter 8), are based on papers that have been accepted, are under review, or are to be submitted to peer-reviewed journals, and are constructed using the technical paper format that is approved by the Graduate School of Louisiana State University. The technical paper format is intended to facilitate and encourage technical publications. Therefore, each chapter is relatively independent. For this reason, some essential information may be repeated in some chapters for the completeness of each chapter. All chapters document the research results of the Ph.D. candidate under the direction of the candidate's advisor as well as the dissertation advisory committee members. Chapters 2 to 4 are on the framework of damage detection and proposed detection methods using dynamic responses of vehicles. Chapters 5 to 7 are on the effect of bridge scour on structure responses and proposed methods to detect and monitor bridge scour. This introductory chapter gives a general background related to the present research. More detailed information can be found in each individual chapter.

1.1 Vibration based damage identification methods

The Federal Highway Administration's 2011 National Bridge Inventory shows that 142,779, or 23.7 percent, of the nation's 602,864 bridges (excluding Puerto Rico) are either structurally deficient or functionally obsolete (FHWA 2011). These deficient structures potentially endanger the safety and economical use of the highway system. The National Bridge Inspection Standards (NBIS) regulates that every bridge on a public road must be inspected at least every 2 years. Nowadays, there is still an evident need to perform a more precise evaluation of structural safety and function and to find effective solutions. Based on the amount of information provided regarding the damage state, the damage detection can be classified into four levels (Rytter, 1993):

- Level 1: Identify that damage has occurred;
- Level 2: Identify that damage has occurred and determine the location of damage;
- Level 3: Identify that damage has occurred, locate the damage, and estimate its severity;
- Level 4: Identify that damage has occurred, locate the damage, estimate its severity, and determine the remaining life of the structure.

Most nondestructive damage identification methods can be categorized as either local or global techniques. Non-destructive testing (NDT) methods can complement visual inspections as an objective method leading to quantifiable results, such as ultrasound, X-ray, dye penetrates, magnetic particle, and acoustic emission. All these experimental methods require that the vicinity of the damage is known a priori and that the portion of the structure being inspected is readily accessible. Subjected to those limitations, these experimental methods can only detect damage on or near the surface of the structure. The need for more global damage detection methods that can be applied to complex structures has led to the development of methods that examine changes in the vibration characteristics of the structure.

Research of vibration-based damage identification was initiated in the late 1970s particularly in the aerospace and offshore oil industries, and has been rapidly expanding to civil engineering over the last decades. The basic idea behind this technology is that changes or damages in the physical properties will cause detectable changes in the modal properties. Doebling et al. (1998) presented an extensive review of vibration-based damage identification methods up to 1998. Sohn et al. (2003) then presented an updated version of this review on the literature up to 2001. Carden and Fanning (2004) reviewed the state of the art in vibration-based condition monitoring with a particular emphasis on structural engineering applications. Yan et al. (2007) introduced the development of modern-type vibration-based structural damage detection and the application of intelligent damage diagnosis. Fan and Qiao (2011) presented a comprehensive review on modal parameter-based damage identification methods for beam- or plate-type structures. The vibration based methods can be classified as response-based methods and model-based methods, as elaborated as follows.

1.1.1 Response based methods

The response-based methods, by interpreting directly or indirectly the experimental response data from structures, establish an analytical relationship between the damage severity and the modal parameters to detect the structural damages. It relies only on the measured dynamic response of the structure, which can be easily measured by a variety of sensors such as accelerometers, strain gauges etc., and the time domain data can be converted into frequency domain or modal domain data by regular transforming techniques. Through finding the difference between the intact and damaged structures, the damage location and severity can be determined. The response based methods can be further classified into various types, depending on the measured response used.

- **Methods based on natural frequencies.** This method is based on the fact that natural frequencies are sensitive indicators of structural integrity. Also, the frequency measurements can be cheaply and easily acquired (only a single sensor is required in many applications). Salawu (1997) reviewed the use of natural frequencies as a diagnostic parameter in structural assessment. The greatest success in the use of natural frequency shifts for damage identification is in small simple laboratory structures with only single damage locations, such as detecting a single crack (Lee and Chung 2000), estimating the tension force in the stay cables of cable-stayed bridges (Gardner-Morse and Huston 1993), and detecting structural faults in frame structures (Zhang et al. 1992) and foundation piles (Zhang et al. 1993). Even though natural frequencies are indicators of structural integrity, methods using only natural frequencies cannot distinguish the damage at symmetrical locations in a symmetric structure, for example, cracks associated with similar crack lengths but at two different locations may cause the same amount of frequency change ((Pandey et al. 1991, Salawu 1997), and the number of measured natural frequencies is generally lower than the number of unknown modal parameters resulting in a non-unique solution (Maeck and De Roeck 1999). Meanwhile, natural frequencies are not sensitive to small structural damages in many cases for field bridges especially when measurement errors and noise are involved.

• **Methods based on mode shapes.** Many modal analysis techniques are available to extract mode shapes from the time domain data (Ewins 1984, Fanning and Carden 2001). The traditional mode shape based methods are intended to establish a relationship between damage location/severity and modal shape change from intact and damaged structures through a finite element analysis or an experimental test. The first systematic use of mode shape information for the location of structural fault without the utilization of a prior finite element model was presented by West (1984). Gandomi et al. (2008) reviewed the development of mode shape based technique for identifying the structural faults. Two indices commonly used to calculate the difference of mode shapes are MAC (modal assurance criterion) and COMAC (the coordinate modal assurance criterion). Furthermore, Shi et al. (2000) extended the damage localization method by using incomplete mode shapes and Lee et al. (2005) presented a neural network-based technique using the modal shape differences or ratios of intact and damaged structures. Mode shapes contain local information, which makes them more sensitive to local damages than frequency-based methods and enables them to be used directly in multiple damage detection (Farrar and James 1997). However, the completed mode shapes of the structure require a large series of sensors and necessity of expansion from incomplete measurements. In general, without further signal processing or pattern recognition technique, methods based on mode shape change can only be adopted for preliminary damage localization rather than accurate localization or quantification of damages.

• **Methods based on mode shape curvatures.** The use of mode shape curvatures in damage identification is based on the assumption that the changes in the curvatures of mode shapes are highly localized to the region of damage and that they are more pronounced than changes in the displacement of the mode shapes (Pandey et al. 1991, Maeck and De Roeck 1999). Also, the curvature is proportional to the bending strain, and it can be estimated by measuring strains instead of displacement or acceleration (Pandey et al. 1991). Wahab and De Roeck (1999) successfully located the damage using curvature-based method on the Z24 Bridge in Switzerland. Moreover, modal curvatures have also been used with other measured data, for example, Oh and Jung (1998) detected damages in a bowstring truss combining mode shape curvature and static displacements. Al-Ghalib et al. (2011) established a non-dimensional expression, Curvature Difference Ratio (CDR), to exploit the ratio of differences in curvature of a specific mode shape for a damaged stage and another reference stage (Ren and De Roeck 2002a, 2002b). The methods based on mode shape curvature are in general very effective in damage localization by either using direct change in curvature or applying signal processing techniques on curvature. However, for high modes, the difference in modal curvatures shows several peaks not only at the damage location but also at other positions, which may lead to a false indication of damage. Hence, in order to reduce the possibility of a false alarm, only first few low curvature mode shapes can be used for damage identification.

• **Methods based on modal strain energy (MSE).** When a particular vibration mode stores a large amount of strain energy in a particular structural load path, the frequency and shape of that mode are highly sensitive to changes in that load path (Carden and Fanning 2004). The MSE, similar to the modal curvature, reflects structural instinct character and serves as an indicator of damage location. The curvature required for calculating the MSE is commonly

extracted from the measured displacement mode shapes using a central difference approximation. Stubbs et al. (1992) first applied this concept to detect structural damage in offshore platforms based on the decrease of its MSE, and developed a severity estimation algorithm later (Stubbs et al. 1995). Cornwell et al. (1999) extended this method to detect the damage in plate-like structures. Shi et al. (1998, 2000, and 2002) used the change of MSE to define a damage index and successfully located structural damage and quantified the damage level. Hu et al. (2006, 2009) successfully applied MSE to detect surface crack in various composite laminates, and detected the surface crack in a circular hollow cylinder by defining a damage index using the ratio of modal strain energies of cylinder before and after damage (Hu et al. 2011).

- **Methods based on modal flexibility.** Pandey and Biswas (1994) first suggested using changes in modal flexibility for damage detection. The flexibility matrix is defined as the inverse of the stiffness matrix and, therefore, relates the applied static force to the resulting structural displacement. Thus, each column of the flexibility matrix represents the displacement pattern associated with a unit force applied at the associated DOF. Many studies have been done (Zhang and Aktan 1998, Li et al. 1999, Dionisio 2002, Wu and Law 2004, 2005). Due to the practical difficulties in measuring the higher modes, the flexibility matrix is generally estimated using just a few low modes. Furthermore, because of the inverse relationship to the square of the modal frequencies, the flexibility matrix is most sensitive to changes in the low frequency modes.

- **Frequency domain methods.** In frequency domain, the data is reduced drastically and compensated the little loss of information averaging the effects of random noise. With the objective of eliminating the modal extraction error, damage detection using measured frequency response function (FRF) has been studied by a number of researchers (Lew 1995; Wang et al. 1997; Vestroni and Capecchi 2000; Lee et al. 2003; Esfandiari et al. 2009 and 2010) and is very promising because the FRF data can be obtained directly without any further extraction and processing. FRF is the relationship between the input and output, which means an input such as the harmonic force is required as an external excitation of the structure vibration. It leads to the development of damage detection using the output transmissibility that only requires the output information. Transmissibilities under variable load conditions have been recently proven to be a promising new approach of output-only modal identification (Canales et al. 2009). The motivation of using the transmissibility for damage detection relies on the fact that transmissibility is a local quantity suggesting a higher sensitivity to detect changes in the dynamic behavior due to some kind of damage (Maia et. al 2011). Devriendt et al. (2007, 2009 and 2010) used the transmissibility to identify modal parameters from output-only transmissibility measurements and multivariable transmissibility measurements.

- **Modern methods.** The modern methods refer to using signal processing techniques and artificial intelligence as analysis tools with good universality and less dependence on structural shape. Such methods include wavelet analysis, empirical modes decomposition (EMD) and Hilbert-Huang Transform (HHT). The main concept using wavelet analysis is to break down the dynamic signal of a structural response into a series of local basis function called wavelets, so as to detect the special characteristics of the structure using scaling and transformation

property of wavelets. Lu and Hsu (2002) compared the discrete wavelet transforms of two sets of vibration signals from the undamaged and damaged structures in the space domain, which is not only able to detect the presence of defects, but also the number and location. Yan and Yam (2002) proposed a method for online detection of initial damages in composite structures based on energy variation of structural dynamic responses decomposed using wavelet analysis. Rajasekaran and Varghese (2005) introduced a wavelet approach for damage detection in beams, plates and delamination of composite plates. Law et al. (2005) analytically derived the sensitivity of wavelet packet transform (WPT) component energy with respect to the local change in the system parameters based on the dynamic response sensitivity, and a sensitivity-based method was then used for damage detection of structures. Similar to Wavelet analysis, EMD and HHT are applied to measured time history data to identify damage occurring time instant and damage location for various test cases (Xu and Chen 2004). Yang et al. (2004) concluded that the method based on EMD and HHT is intended to extract damage spikes due to a sudden change of structural stiffness from the measured data thereby detecting the damage occurring time instants and damage locations.

Among all the methods, the modal domain methods gain great popularity because the modal properties (i.e., natural frequencies, modal damping, modal shapes, etc.) are physically meaningful and are thus easier to be interpreted or interrogated than those abstract mathematical features extracted from the time or frequency domain. However, neither modal nor frequency response parameters are known to be consistent in providing reliable assessment for a structure. For this reason, many researchers have switched to alternative developed parameters including a combination of modal parameters and/or frequency response functions and their derived versions for damage identification (Srinivas et al. 2010).

1.1.2 Model based methods

Model based methods rely on a well-correlated numerical model of the structure in its initial state. Through modifying structural model parameters such as mass, stiffness, and damping, the numerical model is intended to reproduce as closely as possible the measured static or dynamic response from the data. Comparisons of the updated structure to the original correlated structure provide an indication of damage and can be used to quantify the location and extent of damage. The model-based method assumes that a detailed numerical model of the structure is available for damage identification. Based on the model type, the method can be categorized as method using structural matrix, mapping model and meta-model.

- **Structural matrix.** This method updates structural matrix such as the stiffness, damping or mass matrix of the structure to reproduce the measured results. To update the stiffness matrix of the structure, two ways are available, direct methods (Friswell et al. 1997; Friswell and Mottershead 1995) that directly update the elements of stiffness and mass matrices in a one-step procedures to exactly reproduce the measured data, and iterative methods that use the sensitivity matrix of the parameters, and based on a penalty function to maximize the correlation between the measured and analytical results. Yang and Chen (2009) proposed a new direct method for updating the mass and stiffness matrices of a structural model that can

reproduce the measured frequencies. The updated results of direct method are seldom physically meaningful although they are capable of replicating the experimental measurements. The sensitivity matrix methods preserve the structural connectivity in the updated model and provide a direct physical explanation for the updated results. However, the calculation of the sensitivity matrices is usually computationally intensive and the matrices are often ill-conditioned.

- **Mapping model.** A mapping model is to build up a mapping relationship between the structural parameters and dynamic responses when applied to model updating. The representative method is Neural Network (NN) method, which is inspired by the architecture of the neurons and the human brain function (Pérez and González 2011), and has been widely applied in structural analysis due to its strong non-linear mapping ability. It is usually constructed by three layers, an input layer, a hidden layer and an output layer. Structural damage detection based on NN includes the following steps: to determine the network structure; to select the network parameters; to normalize the learning samples; to give initial weight value and to detect structural damage. The first step, build up the network structure, is achieved by training the structure with samples. The known feature information (NN input) and the corresponding status (NN output) of the structural damage are taken as train samples to train the constructed NN. These data can be experimental or numerical. When the NN has been well trained, one can input the experimentally measured real structural damage feature index into the trained NN, and the output of the trained NN will be able to give the location and severity of the structural damage. The NN calculation is relatively fast regardless of the complexity of the structure to be updated, once the model is properly trained. It is well known for its ability to model nonlinear and complex relationship that is exactly the case between the structural parameters and the modal properties. The neural networks (NNs) are found capable of replacing conventional finite element updating methods in solving the inverse problems without utilizing the sensitivity matrix. However, the numbers of training samples for the NNs exponentially increase for high-dimensional problems, resulting in considerable computation efforts. The training process could be very time-consuming and the accuracy of the predictions of this trained NN model depends very much on the training data.

- **Meta- or surrogate model.** Recently, a methodology called meta- or surrogate modeling has been proposed, which focused on the inverse problem optimization. Surrogate models have been extensively used in the design and optimization of computationally expensive problems. Different surrogate models have been shown to perform well in different conditions. It is recommended to use radial basis function for high-order nonlinear problems, Kriging for low order nonlinear problems in high dimension spaces, and polynomial response surfaces for low order nonlinear problems (Goel 2007). Li and Padula (2005) and Queipo et al. (2005) recently reviewed different surrogate models used in the aerospace industry. Russell (2009) summarized the characteristics of different meta-model types and the experiment designs for fitting them. The meta-model types can be separated into two categories: low-order polynomials for a local meta-model-based optimization strategy (also called response surface methodology), and all other models are for global meta-model-based simulation optimization strategies. The parametric approaches presume that the global functional form of the relationship between the response

variable and the design variables is known, while the nonparametric ones use different types of simple, local models in different regions of the data to build up an overall model.

1.1.3 Finite element model updating

The above structural matrix method is only applicable to small problems that can easily derive the stiffness matrix, while for large or complicated problems the FE model is the first choice. FE model updating is concerned with the correction of the FE model when the FE prediction is in conflict with the test results. One common approach is to consider an objective function that quantifies the differences between analytical and experimental results, and to minimize the discrepancy by adjusting the unknowns of the FE model (Kim and Park 2004). Mottershead and Friswell (1993) reviewed model updating using structural dynamic responses. Brownjohn et al. (2001 and 2003) used the FE model updating to assess the highway bridge upgrading, and Teughels and De Roeck (2005) used it to identify unknown structural parameters and determine damage in concrete structural. Generally, the discrepancies could be in eigenfrequencies and mode shapes, modal strains, modal flexibility residual (Jaishi and Ren 2006) or combined with static measurements (Deng and Cai 2010a). Most research requires matching between the measured and predicted modes. Beck et al. (2001) and Yuen et al. (2006) proposed methods without mode matching using the Bayesian probabilistic framework.

Setting up an objective function and minimizing the discrepancy change the problem into an optimization problem that is one of the three crucial steps of model updating (Jaishi and Ren 2007). The choice of optimization algorithms depends on the type of problems being solved. There is no single method to solve all optimization problems efficiently. Hence one has to test various methods in order to choose the best one for computationally efficiency and accuracy. There are two categories of optimization techniques as described next.

- **Gradient-based methods.** These methods mainly use quasi-Newton methods, such as the Large-scale Broyden–Fletcher–Goldfarb–Shanno (LBFGS) and the Nonlinear Programming using a Quadratic or Linear least-square algorithm (NLPQL) (Schittkowski 1985). It starts from a predefined initial parameter set and line search algorithms to ensure the stepwise convergence to an optimum using gradients. Gradient-based methods are recommended for the solution of smooth nonlinear optimization problems under the following restrictions: (1) the number of design variables should not be too large, (2) the functions and gradients can be evaluated with a sufficiently high accuracy, (3) the problem should be smooth and well-scaled.

- **Non-gradient-based algorithms.** In contrast to the gradient-based methods, the other category of optimization methods include decomposition methods, approximation methods, evolutionary algorithms, memetic algorithms, response surface methodology, reliability-based optimization, and multi-objective optimization approaches (Krishna 2009). Evolutionary methods led the way in the exploration of non-gradient methods. It benefited from the availability of massively parallel high performance computers, since it inherently requires many more function evaluations than gradient-based methods. The evolutionary methods imitate natural biological evolution processes such as adaption, selection and variation. To improve the

approximation of the solution of the optimization problem, a population of individuals searches the design space for possible solutions based on Darwin's principle of "survival of the fittest". The three main classes are genetic algorithms (Holland 1975), evolution strategies, and evolutionary programming (Fogel et al. 1966). An advantage of these methods is that they can find a global extremum in the presence of local extrema better than other optimization methods. A drawback is the high numerical effort that becomes necessary since a large number of problem solutions are required. Evolutionary algorithms should be applied to: (1) cases when gradient-based methods and response surface approximations fail, (2) problems where discrete or binary variables dominate the response, and (3) optimization problems with a very high number of variables and/or constraints.

1.2 Vehicle dynamic response in vehicle-bridge system

Bridges in service are subject to a combination of various external loads, such as the traffic load, wind load, earthquake, water flow and wave load, etc. The vertical vibration of bridges is induced mainly due to the road roughness and dynamic traffic loads, while the lateral one is due to the wind and water flow. Interaction analysis between vehicles and continuum structures originated in the middle of the 20th century. Over the years many bridge-vehicle models have been proposed to study the dynamic interaction between bridges and vehicles. The modeling of vehicle loads is developed from the initial model as a constant moving force (Timoshenko et al. 1974) or a moving mass (Blejwas et al. 1979), to a combination of a number of rigid bodies connected by a series of springs and dampers (Guo and Xu 2001), and to the state-of-the-art 3-D suspension vehicle model (Shi et al. 2008). The vehicle-bridge coupled model now can take into consideration of many factors such as the inertial force, the road roughness and time-variant features.

One research branch benefited from the research of bridge-vehicle interaction is making use of the vehicle dynamic response. All of vibration-based damage identification developments discussed earlier makes use of measurements directly from the bridge structure by attaching sensors on it, while in the vehicle-bridge system with time-variant features, the vehicle can serve as a force transducer and a mobile sensor in the system. The vehicle dynamic response such as acceleration, while easy to measure, owns the similar feature as the modal shape and FRFs of bridges mentioned above.

As discussed in Yang et al. (2009a), the vehicle acceleration contains three groups of frequency components: vehicle frequency, bridge-related frequencies, and driving-related frequencies. Yang et al. (2004, 2009a, 2009b, 2012, 2013) and Lin (2005) extracted the fundamental bridge frequency from the acceleration time history of a vehicle passing over the bridge including theoretical, numerical and experimental studies. A few researchers studied damage detection of bridge structures using the response of a moving vehicle. Bu et al. (2006) proposed an approach to detect the damage through the flexural stiffness reduction of finite elements based on dynamic response sensitivity analysis on the coupled system. Lu et al. (2009, 2010 and 2011) assessed local damages in box-girder bridges using measured dynamic responses of both the bridge and a passing vehicle. Kim et al. (2011) experimentally investigated the

feasibility of damage detection for short span bridges using both bridge and vehicle vibration data. Zhang (2012 and 2013) developed a damage detection method based on the approximately extracted structural mode shape squares from the acceleration of a passing tapping "vehicle" and a method based on the operating deflection shape curvature extracted from the dynamic response of a moving vehicle.

1.3 Bridge scour detection and monitoring

Bridge scour is of significant concern in the United States. Of the more than 575,000 bridges in the national bridge inventory, approximately 84 percent are over water. In the last 30 years, more than 1,000 bridges collapsed, and approximately 60% failure of them are related to the foundation scour (Shirhole and Holt 1991, Lagasse and Richardson 2001). However, scour due to severe flooding is not the only concern. The catastrophic collapse of the Schoharie Creek Bridge in New York in 1997 was caused more by the cumulative effect of pier scour of glacial till than the severe flood which ultimately caused its collapse (NTSB 1988; Lagasse and Richardson 2001). I-5 over Los Gatos Creek in California collapsed due to local pier scour during a flood event, but the underlying cause was channel degradation from the previous 28 years of service (Lagasse and Richardson 2001).

Each year in the United States, highway bridge failures cost millions of dollars (Lagasse et al. 1997) as a result of both direct costs necessary to replace or restore bridges and indirect costs related to disruption of transportation facilities. On-going screening and evaluation of the vulnerability of the nations' highway bridges to scour by State Departments of Transportation have identified more than 18,000 bridges that are considered scour-critical and in need of repair or replacement. Furthermore, more than 100,000 bridges over water in the United States have what is known as "unknown foundations" (Lagasse et al. 1995), which means their vulnerability to scour cannot be calculated by normal hydraulic and geotechnical analysis procedures, and there is a need for innovative, effective, and economical techniques to detect and monitor the foundation scour.

1.3.1 Scour mechanism and bridge failure modes

Scouring process excavates and carries away materials from the bed and banks of streams, and from around the piers and abutments of bridges, which may consequently cause bridge failures due to structural instability. The erosion of riverbed material at bridge sites is a result of natural stream processes, particularly seasonal variations in water depth and velocity. The factors affecting bridge scour include channel and bridge geometry, floodplain characteristics, flow hydraulics, bed materials, channel protection measures, channel stability, riprap placement, ice formations, debris, etc. It is classified into three types (Parker et al. 1997): general, contraction and local scour.

Failure of bridges due to scour at their foundations consisting of abutments and piers is a common occurrence. As result of the erosive action of flowing water, excavating and carrying away material from the bed and banks of streams and from around the piers and abutments of

bridges, there is a tendency to expose the foundations of a bridge (Richardson and Davis 2001). Such scour around pier and pile supported structures and abutments can result in structural collapse and loss of life and property. Four modes of scour failure are plunging, buckling, pushover, and kick-out (Donnée 2008).

1.3.2 Scour modeling and prediction

Bridge scour is a very complicated process which involves the interaction between the flow around a bridge pier or abutment and the erodible bed surrounding it. Thus, the effect of bridge scour depends on many factors such as the geometry of the channel, dynamic hydraulic properties of the flow, geometry of the bridge piers and abutments, etc. Deng and Cai (2010b) presented a comprehensive review on the approaches for modeling and predicting bridge scour.

To study the complicated bridge scour process, different numerical models (Melville and Raudkivi 1977; Young et al. 1998; Kassem et al. 2003) as well as laboratory models (Umbrell et al. 1998; Sheppard and William 2006) have been developed in the past few decades. Predicting bridge scour using the available information prior to or during flood events is very important in preventing catastrophic failures of bridges and possible loss of life. Two categories of methods are proposed in the literature, using empirical equations (Laursen and Toch 1956; Jain and Fischer 1979; Melville and Sutherland 1988; Lim 1997; Heza et al. 2007) and using other methods such as Neural Networks (Choi and Cheong 2006).

1.3.3 Scour detection and monitoring

The traditional scour monitoring methods are based on geophysical techniques, such as sonar, radar, time-domain reflectometry, etc. Most of them have found a limited number of applications due to difficulties in the results interpretability, high noise sensitivity and economic sustainability. The impossibility to exploit these techniques during flood events, when scour phenomenon reaches its highest magnitude, is another hard hurdle to overcome. In the early days, radar (Gorin and Haeni 1989; Millard et al. 1998; Park et al. 2004) and sonar (Mason and Shepard 1994; Hayes and Drummond 1995; De Falco and Mele 2002; Hunt 2005) were employed successfully to identify the scour depth. In recent years, techniques using Time-Domain Reflectometry (TDR) (Yankielun and Zabilansky 1999; Yu and Zabilansky 2006; Yu and Yu 2007) and fiber Bragg grating (FBG) sensors (Lin et al. 2004, 2005) have been developed and used for real-time monitoring of bridge scour. Due to the advantages over traditional sensors such as their long-term stability and reliability, resistance to environmental corrosion, and multiplexity along one single fiber (Deng and Cai 2007), Fiber optic sensors become popular in structural motoring. Lin et al. (2005) developed two types of local scour monitoring systems to monitor real-time scour, and Lu et al. (2008) also used a sliding magnetic collar (SMC) and a steel rod to monitor the total bridge scour during floods.

All the methods above appear quite promising but they still suffer from difficulties in the result interpretability, high noise sensitivity and operational limitations. A more direct approach is to investigate the scour consequences, i.e., the structural response and feature changes of the

bridge due to scour. However, till now few studies have been carried out on this topic. Zhang et al. (2005) using HHT-based approach on acceleration recordings from controlled field vibration test of piles in intact, minor-, and severe-damage states singled out some natural frequencies of the structure. Samizo et al. (2007) proposed a method to define the natural frequencies of bridges using long-term microtremor measurements made on existing bridge piers, and concluded that the natural frequencies of bridge piers decline with decreasing foundation depth during scour. Ruocci et al. (2009, 2010 and 2011) built a scaled experimental model of a two-span masonry arch bridge to investigate the effect of the central pile settlement due to riverbank erosion and to identify the most damage sensitive structural symptoms of pier erosion. In 2009, the Typhoon Parma provided Loh et al. (2011a) the opportunity to monitor the bridge response during typhoon, and later excavate a real bridge with 7 spans of 36.6m each. Later, Loh et al. (2011b) constructed a four span bridge model with simply supported girder on each pier to across a flume of 4m wide in the hydraulic lab. Han et al. (2010) studied the influence of scour on the seismic performance of foundations through several elasto-plastic static pushover analyses. Lin et al. (2010) studied scour effects on the response of laterally loaded piles considering the stress history of the remaining sand. Foti and Sabia (2011) performed numerical simulations to assess the sensibility of the overall dynamic response of the system to the foundation scour.

1.4 Overview of the dissertation

The objective of the dissertation is to develop a framework for damage identification using structure vibration measurement. Specifically, methods based on the dynamic response of static or moving vehicles on the bridge are to be investigated. The methodology is then to be applied on bridge scour analysis. The effect of bridge scour on bridge and vehicle response is to be studied first and methods for detecting and monitoring bridge scour are to be proposed. It is expected to detect the foundation scour based on the response of the bridge and foundation, or even on the response of the vehicle.

Chapter 2 discussed the framework of damage identification in four different levels, namely, the damage occurrence, damage location, damage severity, and remaining service life of the structure. It gave a guideline about the three crucial steps for this framework, namely, (1) selecting parameters and objective features, (2) building a reasonable structural model, and (3) adopting optimization techniques to solve the problem. A comparative analysis on a numerical beam with three damage scenarios was conducted to study the following aspects: how to select the parameters and decide its initial values and boundaries, which are the sensitive objective features, and the performance of different optimization techniques, followed by proposing an optimization method combined with Genetic Algorithm (GA) and First Order (FO) method. The proposed optimization method combined the global and local algorithms have shown much faster convergence and better accuracy. The methodology was then demonstrated on a bridge structure with foundation scour, which indicated good performance on detecting damage in superstructure and scour damage in pile foundation.

Chapter 3 developed the damage detection method using the transmissibility of the vehicle-bridge coupled (VBC) system since the vehicle can serve as both a force exciter and a

response receiver. The transmissibility of the VBC system was first theoretically derived in a system consisting of a simply supported beam and a single degree of freedom (SDOF) vehicle. The feasibility of using transmissibility for damage detection was then studied numerically by comparing several damage indicators from bridge responses and vehicle responses. In order to analyze the effectiveness of the selected indicator, a parametric study was conducted on factors such as measurement numbers, road roughness, vehicle speeds, and numbers of vehicles. Based on the numerical study, two methods were proposed for damage detection in a VBC system, and numerical analyses were carried out to study the feasibility of both methods, which shows good results.

Chapter 4 proposed a method to extract the bridge modal properties from the dynamic response of moving vehicles. A testing vehicle consisting of a tractor and two following trailers was proposed. The two trailers towed by the tractor moving along the bridge are used for recording dynamic responses. Furthermore, the residual response of the two trailers is processed with Fourier transform, wavelet analysis and Short-time Fourier Transform (STFT) to extract bridge modal properties. The residual response of the two trailers was derived first in the analytical form and the Short-time Fourier Transform was applied to obtain the time-frequency representation of the response. Numerical studies were then conducted to demonstrate and verify the concept, followed with parametric studies to design a proper test vehicle. For a further verification, the proposed method was applied on a field bridge with measured road roughness, and two vehicle models were proposed to simulate the tractor-trailer test system.

Chapter 5 studied the scour effect on a single pile or pier. A theoretical solution was derived first to obtain the relationship between the scour depth and the pile response including static and dynamic responses. Since the expression of the solution is tedious and not easy to understand, two examples were used for the demonstration and parametric study. Based on the numerical observation, the present study proposed three possible methods for detecting and monitoring the bridge scour. Finally, a monitoring system using fiber optic sensors was designed and tested in the laboratory to verify the theoretical and numerical results and the monitoring mechanisms.

Chapter 6 proposed and compared three designs for a scour monitoring system using fiber Bragg grating (FBG) sensors to measure and monitor scour depth variations including deposition (refilling) process. By a comparative study, one of them is recommended in the present study and its instrumentation manufacture process is also introduced in details. Using this recommended design, the advantages of FBG sensors for monitoring can be fully utilized. Both scour depth variations and entire scour development process including deposition process can be correctly monitored in real time by continuously identifying the locations of emerging FBG sensors from the riverbed. A reliable sensor protection measure is also designed for FBG sensors in harsh environments, especially in floods. Finally, a verification test using a flume is carried out in the laboratory and three experimental cases are conducted to demonstrate the capability of FBG sensors and applicability of the recommended scour monitoring system.

Chapter 7 investigated the scour effect on the entire bridge response including the superstructure and the substructure, and even the vehicle response traveling on the bridge. The foundation soil was simulated as spring elements with p-y curves for its stiffness, and the scour effect was modeled by the removing of spring elements. Then a field bridge with scour history was analyzed. As the pile configuration of the bridge foundation consists of inclined and square piles, the water force was calculated by modified Morison equation. Free vibrations and dynamic analyses under water flow were conducted on a single pile and pile groups with different scour depth. Finally, the vehicle-bridge-wave interaction was analyzed by incorporating the water flow as a time-variant force into the vehicle-bridge coupled equation. The response of bridge and vehicle were all obtained.

In the end, conclusions of this dissertation are summarized in Chapter 8 and possible future research is also recommended.

1.5 References

Barton, R. R. (2009). "Simulation optimization using metamodels." Proceedings of the 2009 Winter Simulation Conference.

Beck, J. L., Au, S. K., Vanik, M. W. (2001). "Monitoring structural health using a probabilistic measure." Computer-Aided Civil and Infrastructure Engineering, 16(1), 1-11.

Blejwas, T. E., Feng, C. C., and Ayre, R. S. (1979). "Dynamic interaction of moving vehicles and structures." Journal of Sound and Vibration, 67, 513-521.

Brownjohn, J. M. W., Xia, P. Q., Hao, H., Xia, Y. (2001). "Civil structure condition assessment by FE model updating: methodology and case studies." Finite Elements in Analysis and Design, 37, 761-775.

Brownjohn, J. M. W., Moyo, P., Omenzetter, P., and Lu, Y. (2003). "Assessment of highway bridge upgrading by dynamic testing and finite-element model updating." J. of Bridge Engineering, ASCE, Vol.8, 3, 162-172.

Bu, J. Q., Law, S. S., and Zhu, X. Q. (2006). "Innovative bridge condition assessment from dynamic response of a passing vehicle." J. of Engineering Mechanics 12: 1372-1379.

Canales, G., Mevel, L., Basseville, M. (2009). "Transmissibility Based Damage Detection." Proceedings of the 27th International Operational Modal Analysis Conference (IMAC XXVII), Orlando, Florida, U.S.A.

Cardenl, E. P., and Fanning, P. (2004). "Vibration Based Condition Monitoring: A Review." Structural Health Monitoring, 3(4), 355-377.

Choi, S. U., and Cheong, S. (2006). "Prediction of local scour around bridge piers using artificial neural networks." J. Am. Water Resour. Assoc., 42, 2, 487–494.

Cornwell, P. J., Dobeling, S. W., Farrar, C. R. (1999). "Application of the strain energy damage detection method to plate-like structures." J. of Sound Vibration, 224(2), 359–74.

De Falco, F., and Mele, R. (2002). "The monitoring of bridges for scour by sonar and sedimetri." NDT and E International, 35(2), 117-123.

Deng, L., and Cai, C. S. (2007) "Applications of fiber optic sensors in civil engineering." Structural Engineering and Mechanics, An International Journal 25(5), 577-596.

Deng, L., and Cai, C. S. (2010a). "Bridge model updating using response surface method and genetic algorithm." J. of Bridge Eng., ASCE, 15(5), 553-564.

Deng, L., and Cai, C. S. (2010b). "Bridge scour: prediction, modeling, monitoring, and countermeasures--review." Practice Periodical on Structural Design and Construction, ASCE, Vol. 15, No. 2, pp. 125–134.

Devriendt, C., Vanbrabant, Guillaume, P. (2007). "The use of transmissibility measurements in output-only modal analysis." Mechanical Systems and Signal Processing, 21, 2689-2696.

Devriendt, C., De Sitter, Vanlanduit, S., Guillaume, P. (2009). "Operational modal analysis in the presence of harmonic excitations by the use of transmissibility measurements." Mechanical Systems and Signal Processing, 23, 621-635.

Devriendt, C., De Sitter, G., Guillaume, P. (2010). "An operational modal analysis approach based on parametrically identified multivariable transmissibilities." Mechanical Systems and Signal Processing, 24, 5, 1250-1259.

Dionisio, B. (2002). "Load vectors for damage localization." Journal of Engineering Mechanics, 128(1), 7–14.

Doebling, S. W., Farrar, C. R., and Prime, M. B. (1998). "A summary review of vibration-based damage identification methods." Shock and Vibration Digest, 30, 91-105.

Donnée, N. E. (2008). "Automated screening tool for stability of highway bridges subject to scour." Master thesis, Auburn University, Auburn, Alabama, USA.

Esfandiari, A., Bakhtiari-Nejad, F., Rahai, A., Sanayei, M. (2009). "Structural model updating using frequency response function and quasi-liner sensitivity equation." J. of Sound and Vibration, 326, 557-573.

Esfandiari, A., Bakhtiari-Nejad, F., Sanayei, M., Rahai, A. (2010). "Structural finite element model updating using transfer function data." Computer and Structures, 88, 54-64.

Ewins, D. J. (1984). "Modal testing: theory and practice." England: Research Studies Press Ltd.

Fan, W., and Qiao, P. Z. (2011). “Vibration-based damage identification methods: a review and comparative study." Structural Health Monitoring, 10: 83-111.

Fanning, P., and Carden, E. P. (2001). “Auto-regression and statistical process control techniques applied to damage indication in telecommunication masts.” Key Engineering Materials, 204–205, 251–260, ISSN 0045-7949.

Farrar, C. R., and James, G. H. (1997). “System identification from ambient vibration measurements on a bridge.” Journal of Sound and Vibration, 205, 1–18.

Fogel, L. J., Owens, A. J., and Walsh, M. J. (1966). “Artificial intelligence through simulated evolution.” John Wiley & Sons, New York.

Foti, S., and Sabia, D. (2011). “Influence of foundation scour on the dynamic response of an existing bridge.” Journal of Bridge Engineering, 16, 295-304.

Friswell, M. I., and Mottershead, J. E. (1995). “Finite element model updating in Structural Dynamics.” Kluwer Academic, Norwell, MA, 1995.

Friswell, M. I., Inman, D. J., and Pilkey, D. F. (1997). “Direct updating of damping and stiffness matrices.” AIAA Journal, Vol.36, 3, 491-493.

Gandomi, A. H., Sahab, M. G., Rahaei, A., and Gorji M. S. (2008). “Development in mode shape based structural fault identification technique.” World Applied Sciences Journal, 5 (1): 29-38.

Gardner-Morse, M. G., and Huston, D. R. (1993). “Modal identification of cable stayed pedestrian bridge.” Journal of Structural Engineering, ASCE, 119 (11), 3384-3404.

Goel, T. (2007). “Multiple surrogates and error modeling in optimization of liquid rocket propulsion components.” Ph.D. dissertation, University of Florida.

Gorin, S. R., and Haeni, F. P. (1989). “Use of surface-geophysical methods to assess riverbed scour at bridge piers.” U.S. Geological Survey Water-Resources Investigations Report 88-4212, 33 p.

Guo, W. H., and Xu, Y. L. (2001). “Fully computerized approach to study cable-stayed bridge-vehicle interaction.” Journal of Sound and Vibration, 248(4), 745-761.

Han, Z. F., Ye, A. J., and Fan, L. C. (2010). “Effects of riverbed scour on seismic performance of high-rise pile cap foundation.” Earthquake engineering and engineering vibration, Vol.9, No.4, 533-543.

Hayes, D. C., and Drummond, F. E. (1995). ‘‘Use of fathometers and electrical-conductivity probes to monitor riverbed scour at bridges and piers.’’ Water Resource Investigations Rep. No. 94-4164, U.S. Geological Survey, Hartford, Connecticut.

Heza, Y. B. M., Soliman, A. M., and Saleh, S. A. (2007). "Prediction of the scour hole geometry around exposed bridge circular-pile foundation." J. Eng. Appl. Sci., 54, 4, 375–392.

Holland, J. H. (1975). "Adaptation in natural and artificial systems." University of Michigan Press.

Hu, H., Wang, B. T., Lee, C.H., Su, J. S. (2006). "Damage detection of surface cracks in composite laminates using modal analysis and strain energy method." Composite Structure, 74, 399–405.

Hu, H., Wang, J. (2009). "Damage detection in woven fabric composite laminates using modal strain energy method." Engineering Structure, 31, 1042–1055.

Hu, H. W., Wu, C. B., Lu, W. J. (2011). "Damage detection of circular hollow cylinder using modal strain energy and scanning damage index methods." Computers and Structures, 89 (2011), 149–160.

Hunt, B. E. (2005). "Scour monitoring programs for bridge health." The 6th International Bridge Engineering Conference: Reliability, Security, and Sustainability in Bridge Engineering, Transportation Research Board, p 531-536, Boston, MA, USA.

Jain, S. C., and Fischer, E. E. (1979). "Scour around bridge piers at high Froude numbers." Rep. No. FHWA-RD-79-104, Federal Highway Administration, Washington D.C.

Jaishi, B., Ren, W. W. (2006). "Damage detection by finite element model updating using modal flexibility residual." J. of Sound and Vibration, 290, 369-387.

Jaishi, B., and Ren, W. X. (2007). "Finite element model updating based on eigenvalue and strain energy residuals using multiobjective optimization technique." Journal of Mechanical systems and signal processing, 21, 2295-2317.

Kassem, A., Salaheldin, T. M., Imran, J., and Chaudhry, M. H. (2003)."Numerical modeling of scour around artificial rock island of Cooper River Bridge." Transp. Res. Rec., 1851, 45–50.

Kim, C. K., Toshinami, T., McGetrick, P. J. (2011). "Experimental investigation of drive-by bridge inspection." 5th International Conference on Structural Health Monitoring of Intelligent Infrastructure (SHMII-5), Dec. 11-15, 2011, Cancun, Mexico.

Kim, G. H., Park, Y. S. (2004). "An improved updating parameter selection method and finite element model update using multiobjective optimization technique." Mechanical Systems and Signal Processing, 18, 59-78.

Krishna, V. (2009). "Structural optimization using ANSYS classic and radial basis function based response surface model." Master thesis, Department of mechanical engineering, University of Texas at Arlington.

Lagasse, P. F., Thompson, P. L., and Sabol, S. A. (1995). "Guarding Against Scour." Civil Engineering Magazine, 65(6), 56–59.

Lagasse, P. F., Richardson, E. V., Schall, J. D., and Price, G. R. (1997). "Instrumentation for measuring scour at bridge piers and abutments." National Cooperative Highway Research Program (NCHRP) Report No. 396, Transportation Research Board, Washington, D.C.

Lagasse, P. F., and Richardson, E. V. (2001). "ASCE compendium of stream stability and bridge scour papers." Journal of Hydraulic Engineering, 12797: 531-533

Laursen, E. M., and Toch, A. (1956). "Scour around bridge piers and abutments." Vol. 4, Iowa Highway Research Board, Ames, Iowa.

Law, S. S., Li, X. Y., Zhu, X. Q., Chan, S. L. (2005). "Structural damage detection from wavelet packet sensitivity." Engineering Structures, 27(9), 1339–1348.

Lee, D. H., Hwang, W. S. (2003). "Parametric optimization of complex systems using a multi-domain FRF-based sub structuring method." Computers and Structures, 81, 2249–2257.

Lee, J. J., Lee, J. W., Yi, J. H., Yun, C. B., and Jung, H. Y. (2005). "Neural networks-based damage detection for bridges considering errors in baseline finite element models." Journal of Sound and Vibration, 280, 555–578.

Lee, Y., and Chung, M. (2000). "A study on crack detection using eigenfrequency test data." Computers and Structures, 77, 327–342.

Lew, J. S. (1995). "Using transfer function parameter changes for damage detection of structures." AIAA Journal, 33, 2189–2193.

Li, G. Q., Hao, K. C., Lu, Y., and Chen, S. W. (1999). "A flexibility approach for damage identification of cantilever-type structures with bending and shear deformation." Computers and Structures, 73, 565–572.

Li, W., Padula, S. (2005). "Approximation methods for conceptual design of complex systems." Approximation Theory XI: Gatlinburg, (eds. Chui C, Neaumtu M, Schumaker L), Nashboro Press, Brentwood, TN, pp241-278.

Lim, S. Y. (1997). "Equilibrium clear-water scour around an abutment." J. Hydraul. Eng., 123, 3, 237–243.

Lin, C., Bennett, C., Han, J., Parsons, R. L. (2010). "Scour effects on the response of laterally loaded piles considering stress history of sand." Computers and Geotechnics, 37, 1008-1014.

Lin, C. W., Yang, Y. B. (2005). "Use of a passing vehicle to scan the fundamental bridge frequencies: an experimental verification." Engineering Structures, 27, 1865-1878.

Lin, Y. B., Chang, K. C., Lai, J. S., and Wu, I. W. (2004). "Application of optical fiber sensors on local scour monitoring." Proceedings of the IEEE Sensors 2004, 2, p 832-835, Vienna, Austria.

Lin, Y. B., Chen, J. C., Chang, K. C., Chen, J. C., and Lai, J. S. (2005). "Real-time monitoring of local scour by using fiber Bragg grating sensors." Smart Materials and Structures, 14(4), 664-670.

Loh, C. H., Wu, F. M., Chao, S. H. (2011a). "In situ structural health monitoring for bridges under ambient stimulus: effect of scouring." The Engineering Mechanics Institute 2011 Conference, June 2-4, Boston, USA.

Loh, C. H., Weng, J. H., Liu, Y. C., Lin, P. Y., and Huang, S. K. (2011b). "Structural damage diagnosis based on on-line recursive stochastic subspace identification." Smart Materials and Structures, 20,

Lu, C. J., Hsu, Y. T. (2002). "Vibration analysis of an inhomogeneous string for damage detection by wavelet transform." International Journal of Mechanical Sciences, 44(4), 745–754.

Lu, J. Y., Hong, J. H., Su, C. C., Wang, C. Y., and Lai, J. S. (2008). "Field measurements and simulation of bridge scour depth variation during floods." Journal of Hydraulic Engineering, 134(6), 810-821.

Lu, Z. R., Liu, J. K., Huang, M., Xu, W. H. (2009). "Identification of damages in coupled beam systems from measured dynamic response." Journal of Sound and Vibration, 326, 177-189.

Lu, Z. R., Huang, M., Chen, W. H. Liu, J. K., Ni, Y. Q. (2010). "Assessment of local damages in box-girder bridges using measured dynamic responses of passing vehicle." Prognostics and Health Management Conference, Jan. 12-14, 2010, Macao, China.

Lu, Z. R., Liu, J. K. (2011). "Identification of both structural damages in bridge deck and vehicle parameters using measured dynamic response." Computers and structures, Vol.89, 13-14, 1397-1405.

Maeck, J., and De Roeck, G. (1999). "Dynamic bending and torsional stiffness derivation from modal curvatures and torsion rates." Journal of Sound and Vibration, Vol. 225, issue 1, pp153-170.

Maia, N. M. M., Almeida, R. A. B., Urgueira, A. P. V., Sampaio, R. P. C. (2011). "Damage detection and quantification using transmissibility." Mechanical System and Signal Processing, 25, 2475-2483.

Mason, R. R., and Shepard, D. M. (1994. "Field performance of an acoustic scour-depth monitoring system." Proceeding of Fundamentals and Advancements in Hydraulic Measurements and Experimentation, p 366–375, New York, USA.

Melville, B. W., and Raudkivi, A. (1977). "Flow characteristics in local scour at bridge piers." J. Hydraul. Res., 15, 4, 373–380.

Melville, B. W., and Sutherland, A. J. (1988). "Design method for local scour at bridge piers." J. Hydraul. Eng., 114, 10, 1210–1226.

Millard, S. G., Bungey, J. H., Thomas, C., Soutsos, M. N., Shaw, M. R., and Patterson, A. (1998). "Assessing bridge pier scour by radar." NDT and E International, 31(4), 251-258.

Mottershead, J. E., and Friswell, M. I. (1993). "Model updating in structural dynamics: a survey." J. of Sound and Vibration, 167(2), 347-375.

Oh, B. H., and Jung, B. S. (1998). "Structural damage assessment with combined data of static and modal tests." Journal of Structural Engineering, 124(8), 956–965.

Pandey, A., Biswas, M., and Samman, M. (1991). "Damage detection from changing in curvature mode shapes." Journal of Sound and Vibration, Vol.145, No.2, pp321-332.

Pandey, A. K., and Biswas, M. (1994). "Damage detection in structures using changes in flexibility." Journal of Sound and Vibration, 169, 3–17.

Park, I., Lee, J., and Cho, W. (2004). "Assessment of bridge scour and riverbed variation by a ground penetrating radar." Proceedings of the Tenth International Conference Ground Penetrating Radar, GPR 2004, p 411-414, Delft, Netherlands.

Parker, G. W., Bratton, L., and Armstrong, D. S. (1997). "Stream stability and scour assessments at bridges in Massachusetts." U.S. Geological Survey Open File Report No. 97-588 (CD-ROM), Massachusetts Highway Dept. Bridge Section, Marlborough, Mass., 53.

Pérez, C. G., and González, J. Y. (2011). "Identification of structural damage in a vehicular bridge using artificial neural networks." Structural Health Monitoring 2011 10: 33 originally published online 23 March 2010.

Queipo, N. V., Haftka, R. T., Shyy, W., Goel, T., Vaidyanathan, R., Tucker, P. K. (2005). "Surrogate-based analysis and optimization." Progress in Aerospace Sciences, 41(1), 1-28.

Rajasekaran, S., Varghese, S. P. (2005). "Damage detection in beams and plates using wavelet transforms." Computers and Concrete, 2 (6), 481–498.

Ren, W. X. and De Roeck, G. (2002a). "Structural damage identification using modal data. I: Simulation verification." Journal of Structural Engineering, 128(1), 87–95.

Ren, W. X. and De Roeck, G. (2002b). “Structural damage identification using modal data. II: Testverification.” Journal of Structural Engineering, 128(1), 96–104.

Richardson, E. V., and Davis, S. R. (2001). “Evaluating scour at bridges (3rd ed.).” Federal Highway Administration Hydraulic Engineering Circular No. 18, FHWA-IP-90-017, 203, Washington, DC.

Ruocci, G., Ceravolo, R., and De Stefano, A. (2009). “Modal identification of an experimental model of masonry arch bridge.” Key Engineering Materials, Vol.413-414, 707–714.

Ruocci, G. (2010). “Application of the SHM methodologies to the protection of masonry arch bridges from scour.” PhD Thesis, Department of Structural and Geotechnical Engineering, Politecnico di Torino, Italy.

Ruocci, G., Quattrone, A., and De Stefano, A. (2011). “Multi-domain feature selection aimed at the damage detection of historical bridges.” The 9th International Conference on Damage Assessment of Structures (DAMAS 2011), Journal of Physics: Conference Series 305 (2011) 012106.

Rytter, A. (1993). “Vibration based inspection of civil engineering structures.” Ph. D. Dissertation, Department of Building Technology and Structural Engineering, Aalborg University, Denmark.

Salawu, O. S. (1997). “Detection of structural damage through changes in frequency: a review.” Engineering Structures, 19(9), 718–723.

Samizo, M., Watanabe, S., Fuchiwaki, A., Sugiyama, T. (2007). “Evaluation of the structural integrity of bridge pier foundations using microtremors in flood conditions.” QR of RTRI, Vol. 48, No.3, 153-157.

Schittkowski, K. (1985). “NLPQL: A fortran subroutine solving constrained nonlinear programming problems.” Annals of Operations Research, 5, 485–500.

Sheppard, D. M., and William, M., Jr. (2006). “Live-bed local pier scour experiments.” J. Hydraul. Eng., 132, 7, 635–642.

Shirhole, A. M., and Holt, R. C. “Planning for a comprehensive bridge safety program, transportation research record 1290.” Transportation Research Board, National Research Council, Washington, D.C., 1, 39-50, 1991.

Shi, X., Cai, C. S., and Chen, S. (2008). "Vehicle induced dynamic behavior of short-Span slab bridges considering effect of approach slab condition." J. of Bridge Engineering, 13(1), 83-92.

Shi, Z. Y., Law, S. S., Zhang, L. M. (1998). “Structural damage localization from modal strain energy change.” J. of Sound Vibration, 218(5), 825–844.

Shi, Z. Y., Law. S. S., Zhang, L. M. (2000). "Structural damage detection from modal strain energy change." J. of Engineering Mechanics, 126(12), 1216–1223.

Shi, Z. Y., Law. S. S., Zhang, L. M. (2002). "Improved damage quantification from elemental modal strain energy change." J. of Engineering Mechanics, 128(5), 521–529.

Sohn, H., Farrar, C., Hunter, N., and Worden, K. (2003). "A review of structural health monitoring literature: 1996–2001." Los Alamos National Laboratory report, (LA-13976-MS).

Srinivas, V., Ramanjaneyulu, K., and Jeyasehar, C.A. (2010). "Multi-stage approach for structural damage identification using modal strain energy and evolutionary optimization techniques." Structural Health Monitoring online First, published on June 14, 2010.

Stubbs, N., Kim, J. T., Topole, K. (1992). "An efficient and robust algorithm for damage localization in offshore platforms." Proceedings ASCE 10th structures congress, 543–6.

Stubbs, N., Kim, J. T., Farrar, C.R. (1995). "Field verification of a non-destructive damage localization and severity estimation algorithm." Proceedings of 13th international modal analysis conference, 210–8.

Tarricone, P. (1990). "Bridges under surveillance." Civil engineering. ASCE, 60(5), 48-51.

Teughels, A., and De Roeck, G. (2005). "Damage detection and parameter identification by finite element model updating." Archives of Computational Methods in Engineering, Vol.12, 2, 123-164.

Timoshenko, S., Young, D. H., and Weaver, W. (1974). "Vibration problems in engineering." Wiley, New York.

Umbrell, E. R., Young, G. K., Stein, S. M., and Jones, J. S. (1998). "Clear-water contraction scour under bridges in pressure flow." J. Hydraul. Eng., 124, 2, 236–240.

Vestroni, F., Capecchi, D. (2000). "Damage detection in beam structure based on frequency measurements." Journal of Engineering Mechanics, 126(7), 761–768.

Wahab, M. M. A., and De Roeck, G. (1999). "Damage detection in bridges using modal curvatures: applications to a real damage scenario." Journal of Sound and Vibration, 226(2), 217–235.

Wang, T. L., and Zong, Z. H. (2002). "Improvement of evaluation method for existing highway bridges." Research Report No. FL/DOT/RMC/6672-818.

Wang, Z., Lin, R. M., Lim, M. K. (1997). "Structural damage detection using measured FRF data." Computer Methods in Applied Mechanics and Engineering, 147, 187–197.

West, W. M. (1984). “Illustration of the use of modal assurance criterion to detect structural changes in an orbiter test specimen.” In the Proceedings of the Air Force Conference on Aircraft Structural Integrity, pp.1-6.

Wu, D., and Law, S. S. (2004). “Damage localization in plate structures from uniform load surface curvature.” Journal of Sound and Vibration, 276, 227–244.

Wu, D., and Law, S. S. (2005). “Sensitivity of uniform load surface curvature for damage identification in plate structures.” Journal of Vibration and Acoustics-Transactions of the ASME, 127, 84–92.

Xu, Y. L., Chen, J. (2004). “Structural damage detection using empirical modes decomposition: Experimental investigation.” Journal of Engineering Mechanics-ASCE, 130 (11), 1279–1288.

Yan, Y. J., Cheng, L., Wu, Z. Y., Yam, L. H. (2007). “Development in vibration-based structural damage detection technique.” Mechanical systems and signal processing, 21, 2198-2211.

Yan, Y. J., Yam, L. H. (2002). “Online detection of crack damage in composite plates using embedded piezoelectric actuators/sensors and wavelet analysis.” Composite Structures, 58 (1), 29–38.

Yang, J. N., Lei, Y., Lin, S., Huang, N. (2004). “Hilbert–Huang based approach for structural damage detection.” Journal of Engineering Mechanics-ASCE, 130(1), 85–95.

Yang, Y. B., Lin, C. W., Yau, J. D. (2004). “Extracting bridge frequencies from the dynamic response of a passing vehicle.” J. of Sound and Vibration, 272, 471-493.

Yang, Y. B., Chang, K. C. (2009a). “Extraction the bridge frequencies indirectly from a passing vehicle: parametric study.” Engineering Structures, 31, 2448-2459.

Yang, Y. B., Chang, K. C. (2009b). “Extraction of bridge frequencies from the dynamic response of a passing vehicle enhanced by the EMD technique.” J. of Sound and Vibration, 322, 718-739.

Yang, Y. B., Chen, Y. J. (2009c). “A new direct method for updating structural models based on measured modal data.” Engineering Structures, 31, 32-42.

Yang, Y. B., Li, Y. C., Chang, K. C. (2012). “Using two connected vehicles to measure the frequencies of bridges with rough surface: a theoretical study.” Acta Mech, 223, 1851-1861.

Yang, Y. B., Chang, K. C., Li, Y. C. (2013). “Filtering techniques for extracting bridge frequencies from a test vehicle.” Engineering Structures, 48, 353-362.

Yankielun, N. E., and Zabilansky, L. (1999). “Laboratory investigation of time-domain reflectometry system for monitoring bridge scour.” Journal of Hydraulic Engineering, 125(12), 1279-1284.

Young, G. K., Dou, X., Saffarinia, K., and Jones, J. S. (1998). “Testing abutment scour model.” Proc., 1998 International Water Resources Engineering Conf., Vol. 1, Memphis, Tenn., 180–185.

Yu, X., and Yu, X. (2007). “Algorithm for time domain reflectometry bridge scour measurement system.” The 7th International Symposium on Field Measurements in Geomechanics, FMGM 2007, p 1-10, Boston, MA, USA.

Yu, X., and Zabilansky, L. J. (2006). “Time domain reflectometry for automatic bridge scour monitoring.” Geotechnical Special Publication, 149, 152-159.

Yuen, K. V., Beck, J. L., Katafygiotis, L. S. (2006). “Efficient model updating and monitoring methodology using incomplete modal data without mode matching.” Special issue in memory of Prof. T.K. Caughey, J. Structural Control and Monitoring, 2006; 13(1): 91-107.

Zhang, K. Y., Gu, A. J., and Li, J. W. (1992). “Diagnosis of a slot fault on a frame structure.” Proceedings of l0th international Modal Analysis Conference, San Diego, California, I, 549-553.

Zhang, K. Y., Cheng, L. J,. and Jin, T. X. (1993). “'Research on the diagnosis of defect on a building foundations pile.” Proceedings of 11th international Modal Analysis Conference, Kissimmee, Florida, I, 690-695.

Zhang, R. R. C., King, R., Olson, L., Xu, Y. L. (2005). “Dynamic response of the Trinity River Relief Bridge to controlled pile damage: modeling and experimental data analysis comparing Fourier and Hilbert-Huang techniques.” Journal of Sound and Vibration, 285, 1049-1070.

Zhang, Z., and Aktan, A. E. (1998). “Application of modal flexibility and its derivatives in structural identification.” Research in Nondestructive Evaluation, 10, 43–61.

Zhang, Y., Wang, L. Q., Xiang, Z. H. (2012). “Damage detection by mode shape squares extracted from a passing vehicle.” J. of Sound and Vibration, 331, 291-307.

Zhang, Y., Lie, S. T., Xiang, Z. H. (2013). “Damage detection method based on operating deflection shape curvature extracted from dynamic response of a passing vehicle.” Mechanical System and Signal Processing, 35, 238-254.

CHAPTER 2. FRAMEWORK OF VIBRATION-BASED DAMAGE DETECTION AND AN IMPROVED OPTIMIZATION METHOD

2.1 Introduction

Deterioration and degradation of structures is a great concern worldwide. According to the U.S. Department of Transportation, of the 600,905 bridges across the country as of December 2008, 72,868 (12.1%) were categorized as structurally deficient and 89,024 (14.8%) were categorized as functionally obsolete (AASHTO 2008). These deficient structures potentially endanger the safety and economical use of the highway system, and even develop to bridge collapse if damages are not detected at the early stage. Although the National Bridge Inspection Standards (NBIS) regulates that every bridge on a public road must be inspected as least every 2 years, a reliable and effective damage detection technique is still crucial to maintain the safety and integrity of structures.

The research on monitoring structures and detecting damage at the earliest possible stage is pervasive throughout the civil, mechanical, and aerospace engineering communities. Most nondestructive damage identification methods can be categorized as either local or global damage identification techniques. Non-destructive testing (NDT) methods can complement visual inspections as an objective method leading to quantifiable results, such as ultrasound, X-ray, dye penetrates, magnetic particle, and acoustic emission (Rens et al. 1997; McCann et al. 2001). All these experimental methods require that the vicinity of the damage is known a priori and that the portion of the structure being inspected is readily accessible. Subjected to these limitations, these experimental methods can detect damages on or near the surface of the structure. The need for more global damage detection methods that can be applied to complex structures has led to the development of methods that examine changes in the vibration characteristics of the structure.

Vibration-based damage identification was initiated in the late 1970s particularly in the aerospace and offshore oil industries, and has been rapidly expanding to civil engineering industries over the last decades. The basic idea behind this technology is that modal parameters (notably frequencies, mode shapes, and modal damping) are functions of the physical properties of the structure (mass, damping, and stiffness). Therefore, changes or damages in the physical properties will cause detectable changes in the modal properties (Doebling et al. 1998). The vibration based methods can be classified as model-based and non-model-based. As for the non-model-based method, by interpreting directly or indirectly the structural dynamic response, it establishes an analytical relationship between the damage severity and the modal parameters to detect the structural damages. Model-based methods assume that the monitored structure responds in some predetermined manner that can be accurately discretized by finite element analysis. Doebling et al. (1998) presented an extensive review of vibration-based damage identification methods up to 1998. Sohn et al. (2003) then presented an updated version of this review on the literature up to 2001. Carden and Fanning (2004) reviewed the state of the art in vibration based condition monitoring with particular emphasis on structural engineering applications. Yan et al. (2007) introduced the development of modern-type vibration-based

structural damage detection and the application of intelligent damage diagnosis. Fan and Qiao (2011) presented a comprehensive review on modal parameter-based damage identification methods for beam- or plate-type structures and conducted a comparative study of five algorithms.

This study developed a framework for damage identification, which is able to detect damage in different levels, that is, the damage occurrence, damage location, damage severity and remaining life of the structure. Three crucial steps for this method were discussed as well, namely, (1) selecting parameters and objective features, (2) building a reasonable structural model, and (3) adopting optimization techniques to solve the problem. A comparative analysis using numerical examples was then conducted to study those important components of the framework, and an optimization method combined with Genetic Algorithm and First Order method was proposed. The methodology was demonstrated on a filed bridge with foundation scour.

2.2 Framework details

The main objective of damage identification is to identify structural damages at a very early stage and predict the remaining service life of structures. Based on the amount of information provided regarding the damage state, damage identification can be classified into four levels (Rytter, 1993):

- Level 1: Identify that damage has occurred;
- Level 2: Identify that damage has occurred and determine the location of damage;
- Level 3: Identify that damage has occurred, locate the damage, and estimate its severity;
- Level 4: Identify that damage has occurred, locate the damage, estimate its severity, and determine the remaining useful life of the structure.

To date, the response-based damage identification methods primarily belong to Level 1 and Level 2 in some cases. When vibration-based methods are coupled with a structural model, Level 2 and Level 3 damage identification can be obtained. In most case, the location and extent of damage are determined simultaneously. Level 4 is generally associated with the fields of fracture mechanics, fatigue-life analysis, or structural assessment, which is not discussed in this study.

Figure 2-1 demonstrates the procedure of damage identification for the four levels. The first step is to take measurements from the structure of study and apply the response-based damage detection methods to determine the occurrence of damages. After the structure is confirmed with damages, a structure model is created using FE method or other methods. The model should be verified first to reflect the structure behavior and the global parameters of the model are updated to assure the applicability of the model. To determine damage location and size, a proper damage index or parameters should be carefully selected based on the sensitivity analysis to ensure its sensitivity to the constructed objective function. After the relationship

between the parameters and the objective function is set up, a proper optimization algorithm is introduced to solve the problem and obtain the solution. The optimization solution needs to be verified to make sure the result is physically meaningful. The above procedure could be repeated several times to obtain a reasonable result. As long as the damage is quantified, assessment methods mentioned earlier are used to evaluate the structure remaining life. More details are discussed below.

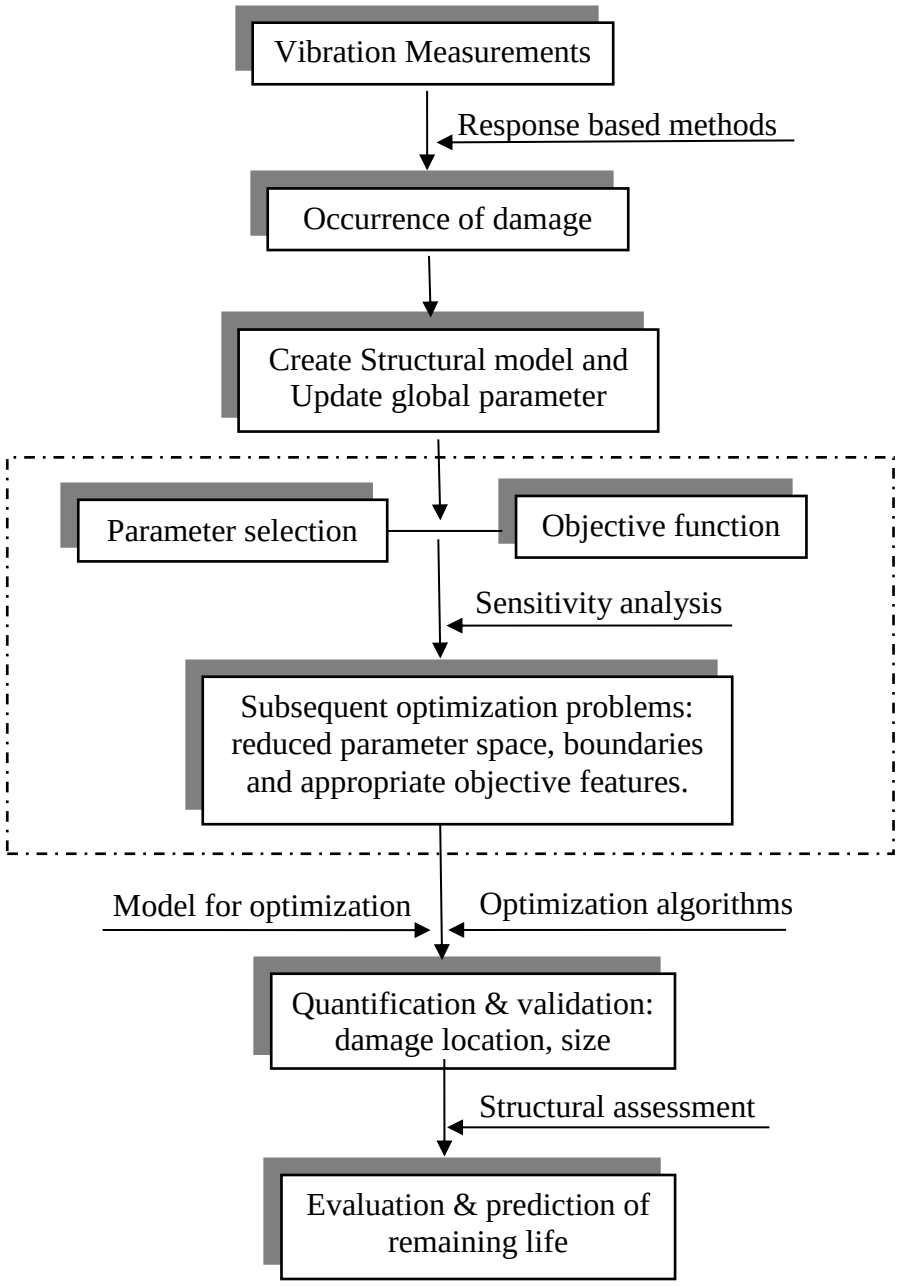

Figure 2-1. Flow chart of damage identification

2.2.1 Damage occurrence

The first level of damage identification is to determine the occurrence of damage in the structure according to the global change in structural integrity. The most popular and effective method is the response based method. By interpreting directly or indirectly the experimental response data from structures, the response based method establishes an analytical relationship between the damage severity and the modal parameters to detect the structural damages. The occurrence of damage is determined through finding the difference between the intact and damaged structures. The vibration response can be easily measured by a variety of sensors, for example, accelerometers, strain gauges etc., and the time domain data can be converted into frequency domain or modal domain data by transforming techniques. Among them, the modal domain methods gain great popularity because the modal properties (i.e., natural frequencies, modal damping, modal shapes, etc.) are physically meaningful and are thus easier to be interpreted or interrogated. The response based methods can be classified into various types, which depend on the types of the measured response.

In the time domain, several techniques were proposed to identify the eigenvalues and eigenvectors associated with each mode of vibrations on the basis of the experimentally measured responses of the structure such as the Ibrahim method (Ibrahim 1984), the random decrement (Vandiver et al. 1982), the eigensystem realization algorithm (ERA) (Juang and Pappa 1985), the Auto-Regressive (AR) or the Auto-Regressive Moving Average (ARMA) models (Ólafsson et al.1995; Ruocci 2010), and Auto-Regressive Moving Average Vector (ARMAV) model (Foti and Sabia2011). Loh et al. (2011a, 2011b, 2011c) introduced the recursive stochastic subspace identification (RSSI) technique to identify the natural frequencies. Ruocci et al. (2011) employed the Kernel Density Estimation (KDE) to characterize the correlation between the vibration signatures acquired in the time domain. All these methods as listed in Table 2-1 are aimed at the definition of a mathematical model that is able to link the theoretical response of a dynamic system to the time-history measurements of the system.

Table 2-1. Response-based methods

Domains	Excitation	Methods
Time domain	Known	Auto-Regressive (AR) Auto-Regressive Moving Average (ARMA) Ibrahim method Random decrement Eigensystem realization algorithm (ERA)
	Unknown	Stochastic Subspace Identification (SSI)
Frequency domain	Unknown	Frequency Response Function (FRF) Power Spectral Density (PSD) Transmissibility Functions (TF). Wavelet analysis, HHT
Time-frequency	Unknown	Short-time Fourier Transform (STFT)

In recent years, signal processing techniques and artificial intelligence as analysis tools are introduced to further extract information from the measured structural vibration responses. Those methods have good universality and less dependence on the structural shape, such as wavelet analysis, empirical modes decomposition (EMD) and Hilbert-Huang Transform (HHT). The main concept using wavelet analysis is to break down the dynamic signal of a structural response into a series of local basis function called wavelets, so as to detect the special characteristics of the structure using scaling and transformation property of wavelets (Lu and Hsu 2002; Yan and Yam 2002; Rajasekaran and Varghese 2005; Law et al. 2005). The method based on the EMD and HHT is intended to extract damage spikes due to a sudden change of structural stiffness from the measured data thereby detecting the damage occurring time instants and damage locations, and determining the natural frequencies and damping ratios of the structure before and after damage (Xu and Chen 2004; Yang et al. 2004).

In the frequency domain, the methods rely on the application of the Fourier Frequency Transform (FFT) that allows reducing drastically the volume of data and compensating the little loss of information by averaging the effects of random noise. The commonly selected features are the shift in the resonance and anti-resonances or changes affecting the amplitudes. In other cases, some projection techniques such as Principal Component Analysis (PCA) and linear/quadratic projections are applied to reduce the dimensionality. When the input force is unknown like in the output-only measurements, the computation of the Frequency Response Function (FRF) is substituted by the Power Spectral Density (PSD) or the Transmissibility Functions (TF). The identified natural frequencies and the sampled range of the transmissibility spectrum were used in the Outlier Analysis (OA) to identify the novelties (Manson and Worden 2003a).

2.2.2 Structural models

As the occurrence of damage has been determined, a structural model is created for a further detection. For the sake of identifying damages, the structure model is performed in two updating processes. In the first process the initial FE model is tuned to the undamaged structure, which is used as a reference model. In the second process the reference FE model is updated to reproduce the experimental modal data under the damaged state. The complexity of the structure model and the corresponding damage index depend on the type of the structure and the required detection level. In the preliminary level, a simplified FE model might be sufficient to achieve the goal, and the damage is modeled as reduction in material properties of elements such as stiffness, elastic modulus, density, section area, moment inertia, damping and etc. With the updated parameters, the FE model is able to reproduce responses close to the measured ones. The change of parameters indicates the existence of damages and can be used to roughly quantify the location and extent of damages. If the damage can be localized in a limited range, a detailed model could be built for the vicinity of the damage while other part of the structure could be simplified. The substructure method is a good alternative to build a fine model for the vicinity of the damage (Kong et al. 2012).

If the substructure method is not applicable or a FE model is not feasible, the method using the surrogate model (Mack et al. 2007; Kamali 2009), such as RSM (Menon 2005; Fang and Perera 2009; Deng and Cai 2010; Ren et al 2010, 2011), Kriging (Gao et al 2012) and RBF (Krishna 2009) method, is an option. This surrogate method replaces the structure model with an approximation model, which is traditionally a polynomial function describing the relation between the structural response and the model parameters. It is extremely fast for convergence. It is recommended to use radial basis function for high-order nonlinear problems, Kriging for low-order nonlinear problems in high dimension spaces, and polynomial response surfaces for low-order nonlinear problems.

2.2.3 Selection of parameters

The success of FE model updating depends heavily on the selection of updating parameters that is basically made with the aim of correcting uncertainties in the model, while for damage detection the parameter selection depends on the identification level. The parameters that have to be updated in the model or serve as damage indication depend on the typology and uncertainty level. In the preliminary level, the parameters are defined as global physical properties such as the Young's modulus, material density, section area, and the moment inertia because they are directly related to the stiffness of the element. In this level, several elements can share the same parameter value or one super element can be used in the case that several close elements are expected to have similar values (Jaishi and Ren 2007, Zapico el al. 2003). As the identification becomes more local, parameters can be crack widths, the stiffness of joints, and physical properties of the uncertain elements. When the damage is located at one element, this specific element can have more than one parameters by dividing the element into small ones with different properties. The parameter selection requires a considerable physical insight into the target structures. In general, only sensitive parameters are selected, otherwise the updating process may be ill-conditioned since insufficient information is available to estimate the parameters accurately.

With respect to a single damage or discrete ones, the stiffness matrix of the whole element is assumed to decrease uniformly. The fractional change in stiffness of an element can be expressed by the damage index (Ren and De Roeck 2002). As for distributed damages, instead of adjusting the stiffness properties of all the elements separately, Teughels et al. (2002) proposed the damage function to reduce the number of unknown variables and to determine the stiffness distribution over the FE model. The updating parameters are the multiplication factors of the damage functions, and this method is useful for structures whose damage pattern can be represented by a reduction factor of the element's bending stiffness.

It is very hard to estimate the variation bound of the parameter. In FE model updating, the parameter bound is assumed as the variation of the true value for uncertain parameters (Zhang et al. 2000, 2001). In damage detection, a damage index bounded from 0 to 1 is adopted by most researchers, which assumes that the structure only deteriorates from the base value. Actually in reality, some parts of the structure are stronger than designed or enhanced by some reasons, more details are discussed next.

2.2.4 Objective features and functions

The capability of a damage identification method strongly depends on the feature used to represent the data. The best features for damage detection are typically application specific, which can come from the time, frequency and modal domains depending on the employed level of data consideration. Research into methods based on all three domains is less likely to stop because no single method has yet been found that identifies every type of damage in every type of structures (Carden and Fanning 2004). The selection of objective functions has a profound impact on the optimization problem. It not only affects the interpretation of the best correlation, but also influences the behavior of the utilized optimization algorithm (Jaishi and Ren 2007). The objective function is normally built up using the residuals between the measurement results and the numerical predictions, such as a sum of squared difference (Teughels and De Roeck 2005):

$$f(\theta) = \frac{1}{2}\sum_{j=1}^{m}\left|z_j(\theta) - \tilde{z}_j\right|^2 = \frac{1}{2}\sum_{j=1}^{m} r_j(\theta)^2 = \frac{1}{2}\left\|r(\theta)\right\|^2 \tag{2-1}$$

where each $z_j(\theta)$ represents an analytical quantity that is a nonlinear function of the variables θ. $\tilde{z}$ refers to the measured value of the quantity z. $\|\bullet\|$ denotes the Euclidean norm. In order to obtain a unique solution, the number m of residuals $r_j = z_j - \tilde{z}_j$ should be greater than the number n of unknowns θ.

Since measurements are always made in time domain, the use of time responses is less likely to be limited by data reduction problems, and the nonlinear behavior is also preserved. The direct use of time response in a model-based, iterative parametric identification procedure was proposed by Banks and Inman (1996, 1998), which is proven to be capable of detecting fairly small defects modeled as geometrical imperfections in the cross section of beams. The direct use of time histories of vehicle acceleration or bridge acceleration in sensitivity-based model updating method can be seen in Bu et al. (2006) and Lu et al. (2009, 2010, 2011). Moreover, the signals acquired from sensors can be treated as random variables and their cross-correlation are used to represent a measure of their similarity. The Probability Density Function (PDF) is the representation of the probability distribution of the residual between the two signals. The variation in the estimated peak amplitude, stand deviation, skewness and kurtosis throughout the stages experienced by a system can be employed to objectively characterize the symptomatic change of the structural state. (Ruocci et al. 2011).

The features in the frequency domain are commonly the shift in the resonance and anti-resonances or changes affecting the amplitudes. If the excitation is known, the Frequency Response Functions (FRF) can provide more information on damage in a desired frequency range compared to modal data that is extracted from a very limited range around resonances. Meanwhile, the transmissibility functions (TF) are the features selected for the damage assessment in the spectral domain, which employ only the measurement of the structural responses and do not require knowledge of the excitation input. This operational advantage is

coupled with remarkable damage sensitivity as proven in the work by Manson and Worden (2003).

Modal information can be identified from output-only data measured under operational conditions and do not require the structure to be excited by artificial forces. The modal domain methods evolve along with the rapid development of experimental modal analysis technique, and they gain their popularity because the modal properties (i.e., natural frequencies, modal damping, modal shapes, etc.) have their physical meanings and are thus easier to be interpreted or interrogated than those abstract mathematical features extracted from the time or frequency domain. The modal domain provides a large set of damage sensitive features, such as the shifts of natural frequencies, MAC or COMAC of modal shapes and derivatives (Ren and De Roeck 2002), modal strain energy (Jaishi and Ren 2007; Srinivas et al. 2010), modal strain (Unger et al. 2005), dynamic flexibility matrix, and residual force vector. It is found that including the modal curvatures in the updating procedures does not improve the convergence of the algorithm. The modal curvatures are useful parameters for damage detection when using the response-based approach (Wahab and De Roeck 1999) but not useful when using the model-based approach (Wahab 2001).

2.2.5 Sensitivity analysis

Up to now, none of those features has proven to work satisfactorily for every type of structure and for every type of damage. The optimality in the feature selection resides in a trade-off between their damage sensitiveness and the concrete possibility to ensure their consistency with the expected structural response to damage. A sensitivity study is therefore recommended to reduce the parameter space, adjust parameter boundaries and select appropriate objective features. For that purpose, the parameter screening that is the variation of a single parameter is the major tool. General Sensitivity Analysis (GSA) is typically conducted by analysts as a fast way to tell which input parameters are important to a particular output feature. Another method was the significant effects variable screening or linear variable screening. A particular input parameter's contribution (linear effects only) to the total model variance is analyzed (Cundy 2003). Significant effects method provides an advantage over GSA because it is a probabilistic assessment of variable importance that is obtained through the analysis of variance (ANOVA) (Fang and Perera 2009). The analysis of variance (ANOVA) method is to evaluate the significance of each parameter according to its statistical F-test value:

$$F_x = \frac{SS_R / k}{SS_E /(n-k-1)} \sim F_{0.05,k,n-k-1} \tag{2-2}$$

where F_x and $F_{0.05,k,n-k-1}$ denote the F-test value of an input parameter x and the selected criterion value, respectively; SS_E and SS_R are the sums of squares due to the corresponding objective value and the residual (error), respectively; k is the number of parameters and n is the number of samples. If F_A exceeds $F_{0.05,k,n-k-1}$, the variance of x can be deemed to have a significant contribution to the total variance of the objective features and thus can be determined to be a significant parameter with respect to the response. In analogy, the design of experiment methods that systematically calculate single parameters and combinations of parameters can be

used in small parameter spaces (Goel 2007; Shahsavani and Grimvall 2011). If the dimension or the nonlinearity of the parameter space increases, stochastic sampling strategies are to be favored for scanning the design space.

Sensitivity studies may enable an adjustment and reduction of the parameter space for subsequent optimization problems. The previous knowledge obtained from the sensitivity study is very helpful for a proper selection of parameters and an adequate formulation of the objective function. Finally, from the sensitivity studies design areas of admissible designs can be identified and adequate starting points for optimization can be obtained. Therefore, with a sensitivity study, the base for a successful optimization is set up.

2.2.6 Optimization algorithms

After selecting the parameters and objective features, and building up the model, the rest work is to solve the problem using optimization techniques.
Gradient-based optimization algorithms that mainly use quasi-Newton methods, such as LBFGS, NLPQL (Nonlinear Programming using a Quadratic or Linear least-square algorithm) (Schittkowski 1985) start from a predefined initial parameter set, and use line search algorithms to ensure the stepwise convergence to an optimum using gradients. Gradient-based methods are recommended for the solution of smooth nonlinear optimization problems under the following restrictions: the number of design variables should not be too large, the functions and gradients can be evaluated with sufficiently high accuracy and the problem should be smooth and well-scaled. Among all the gradient-based methods, Sequential Quadratic Programming (SQP) methods represent the state of the art for solving differentiable nonlinear programs and have gained great attention in the recent years owing to the superior rate of convergence (Schittkowski 1985; Boggs and Tolle 1995; Gould and Toint 1999). All gradient methods involve two major tasks: direction finding or where to go in the design space and step size selection or how far to go.

The formulation of an SQP is based on Newton's method and Karush-Kuhn-Tucker (KKT) optimality conditions for constrained problems that are changed to the unconstrained optimization. At each major iteration, an approximation is made of the Hessian of the Lagrangian function using a quasi-Newton updating method. This is then used to generate a QP subproblem whose solution is used to form a search direction for a line search procedure (Fletcher 2000).

$$\text{Minimize } \frac{1}{2} d^T B_k d + \nabla f(x_k)^T d \qquad (2\text{-}3)$$
$$d \in \Re : \nabla g(x_k)^T d + g(x_k) \geq 0$$

The SQP has several attractions: (1) the starting point can be infeasible. (2) Gradients of only active constraints are needed. (3) Equality constraints can be handled in addition to the inequalities. (4) And nonlinear constrained problems can be solved in less iteration than an unconstrained problem. One of the reasons for this is that, because of the limits on the feasible area, the optimizer can make informed decisions regarding directions of search and step length. Finite element based problems, which involve relatively large number of degrees of freedom and design variables are quite effectively solved using the SQP.

In contrast to the gradient-based methods, evolutionary algorithms belong to the class of stochastic search methods. They imitate natural biological evolution processes such as adaption, selection and variation. To improve the approximation of the solution of the optimization problem, a population of individuals searches the design space for possible solutions based on Darwin's principle of "survival of the fittest". The three main classes are genetic algorithms (Holland 1975), evolution strategies and evolutionary programming (Fogel et al. 1966). An advantage of these methods is that they can find a global extrema in the presence of local extrema better than other optimization methods. A drawback is the high numerical effort that becomes necessary since a large number of problem solutions are required. Evolutionary algorithms should be applied to problems where discrete or binary variables dominate the response and optimization problems with a very high number of variables and/or constraints.

2.3 Comparative study using numerical examples

A simulated simply supported beam is adopted as an example to study the important components of the damage detection framework such as parameter boundaries, sensitive parameters and objective features, different optimization algorithms, etc. Physical properties of the beam are: elastic modulus E=32GPa, mass density D=2.5e3 kg/m^3, length L= 6m, section width= 0.2m and section depth= 0.25m. Most researches of damage detection took the 1D FE model as a numerical example (Jaishi and Ren 2005; Srinivas et al. 2010; Deng and Cai 2010; Liu et al. 2011), while herein a 3D FE model was built. All the elements are divided into 15 big elements, as shown in Figure 2-2. Three damage scenarios are conceived:

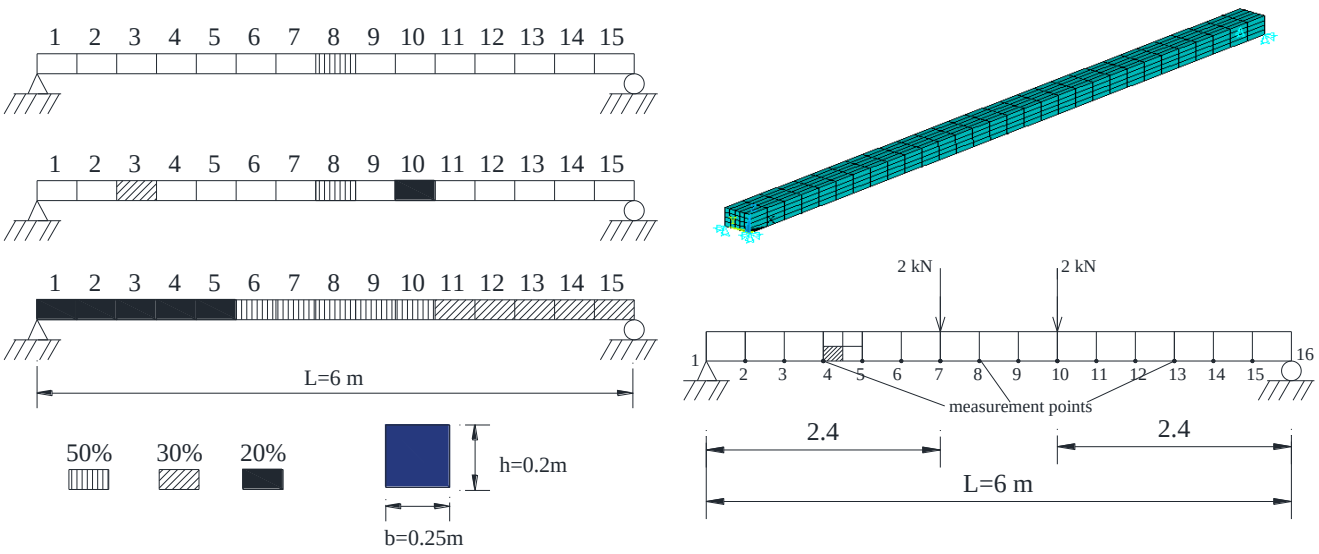

Figure 2-2. Numerical beam.

- Single damage (scenario 1): a single damage is assumed in element 8 with an elastic modulus reduction of 50%.

- Multiple damages (scenario 2): three damage locations are assumed in the beam as shown in Figure 2-2, that is, the elastic modulus of beam elements 3, 8, and 10 are reduced by 30%, 50%, and 20%, respectively.
- Distributed damage (scenario 3): all the elements have damages in different degrees, namely, the elastic modulus of elements 1~5, elements 6~10 and elements 11~15 are reduced by 20%, 50% and 30%, respectively.

The damage of the beam is represented by the reduction of elastic modulus of individual elements. Three cases of parameter numbers (Nps) are considered:

- Np=15: E of all 15 elements are selected as parameters, denoted as Ei (i=1~15), which is the case that structural damages are completely unknown.
- Np = 5: E of element 3, 7, 8, 9 and 12, denoted as Ei (i=3, 7, 8, 9, 12), which is case that some elements can be excluded from damage elements.
- Np=3: E of elements 7, 8 and 9 for scenario 1, denoted as Ei (i=7, 8, 9), and E of elements 3, 8 and 10 for scenario 2, denoted as Ei (i=3, 8, 10). It is the case that the damage locations are almost or exactly known.

Here, the optimization algorithm in ANAYS, First Order Method, was applied. This method transforms a constrained problem into an unconstrained one via penalty functions, and calculates and makes use of derivative information. Derivatives are formed for the objective function and the state variable penalty functions, leading to a search direction in design space. Various steepest descent and conjugate direction searches are performed during each iteration until convergence is reached. This method is usually seen to be more computationally demanding and more accurate.

2.3.1 Parameter ranges and initial values

Damages are defined as the stiffness reduction of assumed elements compared to the counterpart in the undamaged structure, named as damage index or stiffness reduce factor (Srinivas et al. 2010). The values of the parameters in most research fall in the range between 0 and 1. In reality the upper bound could be more than 1, which indicates the increase of the stiffness or other properties compared to the designed value. Furthermore, when using the above gradient-based optimization methods, the initial values are very crucial for the optimal results. This section compared the effect of the parameter range and initial value on the optimal result under the same objective feature, the first five modal frequencies. From the assumption of damage scenario 1, only the true value of E_8 is 0.5, the others are 1.0. For simplicity, all the parameters use the same bounds and initial values. Three cases of the parameters' upper bounds are considered as 1.0, 1.2 and 10, respectively, with three or four different initial values for each case. Table 2-2 lists the results of three cases of parameter numbers (Nps) in damage scenario 1. In this table, the "objective fitness" is the value of objective function when it converged to the optimum solution. The "average error" is the average of error between the predicted parameter value and the true value, the "maximum error" is the maximum error among all the errors, and the "damage error" is the predicted error of the damaged element.

As can be seen in Table 2-2, in general the objective fitness value and all errors of the cases with Np=3 and Np=5 are better than that of Np=15, which implies more parameter numbers will introduce more uncertainty and insensitive parameters. In cases with the upper bound of 1.0 and 10, the best initial value is 0.5 and 1.0 with small errors, while the case with upper bound of 1.2, the best initial value is 1.2. It indicates that initial values that close to the true value will results in small errors. In general, the best initial value is 1.0 that is close to the true value of most parameters.

Table 2-2. Comparison of parameter bounds and initial values, scenario 1

Bound		0≤β≤1.0			0≤β≤1.2				0≤β≤10			
Initial		0.01	0.50	1.00	0.01	0.50	1.00	1.20	0.01	0.50	1.00	10.00
Objective Fitness (×10-2)	Np15	0.51	0.43	0.23	0.15	0.13	0.18	0.15	0.35	0.20	0.29	16.04
	Np5	0.07	0.01	0.15	0.44	0.41	0.30	0.28	1.54	0.52	0.49	11.77
	Np3	0.11	0.07	0.01	0.07	0.06	0.01	0.01	0.22	0.03	0.10	1.11
Average Error (%)	Np15	2.34	2.69	0.78	13.05	14.21	7.41	7.88	20.87	14.22	7.50	225.20
	Np5	0.89	0.10	1.82	17.11	15.59	11.87	10.72	30.27	15.74	12.57	140.33
	Np3	2.17	1.43	0.23	2.16	1.04	0.22	0.22	4.96	0.60	2.09	26.33
Maximum Error (%)	Np15	15.80	21.60	5.41	23.76	40.57	22.77	23.33	39.37	40.18	22.43	802.45
	Np5	2.60	0.30	4.11	26.34	19.58	15.65	14.53	62.24	21.44	18.51	340.42
	Np3	5.22	2.12	0.56	4.12	1.78	0.52	0.41	9.33	1.31	2.60	40.92
Damage Error (%)	Np15	8.09	4.77	2.07	22.68	22.05	17.52	15.81	29.17	22.27	17.32	156.29
	Np5	0.85	0.09	1.74	13.60	12.03	7.94	6.83	62.24	14.68	11.56	62.48
	Np3	1.31	0.83	0.13	0.57	0.53	0.12	0.05	2.65	0.34	1.18	14.63

With the same initial values such as 1.0, the results become worse when the upper bounds increase. When the upper bound is larger than 1.0, the optimized results of some parameters are larger than 1.0, as listed in Table 2-3 for damage scenario 2. It indicates that the optimized result converges to a local optimum instead of the global one. The larger the parameter range is, the easier of the results converge to local optimum instead of the global optimum. It means that the larger range has a higher requirement to the optimization technique.

Table 2-3. Results of damage scenario 2

Bound	0≤β≤1.0			0≤β≤1.2				0≤β≤10			
Initial	0.01	0.50	1.00	0.01	0.50	1.00	1.20	0.01	0.50	1.00	10.00
Run	11	11	13	12	9	9	11	10	9	7	6
EX3	1.0000	0.9998	0.9918	0.8784	0.8840	0.8991	0.9100	0.8990	0.9055	0.9448	4.4042
EX7	0.9740	0.9996	0.9757	0.7366	0.8042	0.8435	0.8547	0.4248	0.8017	0.8188	0.3031
EX8	0.5085	0.5009	0.5174	0.6360	0.6203	0.5794	0.5683	1.1224	0.6468	0.6156	1.1248
EX9	0.9900	0.9970	0.9589	0.8592	0.8234	0.8795	0.8931	1.0343	0.7856	0.8149	0.7598
EX12	1.0000	0.9998	1.0000	1.1938	1.1709	1.1360	1.1252	1.1806	1.1331	1.0915	3.0504

2.3.2 Objective functions

As mentioned earlier, objective features and the constructed objective function are significant to the optimization results. Herein, the responses from both static and modal analyses are compared to investigate the sensitivity of objective features. With respect to the static response, the displacement and strain are used, while for the dynamic response, natural frequencies, mode shapes, modal strain and modal strain energy are extracted. In order to construct the objective function, two types of algorithms are introduced, Root Sum Squares (RSS) and Modal Assurance Criterion (MAC). MAC determines the correlation between two modes for all the measurement locations but has difficulty comparing modes that are close in frequency or that are measured at insufficient transducer locations (Allemang and Brown, 1982).

$$MAC(\phi_m, \phi_p) = \frac{\left|\phi_m^T \phi_p\right|^2}{(\phi_m^T \phi_m)(\phi_p^T \phi_p)} \tag{2-4}$$

where ϕ_p and ϕ_m are the predicted and measured modal shapes, respectively. Similarly, the form of MAC is also used for other features such as modal strain and modal strain energy, as described in Table 2-4.

An objective function is formed to minimize the difference between the predicted value and the measured result, $F(\beta)$. Different types of objective functions were constructed and listed in Table 2-4. The parameter vector $\beta = \{\beta_1, \beta_2, \ldots, \beta_n\}$ is the element stiffness reduction as mentioned earlier, its range is set as $0 \leq \beta_i \leq 1.0$ and initial value as $\beta_i = 1.0$.

Table 2-5 lists the results of different objective functions under all three damage scenarios (S1, S2 and S3). The second column is the iteration numbers for convergence. In terms of the feature from frequencies, the average error and maximum error in damage scenario 1 are much smaller than the other two scenarios, though the objective fitness is close. The natural frequency has prominent performance in the case of single damage (scenario 1), which means it is sensitive to a single damage. Meanwhile, the present study adopted a 3D FE model that has more modal information including lateral mode and torsion mode. The results reveal that, for the 3D model, the objective function based on frequencies of the first five modes performs better than the one based on the first five vertical modes.

Most of the objective functions based on MAC perform better in damage scenarios 1 and 2. Among them, the Modal Strain Energy (MSE) based is the best, which converges very quickly and predicts pretty accurate results with average and maximum error less than 1% in scenarios 1 and 2. It shows that MSE is a very sensitive objective feature. By Comparing with the RSS method of constructing the objective function based on the above modal features, it indicates that the MAC modal shape performs better than RSS modal shape, while the RSS modal strain performs better than the MAC modal strain. Modal shapes and modal strains are relative value instead of absolute value. Therefore, the MAC is better than the RSS to reflect their similarity.

As for the static features, the static strain shows prominent performance in all the three damage scenarios, with extremely small predicting errors.

Table 2-4. Objective functions for comparison

Objective Feature	Description	Formula
Frequencies	RSS of first N frequencies	$F = \sqrt{\sum_{i=1}^{N} \left(\frac{\lambda_{ei} - \lambda_{ai}}{\lambda_{ei}} \right)^2}$
Vertical frequencies	RSS of first N vertical frequencies	
MAC	MAC value of modal shapes	$F = 1 - \frac{1}{m} \sum_{i=1}^{m} MAC$
MAC_Vertical	MAC value of vertical modal shapes	
MAC_MXstrain	MAC value of modal strains at x direction	
MAC_MSE	MAC value of modal strain energy	
RSS_Mshape	RSS of the first mode shape	$F = \sqrt{\sum_{i=1}^{n} (\frac{d_{ei} - d_{ai}}{d_{ei}})^2}$
RSS_MXstrain	RSS of the first mode strain	
RSS_Disp	RSS of static displacement	
RSS_Xstrain	RSS of static strain	

The predicted value of parameters in three cases, first five natural frequencies (5freq), MAC value of MSE, and RSS of static strain, are selected as representatives and demonstrated in Table 2-6. As can be seen, the prediction for all three scenarios is pretty accurate, except a small deviation for natural frequencies based.

Table 2-5. Results of different objective functions

Objective Feature	Iteration #			Objective fitness			Average Error (%)			Maximum Error (%)		
	S1	S2	S3	S1	S2	S3	S1	S2	S3	S1	S2	S3
Frequencies	18	21	21	2.3E-03	1.3E-03	1.7E-03	0.78	7.37	8.16	5.41	24.30	26.18
Vertical frequencies	15	16	21	3.9E-03	1.5E-04	1.7E-03	0.92	9.69	8.16	5.81	24.27	26.18
MAC	21	40	39	3.4E-07	9.1E-06	9.6E-06	6.57	7.78	11.18	11.98	21.05	19.08
MAC_Vertical	22	27	41	2.9E-05	4.7E-07	6.0E-07	6.92	5.68	14.04	8.49	7.38	19.67
MAC_MXstrain	16	18	24	1.5E-04	2.8E-06	3.0E-06	3.39	3.86	14.49	4.91	6.42	20.00
MAC_MSE	7	7	36	8.5E-05	4.7E-07	9.5E-06	0.20	0.03	4.01	0.45	0.34	4.90
RSS_Mshape	11	40	15	1.1E-02	1.2E-02	7.6E-03	8.70	10.70	13.53	24.47	29.41	27.40
RSS_MXstrain	18	26	26	6.1E-03	6.7E-03	3.4E-03	5.24	5.50	13.32	6.62	7.16	17.49
RSS_Disp	38	47	24	6.0E-03	7.0E-03	1.6E-02	3.76	7.56	7.03	19.76	27.69	22.61
RSS_Xstrain	11	37	30	2.3E-04	2.0E-03	3.7E-03	0.005	0.02	1.55	0.03	0.11	0.43

Table 2-6. Representative results

No.	Scenario 1				Scenario 2				Scenario 3			
		5freq	MAC_ MSE	RSS_ Xstrain		5freq	MAC_ MSE	RSS_ Xstrain		5freq	MAC_ MSE	RSS_ Xstrain
EX1	1	1.0000	0.9976	1.0000	1	1.0000	0.9999	1.0000	0.8	0.7745	0.8470	0.7988
EX2	1	0.9998	0.9956	1.0000	1	0.8247	0.9999	1.0000	0.8	0.8347	0.8343	0.8016
EX3	1	0.9969	0.9955	1.0000	0.7	0.8062	0.6992	0.6989	0.8	0.7747	0.8362	0.7968
EX4	1	0.9985	0.9957	1.0000	1	0.9575	0.9966	1.0000	0.8	0.7296	0.8367	0.8039
EX5	1	1.0000	0.9966	1.0000	1	1.0000	1.0000	1.0000	0.8	0.6742	0.8370	0.7957
EX6	1	0.9924	0.9956	1.0000	1	0.9753	0.9999	1.0000	0.5	0.5844	0.5214	0.5013
EX7	1	0.9832	0.9984	0.9997	1	0.7925	0.9999	0.9997	0.5	0.4901	0.5210	0.4980
EX8	0.5	0.5207	0.4988	0.5001	0.5	0.6416	0.4997	0.4994	0.5	0.4610	0.5211	0.5019
EX9	1	0.9459	0.9993	0.9997	1	0.7570	1.0000	0.9991	0.5	0.5083	0.5211	0.4980
EX10	1	1.0000	0.9997	1.0000	0.8	0.9485	0.8003	0.7997	0.5	0.5759	0.5213	0.5015
EX11	1	1.0000	0.9992	1.0000	1	1.0000	1.0000	1.0000	0.7	0.6374	0.7315	0.6968
EX12	1	1.0000	0.9986	1.0000	1	1.0000	1.0000	1.0000	0.7	0.6908	0.7318	0.7015
EX13	1	0.9931	0.9992	1.0000	1	1.0000	1.0000	1.0000	0.7	0.7406	0.7317	0.6985
EX14	1	1.0000	0.9996	1.0000	1	0.9836	1.0000	1.0000	0.7	0.8498	0.7322	0.7017
EX15	1	0.9932	0.9999	1.0000	1	1.0000	1.0000	1.0000	0.7	0.9618	0.7490	0.6981

2.3.3 Optimization techniques

Optimization algorithms can generally be categorized into global and local ones. The local method applies to the convex problem that has only one extremum. The global method has the capability to find the global extremum in the presence of many local extrema. This section compares the performance of two local methods, the First Order (FO) in ANSYS and Sequential Quadratic Programming (SQP) in MATLAB, and one global method, Genetic Algorithm (GA). The parameters are with the range of $0 \leq \beta_i \leq 1.0$ and initial value of $\beta_i = 1.0$. Results of three damage scenarios are shown in Table 2-7.

As for a single damage (scenario 1), the FO and SQP methods with proper initial values easily converge to the true values, except for the GA method that has the largest predicted error. In multiple damages (scenario 2) and distributed damages (scenario 3), the FO and SQP methods perform much better than the GA method, although their error is also large. Based on the performance, we can say that the global GA method is not suitable for the present problem, while FO and SQP methods with appropriate initial values prove themselves their capability in local optimization.

Table 2-7. Results of different optimization algorithms

	Scenario 1					Scenario 2					Scenario 3				
No.	True	FO	SQP	GA	GAFO	True	FO	SQP	GA	GAFO	True	FO	SQP	GA	GAFO
EX1	1	1.00	1.00	0.98	1.00	1	1.00	1.00	0.96	1.00	0.8	0.77	0.77	0.88	0.77
EX2	1	1.00	1.00	0.73	1.00	1	0.82	0.79	0.87	0.87	0.8	0.83	0.82	0.96	0.78
EX3	1	1.00	1.00	1.00	1.00	0.7	0.81	0.82	0.97	0.76	0.8	0.77	0.77	0.69	0.78
EX4	1	1.00	1.00	0.93	1.00	1	0.96	0.97	0.94	0.99	0.8	0.73	0.77	1.00	0.76
EX5	1	1.00	1.00	0.94	1.00	1	1.00	0.95	0.88	1.00	0.8	0.67	0.70	0.98	0.69
EX6	1	0.99	1.00	0.99	1.00	1	0.98	1.00	1.00	0.99	0.5	0.58	0.55	0.49	0.44
EX7	1	0.98	1.00	0.92	0.95	1	0.79	0.85	0.98	0.81	0.5	0.49	0.46	0.93	0.66
EX8	0.5	0.52	0.50	0.64	0.52	0.5	0.64	0.63	0.91	0.61	0.5	0.46	0.48	0.59	0.42
EX9	1	0.95	1.00	0.99	0.99	1	0.76	0.74	0.54	0.81	0.5	0.51	0.53	0.31	0.47
EX10	1	1.00	1.00	0.93	1.00	0.8	0.95	0.96	0.96	0.90	0.5	0.58	0.57	0.88	0.66
EX11	1	1.00	1.00	0.88	1.00	1	1.00	1.00	0.98	1.00	0.7	0.64	0.66	0.32	0.65
EX12	1	1.00	1.00	0.99	1.00	1	1.00	1.00	0.98	1.00	0.7	0.69	0.70	0.85	0.71
EX13	1	0.99	1.00	0.98	1.00	1	1.00	1.00	0.85	1.00	0.7	0.74	0.70	0.91	0.86
EX14	1	1.00	1.00	0.87	1.00	1	0.98	1.00	0.88	1.00	0.7	0.85	0.86	0.46	0.75
EX15	1	0.99	1.00	0.86	1.00	1	1.00	1.00	0.61	0.92	0.7	0.96	0.97	0.36	0.56
AE(%)		0.78	4.6E-4	7.84	0.53		7.37	7.35	15.91	5.87		6.82	5.90	21.00	7.48
ME(%)		5.41	3.8E-3	27.21	5.40		24.30	25.90	45.62	19.39		26.18	26.60	43.02	16.36

2.4 Combination of GA and First Order method in ANSYS (GAFO)

Much work has been done to apply the GA algorithm combined with numerical FE models. For example, execute GA optimization in Matlab or other language as C++ or VC and obtain the objective fitness or numerical results from FE models in ANSYS program (Ali et al. 2003). As for optimization, Zhang et al. (2010) applied the GA method first to search for an approximate solution that was then used as the initial value of the First Order method in ANSYS to determine the optimal solution. From the result in Section 3, the GA method cannot obtain acceptable results, sometimes far away from the true value. The improvement of the later applied FO method with the initial value from GA method is very limited because the result from the GA method decides the accuracy.

In order to solve this problem, a method combined the GA algorithm and FO method is proposed. Since FO method is inherent in ANSYS, the GA algorithm is coded in ANSYS using APDL (ANSYS Parametric Design Language). In this case, the transferring process between ANSYS program and Matlab or similar program is removed, which greatly reduces the computational time. Moreover, instead of applying the FO after the end of GA method, the FO is applied to every generation of GA. In each generation, a set of parameters with the best fitness is selected from all the individuals of the population, which is then inputted as initial values of the first order method in ANSYS. After several iterations in ANSYS, an optimal solution is obtained and outputted back to the GA process. This optimal solution is to replace the worst individual of the current generation, which will increase the elite number of the generation, and goes to the next steps such as crossover and mutation to generate the child population.

Figure 2-3 demonstrates the flowchart of the proposed optimization method. FFO and FGA are the fitness value obtained from the FO method and the GA algorithm, respectively; XGAi is the i-th best individual and XFO is the optimum value obtained from FO method. The proposed method not only speeds up the convergence, also improves the quality of the child generation. The result using GAFO for the above problem is listed in Table 2-7, which shows great improvement compared to the GA result. You may notice that the GAFO result is close to the FO result, which means no improvement to FO result. In fact, the result of FO method greatly depends on the initial value. Only when the initial value is close to the true value, a good result can be obtained. However, the GAFO method has the capability to find a good solution using any initial values, and the convergence of GAFO is much faster than the routine GA, as shown in Figure 2-4. GAFO converges in about the 10th generations, which is a great advantage because the routine GA is very time-consuming due to a required large number of generations.

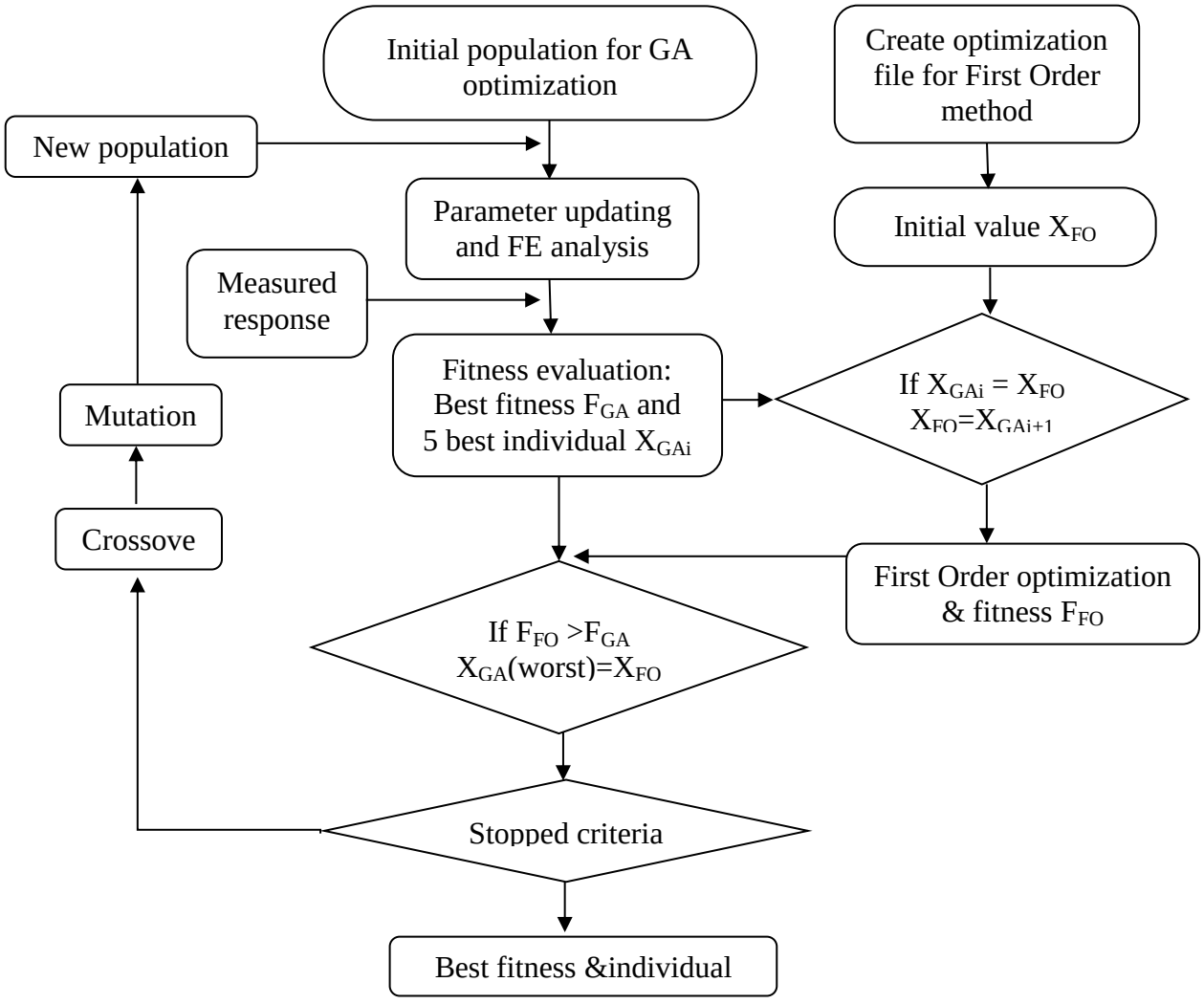

Figure 2-3. Flowchart of GAFO optimization

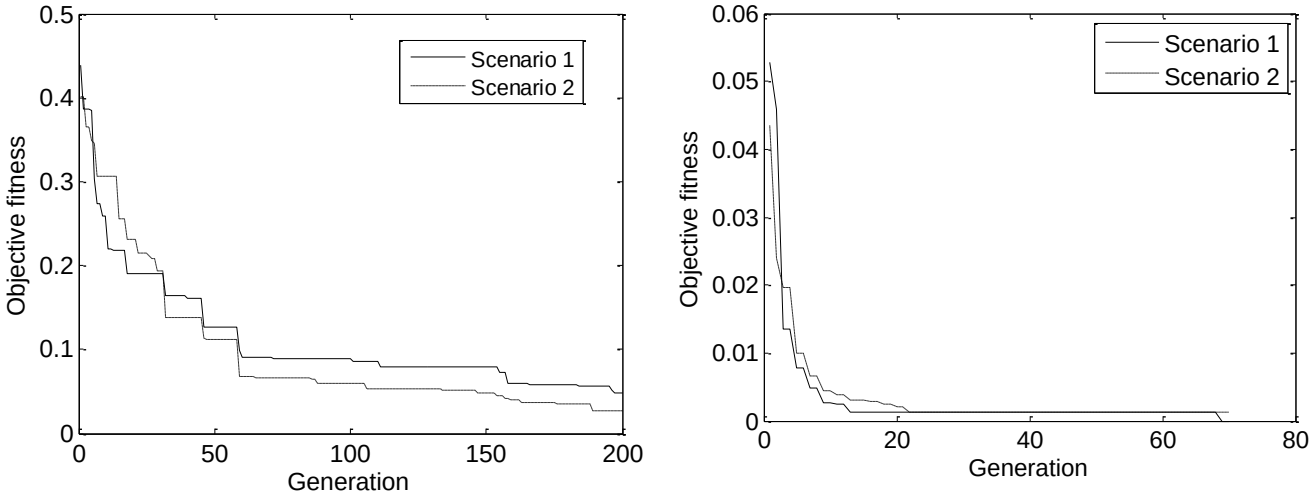

Figure 2-4. Convergence of GA (left) and GAFO (right)

As mentioned before, the First Order method in ANSYS is a gradient-based algorithm and time-consuming, therefore, it accounts for the major part of the computational time of the GAFO method. A balance should be taken between the accuracy and the computational time. The iteration number of the First Order method was studied as shown in Table 2-8.

Table 2-8. Results of different iteration number

Iteration No.	1	2	3	4	5	6	8	10
OBTF	4.0E-4	5.4E-4	3.5E-4	2.9E-4	1.6E-4	5.8E-5	1.5E-4	2.1E-4
AE (%)	11.77	11.98	14.93	14.44	7.48	16.64	16.59	13.03
ME (%)	32.27	37.93	45.47	41.12	16.36	48.93	43.29	43.86

Note: OBTF denotes objective fitness, AE and ME denote average and maximum error, respectively.

Since the required generation is greatly reduced for the GAFO methods, it is possible to increase the population size to improve the result without significantly increasing the computational time because the computational time of the GAFO mainly depends on the iteration of the First Order method. Table 2-9 lists the results of different population size, which indicates that the increasing of the population size does not necessarily mean the increasing accuracy of the result. An appropriate population size should be selected.

Table 2-9. Results of different population size

Population size	100	200	300	500
OBTF	2.2E-04	1.6E-04	1.7E-04	1.7E-03
AE (%)	17.83	7.48	15.29	20.12
ME (%)	36.85	16.36	35.79	42.36

2.5 Case study

The framework of damage detection and the proposed optimization method GAFO were applied to a field bridge.

2.5.1 Bridge description

The bridge is located in LaSalle Parish, Louisiana across Little River and carries the westbound and eastbound lanes of LA 8. The bridge was built in 1981 with a length of 562'-1 ¼" (171.330m), as shown in Figure 2-5. It consists of two 4-span units (4×70ft (21.336m)) that each contains a reinforced concrete deck and continuous Type III precast prestressed girders supported by concrete pile bents with a reinforced concrete bent cap. The clear roadway width is 40ft (12.192m). The bents are constructed perpendicular to the roadway centerline.

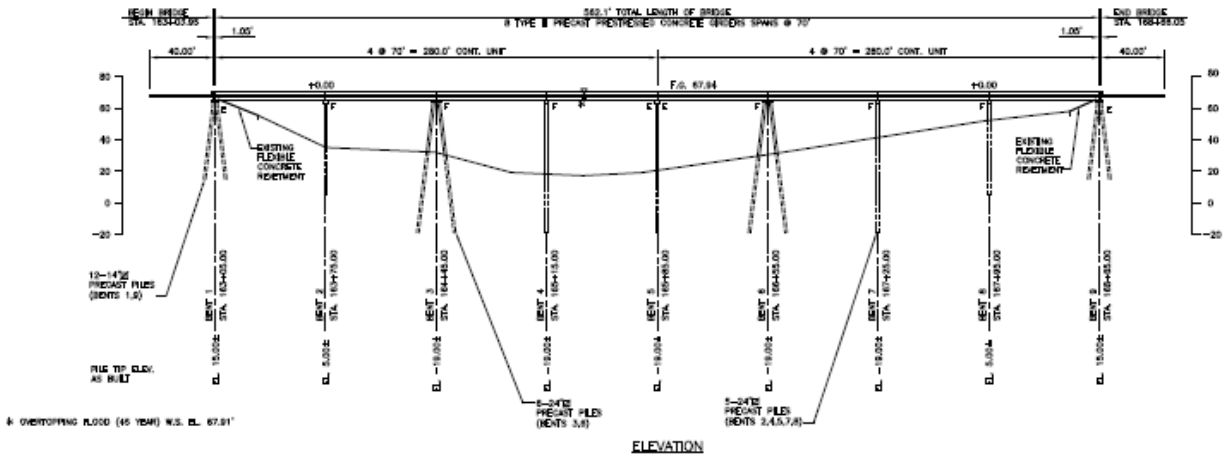

Figure 2-5. Bridge layout

For demonstration, the third span of the bridge is used. The two foundation bents are of different type: Bent type I (bent 4) consists of five 24"-square precast prestressed concrete piles and Bent type II (bent 3) is a double row bent with six 24"-square concrete piles. The outside piles of Bent type I are inclined with a slop of 1.5/12, and that of Bent type II are inclined in both longitudinal and lateral direction with the same slop. Scour information of bent 3 and bent 4 are listed in Table 2-10. Detailed information can be seen in Chapter 7.

Table 2-10. Scour information (ft).

Bent No.	1979 Ground Elev.	2000 Ground Elev.	2009 Ground Elev.	Mudline Change	Pile Length
3	30	28.7	22.5	7.5	80
4	19	16.7	13.3	5.7	80

The FE model of bridge was created in program ANSYS as shown in Figure 2-6. The bridge deck was modeled as shell elements, the girder, diaphragm and pile were modeled using

beam elements. The bent cap was solid elements to better connect the girder and the pile. The soil around the piles was modeled as Combin39 nonlinear spring elements. The right figure shows the real shape of the structure by displaying the section of each element.

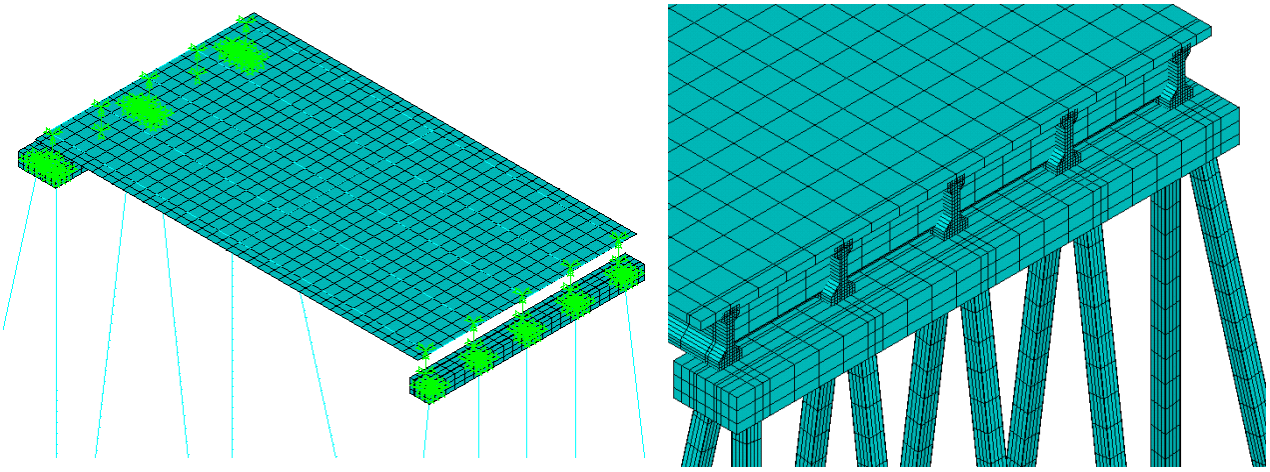

Figure 2-6. Structural FE model

2.5.2 Scour detection

The connection between the girders and the pile caps was assumed as the frame type, that is, the contact nodes between the girder and the cap have the same movements. In order to simplify the structural model for optimization, the pile foundation and soil are equivalent to spring supports, as shown in Figure 2-7. At each end, each pile is substituted by three spring elements. The measurements are taken from the original intact and scour model with pile foundation and soil, which includes static and dynamic responses.

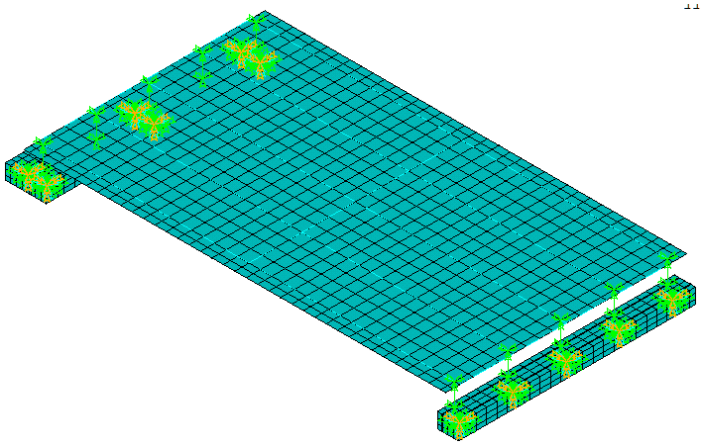

Figure 2-7. Equivalent model

At bent 3, the six skew piles are deemed to be identical, each of which is substituted with one mass element and three spring elements in X, Y and Z direction: Kx3, Ky3, Kz3, and M3.

The mass and stiffness of springs in the same direction at the six points shares the same value. Same as bent 4, five piles are replaced with one mass and three springs at each point: Kx4, Ky4, Kz4, and M4. The equivalent mass and stiffness of all the springs are obtained through optimization method based on the natural frequency and static displacement. The first mode of original model is the lateral bending of all the piles and the rigid moving of the superstructure. The second mode is the longitudinal bending of all piles and the rigid moving of the superstructure. It means that the first two modes of the bridge are only related to the pile foundation, which is used as the objective features to obtain the value of the equivalent support. The displacement of the middle pile top is used as constrained condition for optimization. Table 2-11 lists the mass value and spring stiffness of the equivalent support, and comparison of the displacement and natural frequency between the original model and the equivalent model. The average error of displacement is about 0.3686%, and that of the first three frequencies is 0.0132%. The third mode is the vertical bending of the superstructure, which has small relation with the support condition.

Table 2-11. Equivalent support of intact model

Equivalent values		Displacement			Frequency		
			Original	Equivalent		Original	Equivalent
Kx3	1.7094E+04	Dx3	5.5450E-06	5.5542E-06	f1	0.8597	0.8597
Ky3	1.8135E+06	Dy3	2.1588E-07	2.1692E-07	f2	1.5358	1.5358
Kz3	4.6728E+03	Dz3	1.8223E-05	1.8162E-05	f3	4.6275	4.6293
Kx4	1.5918E+04	Dx4	5.5830E-06	5.5579E-06	f4	5.0923	5.3623
Ky4	1.8574E+06	Dy4	1.9621E-07	1.9708E-07	f5	5.3941	5.7240
Kz4	5.8076E+03	Dz4	1.8039E-05	1.8100E-05	f6	5.5190	11.4540
M3	1.2600E+01	Average Error=0.3686%			Average Error=0.0132%		
M4	2.3577E+01						

Similar procedure is applied on the scour model, which leads to results shown in Table 2-12. The second column that shows the damage index reflected by the equivalent spring stiffness indicates that only the longitudinal and lateral stiffness decrease less than 10 percent. Meanwhile, by comparing the natural frequencies between the intact model and the scour model, only the frequencies related to the foundation decrease significantly. The 13^{th} mode of the original model, vertical bending of the superstructure, corresponds to the third mode of the equivalent model. The equivalent mass and stiffness values in Table 2-11 and Table 2-12 are compared, and the index of each parameter is listed in Table 2-12. The index shows the mass and stiffness reduction of the pile foundation.

Table 2-12. Equivalent support of scour model

Equivalent values			Displacement			Frequency		
	Scour	index		Pile	Spring		Pile	Spring
Kx3	1.6454E+04	0.9625	Dx3	5.6913E-06	5.7481E-06	f1	0.8189	0.8212
Ky3	1.8135E+06	1.0000	Dy3	2.1588E-07	2.1692E-07	f2	1.5065	1.5094
Kz3	4.2549E+03	0.9106	Dz3	1.9844E-05	1.9851E-05	f3	4.3491	4.6292
Kx4	1.5444E+04	0.9702	Dx4	5.7299E-06	5.7515E-06	f4	4.4403	5.3622
Ky4	1.8574E+06	1.0000	Dy4	1.9621E-07	1.9708E-07	f5	4.4462	5.7146
Kz4	5.3079E+03	0.9140	Dz4	1.9588E-05	1.9784E-05	f13	4.6357	11.4540
M3	1.2600E+01	1.0000	Average Error=0.5554%			Average Error=0.1192%		
M4	2.3577E+01	1.0000						

2.6 Conclusions

This study developed a framework for damage identification in different levels and proposed an optimization method. The following conclusions are drawn:

(1) The framework gave a guideline about the three crucial steps for damage detection: (1) selecting parameters and objective features, (2) building a reasonable structural model, and (3) adopting optimization techniques to solve the problem.

(2) A comparative analysis on a numerical beam with three damage scenarios was conducted to study the following aspects: the selection of parameters and determination of its initial values and boundaries, the construction of sensitive objective functions, the creation of structural models, and the performance of different optimization techniques.

(3) The proposed optimization method that combines the Genetic Algorithm (GA) and the First Order (FO) method shows the capability of finding a good solution using any initial values. It can also converge very fast with very few generations.

(4) The methodology was demonstrated on a simplified model of a bridge with scour history.

2.7 References

American Association of State Highway and Transportation Officials (AASHTO). (2008). "Bridging the Gap."

Ali, N., Behdinan, K., Fawaz, Z. (2003). "Applicability and Viability of a GA Based Finite Element Analysis Architecture for Structural Design Optimization." Computers and Structures, Vol. 81, 2259- 2271.

Banks, H. T., D. Inman, J., Leo, D. J., and Wang, Y. (1996). "An experimentally validated damage detection theory in smart structures." Journal of Sound and Vibration, vol.191, No.5, 859-880.

Banks, H.T., and Emeric, P.R. (1998) "Detection of Non-Symmetrical Damage in Smart Plate-Like Structures." NASA/CR-1998-206931, ICASE Report No. 98-15.

Boggs, P. T., Tolle, J. W. (1995). "Sequential quadratic programming." Acta Numerica, Vol. 4, 1-51.

Bu, J.Q., Law, S.S., and Zhu, X.Q. (2006). "Innovative bridge condition assessment from dynamic response of a passing vehicle." J. of Engineering Mechanics 12: 1372-1379.

Cundy, A.L. (2003). "Use of Response Surface Metamodels in Damage Identification of Dynamic Structures." Master thesis in Dept. of Engineering Science and Mechanics, Virginia Polytechnic Institute and State University.

Deng, L., and Cai, C.S. (2010). "Bridge Model Updating Using Response Surface Method and Genetic Algorithm." Journal of Bridge Engineering, Vol. 15, No. 5, 553–564.

Fang, S.E. and Perera, R. (2009). "A response surface methodology based damage identification technique." Smart Mater. Structure.18, 065009 (14pp).

Fletcher, R. (2000). "Practical Methods of Optimization." John Wiley and Sons, 2nd Edition.

Gao, H. Y., Guo, X. L., and Hu, X. F. (2012). "Crack identification based on Kriging surrogate model." Structural Engineering and Mechanics, Vol. 41, No. 1, 25-41.

Goel, T. (2007)."Multiple surrogates and error modeling in optimization of liquid rocket propulsion components." Ph.D. dissertation, University of Florida.

Gould, N. I. M., Toint, Ph. L. (1999). "SQP methods for large-scale nonlinear programming." Proceedings of the 19th IFIP TC7 Conference on System Modelling and Optimization, July 12-16, Cambridge, England, pp.149-178.

Jaishi, B., and Ren, W. X. (2005). "Structural finite element model updating using ambient vibration test results." Journal of Structural Engineering, ASCE, Vol.131, No.4, 617-628.

Jaishi, B., Ren, W. X. (2007). "Finite element model updating based on eigenvalue and strain energy residuals using multiobjective optimization technique." Mechanical Systems and Signal Processing, 21, 2295-2317.

Krishna, V. (2009). "Structural optimization using ANSYS classic and Radial Basis Function based response surface model." Master thesis in Mechanical Engineering, University of Texas at Arlington.

Kamali, M. (2009). “Calibration of hydrologic models using distributed surrogate model.” A doctoral thesis in Systems Design Engineering, University of Waterloo, Ontario, Canada.

Kong, X., Wu, D. J., Cai, C. S., Liu, Y. Q. (2012). “New strategy of substructure method to model long-span hybrid cable-stayed bridges under vehicle-induced vibration.” Engineering Structures, 34, 421–435.

Liu, H., Xin, K. G., Qi, Q. Q. (2011). “Study of structural damage detection with multi-objective function genetic algorithms.” Procedia Engineering, 12, 80-86.

Lu, Z.R., Liu, J.K., Huang, M., Xu, W.H. (2009). “Identification of local damages in coupled beam systems from measured dynamic responses.” J. of Sound and Vibration, 326, 177-189.

Lu, Z.R., Huang, M., Chen, W.H., Liu, J.K., Ni, Y.Q. (2010). “Assessment of local damages in box-girder bridges using measured dynamic responses by passing vehicle.” 2010 Prognostics & System Health Management Conference, Macau.

Lu, Z.R., Liu, J.K. (2011). “Identification of both structural damages in bridge deck and vehicular parameters using measured dynamic responses.” Computers and Structures, 89, 1397-1405.

Manson, G., and Worden, K. (2003). “Experimental validation of a structural health monitoring methodology: Part I. Novelty detection on a laboratory structure.” J. of Sound and Vibration, 259(2), 323-343.

Mack, Y., Goel, T., Shyy, W., and Haftka, R. (2007). “Surrogate model-based optimization framework: A case study in aerospace design.” Studies in Computational Intelligence, 51, 323-342.

McCann, D. M., Forde, M. C. (2001). “Review of NDT methods in the assessment of concrete and masonry structures.” NDT&E International, 34, 71-84.

Menon, A. (2005). “Structural optimization using ANSYS and regulated multiquadric response surface model.” Master thesis, University of Texas at Arlington.

Ren, W.X., and De Roeck, G. (2002). “Structural Damage Identification using Modal Data I: Simulatin Verification.” J. of Structural Engineering, Vol. 128, No.1, 87-95.

Ren, W. X., Chen, H. B. (2010). “Finite element model updating in structural dynamics by using the response surface method.” Engineering Structures, Vol. 32, 8, 2455-2465.

Ren, W. X., Fang, S. E., and Deng, M. Y. (2011), “Response Surface–Based Finite-Element-Model Updating Using Structural Static Responses.” Journal of Engineering Mechanics, Vol. 137, No. 4, 248-257.

Rens, K. L., Wipf, T. J., and Klaiber, F. W. (1997). "Review of nondestructive evaluation techniques of civil infrastructure." J. of Performance of Constructed Facilities, Vol. 11, No. 4, 152-160.

Ruocci, G., Ceravolo, R., and De Stefano, A. (2009). "Modal identification of an experimental model of masonry arch bridge." Key Engineering Materials, Vol.413-414, 707–714.

Ruocci, G. (2010). "Application of the SHM methodologies to the protection of masonry arch bridges from scour." PhD Thesis, Department of Structural and Geotechnical Engineering, Politecnico di Torino, Italy.

Ruocci, G., Quattrone, A., and De Stefano, A. (2011). "Multi-domain feature selection aimed at the damage detection of historical bridges." The 9th International Conference on Damage Assessment of Structures (DAMAS 2011), Journal of Physics: Conference Series 305 (2011) 012106.

Schittkowski, K., "NLQPL: A FORTRAN-Subroutine Solving Constrained Nonlinear Programming Problems." Annals of Operations Research, Vol. 5, 485-500.

Shahsavani, D., Grimvall, A. (2011). "Variance-based sensitivity analysis of model outputs using surrogate models." Environmental Modelling & Software, 26, 723-730.

Srinivas, V., Ramanjaneyulu, K., and Jeyasehar, C.A. (2010). "Multi-stage approach for structural damage identification using modal strain energy and evolutionary optimization techniques." Structural Health Monitoring, 10(2), 219-230.

Teughels, A., Maeck, J., De Roeck, G. (2002). "Damage assessment by FE model updating using damage functions." Computers and Structures, 80, 1869-1879.

Teughels, A., and De Roeck, G. (2005). "Damage detection and parameter identification by finite element model updating." Archives of Computational Methods in Engineering, Vol.12, 2, 123-164.

Unger, J.F., Teughels, A., and De Roeck, G. (2005). "Damage detection of a prestressed concrete beam using modal strains." J. of Structural Engineering, Vol. 131, No. 9, 1456-1463.

Wahab, M.M.A., and De Roeck, G. (1999). "Damage detection in bridges using modal curvatures: application to a real damage scenario." J. of Sound and Vibration, 226(2), 217-235.

Wahab, M.M.A. (2001). "Effect of modal curvatures on damage using model updating." Mechanical Systems and Signal Processing, 15(2), 439-445.

Zapico, J. L., Gonzalez, M. P., Friswell, M. I., Taylor, C. A., Crewe, A. J. (2003). "Finite element model updating of small scale bridge." Journal of Sound and Vibration, 268, 993-1012.

Zhang, J. J., Zhong, J. T., Gao, R. Z., He, L. L. (2010). "A joint optimization method of Genetic Algorithm and numerical algorithm based on MATLAB." 5th IEEE Conference on Industrial Electronics and Applications, 1490-1495.

Zhang, Q. W., Chang, C. C., Chang, T. Y. P. (2000). "Finite element model updating for structures with parametric constraints." Earthquake Engineering Structural Dynamics, 29, 927-944.

Zhang, Q. W., Chang, C. C., Chang, T. Y. P. (2001). "Finite element model updating for the Kap Shui Mun cable stayed bridge." Journal of Bridge Engineering, ASCE 6(4), 229-285.

CHAPTER 3. DAMAGE DETECTION BASED ON TRANSMISSIBILITY IN VBC

3.1 Introduction

Research of vibration-based damage identification was initiated in the late 1970s particularly in the aerospace and offshore oil industries, and has been rapidly expanding to civil engineering over the last decades. The basic idea behind this technology is that changes or damages in the physical properties will cause detectable changes in the modal properties. Doebling et al. (1998) presented an extensive review of vibration-based damage identification methods up to 1998. Sohn et al. (2003) then presented an updated version of this review on the literature up to 2001. Cardenl and Fanning (2004) reviewed the state of the art in vibration-based condition monitoring with a particular emphasis on structural engineering applications. Yan et al. (2007) introduced the development of modern-type vibration-based structural damage detection and the application of intelligent damage diagnosis. Fan and Qiao (2011) presented a comprehensive review on modal parameter-based damage identification methods for beam- or plate-type structures. The major drawback of this approach is that the modal parameters are prone to reflect the global feature of the system while the damages are mostly local changes in a structure. Also, the modal approach assumes a time-invariant structural system but the system is time varying.

With the objective of eliminating the modal extraction error, damage detection using measured frequency response function (FRF) has been studied by a number of researchers (Lew 1995; Wang et al. 1997; Vestroni and Capecchi 2000; Lee et al. 2003; Esfandiari et al. 2009 and 2010) and is very promising because the FRF data can be obtained directly without any further extraction and processing. FRF is the relationship between the input and output, which means an input such as the harmonic force is required as an external excitation of the structure vibration. It leads to the development of damage detection using the output transmissibility that only requires the output information. Transmissibilities under variable load conditions have been recently proven to be a promising new approach of output-only modal identification (Canales et al. 2009). The motivation of using the transmissibility for damage detection relies on the fact that transmissibility is a local quantity, only related to the zeros of FRFs, suggesting a higher sensitivity to detect changes in the dynamic behavior due to some kind of damage (Maia et. al 2011). Devriendt et al. (2007, 2009 and 2010) used the transmissibility to identify modal parameters from output-only transmissibility measurements and Multivariable Transmissibility measurements.

All of the above developments make use of measurements from the bridge structure. The vehicle and bridge coupled (VBC) system has time-variant features and the vehicle can serve as a force transducer and a mobile sensor in the system. Measurement of mode shapes and FRFs requires either a single excitation point and many sensors or a roving exciter with one or more fixed sensors (Cardenl and Fanning 2004). Nevertheless, the vehicle dynamic response such as acceleration owns the similar feature but is easy to measure. Yang et al. (2004, 2009a, and 2009b) and Lin (2005) have done work on extracting the fundamental bridge frequency from the dynamic response time history of a vehicle passing over the bridge. Till now, few studies have

been done on damage detection of a bridge structure using the response of a vehicle moving on it. Bu et al. (2006) proposed an approach to detect the damage through the flexural stiffness reduction of finite elements based on dynamic response sensitivity analysis on the coupled system comprised of a bridge modeled as a Euler-Bernoulli beam and a moving vehicle modeled as a one/two-degree(s)-of-freedom (DOF) system. Lu et al. (2009, 2010 and 2011) assessed local damages in box-girder bridges using measured dynamic responses of passing vehicle. Zhang (2012 and 2013) developed a damage detection method based on the squares of approximately extracted structural mode shape from the acceleration of a passing tapping "vehicle" and a method based on the curvature of the operating deflection shape extracted from the dynamic response of a moving vehicle.

The focus of the present study is therefore to theoretically and numerically study transmissibility in the VBC system and develop a method for bridge damage detection based on the dynamic response of a vehicle-bridge coupled system.

3.2 Theory

In the early 1950, Zadeh (1950) proposed a generalized type of transfer functions, which was briefly discussed by Kwakernaak et al. (1991), and applied to practical problems (Ball et al. 1995; Dalianis et al. 1998). Meanwhile, this concept of transmissibility was presented by Ewins and Liu (1998) and Varoto and McConnell (1998) dealt with the relationships among displacements for certain specific cases. The transmissibility matrix for MDOF systems can be derived using either the FRFs matrix or the measured responses only (Ribeiro et al. 2000; Maia et al. 2001).

3.2.1 FRF and transmissibility in a simplified VBC system

To demonstrate the concept of transmissibility in a VBC system, a simplified vehicle-bridge coupled system is considered. As shown in Figure 3-1, the vehicle is modeled as a SDOF mass with three parameters and the bridge is modeled as a Euler-Bernoulli beam with simple supports.

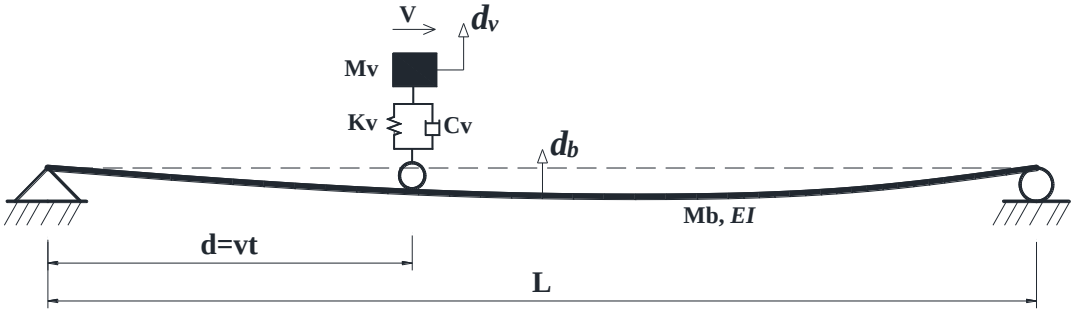

Figure 3-1. Simplified vehicle-bridge system.

The equation of motion for the vehicle and bridge can be expressed as,

$$M_v \ddot{d}_v + K_v\left[d_v - d_b(x=d,t) - r(x=d)\right] + F_G = 0 \tag{3-1}$$

$$M_b \ddot{d}_b + EId_b'''' = K_v[d_v - d_b(x=d,t) - r(x=d)]\delta(x-d) \quad (3\text{-}2)$$

where M_v, K_v are the mass and spring stiffness of the vehicle, and $F_G = M_v g$; M_b, EI are the unit mass and flexible stiffness of the bridge; d_v and d_b are the displacement of vehicle and bridge, respectively; r is the road surface roughness; $d = Vt$ is the distance of the vehicle to the bridge end, assuming a constant speed of the vehicle.

Equation (3-1) can be rewritten as below and its Fourier transform gives,

$$M_v \ddot{d}_v + K_v d_v = K_v d_b(x=d,t) + K_v r(x=d) - F_G$$

$$(-\omega^2 M_v + K_v) D_v(\omega) = \frac{1}{\sqrt{2\pi}} \int_{-\infty}^{\infty} (K_v d_b(x=d,t) + K_v r(x=d) - F_G) e^{-i\omega t} dt$$

$$= K_v D_b(x=d,\omega) + K_v R(\omega) - F_G \sqrt{2\pi}\delta(\omega) \quad (3\text{-}3)$$

Where $D_b(x=d,\omega)$ is the general frequency response function (FRF) (Dalianis 1998) of $d_b(x,t)$ when $x = d = Vt$, and $R(\omega)$ is the FRF of the roughness function $r(x)$.

By separation of variables, the solution of Equation (3-2) can be assumed as,

$$d_b(x,t) = \sum_{j=1}^{\infty} \varphi_j(x) y_j(t) \quad (3\text{-}4)$$

Moreover, the modal shapes satisfy the orthogonal conditions such that

$$\int_0^L \varphi_j(x)\varphi_k(x)dx = \int_0^L \varphi_j^2(x)dx = \Omega_j, \text{ j=k} \quad (3\text{-}5)$$

For a simple beam, the modal shapes are of the sinusoidal form and the angular frequencies can be given by $\omega_j = (\frac{j\pi}{L})^2 \sqrt{\frac{EI}{M_b}}$ and $\varphi_j(x) = \sqrt{2}\sin\frac{j\pi x}{L}$. Substituting Equation (3-4) into (3-2), multiplying by $\varphi_j(x)$, integrating over x, and using the orthogonal conditions, leads to the uncoupled equation of motion,

$$\ddot{y}_j + w_j^2 y_j = G_j(t) \quad (3\text{-}6)$$

where $\omega_j = (\frac{j\pi}{L})^2 \sqrt{\frac{EI}{M_b}}$

$$G_j(t) = \frac{1}{M_b \Omega_j} \int_0^L \varphi_j(x) F(t) \delta(x-d) dx$$

$$F(t) = K_v[d_v - d_b(x=d,t) - r(x=d)]$$

The formal solution to Equation (3-6) is given by the convolution integral

$$y_j(t) = \int_0^t G_j(t-\theta) h_j(\theta) d\theta \quad (3\text{-}7)$$

where $h_j(\theta)$ is the impulse response function.

Substituting Equation (3-7) into (3-6), the modal amplitude can be written as,

$$y_j(t) = \int_0^t \frac{1}{M_b \Omega_j} \int_0^L \varphi_j(x)\delta(x-d)F(t-\theta)dx h_j(\theta)d\theta$$

$$= \frac{\varphi_j(d)}{M_b \Omega_j} \int_0^t F(t-\theta)h_j(\theta)d\theta \tag{3-8}$$

Thus, the bridge displacement can be obtained as,

$$d_b(x,t) = \sum_{j=1}^{\infty} \varphi_j(x) \frac{\varphi_j(d)}{M_b \Omega_j} \int_0^t F(t-\theta)h_j(\theta)d\theta$$

$$= \sum_{j=1}^{\infty} \frac{\varphi_j(x)\varphi_j(d)}{M_b \Omega_j} \int_0^t F(t-\theta)h_j(\theta)d\theta \tag{3-9}$$

The Fourier transform of Equation (3-9) is

$$D_b(x,\omega) = \frac{1}{\sqrt{2\pi}} \int_{-\infty}^{\infty} (\sum_{j=1}^{\infty} \frac{\varphi_j(x)\varphi_j(d)}{M_b \Omega_j} \int_0^t F(t-\theta)h_j(\theta)d\theta) e^{-i\omega t} dt$$

$$= \sum_{j=1}^{\infty} \frac{\varphi_j(x)\varphi_j(d)}{M_b \Omega_j} \frac{1}{\sqrt{2\pi}} \int_{-\infty}^{\infty} \int_0^t F(t-\theta)h_j(\theta)d\theta e^{-i\omega t} dt \tag{3-10}$$

Interchanging the order of integration and introducing the expanding limits of integration leads to (Clough and Penzien 2003),

$$D_b(x,\omega) = \sum_{j=1}^{\infty} \frac{\varphi_j(x)\varphi_j(d)}{M_b \Omega_j} \frac{1}{\sqrt{2\pi}} \lim_{s\to\infty} \left[\int_{-s}^{s} F(t-\theta)e^{-i\omega t} dt \int_0^t h_j(\theta)d\theta \right] \tag{3-11}$$

When a change of variable $\tau = t - \theta$ is substituted, the above equation changes to the form

$$D_b(x,\omega) = \sum_{j=1}^{\infty} \frac{\varphi_j(x)\varphi_j(d)}{M_b \Omega_j} \frac{1}{\sqrt{2\pi}} \lim_{s\to\infty} \int_{-s+\theta}^{s+\theta} F(\tau)e^{-i\omega\tau} d\tau \int_0^s h_j(\theta)e^{-i\omega\theta} d\theta$$

$$= \sum_{j=1}^{\infty} \frac{\varphi_j(x)\varphi_j(d)}{M_b \Omega_j} F(\omega)H_j(\omega) \tag{3-12}$$

where $H_j(\omega) = \dfrac{1}{(\omega_j^2 - \omega^2) + i\beta_j\omega}$ and $F(\omega) = K_v D_v(\omega) - K_v D_b(x=d,\omega) - K_v R(\omega)$.

From Equation (3-3) and (3-12), the transfer function of vehicle and bridge response can be given as,

$$D_v(\omega) = \frac{K_v D_b(x=d,\omega) + K_v R(\omega) - F_G\sqrt{2\pi}\delta(\omega)}{(-\omega^2 M_v + K_v)} \qquad (a)$$

$$D_b(x,\omega) = \left[K_v D_v(\omega) - K_v D_b(x=d,\omega) - K_v R(\omega)\right]\sum_{j=1}^{\infty}\frac{\varphi_j(x)\varphi_j(d)}{M_b\Omega_j}H_j(\omega) \qquad (b) \qquad (3\text{-}13)$$

Substituting (3-13a) into (3-13b) leads to

$$D_b(x,\omega) = \left[\omega^2 M_v D_v(\omega) - F_G\sqrt{2\pi}\delta(\omega)\right]\sum_{j=1}^{\infty}\frac{\varphi_j(x)\varphi_j(d)}{M_b\Omega_j}H_j(\omega) \qquad (3\text{-}14)$$

Ignoring the effect of vehicle gravity F_G, the relation between the bridge response and the vehicle response can be obtained as,

$$D_b(x,\omega) = H_{bv}D_v(\omega) \qquad (3\text{-}15)$$

where $H_{bv} = \omega^2 M_v\sum_{j=1}^{\infty}\frac{\varphi_j(x)\varphi_j(d)}{M_b\Omega_j}H_j(\omega)$, is the transfer function between bridge response and vehicle response. The transmissibility between bridge responses of different locations can be then expressed as,

$$TR_{mn} = \frac{\sum_{j=1}^{\infty}\varphi_j(x_m)\varphi_j(d)H_j(\omega)}{\sum_{n=1}^{\infty}\varphi_j(x_n)\varphi_j(d)H_j(\omega)} \qquad (3\text{-}16)$$

where x_m and x_n are node locations on bridge.

Equation (3-15) is the same as the transfer function discussed in Esfandiari et al. (2010). It indicates that in the vehicle-bridge coupled system, the vehicle can serve as a good exciter and be a substitute for the harmonic input required for obtaining transfer function. The FRF with both system zeros and poles contains the global information about the system and is affected by changes in any of the system parameters (Johnson 2002). While the transmissibility, defined as a ratio of amplitudes using only any two entries of FRF matrix, only remains system zeros that contains the local information about mass, damping, and stiffness. Therefore, the transmissibility function is more sensitive to local system parameters and useful for local structural damage.

3.2.2 Models of VBC system

The above analytical study and simplified VBC system are used to demonstrate the concept of transmissibility in a VBC system. As for more sophisticated or realistic problems, the Finite Element Method is always the first choice. The three crucial parts for a VBC system are: vehicle model, bridge model and roughness model, which are elaborated next.

Vehicle model

The model of vehicles used as response receivers is considered as a SDOF vehicle model, while vehicles of the traffic flow served as random excitation, are modeled as a combination of several rigid bodies connected with several axle mass blocks, springs, and damping devices (Cai and Chen 2004). The suspension systems and elasticity of tires are idealized as liner elastic spring elements and dashpots. The bridge deck and the moving tire are assumed to be point-contact. The axle number may vary from two to five. In the present study, a two-axle vehicle model (Shi 2006 and Deng 2009) is used to establish the equation of motion of the vehicle as well as the vehicle-bridge coupling equations in the following sections.

Bridge model

The equation of motion for a bridge with discretized finite elements can be written as follows:

$$[M_b]\{\ddot{d}_b\}+[C_b]\{\dot{d}_b\}+[K_b]\{d_b\}=\{F_b\} \tag{3-17}$$

where $[M_b]$, $[C_b]$, and $[K_b]$ are the mass, damping, and stiffness matrices of the bridge, respectively; $\{d_b\}$ is the displacement vector for all DOFs of the bridge; $\{\dot{d}_b\}$ and $\{\ddot{d}_b\}$ are the first and second derivative of $\{d_b\}$ with respect to time, respectively; and $\{F_b\}$ is a vector containing all external forces acting on the bridge. With the modal superposition technique, Equation (3-17) can now be rewritten as:

$$[I]\{\ddot{\xi}_b\}+[2\omega_i\eta_i I]\{\dot{\xi}_b\}+[\omega_i^2 I]\{\xi_b\}=[\Phi_b]^T\{F_b\} \tag{3-18}$$

where $\{\Phi_b\}$ and ξ_b are the mode shape matrix of the bridge and the generalized modal coordinate vector, respectively. ω_i is the i th bridge frequency and [I] is a unit matrix. Each mode shape is normalized such that $\{\Phi_i\}^T[M_b]\{\Phi_i\}=1$ and $\{\Phi_i\}^T[K_b]\{\Phi_i\}=\omega_i^2$. In this study, the damping matrix $[C_b]$in Equation (3-17) is assumed to be equal to $2\omega_i\eta_i[M_b]$, where η_i is the percentage of the critical damping for the i th mode of the bridge.

It must be emphasized that the success of damage detection procedures using vibration data requires that the in-built analytical procedures to be accurate enough to discern changes in response due to damages that could be small. This would mean that the analytical models employed here need to be more refined than what otherwise is needed in a routine response analysis.

Road surface condition

The road surface condition is an important factor that affects the dynamic responses of both the bridge and vehicles. A road surface profile is usually assumed to be a zero-mean stationary Gaussian random process and can be generated through an inverse Fourier transformation based on a power spectral density (PSD) function (Dodds and Robson 1973) as:

$$r(X)=\sum_{k=1}^{N}\sqrt{2\varphi(n_k)\Delta n}\cos(2\pi n_k X+\theta_k) \tag{3-19}$$

where θ_k is the random phase angle uniformly distributed from 0 to 2π; $\varphi()$ is the PSD function (m^3/cycle) for the road surface elevation; and n_k is the wave number (cycle/m). In this study, the following PSD function (Huang and Wang 1992) has been used:

$$\varphi(n) = \varphi(n_0)(\frac{n}{n_0})^{-2} \qquad (n_1 < n < n_2) \tag{3-20}$$

where n is the spatial frequency (cycle/m); n_0 is the discontinuity frequency of 1/2π (cycle/m); $\varphi(n_0)$ is the roughness coefficient (m^3/cycle) whose value is chosen depending on the road condition; and n_1 and n_2 are the lower and upper cut-off frequencies.

The vehicle-bridge coupled system

The equation of motion of the VBC system can be rewritten in the matrix form as below (Shi 2006 and Deng 2009):

$$\begin{bmatrix} M_b & \\ & M_v^N \end{bmatrix}\begin{Bmatrix} \ddot{d}_b \\ \ddot{d}_v \end{Bmatrix}+\begin{bmatrix} C_b + C_{b-b} & -C_{b-v} \\ -C_{v-b} & C_v^N \end{bmatrix}\begin{Bmatrix} \dot{d}_b \\ \dot{d}_v \end{Bmatrix}+\begin{bmatrix} K_b + K_{b-vb} + K_{b-cb} & -K_{b-v} \\ -K_{v-b} - K_{v-cb} & K_v^N \end{bmatrix}\begin{Bmatrix} d_b \\ d_v \end{Bmatrix}=\begin{Bmatrix} -F_{b-r} - F_{b-cr} \\ F_{v-r} + F_{v-cr} - F_G^N \end{Bmatrix} \tag{3-21}$$

The additional terms C_{b-b}, C_{b-v}, C_{v-b}, K_{b-vb}, K_{b-cb}, K_{b-v}, K_{v-b}, K_{v-cb}, F_{b-r}, F_{b-cr}, F_{v-r}, and F_{v-cr} in Equation (3-21) are due to coupling effect between the bridge and vehicles. When a vehicle travels on the bridge, the position of the contact point changes with time, which means the road roughness $r(x)$ at the contact point and the shape function are both time-dependent terms, indicating that all the additional terms in Equation (3-21) are time-dependent terms.

Using Equation (3-18), Equation (3-21) can be further rewritten as follows:

$$\begin{bmatrix} I & \\ & M_v \end{bmatrix}\begin{Bmatrix} \ddot{\xi}_b \\ \ddot{d}_v \end{Bmatrix}+\begin{bmatrix} 2\omega_i\eta_i I + \Phi_b^T C_{b-b}\Phi_b & -\Phi_b^T C_{b-v} \\ -C_{v-b}\Phi_b & C_v^N \end{bmatrix}\begin{Bmatrix} \dot{\xi}_b \\ \dot{d}_v \end{Bmatrix}$$
$$+\begin{bmatrix} \omega_i^2 I + \Phi_b^T(K_{b-vb} + K_{b-cb})\Phi_b & -\Phi_b^T K_{b-v} \\ -(K_{v-b} + K_{v-cb})\Phi_b & K_v^N \end{bmatrix}\begin{Bmatrix} \xi_b \\ d_v \end{Bmatrix}=\begin{Bmatrix} -\Phi_b^T(F_{b-r} + F_{b-cr}) \\ F_{v-r} + F_{v-cr} - F_G^N \end{Bmatrix} \tag{3-22}$$

where the vehicle-bridge coupled system contains only the modal properties of the bridge and the physical parameters of the vehicles.

3.3 Numerical study on transmissibility based damage detection

In order to further understand the transmissibility features in a VBC system, a numerical study was conducted to first verify the theoretical solution, compare the transmissibility from vehicle and bridge response, and finally select a proper damage index for damage detection.

A system consisting of a simply supported beam and a SDOF vehicle model was adopted as a numerical example, as shown in Figure 3-2. The beam was discretized into 120 beam elements with physical properties: elastic modulus E=32 GPa, mass density D=2.5e3 kg/m^3, length L=30 m, section width = 1.2 m, and section depth = 2 m. Parameters of the SDOF (three-

parameter) vehicle model are: m_v = 4.0e4 kg, c_v = 1.0e4 Ns/m, and k_v = 6.0e6 N/m. The vehicle frequency is 1.949Hz and the first three vertical frequencies of the bridge are 3.579Hz, 14.012Hz, and 30.503Hz.

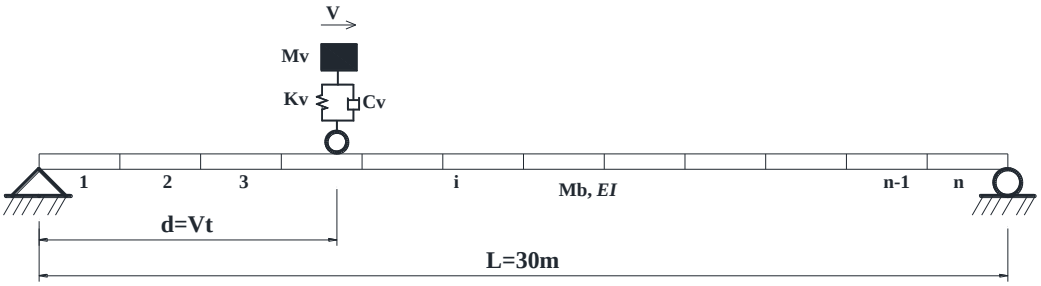

Figure 3-2. Finite element model of VBC system.

3.3.1 Theoretical verification

Equations (3-15) and (3-16) give the relationship between the vehicle and bridge responses. For a simply supported beam, the modal shapes can be assumed as the sinusoidal form $\varphi_j(x) = \sqrt{2}\sin\frac{j\pi x}{L}$, and the angular frequencies can be given by $\omega_j = (\frac{j\pi}{L})^2\sqrt{\frac{EI}{M_b}}$. $\Omega_j = L$ can easily be derived. Thus, Equation (3-15) can be expressed as,

$$H_{bv} = \frac{\omega^2 M_v}{M_b L}\sum_{j=1}^{\infty}\frac{2\sin(j\pi x/L)\sin(j\pi d/L)}{\omega_j{}^2 - \omega^2} \qquad (\mathbf{3}\text{-}23)$$

The transmissibility between bridge responses of two different locations can then be expressed as,

$$TR_{mn} = \frac{\sum_{j=1}^{\infty}\frac{\sin(j\pi x_m/L)\sin(j\pi d/L)}{\omega_j{}^2 - \omega^2}}{\sum_{j=1}^{\infty}\frac{\sin(j\pi x_n/L)\sin(j\pi d/L)}{\omega_j{}^2 - \omega^2}} \qquad (3\text{-}24)$$

In the VBC system, the contact point between the bridge and vehicle is time varied, which means the magnitude and location of the excitation force are varied. The effect of vehicle location on the transmissibility is represented by the variable d as shown in the above equation. For the sake of verification, a FE beam built in ANSYS and a bridge-vehicle coupled analysis in Matlab were introduced to compare the result with the theoretical one. Figure 3-3 and Figure 3-4 show the transmissibility between point $x_m = 12.5m$ and point $x_n = 15m$ when $d = 10m$ (responses of both positions at the same time are used) and $d = x$ (responses of both positions at different time are used), respectively. Both theoretical results from Equation (3-24) and numerical results from FE beam model are displayed in Figure 3-3 and Figure 3-4. The trend of both curves is similar, having the peak and valley at the same frequency, except that the numerical result shows much more oscillation than that of the theoretical one.

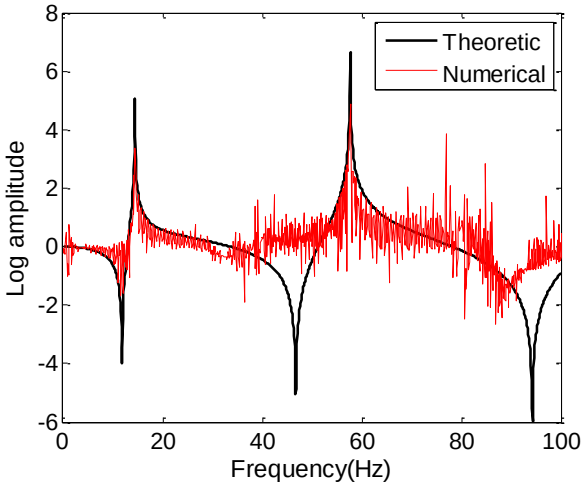

Figure 3-3. TR_{mn} when d=10m

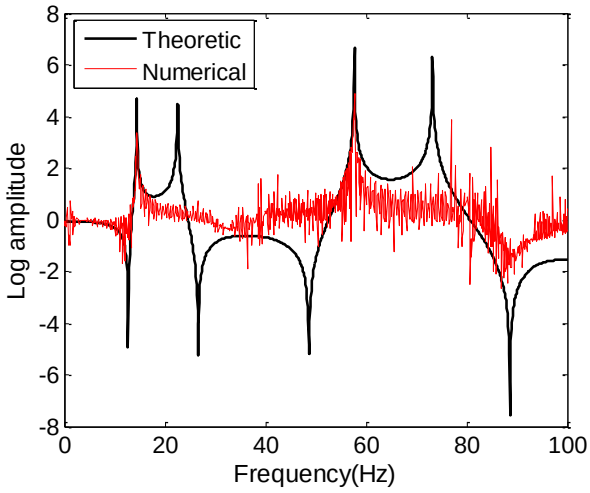

Figure 3-4. TR_{mn} when d=x

In the transmissibility matrix, one column vector represents the operational deflection shape (ODS) at frequency ω, describing the shape of the structure. Therefore, at the natural frequency, the ODS represents the modal shape of the structure. As can be seen in Equation (3-24), it contains the square of modal shape, therefore, the mode shape extracted from the transmissibility is in fact the square value of modal shapes. Figure 3-5 demonstrates the first and second modal shape square extracted from the transmissibility matrix.

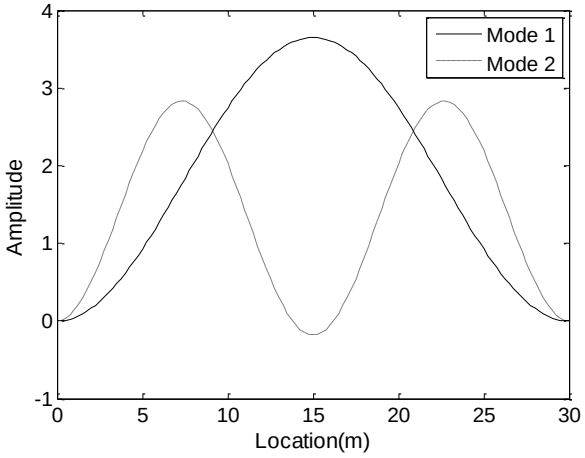

Figure 3-5. The 1st and 2nd mode shape squares

3.3.2 Transmissibility in a bridge-only system

Before using the transmissibility of a VBC system for damage detection, the transmissibility in bridge-only system was studied first for comparison. Except the intact case, four damage cases were considered (the beam is discretized into 120 elements):

- Damage case 1: four elements (1m) have the elastic modulus reduced by 50%, with its center at 10m from the beam left end.
- Damage case 2: four elements (1m) have the elastic modulus reduced by 90%, with its center at 10m from the beam left end.
- Damage case 3: twelve elements (3m) have the elastic modulus reduced by 50%, with its center at 10m from the beam left end.
- Damage case 4: twelve elements (3m) have the elastic modulus reduced by 90%, with its center at 10m from the beam left end.

It is necessary to note that the damage severity in each case that seems too large in reality is adopted for conceptually demonstrating and studying the feasibility of the proposed method. It could happen in reality that some part of a structure is heavily destroyed before it is detected. In the bridge only system, the transfer function is obtained by applying a harmonic force on a particular location of the bridge and recording the dynamic response at various locations attached with sensors such as accelerometers. The transmissibility between different locations is then computed by,

$$TR_{mn} = \frac{H_{mk}(\omega)}{H_{nk}(\omega)} = \frac{X_m(\omega)}{X_n(\omega)} \tag{3-25}$$

where $H_{mk}(\omega)$ and $H_{nk}(\omega)$ are transfer functions at location m and n, respectively, with the force applying at location k. $X_m(\omega)$ and $X_n(\omega)$ are the amplitude of Fourier Transform of acceleration at location m and n, respectively. The transmissibility damage indicator (TDI) (Maia et al. 2011) is used here to indicate the difference between the intact case and damaged case, which is calculated as,

$$TDI = \frac{1}{N_\omega} \sum_{\omega=\omega_1}^{\omega_2} \frac{\left| \sum_{j=1}^{M} \sum_{n=1}^{N} \sum_{m=1}^{N} {}^{d}TR_{mn}^{(j)}(\omega) * TR_{mn}^{(j)}(\omega) \right|^2}{\sum_{j=1}^{M} \sum_{n=1}^{N} \sum_{m=1}^{N} TR_{mn}^{(j)} * TR_{mn}^{(j)} * \sum_{j=1}^{M} \sum_{n=1}^{N} \sum_{m=1}^{N} {}^{d}TR_{mn}^{(j)} * {}^{d}TR_{mn}^{(j)}} \tag{3-26}$$

for the case with N measured positions, M applied forces and N_ω frequencies. Herein, $TR_{mn}^{(j)}$ is the transmissibility between the position m and position n under the applied force at the position j, and ${}^{d}TR_{mn}^{(j)}$ represents the damaged one. This index ranges from 0 to 1, and the larger the number, the better similarity between the two cases such as the value 1 means that both are exactly the same.

In this example, 11 positions with an interval of 2.5m along the beam were chosen for the excitation force positions and measurement points. The force was applied at the 11 positions one by one, with 11 acceleration measurements each time. By summing up all the results, Figure 3-6(a) shows TDI of four damage cases versus the selected frequency range. As can be seen, it is obvious to recognize the damage severity based on the index under about 150Hz, which ranks from slight to severe as case 1, case 3, case 2 and case 4.

In order to study the reliability of TDI, the following conditions were conducted: different excitation force position, force numbers, and measurement numbers. Figure 3-6(b) shows TDI results under one applied force at different positions with a sample frequency of 150Hz. The 11 force positions are distributed uniformly on the beam with an interval of 2.5m. Observed from the figure, the largest TDI is at F3 or F4 for all damage cases. F4 is 10m from the beam end where the damage is located. It indicates that the best excitation position is around the damage location. Furthermore, the TDI decreases with the increase of the distance from the force position to the damage location. Figure 3-6(c) and (d) show the results versus force numbers and measurement numbers, respectively. As the force numbers increase, the TDI decreases, especially for damage case 2 and case 4. From the statistical point of view, more force numbers are included, more reliable the result is, while it also introduces more errors. Meanwhile, the number of measurements has small effect on the results, except for the case with only one measurement, which means the result becomes stable when the measurement number is sufficient.

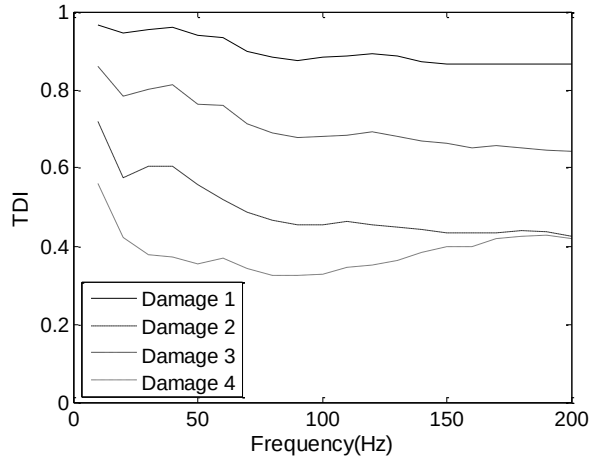

(a) TDI of four damage cases

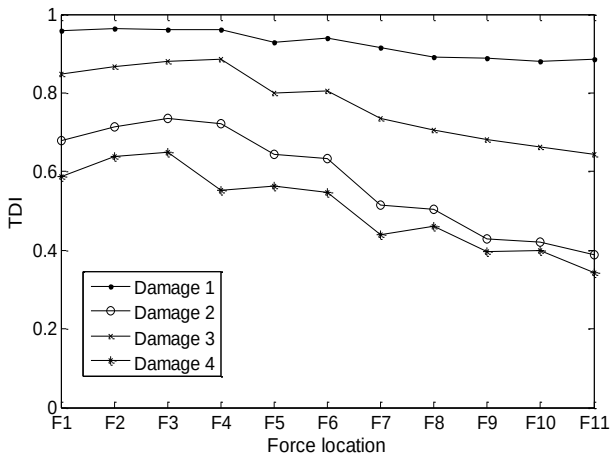

(b) TDI with different force positions

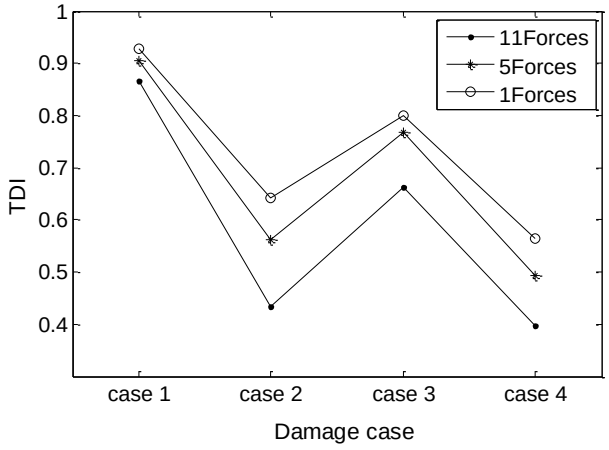

(c) TDI with different force numbers

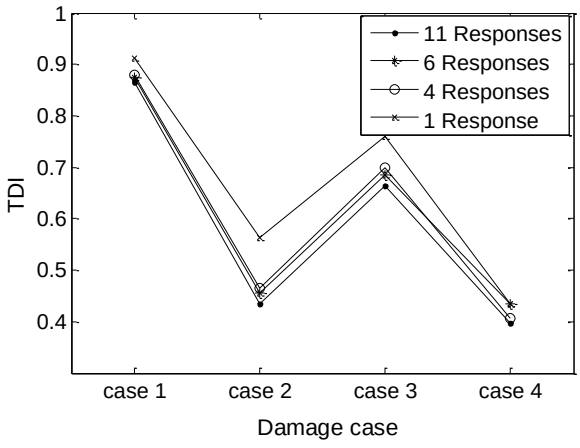

(d) TDI with different measurement numbers

Figure 3-6. TDI. results of bridge only system

As discussed earlier, the "local characteristic" of transmissibility suggests a higher ability to detect changes in the dynamic properties. Every row vector of the transmissibility matrix represents the ratio of one position to other positions. By summing up all the transmissibilities at each row vector, the TDI at each position is obtained and shown in Figure 3-7(a) for all four damage cases with a frequency range of 150Hz. Moreover, the minimum one among all the positions can be easily extracted as shown in Figure 3-7(b). For most of the frequency ranges, the minimum TDI is located at the M4 position, i.e. 10m from the left end. That is where the damage is located.

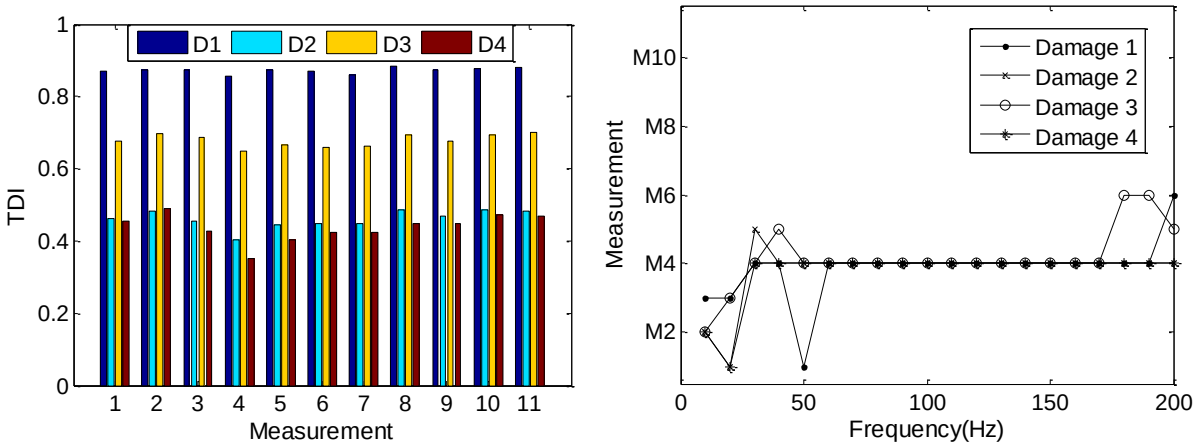

(a)TDI at each position (b) Minimum TDI

Figure 3-7. TDI vectors of all damage cases

All the above reveals that the transmissibility extracted from the bridge-only system is a good feature for damage detection. However, the dynamic response requires an external excitation force and the result is affected by factors such as the excitation force position, force number, and measurement numbers.

3.3.3 Transmissibility in a VBC system

In a vehicle-bridge system, the vehicle is not only an exciter, but also a receiver. The dynamic response measured from the vehicle could be a substitute for that measured from sensors attached on the bridge. For this purpose, 11 "vehicles" were deployed on the bridge at an interval of 2.5m as shown in Figure 3-8, and another vehicle was used as the exciter moving across the bridge. It is worth to note that the 11 "vehicles" here are not like the vehicle used as exciter but more like 11 sensors put on the bridge deck， which are fixed at its position with a vertical vibration only. The parameters of the 11 vehicles are different from the moving vehicle, which are: m_v=40kg, c_v=1000Ns/m, and k_v=6.0e6 N/m. Herein, the large stiffness of the vehicle spring is to prevent its own vibration and make the response of the vehicle as close as to that position of bridge. Dynamic responses of both the 11 vehicles and the bridge at those positions were measured. As clarification, without particularly referred, the "vehicle" refers to those 11 vehicles functioned as sensors, and the "moving vehicle" refers to the one moving across the bridge.

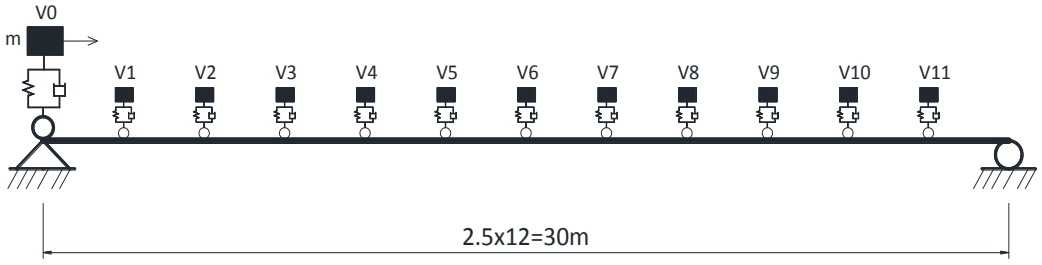

Figure 3-8. The VBC system for transmissibility.

The displacement time histories of the bridge and vehicle are almost the same and not displayed here, and the Fourier Transform of accelerations is demonstrated in Figure 3-9. The two responses match much better in the low frequency range than in the high frequency range. The amplitude of the vehicle response in high frequency range is much smaller than that of the bridge response. As mentioned earlier, the stiffness of the vehicle spring is very large, i.e. the vehicle frequency is very large. Therefore, the vehicle vibration is excited mostly by the bridge vibration with small vibration from itself and no vibration interaction between the vehicle and bridge. From the comparison in Figure 3-9, only the low frequency component of the bridge vibration is transmitted to the vehicle.

The correlation between the vehicle spectrum and bridge spectrum can be described by the MAC (Modal Assurance Criterion) value, as shown in Figure 3-10 for different vehicle positions with different frequency range. The MAC value of the logarithmic amplitudes shows that the correlation is much better in the low frequency range than that in the high frequency range, and the middle vehicles have better correlation than the side ones.

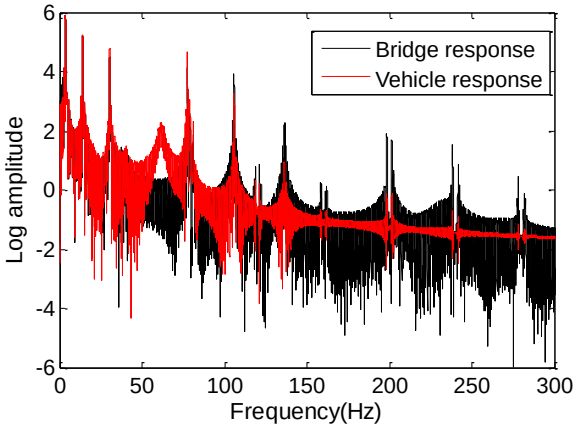

Figure 3-9. FFT of acceleration at position 3

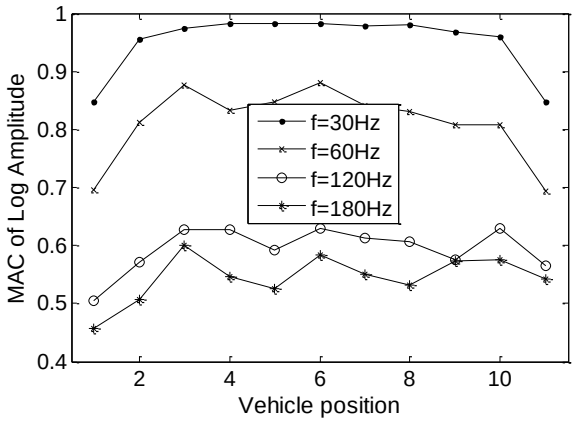

Figure 3-10. MAC versus the vehicle position

Damage index

In the study of FRF, the frequency response assurance criterion (FRAC) is a useful index to compare the relationship between any two FRFs under the same input. To measure the

correlation between the transmissibility of the intact and damaged structures, a damage index is needed with the objective of using transmissibility for damage detection. Similar to the TDI (Maia et al. 2011; Yi et al. 2010), several indicators were proposed in the present study and compared to find the appropriate one. Since the acceleration transmissibility is a complex value, both the complex value and the amplitude value were used as a basis to calculate the TDI. A total of six indicators were proposed for comparison: four for amplitudes and two for complex values.

- TDI1: Successive pairs are compared in the transmissibility matrix with amplitude values between the intact structure and damaged structure at each frequency, and then all the results are summed up in the frequency range, as demonstrated in Equation (3-27).

$$TDI1 = \frac{1}{N_\omega}\sum_{\omega=\omega_1}^{\omega_2}\frac{\left|\sum_{m=1}^{N-1} {}^{d}TR_{mn}(\omega) * TR_{mn}(\omega)\right|^2}{\sum_{m=1}^{N-1} TR_{mn} * TR_{mn} * \sum_{m=1}^{N-1} {}^{d}TR_{mn} * {}^{d}TR_{mn}}, \qquad n = m+1 \tag{3-27}$$

  where, ${}^{d}TR_{mn}$ represents the damaged transmissibility between position m and position n, and TR_{mn} represent the intact one.

- TDI2: In the transmissibility matrix, one column vector represents the operational deflection shape (ODS) at the frequency ω, describing the shape of the structure. It means that the pattern of each column vector is the same for amplitude values, i.e. the relation between each column is a constant. Therefore, only one column was used, i.e. n is fixed as n=1 (not n=m+1) and m start from 2 till N in Equation (3-27).

- TDI3: Successive pairs of the logarithmic amplitude matrix are compared, similar to TDI1 with $TR_{mn}(\omega) = \log\left|TR_{mn}(\omega)\right|$ and ${}^{d}TR_{mn}(\omega) = \log\left|{}^{d}TR_{mn}(\omega)\right|$.

- TDI4: One column of the logarithmic amplitude matrix are compared, similar to TDI2.

- TDI5: All the entries in the transmissibility matrix with complex values are compared.

- TDI6: Successive pairs in the transmissibility matrix with complex values are compared, as shown in Equation (3-28).

$$TDI6 = \frac{1}{N_\omega}\sum_{\omega=\omega_1}^{\omega_2}\frac{\left|\sum_{m=1}^{N-1} {}^{d}TR_{mn}(\omega) * \overline{TR_{mn}(\omega)}\right|^2}{\sum_{m=1}^{N-1} TR_{mn} * \overline{TR_{mn}} * \sum_{m=1}^{N-1} {}^{d}TR_{mn} * \overline{{}^{d}TR_{mn}}}, \qquad n = m+1 \tag{3-28}$$

  where, $\overline{\quad}$ represents the complex conjugate.

The transmissibility can be compared over the full or partial frequency range as long as the same discrete frequencies are used in the comparison. The TDI ranges from 0 to 1 and the smaller the value, the larger the damage.

As transmissibilities from bridge responses and vehicle responses were both obtained, six TDIs for both of them were compared. Herein, only two cases were listed below for demonstration. Figure 3-11(a) is TDI3 of the bridge response for four damage cases, which shows obvious distinction between each damage case along the entire frequency range, and the damage severity can be easily ranked from slight to severe as damage case 1, 3, 2 and 4. Figure 3-11(b) is TDI3 of the vehicle response for four damage cases and the damage distinction can be identified correctly under about 300Hz. The TDI3 works very well for the bridge response, while it works only well under 300Hz for the vehicle response.

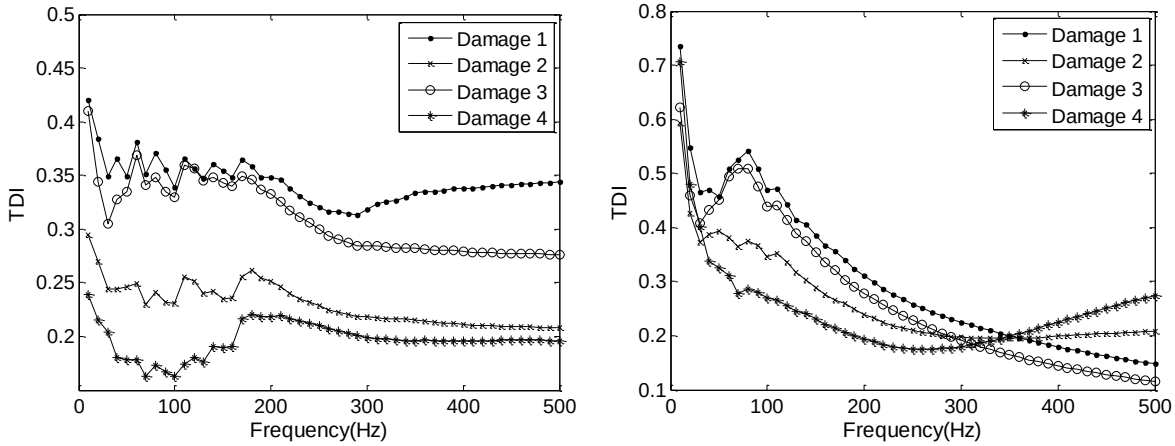

(a) TDI3 of bridge responses (b) TDI3 of vehicle responses

Figure 3-11. TDIs of bridge and vehicle response

In order to quantify the detection ability of those TDIs, the average discrepancy between TDI values of each damage case at a certain frequency range is calculated. As discussed earlier, the damage severity sequence should be 1, 3, 2 and 4. Thus, the TDI discrepancies between damage 1 and damage3, damage 3 and damage2, and damge 2 and damage 4 at each frequency are calculated and summed up. Table 3-1 lists the comparion of TDIs from the bridge response or vehicle response at different frequency ranges, only 6 of the twevle cases are listed in the table. It shows that both TDI3 and TDI4 work well for bridge response, and TDI4 and TDI5 are good for vehicle response. At the column of TDI3_V, a few negative values are observed at high frequency range, namely, the sequence of damage cases is not correctly identified.

As to distinguish the positive value and negative value, a distinction coefficient (DC) was proposed to estimate the ability of each TDI identifying the damage correctly and the error of misidentifying the damage.

$$DC = \varphi[TDI(1) - TDI(3)] + \varphi[TDI(3) - TDI(2)] + \varphi[TDI(2) - TDI(4)] \tag{3-29}$$

where $TDI(i), i = 1,2,3,4$ is the TDI of damage case i. $\varphi(a-b) = \begin{cases} a-b, & a > b \\ 0, & a \le b \end{cases}$. This function means that only if the distance is positive, it is included in the DC equation. It is useful to

eliminate the negative distance that leads to misidentification. On the other hand, if the error is to be estimated, $\varphi(a-b)=\begin{cases}0, & a\geq b\\ a-b, & a<b\end{cases}$.

Table 3-1. Average discrepancy of TDI

Frequency	TDI3_B	TDI4_B	TDI5_B	TDI3_V	TDI4_V	TDI5_V
10	0.0603	0.0094	0.0564	0.0096	0.0056	0.0466
50	0.0568	0.0373	0.0215	0.0436	0.0407	0.0433
100	0.0587	0.0518	0.0287	0.0667	0.0599	0.0510
150	0.0548	0.0540	0.0350	0.0518	0.0571	0.0505
200	0.0432	0.0434	0.0361	0.0391	0.0506	0.0424
250	0.0367	0.0389	0.0340	0.0276	0.0466	0.0383
300	0.0398	0.0380	0.0297	0.0152	0.0415	0.0363
350	0.0457	0.0446	0.0253	0.0000	0.0348	0.0389
400	0.0473	0.0491	0.0216	-0.0151	0.0272	0.0389
450	0.0480	0.0522	0.0178	-0.0295	0.0193	0.0374
500	0.0492	0.0547	0.0145	-0.0422	0.0119	0.0363
Average	0.0492	0.0430	0.0291	0.0152	0.0359	0.0418

Note: B denotes the bridge response, and V denotes the vehicle response.

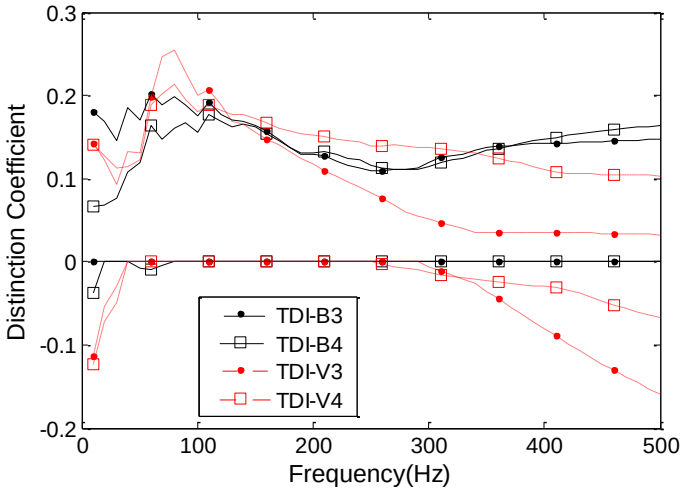

Figure 3-12. Distinction coefficient of TDI

In Figure 3-12, four best cases are selected for demonstration: TDI3 and TDI4 of bridge response, TDI3 and TDI4 of vehicle response. The curves above the zero line are those that use the DC for correctly identifying the damage, while the underneath ones are those that use the DC to estimate the error of identifying damage. As it is shown, TDI-B3 and TDI-B4 have good identifying ability and very slight error. TDI-V3 and TDI-V4 are not stable and only work well

between 100Hz and 300Hz and significant discrepancy appears for the frequencies over 300Hz. This again indicates that only the low frequency part of vehicle response is useful. For the present case, TDI3 works better than other five TDIs for bridge response, while TDI4 is the best for vehicle response.

3.4 Parametric study

After a proper damage indicator was selected, parametric studies were conducted to investigate the effectiveness of the indicator under various conditions.

3.4.1 Effect of measurement numbers

Measurement numbers reflect the amount of information known about the system, namely, larger measurement numbers results more information known about the bridge. Figure 3-13(a) and Figure 3-13 (b) show the results of TDI5 of the bridge and vehicle response, respectively. The figures indicate that more measurements lead to lower TDI values. Here, the reason could be that the correlation was calculated between the intact and damaged structure with the same measurement numbers. The case with larger measurement numbers has more points to compare and is easy to accumulate the uncorrelated data. Hence, a proper measurement number shoule be used.

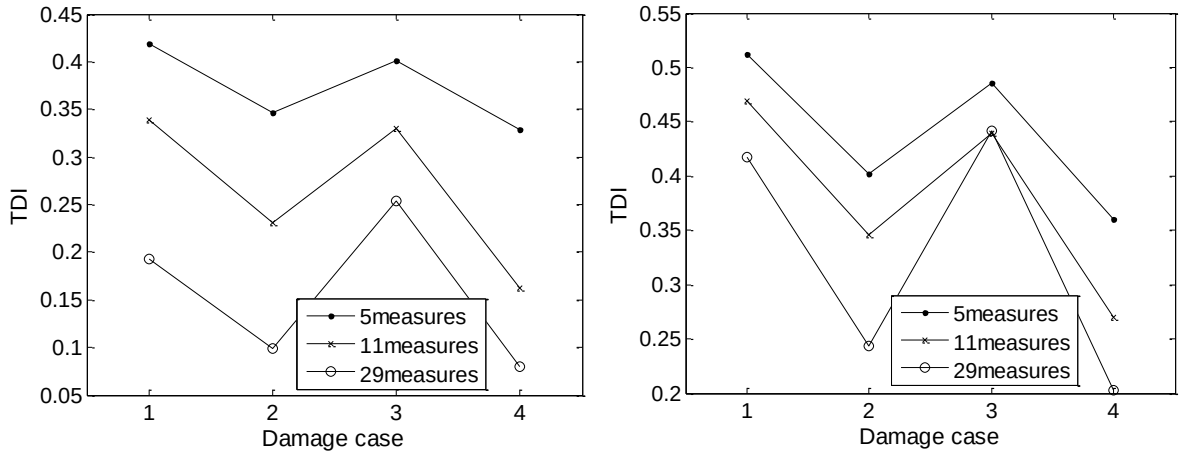

(a) TDI5-B of bridge response (b) TDI6-V of vehicle response

Figure 3-13. TDI versus measurement numbers

3.4.2 Effect of surface roughness

Road Roughness is an important contribution to the vehicle vibration, and is classified as five levels: very good, good, fair (average), poor and very poor. The International Organization for Standardization (1995) used road roughness coefficient (RRC) to define the road roughness classification and the ranges were listed in Table 3-2. Herein, four roughness levels were analyzed, level 5 to level 2.

Table 3-2. Roughness classifications (m^3/cycle).

Roughness classifications	Levels	Ranges for RRCs
Very good	Level 5	$2\times10^{-6} \sim 8\times10^{-6}$
Good	Level 4	$8\times10^{-6} \sim 32\times10^{-6}$
Fair (average)	Level 3	$32\times10^{-6} \sim 128\times10^{-6}$
Poor	Level 2	$128\times10^{-6} \sim 512\times10^{-6}$
Very poor	Level 1	$512\times10^{-6} \sim 2048\times10^{-6}$

TDIs of the bridge response and vehicle response at different roughness levels for four damage cases are shown in Figure 3-14(a) and Figure 3-14(b), respectively. The roughness level has very little effect on the TDI of bridge response. The reason could be that the bridge vibration is excited mostly by the vehicle, and the roughness only affect the local vibration. While the effect of roughness on TDI of vehicle response is significant, especially for small damage such as damage case 1 and 3.

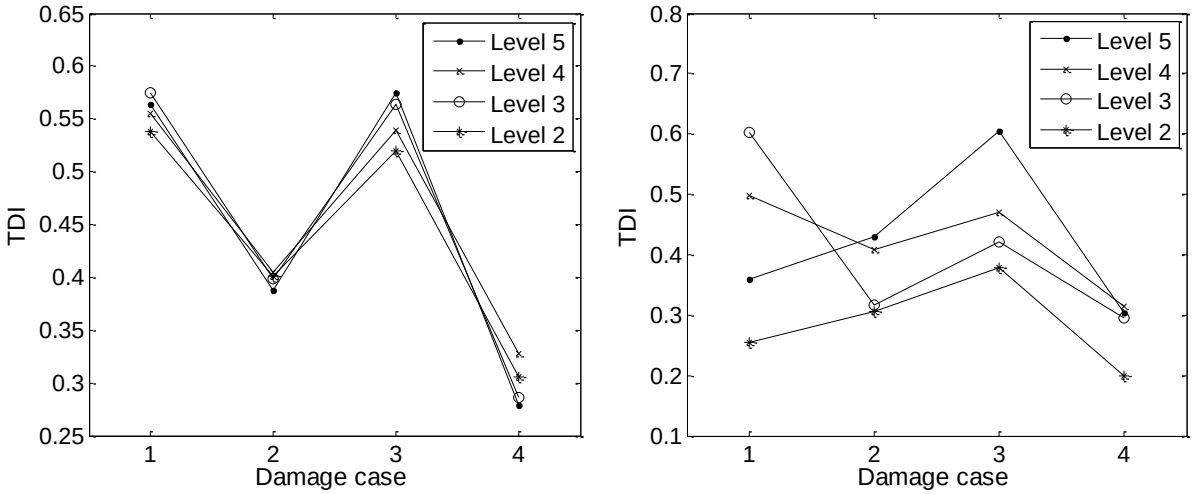

(a) TDI5-B of bridge response (b) TDI6-V of vehicle response

Figure 3-14. TDI at different roughness levels

3.4.3 Effect of vehicle speeds

Four speeds were considered for the moving vehicle: 5m/s, 10m/s, 20m/s and 30m/s. The speed of the moving vehicle affects the contacting time between the bridge and vehicle and the recording time of the dynamic response. For example, when the vehicle travels at speed of 30m/s, the interaction time is only one second. As shown in Figure 3-15(a), the vehicle speed affect little on the TDI of bridge response, but significantly on the TDI of vehicle response as shown in Figure 3-15(b). The TDIs at 5m/s and 30m/s varies largely, which means a modest vehicle speed shoule be used for the vehicle.

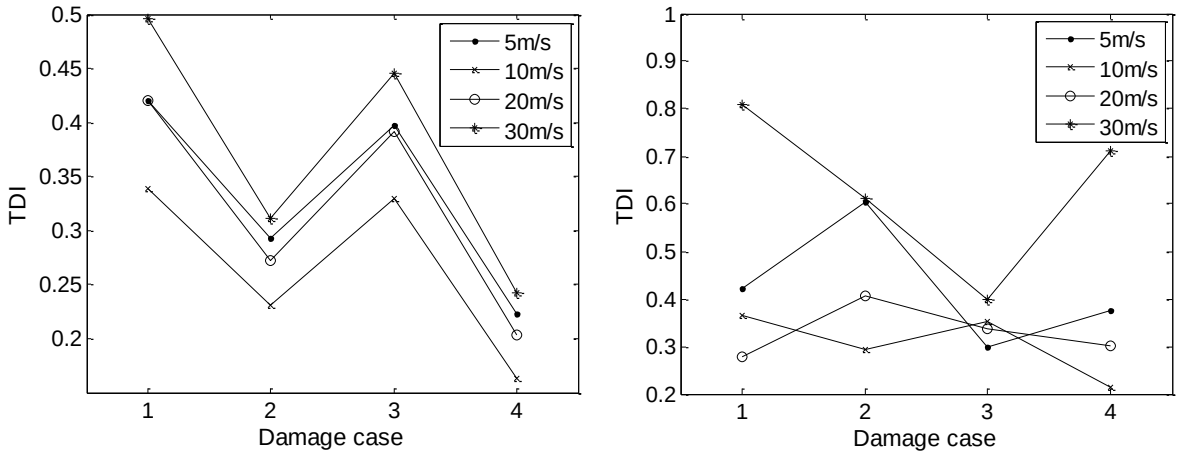

(a) TDI5-B of bridge response (b) TDI6-V of vehicle response

Figure 3-15. TDI at different vehicle speeds

3.4.4 Effect of vehicle numbers

In the daily traffic condition, many vehicles are on the bridge simultaneously. It is necessary to consider the situation with more than one moving vehicle. Herein, two situations were analyzed: the regular vehicle flow and random vehicle flow. As for regular vehicle flow, a fleet of 12 vehicles with a fix distance of 2.5m between each other and the same speed of 10 m/s on the bridge were considered. While for the random vehicle flow, the fleet is consisted of 12 vehicles with different speeds at various initial positions. Results are shown in Figure 3-16(a) and Figure 3-16(b). In the left figure, the sequence of damage case 1 and 3 changed, while in the right figure the damage sequence match the true sequence althought it becomes not easy to recognize in high frequency. The result of random flow is better than that of the regular flow, which benefits for the application in reality.

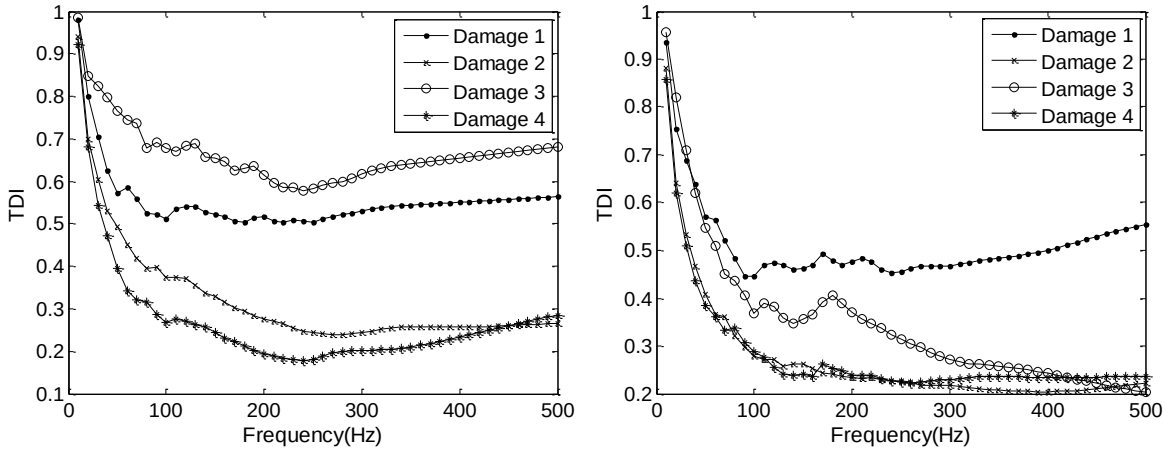

(a) TDI5_B of regular flow (b) TDI5_B of random flow

Figure 3-16. TDI with traffic flows

3.5 Method I-one reference vehicle and one moving vehicle

Attaching sensors on bridges is a routine way to measure the dynamic response of bridges and a large number of sensors are required to obtain responses at multiple locations along the bridge. As discussed earlier, a vehicle that serves as a receiver also carries information of the bridge vibration. Therefore, the vehicle response could be a substitution of the bridge response and is very easy to measure in a VBC system. Based on this, a method is proposed to obtain dynamic responses along the bridge by using two vehicles. The procedure is explained with a simple example as demonstrated in Figure 3-17: vehicle V_1 stands permanently at position x_1 serving as the reference point and vehicle V_2 initially stands at position x_2 with a distance of d. After staying for a few seconds to record vibration signal, vehicle V_2 moves to the next position x_3 and stays for recording data. Vehicle V_2 keeps this procedure until all the required positions is measured. For simplicity, vehicle V_2 moves with the same distance each time. Both vehicles record signal at the same pace. After finishing all the procedures along the bridge, n-1 pairs of dynamic responses are measured for the n positions. By extracting the transmissibility between vehicle V_2 and vehicle V_1 at each step, a transmissibility vector between the n-1 positions and the reference position are then derived.

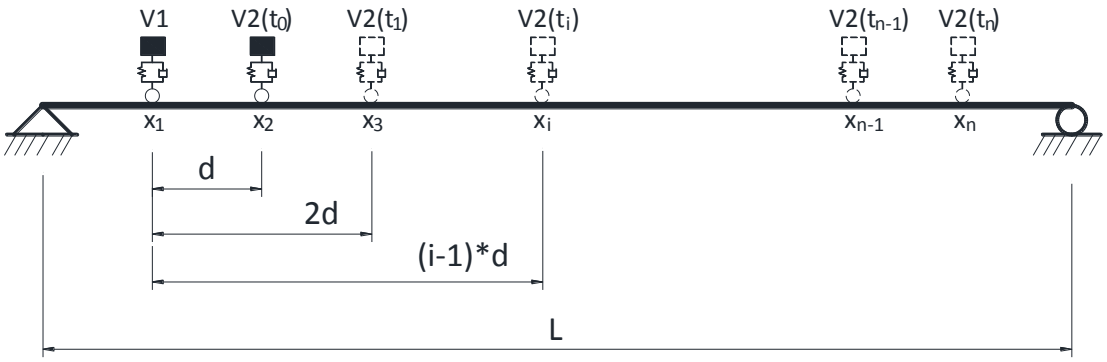

Figure 3-17. Measuring procedure of Method I.

Herein, the previous numerical VBC system with a random traffic flow was adopted as an example, and the mass of the two test vehicles is very small and can be neglected compared to vehicles of the traffic flow. The reference vehicle V_1 was at the position of $x = 17.5m$ from the left end, and vehicle V_2 was initially at the position of $x = 1.0m$, and moved forward with 1m at each step. A total of 29 positions along the bridge were measured by vehicle V_2 and a transmissibility vector with 29 entries was then derived. As discussed earlier, the modal information can be extracted from the transmissibility matrix or vector. Therefore, based on the transmissibility vector, the first three mode shape squares of the bridge with undamaged and damaged conditions are obtained and shown in Figure 3-18. The modal shape squares are normalized as the maximum value to be 1.

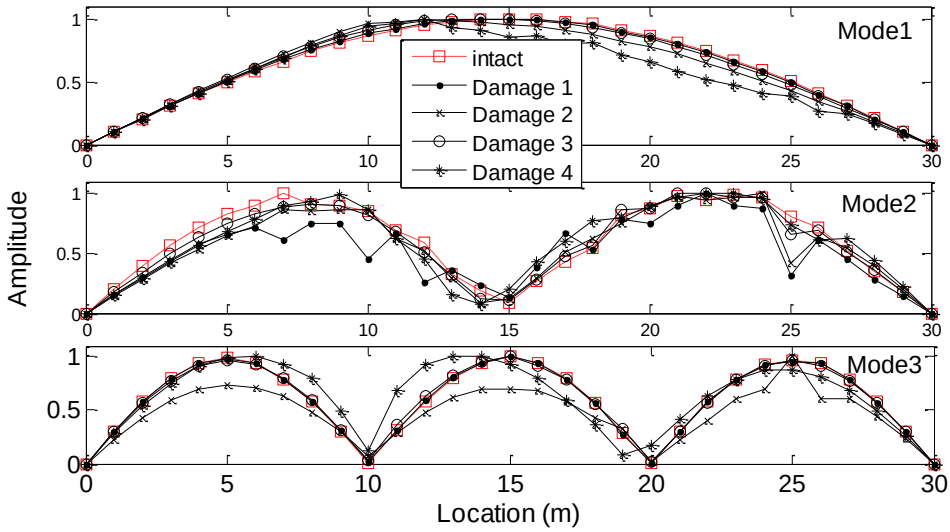

Figure 3-18. Mode shape squares of the first three modes.

The damage indicator TDI4 using the logarithmic amplitud was estimated as shown in Figure 3-19 for the full frequency range, which shows good results and the damage severity of the four damage cases can be easily recognized. The MAC value was also calculated on each transmissibility pair between the intact and damaged structure, and the result of damage case 4 was demonstrated in Figure 3-20. Around the position of 10m, the correlation is very small, which is right at the damage location.

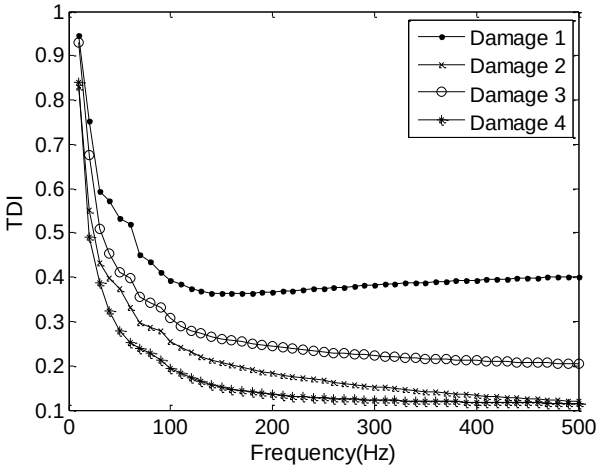

Figure 3-19. TDI of four damages

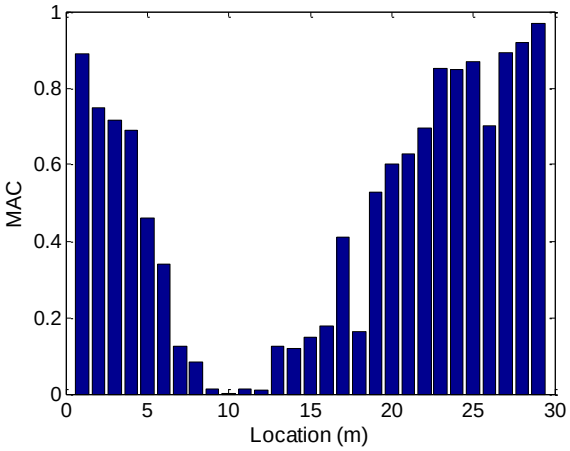

Figure 3-20. MAC of damage case 4

3.5.1 Position effect of the reference vehicle

In this method, all the transmissibilities at positions along the bridge are calculated on the basis of the response of the reference vehicle. The position of the reference vehicle is import and needs to select carefully. Since the structure is symmetric, only positions on the half part of the

bridge were investigated, i.e. different reference positions were chosen as1.0m, 7.5m, 10m or 15m. The second and third mode shape squares were extracted and shown in Figure 3-21. With respect to the second mode, the result is not good when the reference position is 15m, i.e. the middle of the bridge. It is well known that the second mode shape of a simply supported bridge has zero amplitude in the middle. Similarly, the point of one third is of zero amplitude for the third mode, which explains the bad result of the third mode extracted when the reference position is 10m (one third point). Therefore, the reference vehicle should be avoided at the position with zero amplitude in each mode shape, especially for the first few modes that greatly affect the measured results.

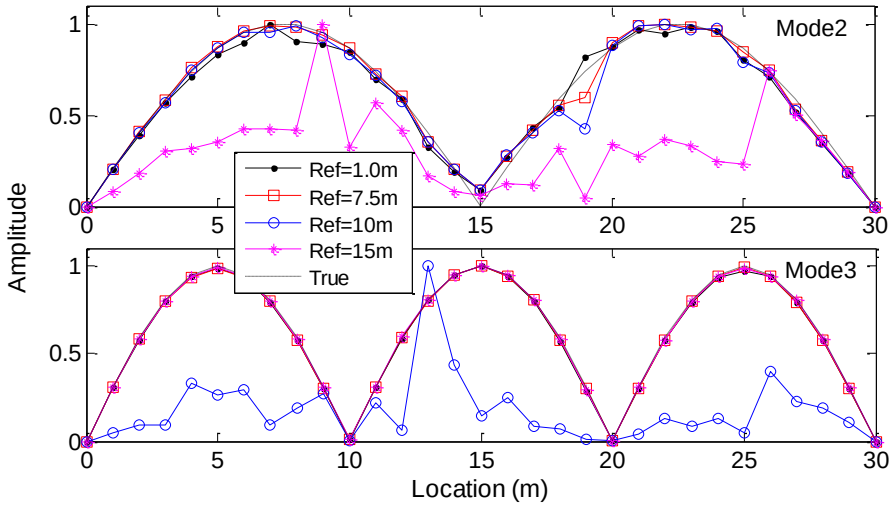

Figure 3-21. The 2nd and 3rd mode shape squares of intact bridge.

The correlation between the true mode shape squares obtained from FE analysis and the one extracted by the present method from cases with different reference positions is listed in Table 3-3. The MAC value of the first mode is almost equal to 1 except for the damage case 4. As for the second mode, the result with the reference position of 15m is the worst as expected.

Besides the position of the reference vehicle, the moving distance of each step for the second vehicle is also an important factor. The larger the moving step is, the fewer the measurement positions for the bridge is. Its effect is equivalent to that of the measurement numbers that was discussed earlier.

3.5.2 Effect of road roughness

The effect of road roughness is investigated below. The reference vehicle was at the position of 1m, and four roughness levels were considered from level 2 (poor) to level 5 (good). Figure 3-22 shows the second and third mode shape squares of the intact structure with different roughness levels, which indicates that the roughness has significant effect on the results, especially for the third mode. The road roughness has large effect on the high modes.

Table 3-3. MAC of mode shape squares

Reference position		Ref=1.0m	Ref=7.5m	Ref=10m	Ref=15m
Mode 1	D0	1.0000	1.0000	1.0000	1.0000
	D1	1.0000	1.0000	1.0000	1.0000
	D2	1.0000	1.0000	1.0000	1.0000
	D3	1.0000	1.0000	1.0000	1.0000
	D4	0.9990	0.9994	0.9994	0.9994
Mode 2	D0	0.9965	0.9968	0.9911	0.7919
	D1	0.9433	0.9072	0.8945	0.6936
	D2	0.9860	0.9930	0.9951	0.9734
	D3	0.9952	0.9937	0.9926	0.9338
	D4	0.9968	0.9968	0.9962	0.8609
Mode 3	D0	0.9999	1.0000	0.5592	0.9999
	D1	0.9998	0.9999	0.8963	0.9999
	D2	0.9871	0.9934	0.6533	0.9952
	D3	0.9996	0.9996	0.9640	0.9997
	D4	1.0000	0.9999	0.9987	0.9999

Note: D0 denotes intact bridge. D1, D2, D3 and D4 denote and damage case 1, 2, 3 and 4, respectively.

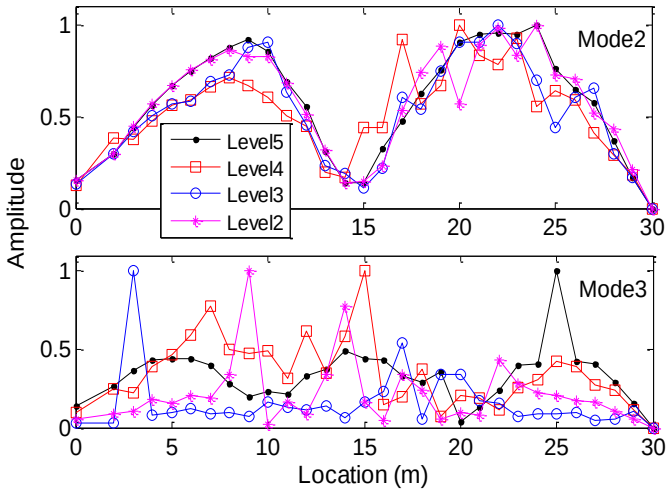

Figure 3-22. Mode shape squares of intact bridge with different roughness

The correlation between the true mode shape squares and the one with different roughness levels is listed in Table 3-4. As can be seen, the MAC value decreases as the roughness becomes worse in general trend, but the level 4 is the worst among all the roughness levels.

Table 3-4. MAC of mode shape squares with different roughness

	Mode 2					Mode 3				
	D0	D1	D2	D3	D4	D0	D1	D2	D3	D4
Level 5	0.9889	0.9700	0.9975	0.9974	0.9942	0.9873	0.9994	0.9078	0.9976	0.9983
Level 4	0.8475	0.8333	0.9419	0.9657	0.5165	0.7399	0.9812	0.7688	0.8831	0.7742
Level 3	0.9367	0.6767	0.9763	0.8779	0.8066	0.5545	0.9477	0.3428	0.8767	0.9506
Level 2	0.9890	0.7408	0.9866	0.9932	0.6871	0.9296	0.9000	0.5050	0.9538	0.8933

3.6 Method II--two vehicles at a constant distant

As discussed in Method I, the position of the reference vehicle is an important factor that affects the result significantly. If the position is at the zero amplitude point of one modal shape, the result for that mode will be not reasonable. Therefore, Method II is proposed, which uses two vehicles that are at a constant distant moving, stopping and recording in the same pace. The procedure is demonstrated as in Figure 3-23 : vehicle V_1 and V_2 stand initially with a distance of d, at position x_1 and x_2, respectively. After staying for a few seconds to record the vibration signal, both vehicles move with the same distance to the next position x_3 and x_4 and stop for recording signals. This procedure is continued until all the required positions are measured. During the entire procedure, the distance of the two vehicles remains constant.

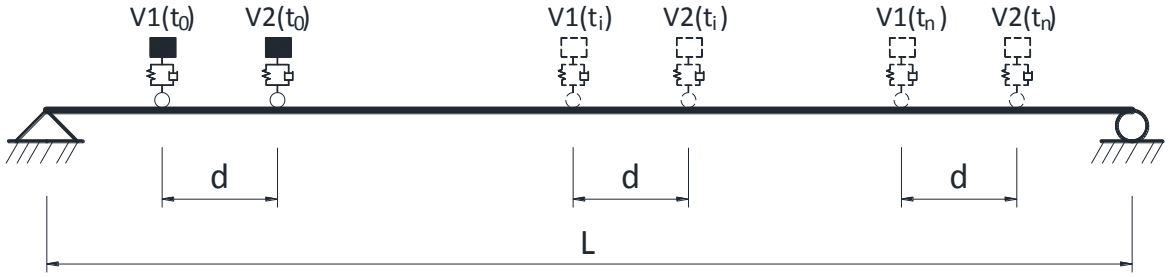

Figure 3-23. Measuring procedure of Method II.

To make the procedure regularly and easy to process the data, the moving distance of each step is set to be the distance of the two vehicles, in the sense that the next position of vehicle V_1 is the current position of V_2. Following this procedure, the bridge is uniformly measured if the bridge length is times of the vehicle distance. The transmissibility between each position can then be obtained along the bridge. For the same numerical VBC system discussed earlier, two vehicles at a distance of 1m were applied on it. The two vehicles initially stood at the position of 1m and 2m, respectively. After moving along the bridge, 28 pairs of dynamic responses were measured. The end of the bridge has no response. The transmissibility between vehicle V_2 and vehicle V_1 at each step was then extracted and formed a transmissibility vector with 28 entries. The formed vector includes transmissibilities between each successive position, that is, $[tr_{21}, tr_{32}, ...tr_{i,i-1}, ...tr_{n,n-1}]$. The result of TDI using the above transmissibility vector is showed in Figure 3-24, which indicates good results for the low frequency except damage case 2.

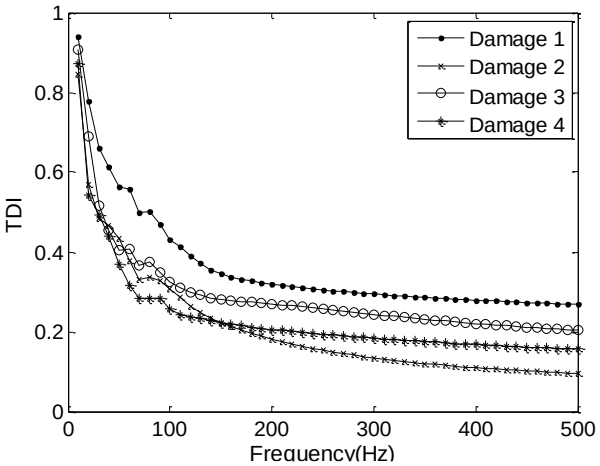

Figure 3-24. TDI of successive vector

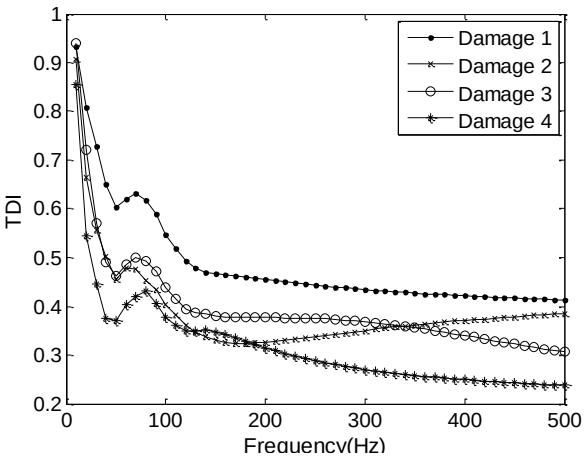

Figure 3-25. TDI of new vector

Using successive pairs of transmissibilities cannot extract the mode shape square. To this end, the first position is used as reference, and the transmissibility between the other positions and the first position can be obtained as, $TR_{i,i-1} = tr_{21} * tr_{32} * \cdots tr_{i,i-1}, i = 2,3,\cdots n.$ Base on this vector, the normalized mode shape squares for the intact and damaged bridges were obtained as shown in Figure 3-26. Compared to the result of Method I in Figure 3-18, the second and third modes of Method II are worse. Furthermore, the result of TDI using the new transmissibility vector for four damage cases is shown in Figure 3-25, which shows good results for most of the frequency range except for damage case 2.

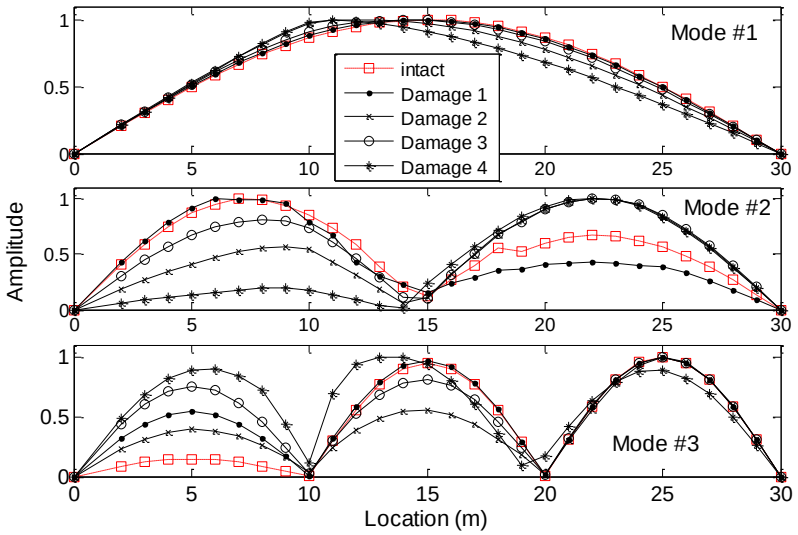

Figure 3-26. Mode shape squares of Method II

Effect of vehicle distances

In Method II, the distance between the two vehicles is important. Three distances were investigated, i.e. 1.0m, 1.5m and 2.5m. The second and third mode shape squares of the intact structure were shown in Figure 3-27 with the true one obtained from FE analysis. The right half of the extracted mode shape squares of the second mode has large error, while the same is true for the left one third of the third mode. As for the second mode, the result from the case with distance of 1.0m is the best, while the best is the distance of 1.5m for the third mode.

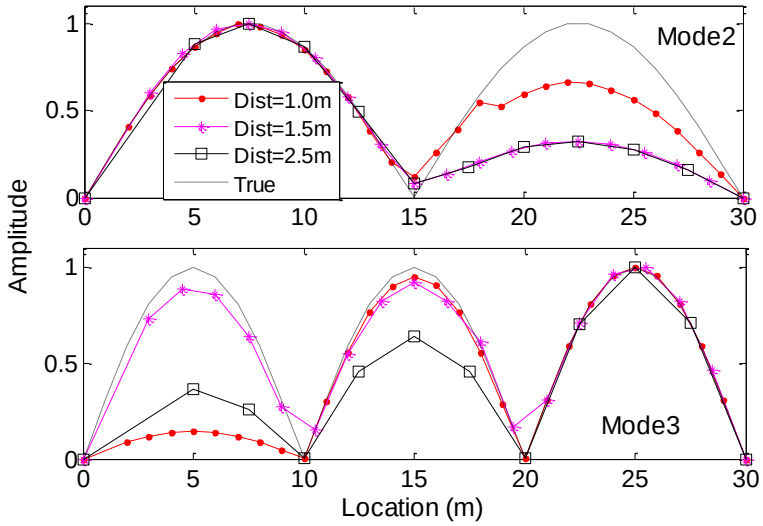

Figure 3-27. Mode shape squares with different distances

The correlation between the true mode shape squares and the one extracted by method II from cases with different vehicle distances is listed in Table 3-5. The MAC value decreases greatly when the vehicle distance increases to 2.5m, especially for the third mode. A short distance between the two vehicles is recommended.

Table 3-5. MAC of mode shape squares with different distance

Distance	Mode 2					Mode 3				
	D0	D1	D2	D3	D4	D0	D1	D2	D3	D4
1.0m	0.9600	0.8626	0.9394	0.9872	0.7518	0.7597	0.9362	0.8605	0.9780	0.9924
1.5m	0.7311	0.8238	0.9357	0.8407	0.8955	0.8483	0.8498	0.8530	0.8522	0.8588
2.5m	0.6521	0.7619	0.8294	0.7252	0.7971	0.4442	0.5189	0.3411	0.5589	0.6096

In addition, the effect of road roughness is similar to that of Method I, which is not discussed here.

3.7 Conclusions

Due to the local characteristic of transmissibility, the present study derived the transmissibility in the vehicle-bridge coupled system, studied the feasibility of its application for damage detection, and finally proposed two methods to measure the vehicle dynamic response and extract the transmissibility for damage detection. The following conclusions can be drawn:

(1) The transmissibility extracted from bridge-only system embodies very stable and effective results, but it requires external excitation forces. As for the transmissibility extracted from the VBC system, six TDIs were compared. TDI3 and TDI4 have better results than others. Moreover, the low frequency part of the vehicle transmissibility is useful, although the transmissibility from the response measured directly from the bridge is much better than the one from the vehicle.

(2) The parametric study on the effect of measurement numbers, road surface roughness, vehicle speed, and vehicle numbers shows: The road roughness level and the vehicle speed have very small effect on the TDI of bridge response but large effect on the TDI of vehicle response, especially for the small damage cases. It suggests a moderate vehicle speed for field testing. The result with random traffic flow is much better than that with the regular traffic flow.

(3) In method I, the first vehicle stands at a fixed position as reference and the second vehicle moves step by step to record responses at positions along the bridge. The modal information such as natural frequencies and mode shape squares are successfully extracted from the transmissibility of vehicle response. Nevertheless, the result is affected by the position of the reference vehicle. The reference vehicle should not be put at the position with zero amplitude in each mode shape, especially for the first few modes that greatly affect the measuring results.

(4) Method II uses two vehicles that are at a constant distance stopping at the designated position, recording signals and moving to the next position in the same pace. This method does not need one vehicle stant at the reference postion and the responses of the two vehicles have closer relationship, although the result shows a little worse than Method I. The distance between those two vehicles is an important factor.

(5) The transmissibility and dynamic response of the vehicle are measured in the condition that both vehicles stopped at the designated position with vertical vibration only. The ideal method is to have both vehicles move along the bridge and take measurements at the same time, which is the further research of the present study.

3.8 References

Ball, J. A., Gohberg, I., and Kaashoek, M. A. (1995). “A frequency response function for linear, time-varying systems.” Mathematics of Control, Signals, and Systems (MCSS), 8(4), 334-351.

Bu, J. Q., Law, S. S., and Zhu, X. Q. (2006). “Innovative bridge condition assessment from dynamic response of a passing vehicle.” J. of Engineering Mechanics, 12, 1372-1379.

Canales, G., Mevel, L., Basseville, M. (2009). “Transmissibility Based Damage Detection.” Proceedings of the 27th International Operational Modal Analysis Conference (IMAC XXVII), Orlando, Florida, U.S.A.

Cardenl, E. P., and Fanning, P. (2004). “Vibration Based Condition Monitoring: A Review." Structural Health Monitoring, 3(4), 355-377.

Clough, R., and Penzien, J. (2003). “Dynamics of Structures.” Computer and Structures, Inc.

Dalianis, S. A., Hammond, J. K., White, P. R., and Cambourakis, G. E. (1998). “Simulation and identification of nonstationary systems using linear time-frequency methods.” J. of Vibration and Control, 4(1), 75-91.

Deng, L. (2009). “System identification of bridge and vehicle based on their coupled vibration.” Ph.D. Dissertation, Louisiana State University, Baton Rouge, LA.

Devriendt, C., Vanbrabant, Guillaume, P. (2007). “The use of transmissibility measurements in output-only modal analysis.” Mechanical Systems and Signal Processing, 21, 2689-2696.

Devriendt, C., De Sitter, Vanlanduit, S., Guillaume, P. (2009). “Operational modal analysis in the presence of harmonic excitations by the use of transmissibility measurements.” Mechanical Systems and Signal Processing, 23, 621-635.

Devriendt, C., De Sitter, G., Guillaume, P. (2010). “An operational modal analysis approach based on parametrically identified multivariable transmissibilities.” Mechanical Systems and Signal Processing, 24, 5, 1250-1259.

Dodds, C. J., and Robson, J. D. (1973). “The description of road surface roughness.” J. of Sound and Vibration, 31(2), 175-183.

Doebling, S.W., Farrar, C. R., and Prime, M. B. (1998). “A summary review of vibration-based damage identification methods.” The Shock and Vibration Digest, 30(2), 91-105.

Esfandiari, A., Bakhtiari-Nejad, F., Rahai, A., Sanayei, M. (2009). “Structural model updating using frequency response function and quasi-liner sensitivity equation.” J. of Sound and Vibration, 326, 557-573.

Esfandiari, A., Bakhtiari-Nejad, F., Sanayei, M., Rahai, A. (2010). “Structural finite element model updating using transfer function data.” Computer and Structures, 88, 54-64.

Ewins, D. J., Liu, W. (1998). “Transmissibility properties of MDOF systems.” Proceedings of the 16th International Modal Analysis Conference (IMAC XVI), Santa Barbara, California, 847- 854.

Fan, W. and Qiao, P. Z. (2011). “Vibration-based damage identification methods: a review and comparative study." Structural Health Monitoring, 10, 83-111.

Huang, D. Z., and Wang, T. L. (1992). “Impact analysis of cable-stayed bridges.” Computers and Structures, 43(5), 897-908.

International Standard Organization. (1995). "Mechanical vibration - Road surface profiles-Reporting of measured data." Geneva.

Johnson, T. (2002). “Analysis of dynamic transmissibility as a feature for structural damage detection.” Master thesis in Mechanical Engineering, Purdue University.

Kwakernaak, H., Sivan, R., and Strijbos, R. C. W. (1991). “Modern signals and systems.” Prentice-Hall, Englewood Cliffs, NJ, USA.

Lee, D. H., Hwang, W. S. (2003). “Parametric optimization of complex systems using a multi-domain FRF-based sub structuring method.” Computers and Structures, 81, 2249–2257.

Lew, J. S. (1995). “Using transfer function parameter changes for damage detection of structures.” AIAA Journal, 33, 2189–2193.

Lin, C. W., Yang, Y. B. (2005). “Use of a passing vehicle to scan the fundamental bridge frequencies: an Experimental Verification.” Engineering Structures, 27, 1865-1878.

Lu, Z. R., Liu, J. K., Huang, M., Xu, W. H. (2009). “Identification of damages in coupled beam systems from measured dynamic response.” Journal of Sound and Vibration, 326, 177-189.

Lu, Z. R., Huang, M., Chen, W. H. Liu, J. K., Ni, Y. Q. (2010). “Assessment of local damages in box-girder bridges using measured dynamic responses of passing vehicle.” Prognostics and Health Management Conference, Jan. 12-14, 2010, Macao, China.

Lu, Z. R., Liu, J. K. (2011). “Identification of both structural damages in bridge deck and vehicle parameters using measured dynamic response.” Computers and Structures, 89, 13-14, 1397-1405.

Maia, N. M. M., Silva, J. M. M., Ribeiro, A. M. R. (2001). “The transmissibility concept in multi-degree-of-freedom systems.” Mechanical Systems and Signal Processing, 15(1), 129-137.

Maia, N. M. M., Almeida, R. A. B., Urgueira, A. P. V., Sampaio, R. P. C. (2011). “Damage detection and quantification using transmissibility.” Mechanical System and Signal Processing, 25, 2475-2483.

Ribeiro, A. M. R., Maia, N. M. M., Silva, J. M. M. (2000). “On the generalization of the transmissibility concept.” Mechanical Systems and Signal Processing, 14 (1), 29–35.

Shi, X. M. (2006). “Structural performance of approach slab and its effect on vehicle induced bridge dynamic response.” Ph.D. Dissertation, Louisiana State University, Baton Rouge, LA.

Sohn, H., Farrar, C., Hunter, N., and Worden, K. (2003). “A review of structural health monitoring literature: 1996-2001.” Los Alamos National Laboratory report, LA-13976-MS.

Varoto, P. S., McConnell, K. G. (1998). “Single point vs. multi point acceleration transmissibility concepts in vibration testing.” Proceedings of the 16th International Modal Analysis Conference (IMAC XVI), Santa Barbara, California, 83-90.

Vestroni, F., Capecchi, D. (2000). “Damage detection in beam structure based on frequency measurements.” Journal of Engineering Mechanics, 126(7), 761–768.

Wang, Z., Lin, R. M., Lim, M. K. (1997). “Structural damage detection using measured FRF data.” Computer Methods in Applied Mechanics and Engineering, 147, 187–197.

Yan, Y. J., Cheng, L., Wu, Z. Y., Yam, L. H. (2007). “Development in vibration-based structural damage detection technique.” Mechanical Systems and Signal Processing, 21, 2198-2211.

Yang, Y. B., Lin, C. W., Yau, J. D. (2004). “Extracting bridge frequencies from the dynamic response of a passing vehicle.” J. of Sound and Vibration, 272, 471-493.

Yang, Y. B., Chang, K. C. (2009). “Extraction of bridge frequencies from the dynamic response of a passing vehicle enhanced by the EMD technique.” J. of Sound and Vibration, 322, 718-739.

Yang, Y. B., Chang, K. C. (2009). “Extraction the bridge frequencies indirectly from a passing vehicle: parametric study.” Engineering Structures, 31, 2448-2459.

Yi, X., Zhu, D., Wang, Y., Guo, J., and Lee, K. M. (2010). "Embedded transmissibility function analysis for damage detection in a mobile sensor network." Proceedings of SPIE, Sensors and Smart Structures Technologies for Civil, Mechanical, and Aerospace Systems 2010, 7647: 764729, San Diego, CA, March 8, 2010.

Zadeh, L. A. (1950). “Frequency analysis of variable networks.” Proceedings of the IRE, 38(3), 291-299.

Zhang, Y., Wang, L. Q., Xiang, Z. H. (2012). “Damage detection by mode shape squares extracted from a passing vehicle.” J. of Sound and Vibration, 331, 291-307.

Zhang, Y., Lie, S. T., Xiang, Z. H. (2013). “Damage detection method based on operating deflection shape curvature extracted from dynamic response of a passing vehicle.” Mechanical System and Signal Processing, 35, 238-254.

CHAPTER 4. EXTRACTING BRIDGE MODAL PROPERTIES FROM DYNAMIC RESPONSES OF MOVING VEHICLES

4.1 Introduction

The vibration-based damage detection method gains great research interests over the last decades ever since it was introduced into civil engineering (Doebling et al. 1998; Sohn et al. 2003; Carden and Fanning 2004; Yan et al. 2007; Fan and Qiao 2011). The prerequisite of those methods is the reliable measured data. Most developments make use of measurements directly from the bridge structure by attaching sensors on it. Measurement of natural frequencies of structures can be easily obtained by one or a few sensors, but measurement of mode shapes and Frequency Response Functions (FRFs) requires either a single excitation point and many sensors or a roving exciter with one or more fixed sensors (Carden and Fanning 2004). The entire process is very time and energy consuming.

During the interaction between the vehicle and bridge, the vehicle serves as both an active actuator and a response receiver in the coupled system. As discussed in Yang et al. (2009a), the vehicle acceleration contains three groups of frequency components: vehicle frequency, bridge-related frequencies and driving-related frequencies. The vehicle dynamic responses such as accelerations, while easy to measure, own the similar features as the modal shapes and FRFs of bridges. Therefore, vibration-based methods become very attractive. Yang et al. (2004, 2009a, and 2009b, 2012, 2013) and Lin (2005) have done work on extracting the fundamental bridge frequency from the acceleration time history of a vehicle passing over the bridge. A few researchers studied damage detection of bridges using the response of moving vehicles. Bu et al. (2006) proposed an approach to detect the damage through the flexural stiffness reduction of finite elements based on dynamic response sensitivity analysis on the coupled system. Lu et al. (2009, 2010 and 2011) assessed local damages in box-girder bridges using measured dynamic responses of both the bridge and a passing vehicle. Kim et al. (2011) experimentally investigated the feasibility of damage detection for short span bridges using both bridge and vehicle vibration data. Zhang (2012 and 2013) developed a damage detection method based on the squares of the approximately extracted structural mode shape from the acceleration of a passing tapping "vehicle" and a method based on the curvature of the operating deflection shape extracted from the dynamic response of a moving vehicle.

Since the vehicle responses contain more information than the vehicle and bridge modal information, such as the driving-related frequencies and the road roughness, the focus of the present study is therefore to eliminate the effect of other factors and efficiently extract the bridge modal properties from the vehicle response. A test vehicle consisting of a tractor and two following trailers are proposed to take the measurement and the residual response of the two trailers are processed using Fourier Transform, wavelet analysis and STFT to extract the modal properties of the bridge. By designing a specific test vehicle equipped with sensors and data acquisition system, it would be very convenient to measure the bridge response without pre-installed sensors, which saves a large amount of time and effort.

4.2 Theory

4.2.1 Response of moving vehicles

The present study proposed a methodology using a test vehicle consisting of a tractor and two following trailers to take the measurement and extract the modal properties of bridges. To demonstrate the concept, a simplified vehicle-bridge coupled system was adopted as shown in Figure 4-1. The tractor is modeled as a single degree-of-freedom (SDOF) vehicle with three parameters and each of the two trailers is a SDOF model with a small mass. The two trailers are identical. The excitation effect of the two trailers on the bridge vibration is ignored du to its small mass, but the response of the two trailers induced by the bridge vibration and road roughness is calculated. The bridge is modeled as an Euler-Bernoulli beam with simple supports.

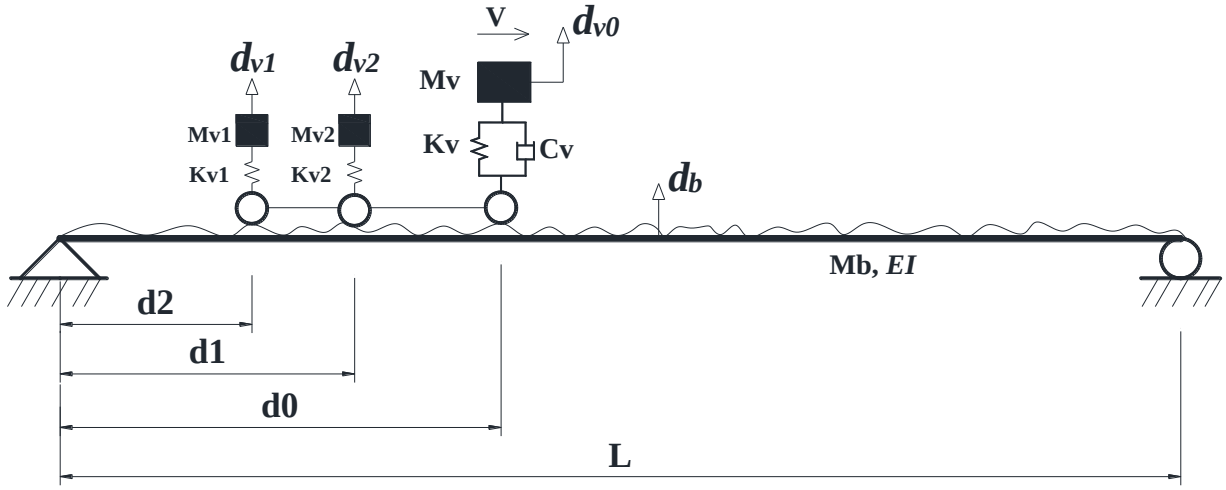

Figure 4-1. A simplified vehicle-bridge system.

When the test vehicle is traveling on a bridge, the equation of motion for the vehicle and bridge can be expressed as,

$$M_v \ddot{d}_{v0} + K_v[d_{v0} - d_b(x = d_0, t) - r(x = d_0)] + F_G = 0 \tag{1a}$$

$$M_{v1} \ddot{d}_{v1} + K_{v1}[d_{v1} - d_b(x = d_1, t) - r(x = d_1)] + F_{G1} = 0 \tag{1b}$$

$$M_{v2} \ddot{d}_{v2} + K_{v2}[d_{v2} - d_b(x = d_2, t) - r(x = d_2)] + F_{G2} = 0 \tag{1c}$$

$$M_b \ddot{d}_b + EId_b'''' = K_v[d_{v0} - d_b(x = d_0, t) - r(x = d_0)]\delta(x - d_0) \tag{4-1d}$$

where M_v, K_v are the mass and spring stiffness of the tractor, respectively, $F_G = M_v g$; M_b, EI are the unit mass and flexible stiffness of the bridge, respectively; d_{v0}, d_{v1}, d_{v2} and d_b are the displacements of the tractor, two trailers and the bridge, respectively; r is the road surface roughness; and $d_0 = Vt$ is the distance of the tractor to the bridge end, assuming a constant speed of the vehicle.

Substituting Equation (4-1a) into Equation (4-1d) gives,

$$M_b \ddot{d}_b + EId_b'''' = (-M_v \ddot{d}_{v0} - F_G)\delta(x - d_0) \tag{4-2}$$

By separating the displacement variable d_b into time and space domains, the solution of Equation (4-2) can be assumed as,

$$d_b(x,t) = \sum_{j=1}^{\infty} \varphi_j(x) y_j(t) \tag{4-3}$$

For a simple beam, the modal shapes are of the sinusoidal form $\varphi_j(x) = \sin\frac{j\pi x}{L}$ and the angular frequencies can be given by $\omega_j = (\frac{j\pi}{L})^2 \sqrt{\frac{EI}{M_b}}$. By assuming that the vehicle mass is much less than the bridge mass, i.e. $M_v / M_b << 1$ （Yang et al. 2009a), the inertia force of the test vehicle could be omitted. Substituting Equation (4-3) into Equation (4-2), multiplying by $\varphi_j(x)$, integrating over x, and using the orthogonal conditions lead to the uncoupled equation of motion,

$$\begin{aligned} \ddot{y}_j + \omega_j^2 y_j &= \int_0^L \frac{2\varphi_j(x)}{M_b L}\left[-F_G \delta(x - d_0)\right]dx \\ &= \frac{-2M_v g}{M_b L}\sin\frac{j\pi Vt}{L} \end{aligned} \tag{4-4}$$

The solution to Equation (4-4) under zero initial conditions is given by

$$y_j(t) = \frac{\Delta_j}{1 - S_j^2}\left[\sin\frac{j\pi Vt}{L} - S_j \sin\omega_j t\right] \tag{4-5}$$

where $\Delta_j = \frac{-2M_v g L^3}{j^4 \pi^4 EI}$ and $S_j = \frac{j\pi V}{L\omega_j}$.

Substituting Equation (4-5) into Equation (4-3), the displacement response of the bridge can then be expressed as,

$$d_b(x,t) = \sum_{j=1}^{\infty} \frac{\Delta_j}{1 - S_j^2}\sin\frac{j\pi x}{L}\left[\sin\frac{j\pi Vt}{L} - S_j \sin\omega_j t\right] \tag{4-6}$$

By ignoring the self-weight force, the vehicle equation Equation (4-1a) and (4-1b) can be rewritten as,

$$\ddot{d}_{v1} + \omega_{v1}^2 d_{v1} = \omega_{v1}^2\left[d_b(x = d_1, t) + r(x = d_1)\right] \tag{4-7a}$$

$$\ddot{d}_{v2} + \omega_{v2}^2 d_{v2} = \omega_{v2}^2\left[d_b(x = d_2, t) + r(x = d_2)\right] \tag{4-7b}$$

where $\omega_{v1}^2 = \sqrt{k_{v1} / m_{v1}}$ and $\omega_{v2}^2 = \sqrt{k_{v2} / m_{v2}}$ are frequencies of the two following trailers, respectively.

By assuming the first derivative of the roughness exists, substituting the bridge displacement in Equation (4-6) into Equation (4-7a) and (4-7b), and using Duhamel's integral, the vehicle displacement can be derived as,

$$d_{v1}(t)=\sum_{j=1}^{\infty}\left\{A_1\cos\frac{(j-1)\pi d_1}{L}-A_2\cos\frac{(j+1)\pi d_1}{L}+A_3\cos\omega_{v1}t-A_4\cos(\omega_j t-\frac{j\pi d_1}{L})+A_5\cos(\omega_j t+\frac{j\pi d_1}{L})\right\}$$
$$+\frac{r'(d_1)}{\omega_{v1}}+r(d_1) \tag{4-8}$$

where the coefficients are,

$$A_1=\frac{\Delta_j}{2(1-S_j^2)(1-\mu_{j-1}^2S_{j-1}^2)},\qquad A_2=\frac{\Delta_j}{2(1-S_j^2)(1-\mu_{j+1}^2S_{j+1}^2)},$$
$$A_3=\frac{2\Delta_j\mu_j^2S_j^2}{(1-S_j^2)}\left[\frac{1}{(1-\mu_{j-1}^2S_{j-1}^2)(1-\mu_{j+1}^2S_{j+1}^2)}-\frac{1}{(1-\mu_j^2(1-S_j)^2)(1-\mu_j^2(1+S_j)^2)}\right],$$
$$A_4=\frac{\Delta_jS_j}{2(1-S_j^2)(1-\mu_j^2(1-S_j)^2)},\qquad A_5=\frac{\Delta_jS_j}{2(1-S_j^2)(1-\mu_j^2(1+S_j)^2)},\text{ and }\mu_1=\frac{\omega_j}{\omega_{v1}}$$

The displacement response of the second trailer, d_{v2}, can be similarly derived by replacing d_1 with d_2 into Equation (4-8).

Therefore, the residual response of the two following trailers can be expressed as,

$$\Delta d_{12}(t)=d_{v1}(t)-d_{v2}(t+\frac{d_1-d_2}{V}) \tag{4-9}$$

It is noted that a time shift is introduced here to make sure the response of the same location is subtracted. Since the effect of the roughness on the vehicle response is an independent part, the residual response could be a good idea to remove the roughness effect and efficiently extract the bridge frequencies from the vehicle response. The residual acceleration response of the two trailers can be obtained by doubly differentiating the residual displacement in Equation (4-9).

4.2.2 Extract mode shape squares

Many studies have been done to extract bridge frequencies from the vehicle response in the frequency domain. Short-time Fourier Transform (STFT) as a useful tool is able to present a signal in both the time and frequency domain. After applying STFT, we can observe the signal's frequency component at any time point. By applying the STFT to Equation (4-9), we can obtain the frequency spectrum at the time that the vehicle travels to the position $x_0=Vt$ (Zemmour 2006) as

$$S(x_0,\omega)=\int_{-\infty}^{\infty}\Delta\ddot{d}_{12}(t)\bullet w(t-t_0)e^{-i\omega t}dt \tag{4-10}$$

where $w(t-t_0)$ is a window function that will be discussed later. A discrete STFT is more useful by picking certain time points. Following this method, the frequency spectrum at any position along the bridge can be obtained. Since the spectrum contains the bridge frequencies, if the magnitude at a specific bridge frequency in the spectra at different positions along the bridge is

extracted, the mode shape of the bridge can then be formed, as shown in Figure 4-2. Generally, the power spectral density (PSD) ,

$$\left|S(x_1,\omega_j)\right|^2, \quad \left|S(x_2,\omega_j)\right|^2, \quad \left|S(x_3,\omega_j)\right|^2, \ldots\ldots \quad \left|S(x_n,\omega_j)\right|^2$$

are calculated and displayed, and the mode shapes extracted are named as mode shape squares, where $x_i = Vt_i$ is the vehicle position on the bridge and ω_j is the jth bridge frequency.

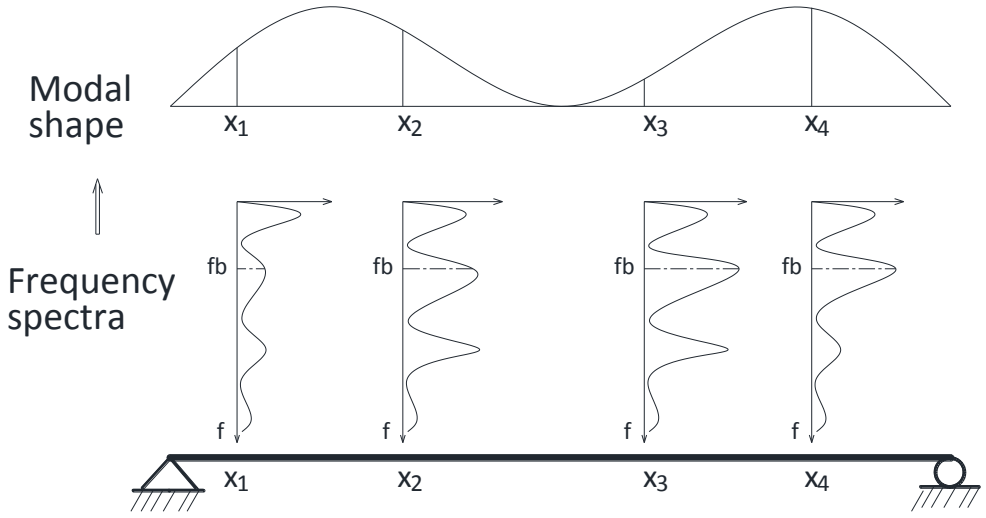

Figure 4-2. Extracting mode shape squares using STFT

4.2.3 Models of VBC system

The above analytical study and simplified VBC system are used to demonstrate the concept. As for more sophisticated or realistic problems, the Finite Element (FE) method is always the first choice. Three crucial parts for a VBC system are: vehicle model, bridge model, and roughness model (Shi 2006 and Deng 2009).

The vehicle model served as a response receiver is a SDOF vehicle model, while vehicles of the traffic flow are modeled as a full-scale vehicle model combined with several rigid bodies connected with several axle mass blocks, springs, and damping devices (Cai and Chen 2004). The suspension systems and elasticity of tires are idealized as liner elastic spring elements and dashpots. The bridge deck and the moving tire are assumed to be point-contact. The axle number may vary from two to five.

The bridge can be simulated as a FE model using different element types such as beam, shell, or solid elements. The equation of motion for a bridge with discretized finite elements can be written as follows:

$$[M_b]\{\ddot{d}_b\} + [C_b]\{\dot{d}_b\} + [K_b]\{d_b\} = \{F_b\} \tag{4-11}$$

where $[M_b]$, $[C_b]$, and $[K_b]$ are the mass, damping, and stiffness matrices of the bridge, respectively; $\{d_b\}$ is the displacement vector for all DOFs of the bridge; $\{\dot{d}_b\}$ and $\{\ddot{d}_b\}$ are the first and second derivative of $\{d_b\}$ with respect to time, respectively; and $\{F_b\}$ is a vector containing all external forces acting on the bridge. With the modal superposition technique and the normalized condition such that $\{\Phi_i\}^T[M_b]\{\Phi_i\}=1$ and $\{\Phi_i\}^T[K_b]\{\Phi_i\}=\omega_i^2$, Equation (4-11) can now be rewritten as:

$$[I]\{\ddot{\xi}_b\}+[2\omega_i\eta_i I]\{\dot{\xi}_b\}+[\omega_i^2 I]\{\xi_b\}=[\Phi_b]^T\{F_b\} \tag{4-12}$$

where Φ_b and ξ_b are the mode shape matrix of the bridge and the generalized modal coordinate vector, respectively. In this study, the damping matrix $[C_b]$ in Equation (4-11) is assumed to be equal to $2\omega_i\eta_i[M_b]$, where η_i is the percentage of the critical damping for the ith mode of the bridge. [I] = unit matrix.

The road surface condition is an important factor that affects the dynamic responses of both the bridge and vehicles. A road surface profile is usually assumed to be a zero-mean stationary Gaussian random process and can be generated through an inverse Fourier transformation based on a power spectral density (PSD) function (Dodds and Robson 1973) as:

$$r(X)=\sum_{k=1}^{N}\sqrt{2\varphi(n_k)\Delta n}\cos(2\pi n_k X+\theta_k) \tag{4-13}$$

where θ_k is the random phase angle uniformly distributed from 0 to 2π; φ is the PSD function (m^3/cycle) for the road surface elevation; and n_k is the wave number (cycle/m). In this study, the following PSD function (Huang and Wang 1992) has been used:

$$\varphi(n)=\varphi(n_0)\left(\frac{n}{n_0}\right)^{-2} \qquad (n_1<n<n_2) \tag{4-14}$$

where n is the spatial frequency (cycle/m); n_0 is the discontinuity frequency of $1/2\pi$ (cycle/m); $\varphi(n_0)$ is the roughness coefficient (m^3/cycle) whose value is chosen depending on the road condition, such as from very good to poor condition based on ISO (ISO 1995); and n_1 and n_2 are the lower and upper cut-off frequencies.

The vehicle-bridge coupled system

The equation of motion of the VBC system can be rewritten in the matrix form as below (Shi 2006 and Deng 2009):

$$\begin{bmatrix} M_b & \\ & M_v^N \end{bmatrix}\begin{Bmatrix} \ddot{d}_b \\ \ddot{d}_v \end{Bmatrix}+\begin{bmatrix} C_b+C_{b-b} & -C_{b-v} \\ -C_{v-b} & C_v^N \end{bmatrix}\begin{Bmatrix} \dot{d}_b \\ \dot{d}_v \end{Bmatrix}+\begin{bmatrix} K_b+K_{b-vb}+K_{b-cb} & -K_{b-v} \\ -K_{v-b}-K_{v-cb} & K_v^N \end{bmatrix}\begin{Bmatrix} d_b \\ d_v \end{Bmatrix}=\begin{Bmatrix} -F_{b-r}-F_{b-cr} \\ F_{v-r}+F_{v-cr}-F_G^N \end{Bmatrix} \tag{4-15}$$

The additional terms C_{b-b}, C_{b-v}, C_{v-b}, K_{b-vb}, K_{b-cb}, K_{b-v}, K_{v-b}, K_{v-cb}, F_{b-r}, F_{b-cr}, F_{v-r}, and F_{v-cr} in Equation (4-15) are due to coupling effect between the bridge and vehicles. When a vehicle travels on the bridge, the position of the contact point changes with time, which means

the road roughness $r(x)$ at the contact point and the shape function are both time-dependent terms, indicating that all the additional terms in Equation (4-15) are time-dependent terms. Using Equation (4-12), Equation (4-15) can be further rewritten as follows:

$$\begin{bmatrix} I & \\ & M_v \end{bmatrix}\begin{Bmatrix} \ddot{\xi}_b \\ \ddot{d}_v \end{Bmatrix}+\begin{bmatrix} 2\omega_i\eta_i I+\Phi_b{}^T C_{b-b}\Phi_b & -\Phi_b{}^T C_{b-v} \\ -C_{v-b}\Phi_b & C_v{}^N \end{bmatrix}\begin{Bmatrix} \dot{\xi}_b \\ \dot{d}_v \end{Bmatrix} + \begin{bmatrix} \omega_i{}^2 I+\Phi_b{}^T(K_{b-vb}+K_{b-cb})\Phi_b & -\Phi_b{}^T K_{b-v} \\ -(K_{v-b}+K_{v-cb})\Phi_b & K_v{}^N \end{bmatrix}\begin{Bmatrix} \xi_b \\ d_v \end{Bmatrix}=\begin{Bmatrix} -\Phi_b{}^T(F_{b-r}+F_{b-cr}) \\ F_{v-r}+F_{v-cr}-F_G{}^N \end{Bmatrix} \tag{4-16}$$

where the vehicle-bridge coupled system contains only the modal properties of the bridge and the physical parameters of the vehicles.

4.3 Numerical analysis

A numerical study was conducted to first investigate the feasibility of extracting bridge modal properties using dynamic responses of two moving vehicles in a VBC system. The system consists of a simply supported beam and a tractor-trailer vehicle, as shown in Figure 4-3. V1 and V2 in the figure denote the first and secone trailers, respectively. The tractor travels on the bridge to excite the bridge vibration and the two following trailers equipped with sensors are used to receive dynamic responses. The beam was discretized into 120 beam elements with physical properties: elastic modulus E=32 GPa, mass density D=2.5e3 kg/m^3, length L=30 m, section width = 1.2 m, and section depth = 2 m. The first four vertical frequencies of the bridge are 3.579Hz, 14.012Hz, 30.503Hz, and 50.84Hz. Parameters of the tractor model are: m_v = 4.0e4 kg, c_v = 1.0e4 Ns/m, and k_v = 6.0e6 N/m. The two trailers have the same parameters as m_v = 120 kg, c_v = 1.0e3 Ns/m, and k_v = 6.0e4 N/m. The natural frequencies of the tractor and the trailer are 1.949Hz and 3.559Hz, respectively. The distance between the tractor and the first trailer is d1=0.5m and two trailers are at a distance of d=0.5m. Surface roughness is assumed as in good condition in terms of ISO (1995).

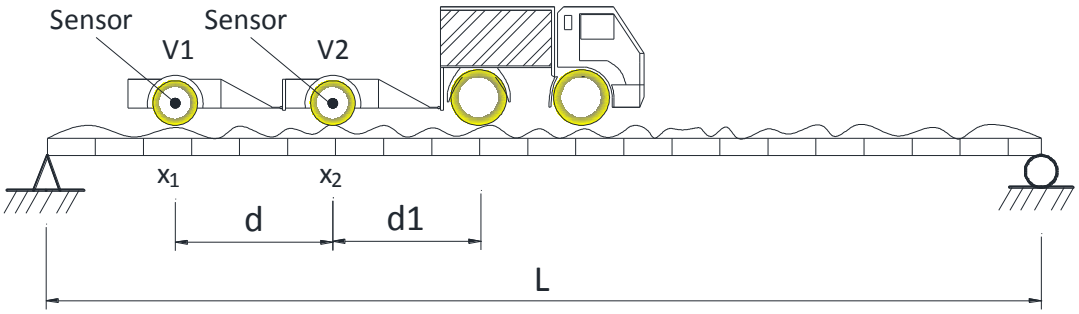

Figure 4-3. Vehicle and bridge system with test vehicles

4.3.1 Without traffic flows

The acceleration time histories of vehicles are measured and transferred into the frequency domain, as shown in Figure 4-4 with the tractor results as well. Only the frequency of

the tractor can be recognized from the figure. Yang et al. (2012) studied the residual spectrum by subtracting the distribution function in one Fourier spectrum from the other. In the present study, the response of the two trailers is subtracted first in the time domain and transferred then into the frequency domain, which is called "spectrum of the residual response". Both results are shown in Figure 4-5. The frequencies are not easy to be extracted from the residual spectrum (FFT(V1)-FFT(V2)), while the first four frequencies of the bridge are obvious and easily recognized from the spectrum of the residual response (FFT(V1-V2)). Hence, the spectrum of the residual response proposed in present study is much more effective.

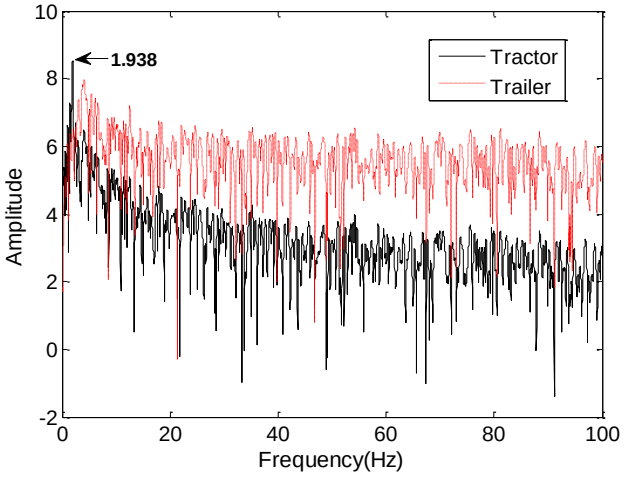

Figure 4-4. FFT of accelerations

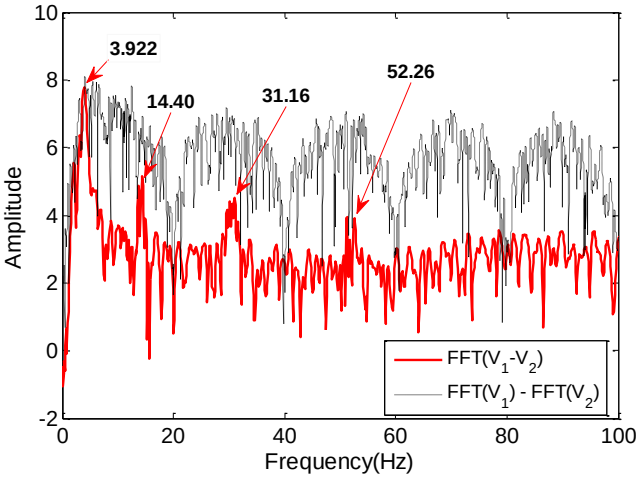

Figure 4-5. FFT of acceleration residuals

The bridge frequencies extracted from the residual vehicle response are 3.92, 14.40, 31.16 and 52.26 Hz versus the true values of 3.579, 14.012, 30.50, and 50.84Hz. The error is due to the shifting effect (Yang et al. 2004) due to vehicle movement. It can be observed in Figure 4-5 that two close peaks appear around each bridge frequency such as 51.27 and 52.49 Hz around the fourth frequency.

Since the vehicle response contains the effects of vehicle, bridge and many other environmental factors, the wavelet analysis was conducted to separate those effects and to obtain more reliable results. In wavelet analysis a signal is broken into scaled and shifted versions of the original (or mother) wavelet (Zemmour 2006). As one of them, the analysis using the discrete wavelet transform (DWT), by choosing scales and positions based on powers of two, is very efficient and just as accurate as the continuous transform. The mother wavelet used for the present study is the Debauchies (db4) that has the orthonormal characteristic. Figure 4-6(a) shows the DWT results of approximations and details at 6 levels in the time domain. The approximation represents the low-frequency components and the detail is for the high-frequency ones. Figure 4-6(b) is the FFT results of all the approximations and details in each level. As can be seen, the first three levels separate very high frequency components. Level 4~6 only include the first three frequencies of the bridge, and level 6 even separate the fundamental and the second frequency of the bridge. Wavelet analysis gives high resolution to extract the low frequency.

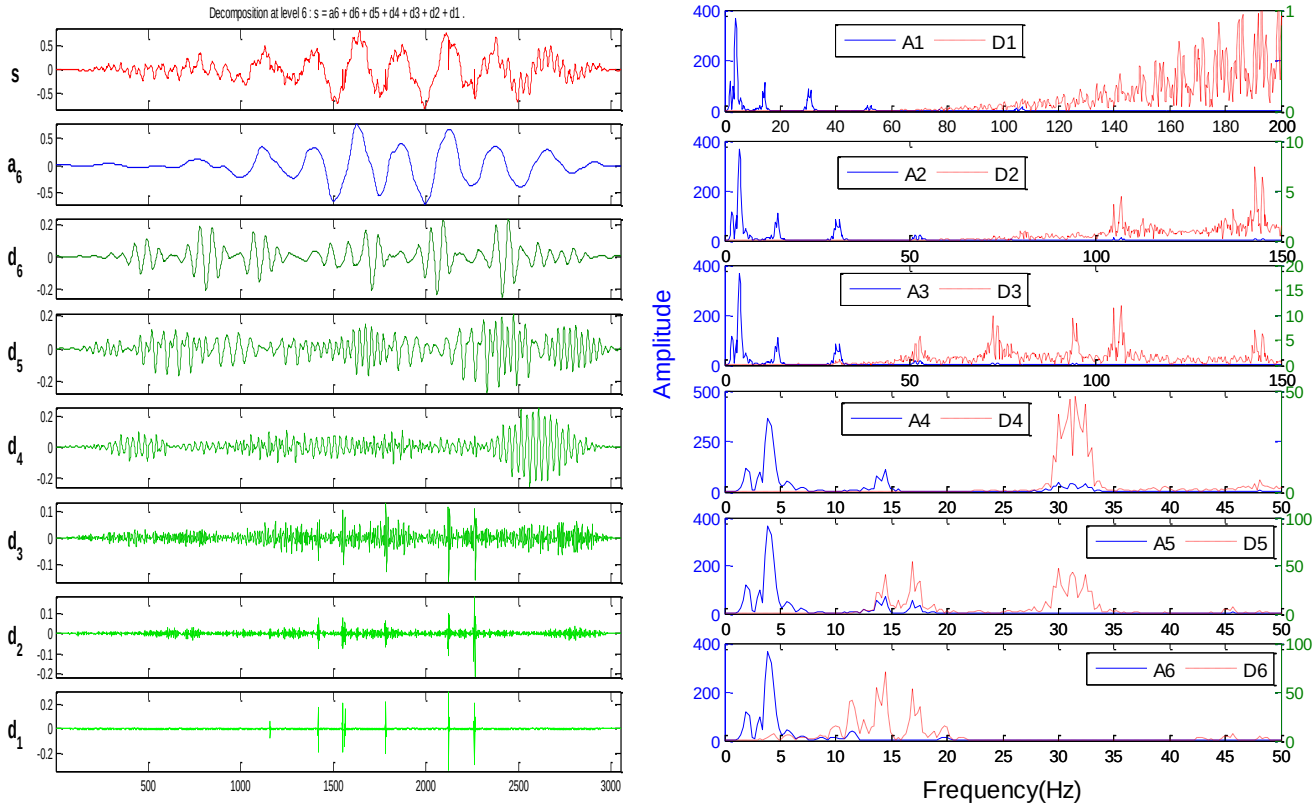

(a) Wavelet decomposition (b) FFT of wavelet components

Figure 4-6. Wavelet analysis results

Mode shape extracted by Short-time Fourier Transform (STFT)

The vehicle response is time dependent and non-stationary, which means that the frequency changes with time. In the STFT approach the Fourier transform with a fixed-sized and moving window is applied to the input time series. The most common ones are the Hann and Hamming windows as shown in Figure 4-7 and the coefficients of a hamming window with a length of L=N+1 are computed as (Rabiner and Schafer 1978; Oppenheim and Schafer 1989),

$$w(n,\tau) = 0.54 - 0.46\cos\left(2\pi\frac{n}{N}\right), \quad 0 \le n \le N \tag{4-17}$$

The spectrogram of the vehicle response is shown in Figure 4-8. Since the frequency resolution is proportional to the bandwidth, it will decrease at higher frequencies and increase at lower frequencies. Accordingly, in order to have the same resolution, higher frequencies require higher time resolutions, i.e. a small bandwidth is required for high frequencies. This is not the case for the STFT, where the frequency resolution is the same over all frequencies.

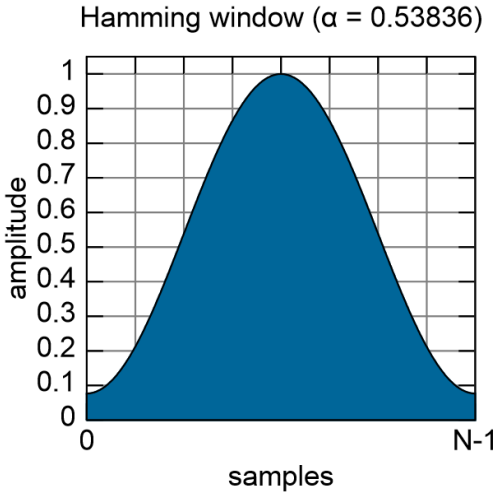

Figure 4-7. Hamming window

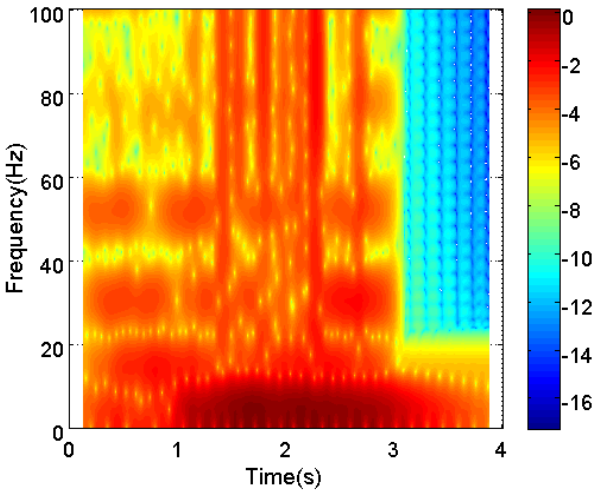

Figure 4-8. STFT of residual response

In the time-frequency representation of the vehicle response, the time scale is equivalent to the space scale by multiplying the vehicle speed. Therefore, the spectrogram represents the dynamic response at every point along the bridge at a certain frequency range. If the amplitudes of all the time point along the bridge at a specific bridge frequency are extracted, we can obtain the modal shape of the bridge. Since the spectrogram is of square amplitude, the modal shape we obtained here is actually the modal shape squares. Figure 4-9 shows the first three mode shape squares extracted by STFT. Figure 4-9(a) is the second mode shape squares extracted from the residual acceleration response of two trailers, which is close to the true value and much better than that extracted from the original response of a trailer. The first and third mode shape squares in Figure 4-9(b) has some error to the true value.

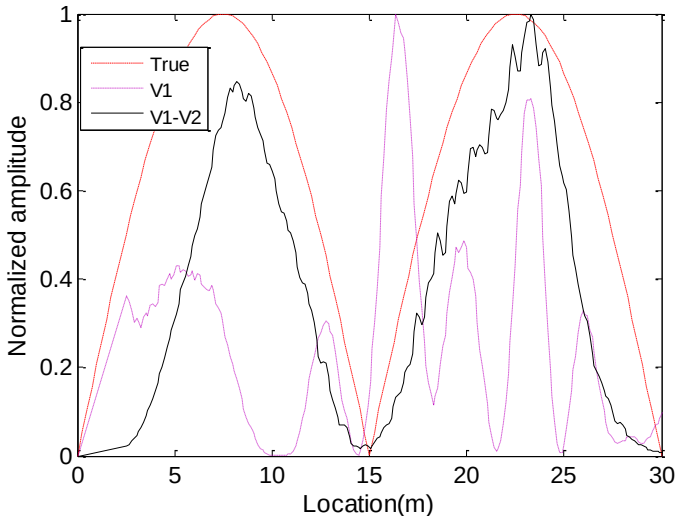

(a) the 2nd mode

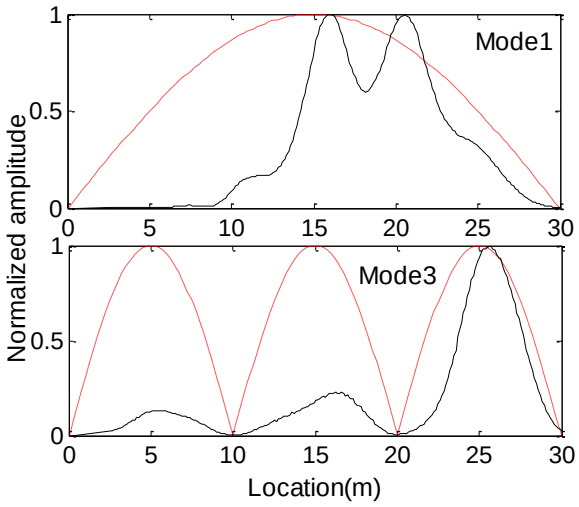

(b) the 1st and 3rd mode

Figure 4-9. Mode shape squares

As mentioned above, the STFT results depend on the window parameters, such as the window width, window overlap and window types. Figure 4-10 and Figure 4-11 show the effect of window width and overlap, respectively. The effect of window width is significant. As the window width becomes smaller, the result becomes worse. As shown in Figure 4-10, when the window width is 128, the result does not make sense. When the window is too small, the information for transforming is not sufficient. However, the window overlap that is equivalent to the divided segment of the time length only affects the smoothness of the shape. It is suggested that the window width should be large enough to have sufficient information and the window overlap should be a reasonable value to assure the result to be acceptable.

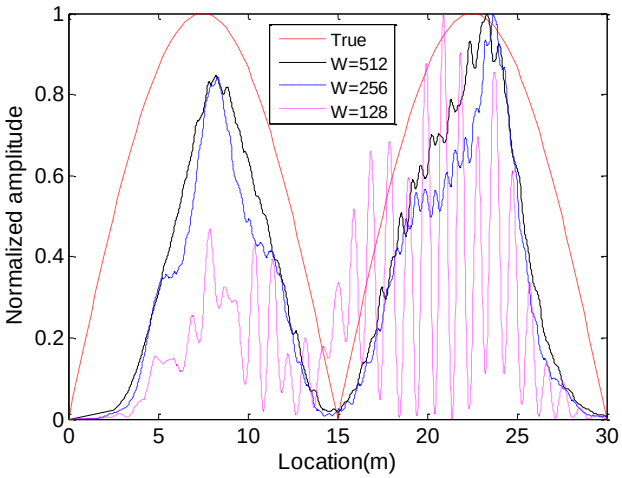

Figure 4-10. Effect of window width

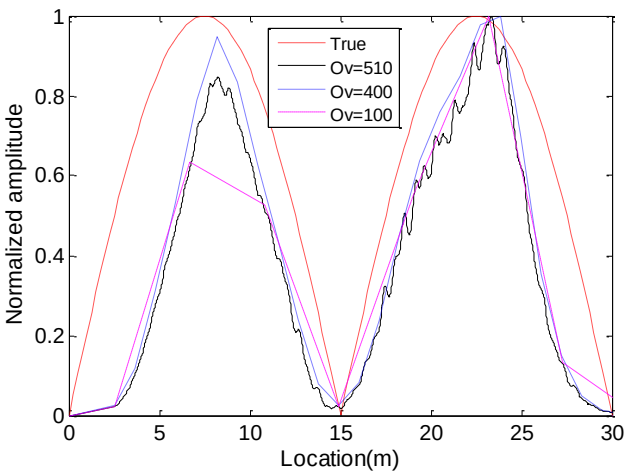

Figure 4-11. Effect of window overlap

4.3.2 With traffic flows

All the cases discussed above are under the condition that the bridge is excited by the test vehicle only. In order to consider more general applications, the situation with ongoing traffic vehicles was investigated next. Besides the test vehicle, other ten vehicles with different vehicle types, initial locations and traveling speeds were applied on the bridge. The FFT and STFT of the residual response were computed and the mode shape squares were extracted with the same procedure as that discussed earlier. The FFT result shown in Figure 4-12 reveals again that the present study obtains better results than the residual spectrum in Yang et al. (2012). The first three mode shape squares are shown in Figure 4-13. The results of the first and third modes are much better than that of the case without traffic flow in Figure 4-9. In Figure 4-9, the amplitude before 10m of the first mode is almost zero because the bridge is not sufficiently excited when the test vehicle travels in that range. Nevertheless, with ongoing traffic the bridge is sufficiently excited by other vehicles during the entire time when the test vehicle passes the bridge. In this sense, the ongoing traffic benefits this testing method.

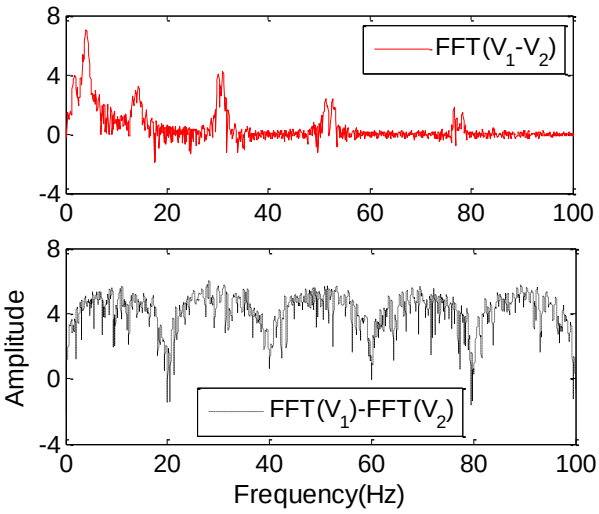

Figure 4-12. Residual--distance=0.5m

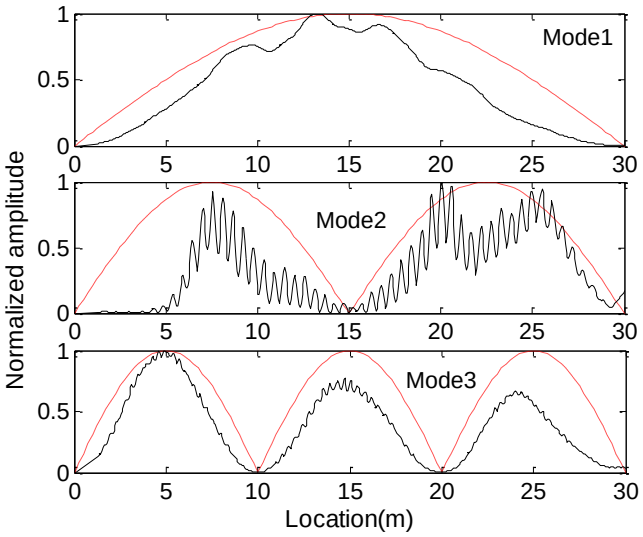

Figure 4-13. Mode shape squares with traffic flows

4.4 Vehicle design

The residual response of the two trailers is affected not only by the environmental factors but also parameters such as vehicle mass and stiffness, vehicle traveling speed, the space between the two trailers, etc. To apply this method in reality, the test vehicle should be designed with many considerations. In this section, a few parameters were studied numerically to have a preliminary design for the test vehicle.

4.4.1 Trailer parameters

The effect of vehicle mass and stiffness were studied first. Since the vehicle is a SDOF model, only two parameters, spring stiffness K and wheel mass M, were considered. When the mass is fixed as 120kg, the stiffness varies from 6.0e2 to 6.0e6 N/m, as shown in Table 4-1 for case 1~5. When the stiffness is 6.0e4 N/m, the mass varies from 12 to 12000kg.

In order to evaluate the results of different cases, the visibility index was introduced to evaluate the visibility of bridge frequencies from the frequency spectrum, which is defined as,

$$VI(\omega_i) = \frac{V(\omega_i) - \frac{1}{n}\sum_{\omega=\omega 1}^{\omega 2} V(\omega)}{\left|\frac{1}{n}\sum_{\omega=\omega 1}^{\omega 2} V(\omega)\right|} \tag{4-18}$$

where $VI(\omega_i)$ denotes the visibility index of bridge frequency ω_i; $V(\omega_i)$ is the logarithmic amplitude at the i-th bridge frequency ω_i in the spectrum and $V(\omega)$ is the logarithmic amplitude at frequency ω in the range; $\omega 1$ and $\omega 2$ are the lower and upper limits of frequency range used for summation, respectively. Herein, $\omega 1 = 0.8\omega$ and $\omega 2 = 1.2\omega$ are adopted and n is the frequency numbers.

The FFT of the residual response of two cases: case 5 with high visibility and case 8 with low visibility are presented in Figure 4-14, in which the vertical ordinate is the logarithmic amplitude. The visibility index reflects the ratio of the amplitude at the bridge frequency to the average amplitude around it. The larger the index is, the easier to distinguish the bridge frequency from the spectrum. The negative value stands for the case that the amplitude at the bridge frequency is smaller than that around.

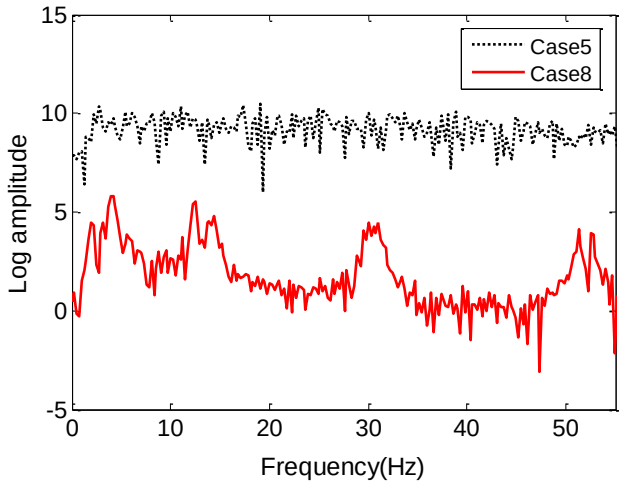

Figure 4-14. FFT spectrum of case 5&8

For various stiffness values as shown in Figure 4-15, the visibility index decreases as the stiffness increases. The contact between the vehicle and bridge is a major factor to assure the bridge vibrations being transferred to the vehicle and to ensure the vehicle responses to contain sufficient information about the bridge vibration, which benefits the extraction of bridge properties from the vehicle responses. As for the case with a fixed mass, the increase of the tire stiffness could weaken the contact between the tire and the bridge surface. It even makes the wheel lose the contact, which results in many zeros in the vehicle responses for small vehicle mass. Therefore, small tire stiffness is recommended for the trailer. With respect to the various mass values as shown in Figure 4-16, the visibility index increases with the increasing of mass. The reason is similar because the increase of mass makes the contact closer. A tradeoff should make between mass and stiffness as discussed below. The results are summarized in Table 4-1. The suggested stiffness for m=120kg is k=6.0e2~6.0e4 N/m, and the suggested mass for k=6.0e4N/m is m=120~1200kg.

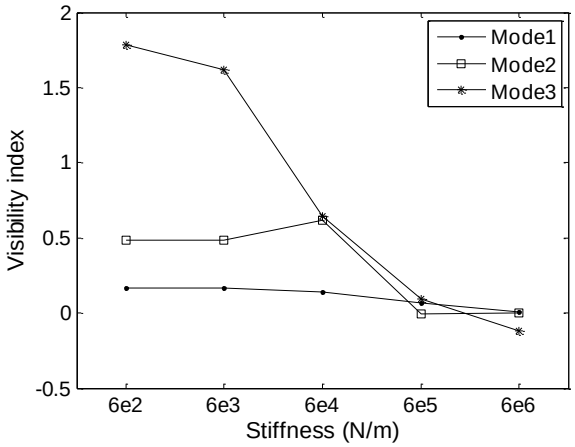

Figure 4-15. VI vs. stiffness change

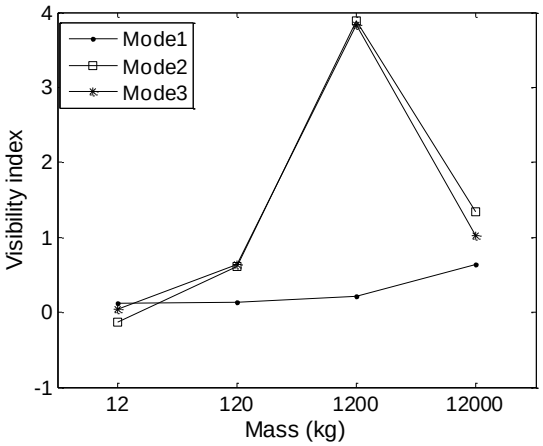

Figure 4-16. VI vs. mass change

Table 4-1. Visibility index of cases with different K and M

	Stiffness change						Mass change			
	Case1	Case2	Case3	Case4	Case5		Case6	Case7	Case3	Case8
M (kg)	120	120	120	120	120		12000	1200	120	12
K (N/m)	6.E+06	6.E+05	6.E+04	6.E+03	6.E+02		6.E+04	6.E+04	6.E+04	6.E+04
f (Hz)	35.588	11.254	3.559	1.125	0.356		0.356	1.125	3.559	11.254
VI(ω1)	0.01	0.07	0.14	0.16	0.17		0.64	0.22	0.14	0.12
VI(ω2)	0.00	-0.01	0.62	0.49	0.49		1.35	3.89	0.62	-0.13
VI(ω3)	-0.12	0.09	0.64	1.62	1.78		1.03	3.84	0.64	0.05
sum	-0.10	0.16	1.40	2.27	2.44		3.01	7.95	1.40	0.03

The relationship between the mass and stiffness can be represented by the frequency, which implies that the effect of mass and stiffness could be combined as one parameter, the vehicle frequency. Their effects were investigated using four cases with different mass and stiffness but the same vehicle frequency. As shown Table 4-2, for the same vehicle frequency, different combinations of mass and stiffness makes the results different. It may have a peak at the same frequency, similar to resonant peak, though the magnitude is different, as shown in Figure 4-17. The difference is expected because the mass is different though with the same frequency. Therefore, the effect of mass and stiffness cannot be represented by a single frequency. In addition, if the frequency of the test vehicle is close to a specific bridge frequency, the spectrum magnitude of that frequency would be large due to the resonant effect. On the other hand, it makes other bridge frequencies less visible. Thus, the frequency of the test vehicle is recommended not to be close to the bridge frequency.

Table 4-2. Visibility index of cases with same frequency

	Case9	Case10	Case3	Case11
M (kg)	12000	1200	120	12
K (N/m)	6.E+06	6.E+05	6.E+04	6.E+03
f (Hz)	3.559	3.559	3.559	3.559
VI(ω1)	-0.05	0.10	0.14	0.13
VI(ω2)	0.05	0.60	0.62	0.04
VI(ω3)	0.15	1.26	0.64	0.05
sum	0.16	1.97	1.40	0.22

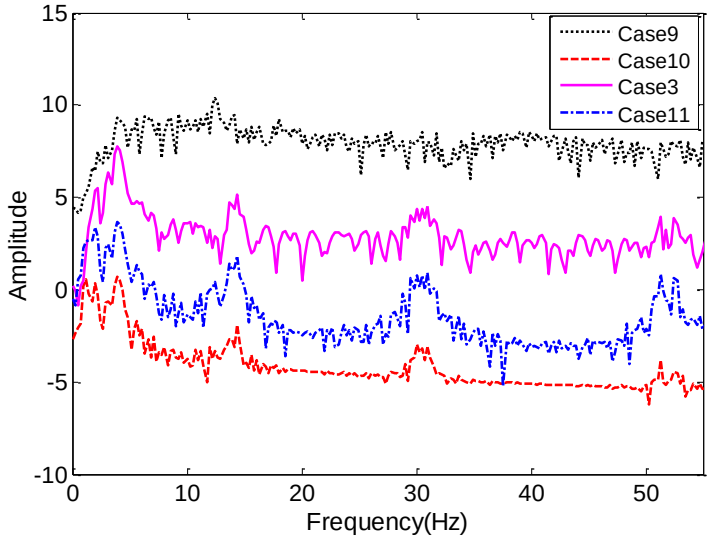

Figure 4-17. FFT spectrum with same vehicle frequency

4.4.2 Trailer spacing

Besides the physical properties of the trailer itself, the spacing between the two trailers is another important aspect for the testing system. Four types of spacing were considered here, 0.5m, 1.0m, 2.5m and 5.0m. The frequency spectrum of the residual acceleration with different spacing is shown in Figure 4-18. In the case of 0.5m, 1.0m and 2.5m, all the first three frequencies are clearly recognized except for the third frequency for the1.0m. When the spacing is 5.0m, only the first frequency can be identified, which indicates large spacing will not lead to a good result. When the spacing of the two trailers is too large, their responses are not highly correlated, which makes the residual response meaningless. This observation is further confirmed in Table 4-3 that compares the visibility index between the response of trailer 1 (T1) and residual response of two trailers (T12). For the first frequency, T12 is smaller than T1 when the spacing is 2.5m and 5.0m and the same is observed for the second frequency when the spacing is 5.0m. Therefore, it is recommended that the spacing of the two test trailers should be less than 5.0m.

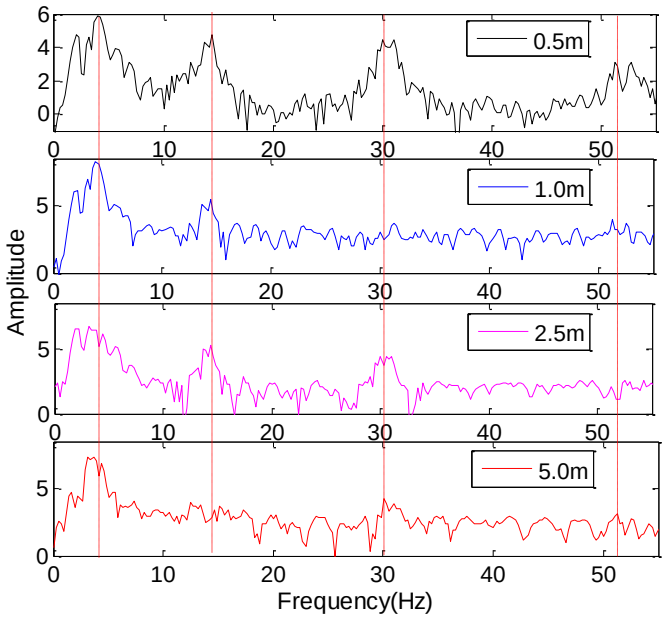

Figure 4-18. FFT spectrum with different spacing

Table 4-3. Visibility index of different spacings

Spacing (m)	ωb1			ωb2			ωb3		
	T1	T12	Ratio	T1	T12	Ratio	T1	T12	Ratio
0.5	0.08	0.82	9.78	0.50	4.10	8.17	0.34	5.51	15.99
1.0	0.32	1.03	3.23	0.52	3.66	6.98	0.27	1.16	4.30
2.5	0.32	0.14	0.42	0.51	4.56	8.98	0.27	4.35	16.37
5.0	0.32	0.065	0.20	0.51	-0.30	-0.59	0.27	2.21	8.14

4.4.3 Vehicle speed

The traveling speed of the test vehicle is also important. Five vehicle speeds of 1.0, 2.0, 5.0, 10 and 15m/s were studied to investigate the speed effect of the test vehicle as shown in Table 4-4. As for the first frequency, 5m/s have better results than the other speeds, while for the second and third frequencies, the speed of 2 m/s has the largest visibility index ratio. In the case of only the test vehicle on the bridge, a low speed cannot sufficiently excite the bridge vibration while high speed would make the recording data too short to process. Therefore, a vehicle speed of 5~10m/s is suggested.

Table 4-4. Visibility index of different speeds

Speed (m/s)	ωb1			ωb2			ωb3		
	T1	T12	Ratio	T1	T12	Ratio	T1	T12	Ratio
1.0	1.80	3.62	2.01	2.93	5.33	1.82	3.42	78.67	22.99
2.0	1.17	2.78	2.38	1.19	21.40	17.91	0.05	21.47	475.42
5.0	0.14	1.38	9.98	0.47	3.01	6.37	0.23	1.27	5.50
10	-0.004	0.27	-69.75	-0.11	1.12	-10.39	0.68	2.52	3.70
15	-0.21	0.486	-2.29	-0.14	0.87	-6.19	0.56	0.05	0.09

4.5 Case study on a field bridge

The proposed method was applied on a field bridge. A static and dynamic test was done on the bridge in 2006, but only measurements of the bridge were recorded by attaching strain and acceleration sensors on the deck (Shi 2006 and Deng 2009). Measurements of vehicle response are not available since it was not among the objectives of the test. Therefore, for the sake of application in the present study, the numerical model of the bridge was updated using the measured data and then used to obtain numerically the vehicle response.

4.5.1 Vehicle and bridge models

Bridge model

The tested bridge is a two-way bridge with three straight simple spans across over Cypress Bayou in District 61, on LA 408 East, Louisiana, as shown in Figure 4-19. The bridge structure with a length of 16.764 m (55 ft) for each span consists of seven AASHTO Type II prestressed concrete girders spaced 2.13m (7 ft) from center to center. All girders are supported by rubber bearings at both ends. The third span of the bridge was instrumented. Seven measurement stations, one for each girder and with a distance of 0.305m (1 ft) from the mid-span of the corresponding girder to avoid stress concentration near the diaphragm, were installed with strain gauges and accelerometers.

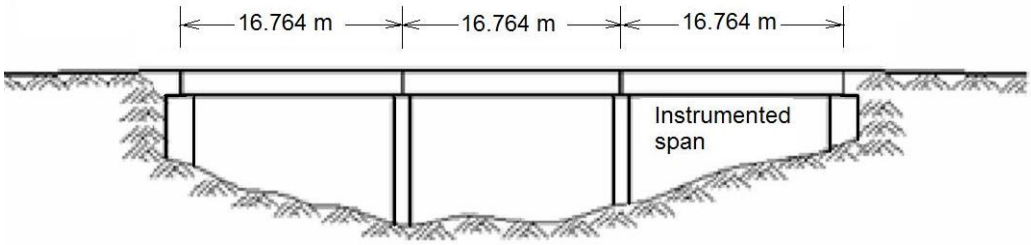

Figure 4-19. Profile of the test bridge

Based on the bridge configuration, a FE bridge model was created using the ANSYS program as shown in Figure 4-20, more details refer to Deng (2009). The bridge model was updated by Deng and Cai (2008) based on the measured first three natural frequencies and strains on the seven girders. The first three frequencies of the bridge from the measured result are 8.19, 11.11 and 15.79Hz, respectively, and the frequencies of the updated bridge model are 8.19, 10.79 and 16.23 Hz, respectively.

Road roughness profile

The road roughness of the bridge deck was measured by a laser profiler, which obtains the longitudinal road surface profile along each wheel track. In this study, a two-dimensional road surface profile is used without considering the change of road elevation along the lateral direction. In order to excite the dynamic effect of the vehicle, two wooden bumps (named Bump1 and Bump2) with equal widths of 0.18m and heights of 0.025m (1 inch) and 0.038m (1.5 inches) were used for Bump1 and Bump2, respectively. The two wooden bumps, one at a time,

were placed at the entry end of the third span. Figure 4-21 shows the measured road surface profile of Lane-1 with the wooden Bump1 along the track of the right wheel of the test truck.

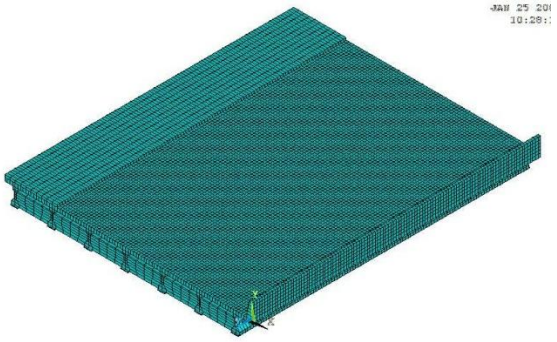

Figure 4-20. Numerical model of bridge

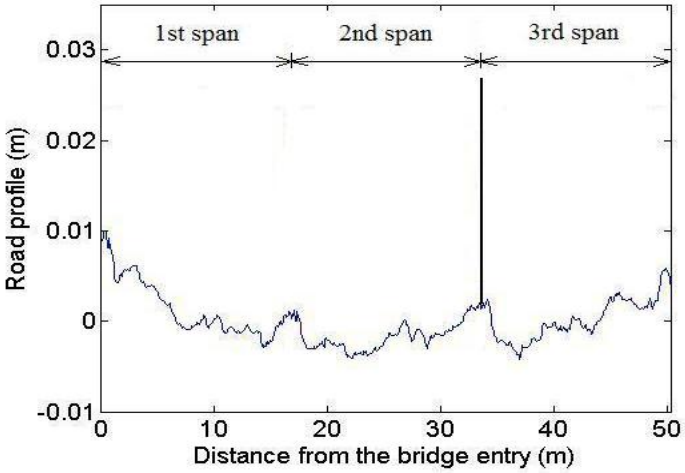

Figure 4-21. Roughness along Lane-1 with Bump1

Test truck

The truck used in the bridge test is a dump truck with a single front axle and a two-axle group for the rear (Figure 4-22). The static weights for the first, second, and third axle of this truck are 80.0 kN, 95.6 kN, and 95.6 kN, respectively. The distance between the front axle and the center of the two rear axles is 6.25 m, and the distance between the two rear axles is 1.2 m. This 3-axle truck was simulated as a 2-axle model by compressing the rear two axles into one axle as shown in Figure 4-23 (Shi 2006).

Figure 4-22. Dump truck used in bridge testing

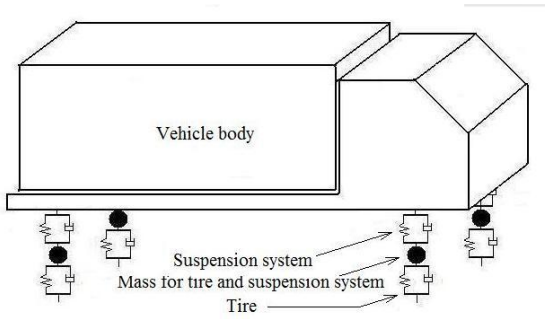

Figure 4-23. Model 1 for the test vehicle

As for the present study, the test vehicle should be a tractor-trailer vehicle. To this end, two vehicle models were proposed. Vehicle model I is to modify the above 2-axle truck model by adding two SDOF vehicle models behind the truck model. The 2-axle truck model is to simulate the tractor and each SDOF model is for the following trailer. Meanwhile, vehicle model II is to modify the five-axle model (Cai and Chen 2004) in Figure 4-24, in which the fourth and fifth axles are simulated as the two trailer models and parameters of the rear body are set to be very small values to eliminate its effect. Each axle has two wheels, which means each trailer

model is a 2-DOFs model and has two vertical responses. The main parameters of the test truck are measured and listed in Table 4-5. The tractor of both vehicle models is adjusted to have the same parameters as the test truck.

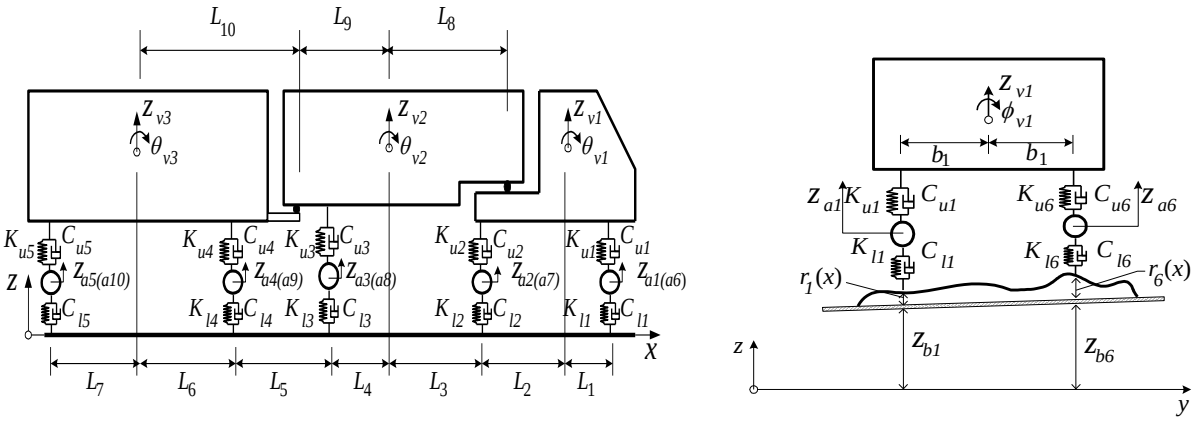

Figure 4-24. five axle model for the test vehicle

Table 4-5. Main parameters of the test vehicle

Parameter	Value	Unit
Mass of vehicle body M	24,808	Kg
Moments of inertia of the vehicle body I_{zy}	31,496	kg.m2
Moments of inertia of the vehicle body $I_{xz} = I_{xy}$	172,160	kg. m2
Mass combination of tire and suspension system m	725.4	Kg
Stiffness of the suspension systems front axle: K_{sf}	727,812	N/m
Stiffness of the suspension systems rear axle: K_{sr}	1,969,034	N/m
Damping of the suspension systems front axle: C_{sf}	2,189. 6	Ns/m
Damping of the suspension systems rear axle: C_{sr}	7,181.8	Ns/m
Stiffness of the tires front axle: K_{tf}	1,972,900	N/m
Stiffness of the tires rear axle: K_{tr}	4,735,000	N/m
Damping of the tires front axle: C_{tf}	0	Ns/m
Damping of the tires rear axle: C_{tr}	0	Ns/m
Distance between the two axles and the gravity center of vehicle body front axle: L_f	4.56	M
Distance between the two axles and the gravity center of vehicle body rear axle: L_r	1.69	M
Distance between the two tires of the same axle L_{ax}	2.2	M

4.5.2 Result of vehicle model I

The dynamic response of the vehicle on the field bridge was obtained by analyzing the system consisting of the test vehicle, the updated bridge model and the measured road roughness. All the cases with and without bump in the roughness profile were computed and shown in Figure 4-25. The acceleration FFT of trailer 1 is also shown in the figure and only the trailer frequency can be observed. Nevertheless, all the first three frequencies can be recognized from the spectrum of the residual acceleration. The visibility of the frequencies in the case with bump 2 (0.038m) is better than the other two cases. The bump here is not to increase the roughness level but to help excite the bridge vibration, which consequently enhances the vehicle response. As shown in the figure, fro the case from no bump to bump 1 and bump 2, the amplitude at the bridge frequency (B1 to B3) becomes larger and the amplitude at the vehicle frequency (V1) becomes smaller. It implies that high response of the test vehicle benefits the visibility of the bridge frequency.

For the sake of increasing the response, the situation with ongoing traffic flows was calculated. Except the tractor-trailer vehicle, other seven vehicles with different initial positions and travel speeds are arranged on the two lanes, and the result is shown in Figure 4-26. The amplitude of the first bridge frequency is now larger than that of the vehicle frequency, and the visibility of bridge frequencies become much higher than that in Figure 4-25. It indicates again that the method of the present study works better in the presence of ongoing traffic flows.

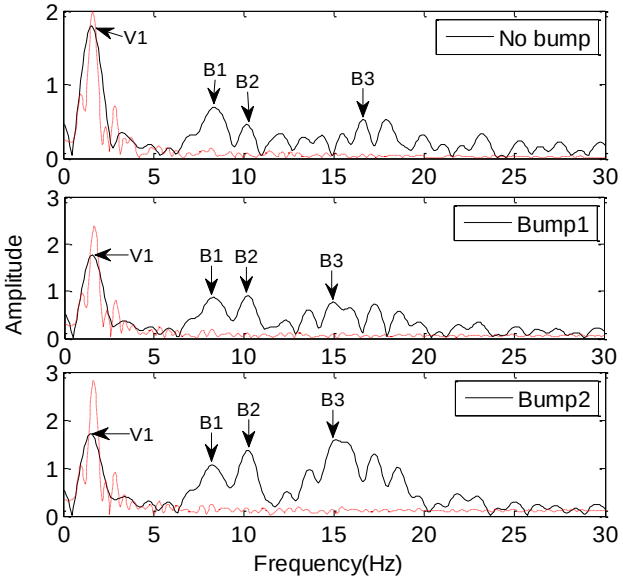

Figure 4-25. FFT of residual response of two trailers (— residual; ----- trailer 1)

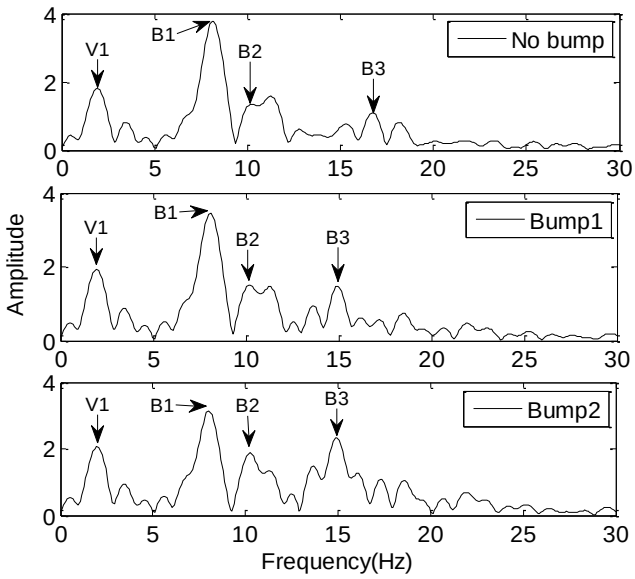

Figure 4-26. FFT of residual response of two trailers under ongoing traffic

The effects of traveling speed and trailer spacing were studied as well. Four different speeds were considered, namely 4.44m/s (10mph), 8.89m/s (20mph), 17.78m/s (40mph) and 26.67m/s (60mph), as shown in Figure 4-27. In the case of low speeds, the vehicle frequency

dominates in the spectrum. The high speed has higher visibility than the low speed, which is inconsistent with the observation made from Table 4-4.

As for the trailer spacing effect shown in Figure 4-28, the visibility decreases as the spacing increases and the case with spacing of 0.5m and 1.0 have more reliable results. When the spacing becomes 2.0m and larger, the bridge frequency becomes difficult to recognize. The observation is consistent with that discussed earlier. The spacing between the two trailers is suggested to be less than 2.0m.

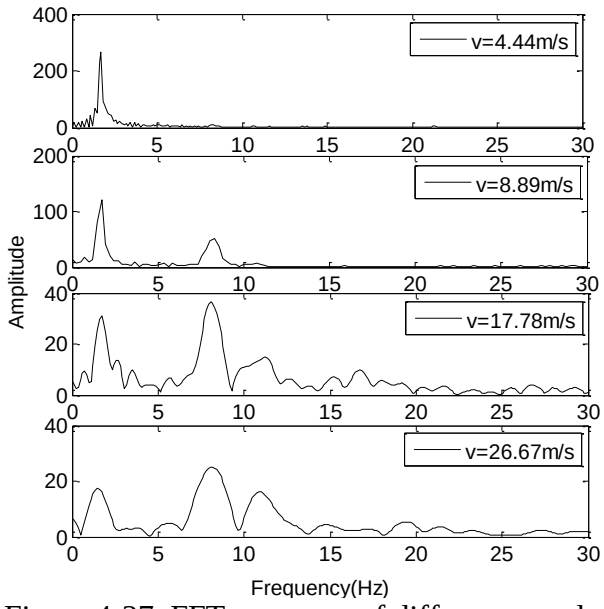

Figure 4-27. FFT spectrum of different speeds

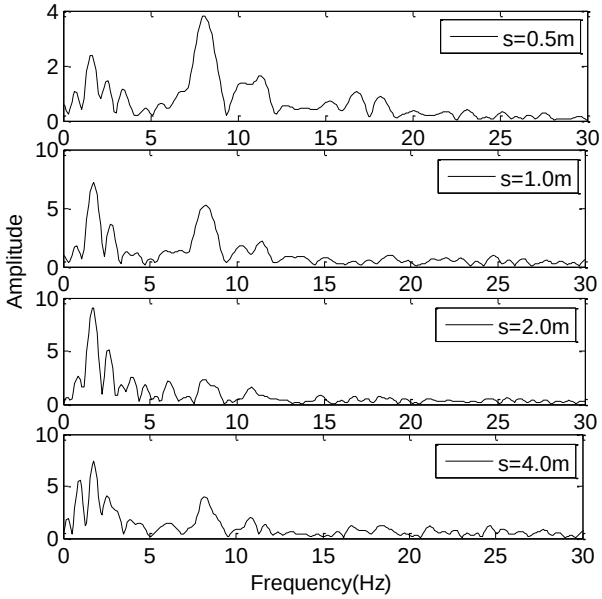

Figure 4-28. FFT spectrum of different spacing

As mentioned earlier, the spectrogram is able to present the frequency component at different time point as shown in Figure 4-30. The major frequency component is around 10Hz. It indicates that the vehicle acceleration contains mainly the first three frequencies of the bridge, and those messages are transferred to the vehicle in the first part of the time after the vehicle enters the bridge. The modal shape squares of the bridge are extracted from the time-frequency representation and compared with the ones calculated from the FE bridge model. The first three modal shapes of the bridge obtained from the FE analysis are shown in Figure 4-29. The first mode is the vertical moving of the middle part as can be seen in the x-y plane; the second mode is the mainly bending in the y-z plane, and the third mode is bending in x-y plane. As the vehicle only moves in a specific lane, the mode shape of nodes only on the vehicle track were extracted from the entire bridge mode shape for comparison with the STFT results.

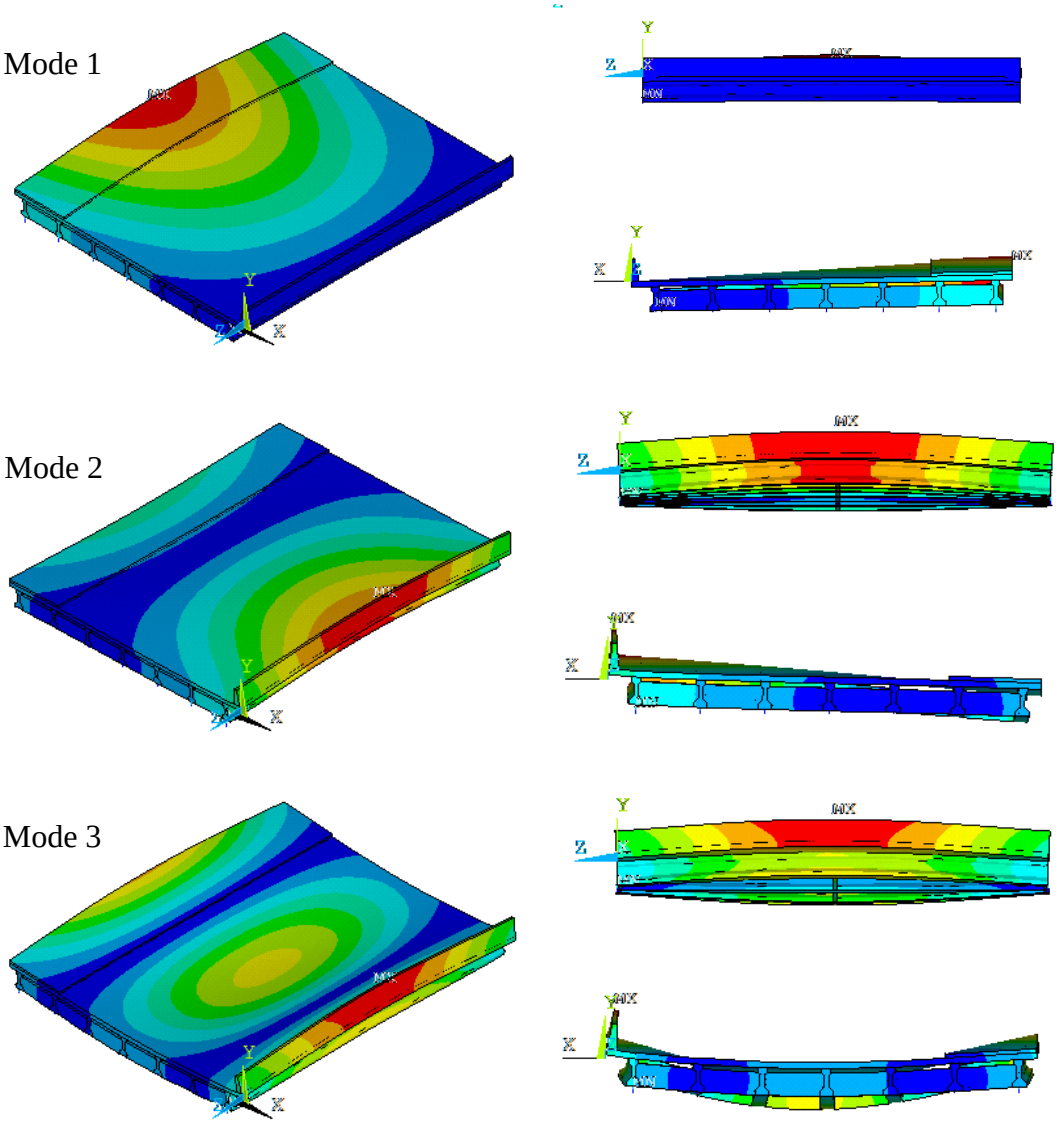

Figure 4-29. Bridge modes from FE analysis

The mode shape squares of the present stud and the FE analysi are shown in Figure 4-31 and have large difference. The possible reason could be that the modal shape is formed only from nodes along the track of the vehicle, not the entire bridge nodes.

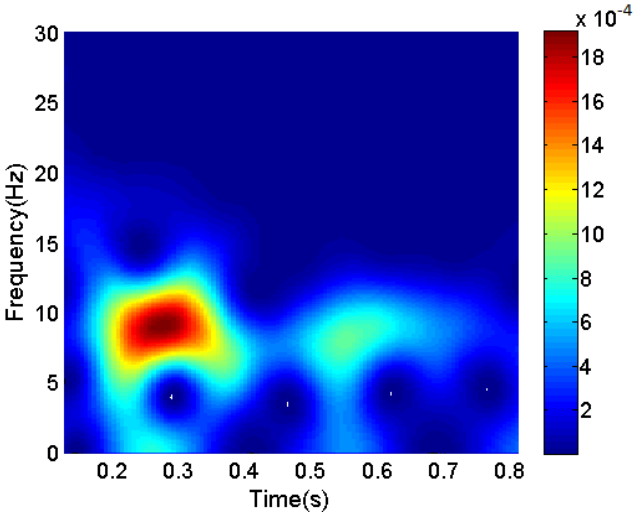

Figure 4-30. STFT of residual response

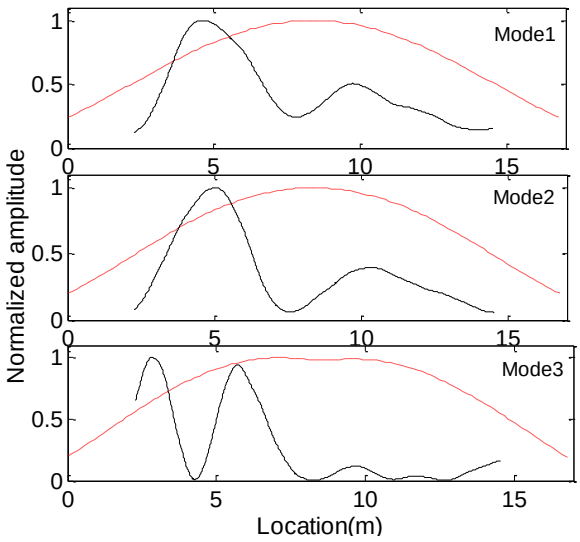

Figure 4-31. Mode shape squares
(— Present method result; ----- True value)

4.5.3 Result of vehicle model II

In vehicle model II, each trailer has two responses from two wheels with the same position in the longitudinal direction of the bridge. In total, four accelerations can be obtained from the two trailers: A_{1L} and A_{1R} from the front trailer, A_{2L} and A_{2R} from the back trailer (L denotes the left wheel and R denotes the right wheel). The following residual responses are considered: residual response of the same trailer A_{1L}-A_{1R} and the residual response of the two trailers A_{1L}-A_{2L}. The FFT of the residual response is normalized and shown in Figure 4-32. In the case of no bump, the peak around the second bridge frequency is obvious, while the first and third frequencies cannot be identified. The result of A_{1L}-A_{2L} in this case is slightly better than that of A_{1L}-A_{1R} and the reverse is true for the other two cases. In the case with bump 1 and bump 2, the visibility of the first and third bridge frequency is better. Generally speaking, the result of the same trailer A_{1L}-A_{1R} is better than that using the two trailers A_{1L}-A_{2L}. The possible reason could be the existing vehicle body between the two trailers makes them not exactly independent. The response of the two trailers is affected by the vehicle body.

Similar to the vehicle model I, the spectrogram was obtained from the residual response, $A_{1L} - A_{2L,}$ under ongoing traffic flows and shown in Figure 4-33. The figure demonstrates more clearly that the frequency component concentrates around 5Hz to 15Hz. Furthermore, the modal shape squares of the bridge extracted from the time-frequency representation as shown in Figure 4-34 match with the true value better than that of Model I.

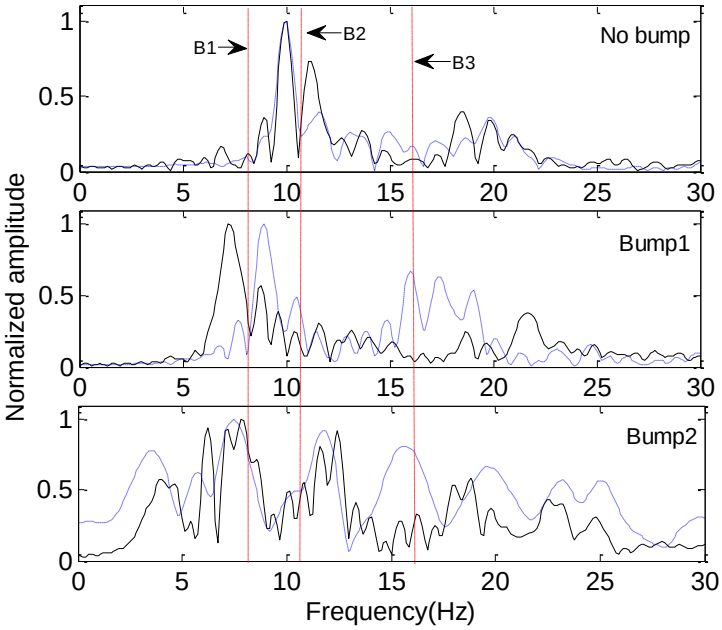

Figure 4-32. FFT of residual response (—A_{1L}-A_{2L}; ----- A_{1L}-A_{1R})

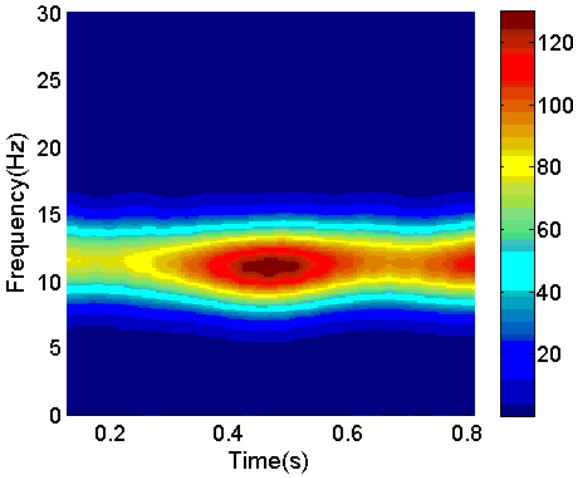

Figure 4-33. STFT of residual response

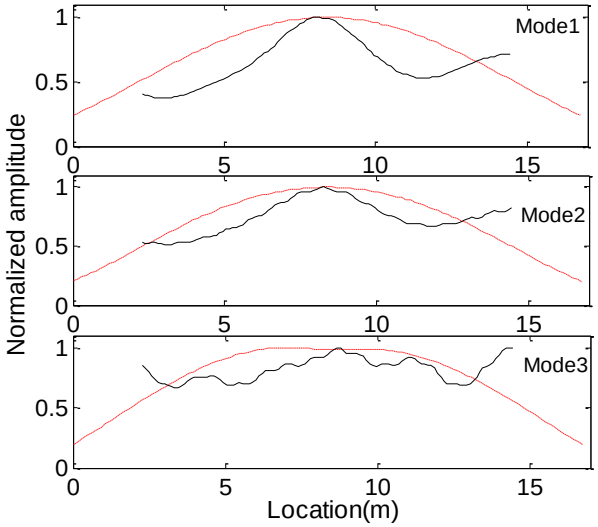

Figure 4-34. Mode shape squares
(— Present method result; ----- True value)

4.6 Conclusions

Since the vehicle response carries the vibration information of the bridge, a testing vehicle consisting of a tractor and two following trailers is proposed in the present study to extract bridge modal properties from the vehicle response. Based on the analysis on a numerical beam example and a field test bridge, conclusions can be obtained as the following:

(1) The proposed method that extracts bridge modal properties from the residual response of two trailers is more effective than that from the individual trailer or from the residual spectrum of the two trailers reported in the literature. Especially, in the case with ongoing traffic when the bridge is sufficiently excited by other vehicles, the proposed method work even better.

(2) The effect of the trailer mass and stiffness, the spacing between the two trailers and the traveling speed were investigated. Results indicate that a sufficient trailer weight is required to assure its contact with the bridge deck and obtain better results. Similarly, it is recommended that the spacing of the two test trailers should not be too large, at least less than 5.0m and a suggested speed ranges are 5~10m/s.

(3) As for the application on the field bridge, two types of test vehicle models were proposed. The result of vehicle model I using an independent SDOF vehicle to simulate the trailer has high visibility in extracting the bridge frequencies.

(4) The vehicle model II with the two trailers simulated by the rear two axles of a modified 5-axle vehicle model. Both the residual response of two wheels of the same trailer and that of wheels of the two trailers were considered but they do not produce good results.

The vehicle model II is more practical in reality. However, due to the effect of the vehicle body connected the two trailers, the result is not good. The future work of the present study is to create a better vehicle model to simulate the two trailers. Meanwhile, the noise effect is not considered here and needs to be investigated in future.

4.7 References

Bu, J. Q., Law, S. S., and Zhu, X. Q. (2006). "Innovative bridge condition assessment from dynamic response of a passing vehicle." J. of Engineering Mechanics 12: 1372-1379.

Cai, C. S., Chen, S. R. (2004). "Framework of vehicle-bridge-wind dynamic analysis." J. of Wind Engineering and Industrial Aerodynamics, 92, 579-607.

Carden, E.P. and Fanning, P. (2004). "Vibration Based Condition Monitoring: A Review." Structural Health Monitoring, 3(4), 355-377.

Deng, L. (2009). "System identification of bridge and vehicle based on their coupled vibration." Ph.D. Dissertation, Louisiana State University, Baton Rouge, LA.

Doebling, S.W., Farrar, C.R., and Prime, M.B. (1998). "A summary review of vibration-based damage identification methods." The Shock and Vibration Digest, 30(2), 91-105.

Kim, C. K., Toshinami, T., McGetrick, P. J. (2011). “Experimental investigation of drive-by bridge inspection.” 5th International Conference on Structural Health Monitoring of Intelligent Infrastructure (SHMII-5), Dec. 11-15, 2011, Cancun, Mexico.

International Standard Organization. (1995). "Mechanical vibration - Road surface profiles-Reporting of measured data." Geneva.

Lin, C.W., Yang, Y. B. (2005). “Use of a Passing Vehicle to Scan the Fundamental Bridge Frequencies: an Experimental Verification.” Engineering Structures, 27, 1865-1878.

Luna Majumder, C.S.Manohar. (2002). “A time-domain approach for damage detection in beam structures using vibration data with a moving oscillator as an excitation source.” J. of Sound and Vibration, 268, 699-716.

Oppenheim, A.V., and Schafer, R.W. (1989). “Discrete-time signal processing.” Prentice-Hall, 1989, pp. 447-448.

Rabiner, L. R., and Schafer, R. W. (1978). “Digital processing of speech signals.” Prentice-Hall, Englewood Cliffs, NJ, 1978.

Shi, X. M. (2006). “Structural performance of approach slab and its effect on vehicle induced bridge dynamic response.” Ph.D. Dissertation, Louisiana State University, Baton Rouge, LA.

Sohn, H., Farrar, C., Hunter, N. and Worden, K. (2003). “A Review of Structural Health Monitoring Literature: 1996-2001.” Los Alamos National Laboratory report, LA-13976-MS.

Srinivas, V., Ramanjaneyulu, K. and Jeyasehar, C.Antony. (2011). “Multi-stage approach for structural damage identification using modal strain energy and evolutionary optimization techniques.” Structural Health Monitoring, 10 (2), 219-230

Wei, F. and Qiao, P.Z. (2011). “Vibration-based Damage Identification Methods: A Review and Comparative Study." Structural Health Monitoring, 10: 83-111.

Yan, Y.J., Cheng, L., Wu, Z.Y., Yam, L.H. (2007). “Development in vibration-based structural damage detection technique.” Mechanical Systems and Signal Processing, 21, 2198-2211.

Yang, Y.B., Lin, C.W., Yau, J.D. (2004). “Extracting Bridge Frequencies from the Dynamic Response of a Passing Vehicle.” J. of Sound and Vibration, 272, 471-493.

Yang, Y.B., Chang, K.C. (2009a). “Extraction of Bridge Frequencies from the Dynamic Response of a Passing Vehicle Enhanced by the EMD Technique.” J. of Sound and Vibration, 322, 718-739.

Yang, Y.B., Chang, K.C. (2009b). “Extraction the Bridge Frequencies Indirectly from a Passing Vehicle: Parametric Study.” Engineering Structures, 31, 2448-2459.

Yang, Y. B., Li, Y. C., Chang, K. C. (2012). “Using two connected vehicles to measure the frequencies of bridges with rough surface: a theoretical study.” Acta Mech, 223, 1851-1861.

Yang, Y. B., Chang, K. C., Li, Y. C. (2013). “Filtering techniques for extracting bridge frequencies from a test vehicle.” Engineering Structures, 48, 353-362.

Zemmour, A. (2006). “The Hilbert-Huang transform for damage detection in plate structures.” Master thesis, Department of Aero Engineering, University of Maryland, College Park.

Zhang, Y., Wang, L. Q., Xiang, Z. H. (2012). “Damage detection by mode shape squares extracted from a passing vehicle.” J. of Sound and Vibration, 331, 291-307.

Zhang, Y., Lie, S. T., Xiang, Z. H. (2013). “Damage detection method based on operating deflection shape curvature extracted from dynamic response of a passing vehicle.” Mechanical System and Signal Processing, 35, 238-254.

CHAPTER 5. SCOUR EFFECT ON A SINGLE PILE AND DEVELOPMENT OF CORRESPONDING SCOUR MONITORING METHODS

5.1 Introduction

Bridge scour is a significant issue in the United States. In the last 30 years, more than 1,000 bridges have collapsed and approximately 60% failures of them are related to the foundation scour (Shirhole and Holt 1991, Lagasse and Richardson 2001). On-going screening and evaluation of the vulnerability of the nation's highway bridges to scour by different state Departments of Transportation have identified more than 18,000 bridges that are considered as scour-critical and in need of repair or replacement. Furthermore, more than 100,000 bridges over water in the United States have "unknown foundations" (Lagasse et al. 1995), which means that their vulnerability to scour cannot be calculated by normal hydraulic and geotechnical analysis procedures. Therefore, there is an urgent need for innovative, effective, and economical techniques to detect and monitor the foundation scour.

Bridge scour is a very complicated process that involves the interaction between the flow, the erodible riverbed, and the bridge pier or abutment. Deng and Cai (2010) presented a comprehensive review on approaches for modeling and predicting bridge scour. In the past few decades, the previous research mainly focused on studying the scour mechanism by developing numerical models (Melville and Raudkivi 1977; Young et al. 1998; Kassem et al. 2003) as well as laboratory models (Umbrell et al. 1998; Sheppard and William 2006). Based on these studies, different methods to predict bridge scour using the available information prior to or during flood events were proposed including empirical equations (Laursen and Toch 1956; Breusers et al. 1977; Melville and Sutherland 1988; Lim 1997; Heza et al. 2007), and neural network method (Lee et al. 2007; Mohammad et al. 2009) to establish a relationship between the scour depth and various factors.

A more direct approach is to investigate the scour consequences, i.e., the structural response and feature changes of the bridge due to scour. However, till now only few studies have been carried out on this topic. Han et al. (2010) studied the influence of scour on the seismic performance of foundations through several elasto-plastic static pushover analyses. Lin et al. (2010) studied scour effects on the response of laterally loaded piles considering the stress history of the remaining sand. Foti and Sabia (2011) performed numerical simulations to assess the sensibility of the overall dynamic response of the system to the foundation scour.

The present study mainly focuses on the scour effect on a single pile or pier, from which scour monitoring strategies can be developed. By considering the scour depth as a variable, piecewise differential equations were derived first to establish the relationship between the scour depth and the pile responses under static loading and free vibrations. A program in MATLAB was developed to obtain the solution and two examples were used to demonstrate and parametrically study the structural response due to changes of different factors. Based on observations of these analyses, the present study proposed three possible methods for detecting

and monitoring bridge scour. Finally, a monitoring system using fiber optic sensors has been designed and tested in the laboratory.

5.2 Analytical study

5.2.1 Static solution

Beams and columns supported along their length are very common structure configurations, and the most routine method to treat the elastic foundation is the Winkler model (Ding 1992 and Coskun 2003). A pile embedded in soil is similar to a beam resting on a Winkler elastic foundation. Herein, assume the pile is fully buried in soil at the beginning. After the soil is eroded, the top part of the pile is exposed to the water flow as shown in Figure 5-1. The pile length is L with the origin at the top of the pile, and the unsupported depth is l that is also the loading length with a distributed load $q(x)$. The unsupported length l, due to initial scour and/or initial construction, is generically called initial scour depth hereafter. The rest of the pile is embedded in the soil with an elastic spring coefficient $k(x)$. The governing equation of the pile with a uniform cross-section and flexural rigidity and partially embedded in soil as shown in Equation (5-1) can be expressed as,

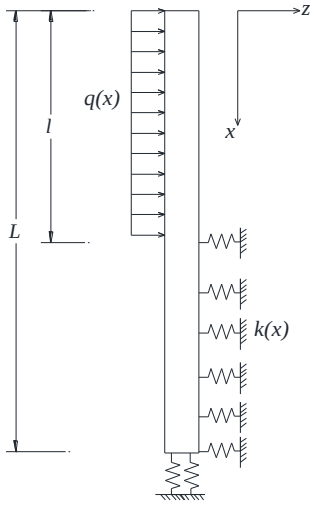

Figure 5-1. Schematic of pile under scour

$$\begin{cases} EI\frac{d^4w}{dx^4} = q & 0 \le x \le l \quad (a) \\ EI\frac{d^4w}{dx^4} + k(x)w = 0 & l \le x \le L \quad (b) \end{cases} \tag{5-1}$$

where $w(x)$ is the lateral displacement of the pile. Herein, $k(x)$ is considered as a constant. The general solution of Equation (5-1) consists of two parts, namely, the deflection of the pile is divided piecewise as,

$$\mathrm{w(x)} = \begin{cases} w_1(x) = C_1\frac{x^3}{6} + C_2\frac{x^2}{2} + C_3x + C_4 + \frac{qx^4}{24EI}, & 0 \le x \le l \\ w_2(x) = e^{\beta x}(A_1 sin\beta x + A_2 cos\beta x) + e^{-\beta x}(A_3 sin\beta x + A_4 cos\beta x), & l \le x \le L \end{cases} \tag{5-2}$$

where $\beta = (k/4EI)^{1/4}, C_i \; and \; A_i \; (i = 1, 2, 3, 4)$ are unknown constants. The boundary condition at $x = l$ requires the geometric continuity of displacement and slope, and the continuity of bending moment and shear force, which are expressed as

$$w_1(l) = w_2(l), \quad w_1'(l) = w_2'(l), \quad w_1''(l) = w_2''(l) \quad \text{and} \quad w_1'''(l) = w_2'''(l)$$

Four additional conditions can be derived from boundaries at $x = 0$ and $x = L$. For a free–fixed pile, we have:

$$w_1''(0) = 0, \quad w_1'''(0) = 0, \quad w_2\,(L) = 0 \quad \text{and} \quad w_2'(L) = 0$$

From $w_1''(0) = 0$ and $w_1'''(0) = 0$, we have $C_1 = C_2 = 0$. This leads to six condition equations to solve six constants, C_3, C_4 *and* $A_i (i = 1, 2, 3, 4)$. The six equations can be rewritten in the matrix form as,

$$\mathrm{M}^* \begin{bmatrix} C_3 \\ C_4 \\ A_1 \\ A_2 \\ A_3 \\ A_4 \end{bmatrix} = \begin{bmatrix} 0 \\ 0 \\ ql^4/24EI \\ ql^3/6 \\ ql^2/2 \\ ql/EI \end{bmatrix} \tag{5-3}$$

where M=

$$\begin{bmatrix} 0 & 0 & e^{L\beta}sinL\beta & e^{L\beta}cosL\beta & e^{-L\beta}sinL\beta & e^{-L\beta}cosL\beta \\ 0 & 0 & \beta e^{L\beta}(cosL\beta + sinL\beta) & \beta e^{L\beta}(cosL\beta - sinL\beta) & \beta e^{-L\beta}(cosL\beta - sinL\beta) & -\beta e^{L\beta}(cosL\beta + sinL\beta) \\ -l & -1 & e^{L\beta}sin\beta l & e^{L\beta}cos\beta l & e^{-L\beta}\sin(\beta * l) & e^{-L\beta}\cos(\beta * l) \\ -1 & 0 & \beta e^{L\beta}(cos\beta l + sin\beta l) & \beta\, e^{L\beta}(cos\beta l - sin\beta l) & \beta e^{-L\beta}(cos\beta l - sin\beta l) & -\beta e^{-L\beta}(cos\beta l + sin\beta l) \\ 0 & 0 & 2\beta^2 e^{L\beta}cos\beta l & -2\beta^2 e^{L\beta}sin\beta l & -2\beta^2 e^{-L\beta}cos\beta l & 2\beta^2 e^{-L\beta}sin\beta l \\ 0 & 0 & 2\beta^3 e^{L\beta}(cos\beta l - sin\beta l) & -2\beta^3 e^{L\beta}(cos\beta l + sin\beta l) & 2\beta^3 e^{-L\beta}(cos\beta l + sin\beta l) & 2\beta^3 e^{-L\beta}(cos\beta l - sin\beta l) \end{bmatrix}$$

This equation can be solved by mathematical tools, such as Mathcad or MATLAB. The six constants, expressed as the function of the scour depth and other variables, are not presented her. For a pined–pined pile, the boundary conditions are expressed as,

$$w_1\ (0) = 0, \quad w_1''(0) = 0, \quad w_2\ (L) = 0 \ \text{ and } \quad w_2''(L) = 0$$

and equations and solutions can be similarly obtained.

5.2.2 Dynamic solution

As for the dynamic free vibration, the equation of motion of the same system can be derived as

$$\begin{cases} EI\dfrac{\partial^4 w(x,t)}{\partial x^4} + \rho A\dfrac{\partial^2 w(x,t)}{\partial t^2} = 0, & 0 \le x \le l \quad (a) \\ EI\dfrac{\partial^4 w(x,t)}{\partial x^4} + \rho A\dfrac{\partial^2 w(x,t)}{\partial t^2} + k(x)w(x,t) = 0, & l \le x \le L \quad (b) \end{cases} \tag{5-4}$$

where $w(x,t)$ is the time-dependent displacement of the pile, ρ is the mass density, and A is the cross-section area. The coefficient $k(x)$ is also considered as a constant, K. A general solution can be obtained easily by separating the variables into time and space domains using

$$w(x,t) = W(x)e^{i\omega t} \tag{5-5}$$

The solution of the governing equation thus reduces to that of

$$\begin{cases} \dfrac{d^4W(x)}{dx^4} - \lambda^4 W(x) = 0, & 0 \le x \le l \quad (a) \\ \dfrac{d^4W(x)}{dx^4} - (\lambda^4 - K/EI)W(x) = 0, & l \le x \le L \quad (b) \end{cases} \tag{5-6}$$

in which $\lambda = \sqrt[4]{\omega^2 \rho A/EI}$. The characteristic roots of Equation (5-6) are derived as,

$$m_{1,2,3,4} = \pm\sqrt{\pm\sqrt{\lambda^4 - K/EI}} = \pm\sqrt{\pm\sqrt{(\omega^2 \rho A - K)/EI}}$$

Depending on the relationship between λ^4 and K/EI, different solutions can be obtained.

If $\lambda^4 > K/EI$, the general solution is,

$$W(x) = \begin{cases} W_1 = C_1 \sin \lambda x + C_2 \cos \lambda x + C_3 \sinh \lambda x + C_4 \cos h\, \lambda x, & 0 \le x \le l \\ W_2 = A_1 sin\lambda_2 x + A_2 \cos \lambda_2 x + A_3 \sinh \lambda_2 x + A_4 \cos h \lambda_2 x, & l \le x \le L \end{cases} \quad (5\text{-}7)$$

where $\lambda_2 = \sqrt[4]{(\omega^2 \rho A - K)/EI}$.

If $\lambda^4 < K/EI$,

$$W(x) = \begin{cases} W_1 = C_1 \sin \lambda x + C_2 \cos \lambda x + C_3 \sinh \lambda x + C_4 \cos h\, \lambda x, & 0 \le x \le l \\ W_2 = e^{\lambda_2 x}(A_1 \sin \lambda_2 x + A_2 \cos \lambda_2 x) + e^{-\lambda_2 x}(A_3 \sin \lambda_2 x + A_4 \cos \lambda_2 x), & l \le x \le L \end{cases} \quad (5\text{-}8)$$

where $\lambda_2 = \sqrt[4]{(K - \omega^2 \rho A)/4EI}$.

If $\lambda^4 = K/EI$, namely, $\omega^2 = K/\rho A$,

$$W(x) = \begin{cases} W_1 = C_1 \sin \lambda x + C_2 \cos \lambda x + C_3 \sinh \lambda x + C_4 \cos h\, \lambda x, & 0 \le x \le l \\ W_2 = A_1 \frac{x^3}{6} + A_2 \frac{x^2}{2} + A_3 x + A_4, & l \le x \le L \end{cases} \quad (5\text{-}9)$$

Similar to the static solution, the boundary condition at $x = l$ requires the geometric continuity of displacement and slope, and the continuity of bending moment and shear force. They are expressed as:

$$W_1(l) = W_2(l), \quad W_1'(l) = W_2'(l), \quad W_1''(l) = W_2''(l) \text{ and } W_1'''(l) = W_2'''(l)$$

Four additional conditions from the boundaries at $x = 0$ and $x = L$ depend on the particular geometry under consideration. For a free–fixed pile, we have:

$$W_1''(0) = 0, \quad W_1'''(0) = 0, \quad W_2(L) = 0 \text{ and } W_2'(L) = 0$$

From $W_1''(0) = 0$ and $W_1'''(0) = 0$, we have $C_1 = C_3$ and $C_2 = C_4$.The rest six equations can be rewritten in the matrix form as:

$$M * [C_1 \; C_2 \; A_1 \; A_2 \; A_3 \; A_4]^T = 0 \quad (5\text{-}10)$$

The frequency equation is given by setting the determinant of the coefficient matrix M to be zero, i.e., $|M| = 0$. Different coefficient matrices can be derived for the three cases discussed above. Therefore, the natural frequency in different ranges should be solved by different frequency equations derived from the corresponding coefficient matrix, as described below.

If $\omega > \sqrt{K/\rho A}$, i.e. $\lambda^4 > K/EI$, the coefficient matrix is derived from Equation (5-7) and denoted as M_1. The natural frequencies are obtained by solving $|M_1| = 0$.

If $\omega < \sqrt{K/\rho A}$, i.e. $\lambda^4 < K/EI$, the coefficient matrix is derived from Equation (5-8) and denoted as M_2. The natural frequencies are obtained by solving $|M_2| = 0$.

If $\omega = \sqrt{K/\rho A}$, the natural frequencies are automatically obtained.

5.2.3 Numerical examples and parametric analyses

Example 1 for static solution. On the basis of the above analytical solution, an example was used for a demonstration. A square concrete pile with properties: L=24.38m (40ft), A=0.37m^2 (24*24in^2), EI=2.48e8N-m^2 (599424kips-ft^2), and q=146kN/m (10kips/ft). The elastic coefficient of soil per unit is k=2.76e5kN/m^2 (5760kips/ft^2). The pile head is free and the pile bottom is assumed to be fixed. A program was developed in MATLAB to solve the analytical equations. In the case of l=L, the pile without soil supporting is identical to a cantilever beam with a distributed loading, which is a special case and can be used for validation. Figure 5-2 shows that the pile deflections of both cases (cantilever beam and l/L= 1) are exactly the same as they are supposed to be, which validates the numerical solution procedure of the present study.

The scour ratio is defined as the ratio between the length without soil supporting and the pile length, l/L, and ranges from 0 to 1. The pile deflection and moment at various scour ratios are shown in Figure 5-2 and Figure 5-3. It can be easily seen that the pile displacement, moment, and the location of the maximum moment increase with the increase of the scour ratio. There exists a turning point in the moment curve at a location close to the interface between the water and soil. More details will be described in the next section.

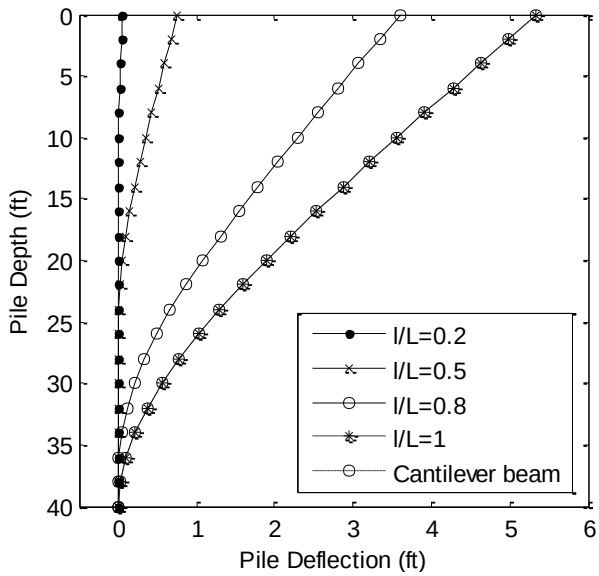

Figure 5-2. Pile deflections at varied scour ratios

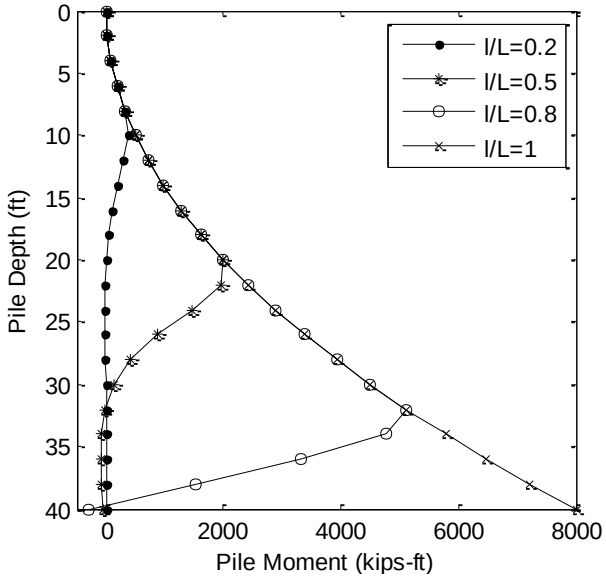

Figure 5-3. Pile moments at varied scour ratios

Figure 5-4 shows the pile displacement at different positions versus the scour ratio and all the curves have the same trend. Figure 5-5 shows the pile moment (curvature) at different

positions versus the scour ratio. It is found that for any position of the pile, if it is buried deeply in the soil, its moment is not significant. Only if the scour depth approaches to that position, the moment becomes significant. Take x=0.8L section as an example. As the scour ratio increases from 0 to about 0.6, the moment of this section is small and hardly changes because the section is buried in the soil. However, when the scour ratio is larger than 0.6, the moment increases quickly from a small negative value to a positive value. It reaches the maximum at the scour ratio of 0.8 and remains constant since the section is totally exposed to the water at and after this scour ratio. Figure 5-6 and Figure 5-7 demonstrate the influence of pile stiffness represented by beta = EI/k and soil stiffness represented by k.

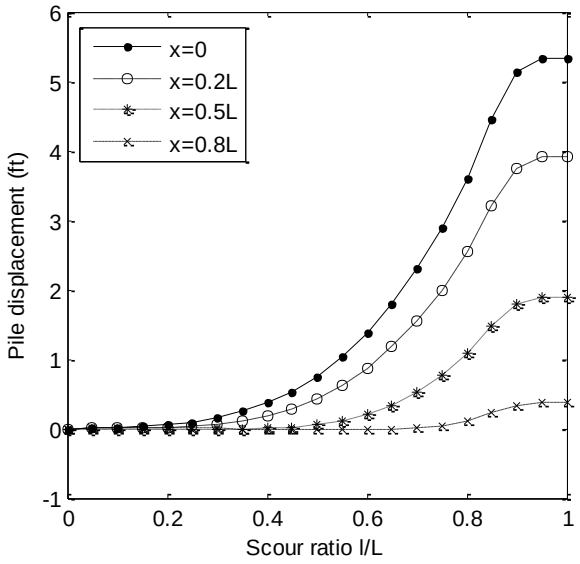

Figure 5-4. Displacements at different positions

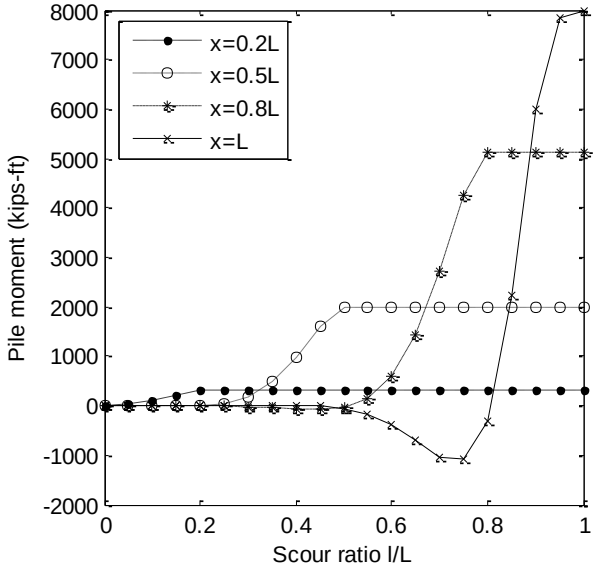

Figure 5-5. Moments at different positions

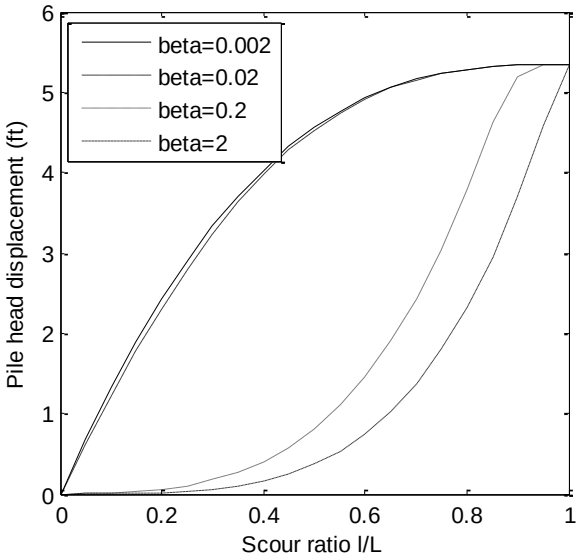

Figure 5-6. Pile head deflections with different beta

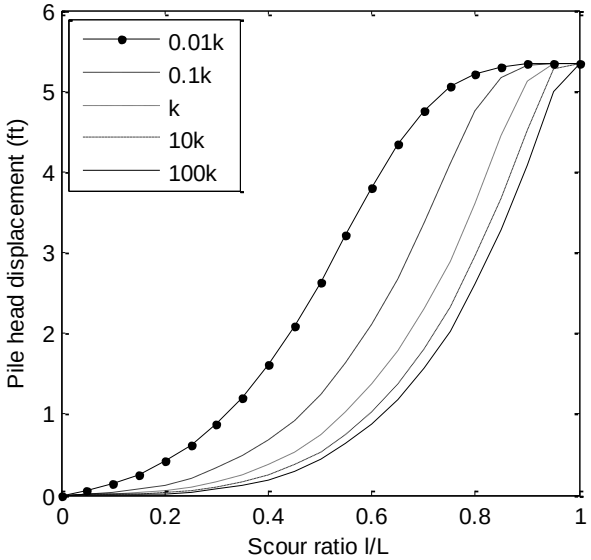

Figure 5-7. Pile head deflections with different k

Example 2 for dynamic solution. A pile similar to example 1 was adopted for a demonstration of the dynamic solution: L=24.38m (40ft), A=0.37m^2 (24*24in^2), E=2.15e10Pa (3122ksi), I=0.0115m^4 (1.333ft^4), and density=2403kg/m^3 (150pcf). In order to validate the relationship between ρA and K for different cases, the coefficient of soil here is 2760kN/m^2 (57.6kips/ft^2). The pile head is free and the pile bottom is assumed to be fixed. A program was developed in MATLAB to obtain the frequency equation from the determinant and then to solve the equations. Again, the special case of l=L was used for verification. The first four natural frequencies from the present study are 0.4957Hz, 3.1059Hz, 8.6986Hz and 17.038Hz, respectively, while they are 0.4957Hz, 3.1065Hz, 8.6992Hz and 17.0459Hz from the reference (Clough and Penzien 2003), which are very close to each other.

Figure 5-8 and Figure 5-9 show the first and fourth natural frequencies of the pile versus the scour ratio. The results of the second and third frequencies are the same as that of the first frequency, which is not shown here. The natural frequency decreases as the scour ratio increases, with the frequency of the first mode dropping much faster than that of the fourth mode. It means that the scour effect on the lower mode is more significant than on the higher mode, which will benefit the scour monitoring discussed later. Figure 5-10 shows the effect of the soil stiffness on the first natural frequency, and it mainly affects the natural frequency when the scour ratio is small.

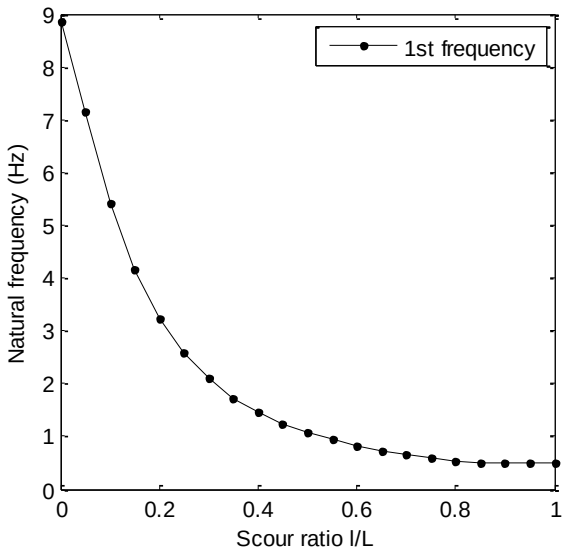

Figure 5-8. 1st frequency with scour ratio

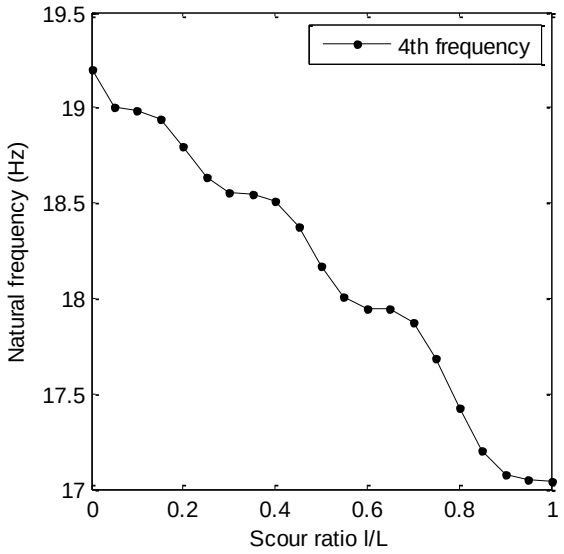

Figure 5-9. 4th frequency with scour ratio

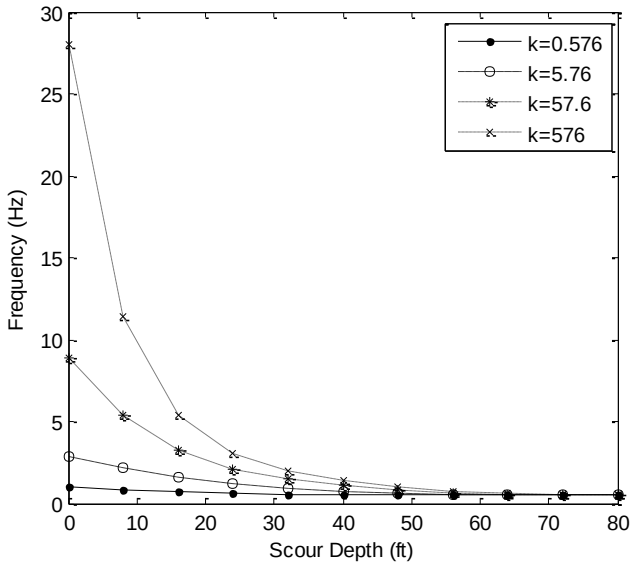

Figure 5-10. 1st frequency with various K

5.3 Proposed methods for scour detection and monitoring

Many methods have been developed for the short-term detection and long-term monitoring of bridge scour. In the early days, methods based on geophysical techniques, such as radar and sonar, were employed to identify the scour depth. However, most of them have just found very limited applications due to difficulties in such as the result interpretability, high noise sensitivity, and different issues during flood events (Deng and Cai 2010). In recent years, techniques using Time-Domain Reflectometry (TDR) and fiber Bragg grating (FBG) sensors are under development and used for real-time field monitoring. Due to their advantages over traditional sensors, such as their long-term stability and reliability, good resistance to environmental corrosion, and multiplexity along one single fiber (Deng and Cai 2007), fiber optic sensors become popular in structural performance monitoring. The challenge of FBG applications in bridge scour is how to design the instruments and mount the sensors to obtain useful data. Lin et al. (2005) developed two types of local scour monitoring systems, using a cantilever beam or plate that is fixed to the pier. Lu et al. (2008) used a sliding magnetic collar (SMC) and a steel rod to monitor bridge scour.

In the present study, methods based on a single pile were proposed. Instead of attaching an instrument to the bridge pier/pile, a separate pile or similar structure installed with FBG sensors was adopted and to be driven beside the monitored pile group. Anti-collision piers can be used for this purpose. Based on the analytical and numerical analyses of scour effects on the pile response discussed earlier, three possible methods to detect and monitor the foundation scour were proposed and discussed below. They are the methods based on (a) the pile's natural frequency change, (b) bending moment profile, and (c) modal strain profile.

5.3.1 Scour monitoring based on frequency change

The first step of damage detection is to determine the occurrence of damage (Rytter 1993). From the results of example 2 shown in Figure 5-8~Figure 5-10, it is found that the reduction of soil around the pile reduces the pile's natural frequency, especially the low order frequencies. Since the low order frequencies are easy to be measured, the change of frequency is an alternative feature for detecting the occurrence of scour damage. Figure 5-11 presents the change ratio of the first natural frequency versus the initial scour depths (the initial position of the interface between soil and water) for three different additional scour ratios, namely 5% (scour depth=4ft), 10% (8ft) and 15% (12ft). It can been seen that for this 34.384m (80ft) pile, when the initial soil position is above the 15.24m (50ft) line (measured from the pile top), an additional scour ratio of 5% (4ft) can result in more than 10% change in the first natural frequency. It implies that if an additional scour with a ratio of more than 5% occurs on a pile with an unsupported length of less than 62.5% (50/80 = 0.625), it can be detected through the change of the fundamental frequency. Figure 5-12 shows the same observation on the piles supported with soil of different stiffness.

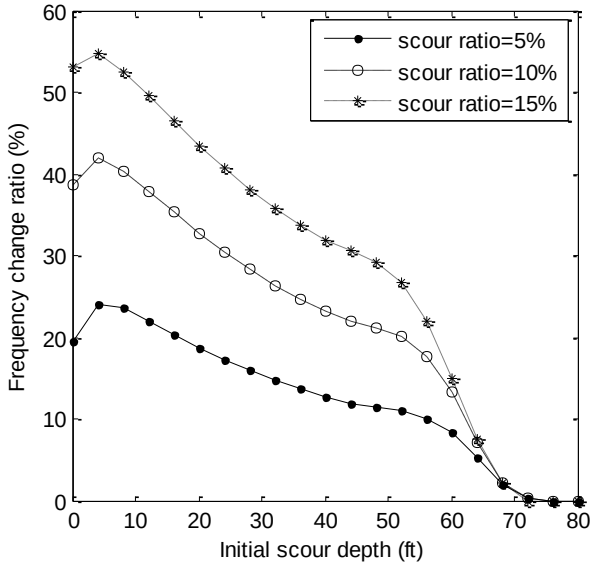

Figure 5-11. Change ratio of 1st frequency

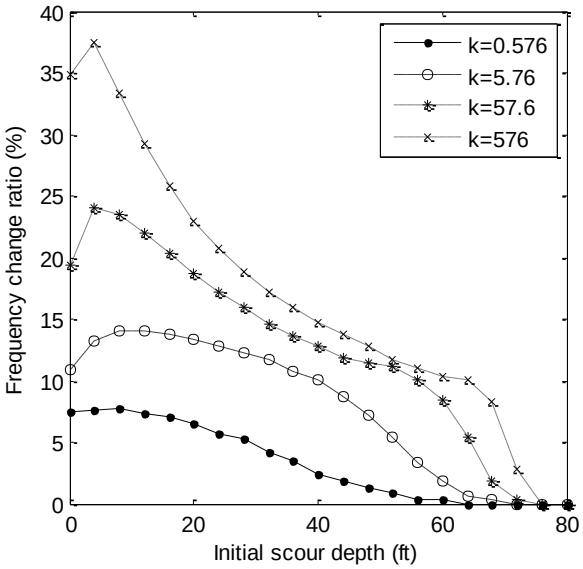

Figure 5-12. Change ratio of 1st frequency with scour ratio=5% (4ft)

5.3.2 Scour monitoring based on bending moment profile

Figure 5-3 and Figure 5-5 have shown that the maximum moment of the pile changes with the scour ratio and its location is slightly below but close to the scour depth. Therefore, a method based on the bending moment profile was proposed here for scour monitoring. As shown in Figure 5-13, the turning points of the three curves are 2.68m (8.8ft), 5.12m (16.8ft) and 7.56m (24.8ft), compared to the total unsupported length (scour depth) of 2.44m (8ft), 4.88m (16ft), and 7.32m (24ft), respectively. As expected, the detected turning point of moments is typically lower than the true soil (scour) line because the soil provides an elastic (not rigid) support to the pile.

The turning point of the pile moment profile can still be considered as the detected scour depth since it is very close to the true scour depth. From an engineering practice point of view, the top soil is typically weak after being disturbed and it does not provide much support to the pile. Therefore, the fact that the detected scour depth is slightly lower than the true soil position has a practical significance. For a single pile, it is easy to obtain the moment profile through strain sensors attached along the pile under applied testing loads or hydraulic loads.

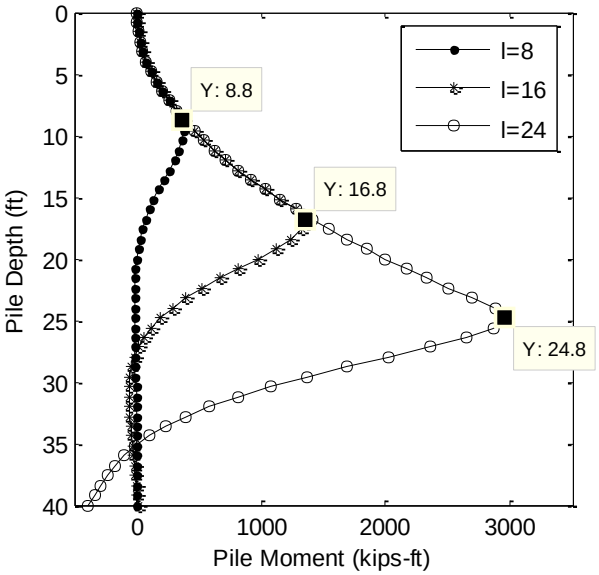

Figure 5-13. Bending moment profile

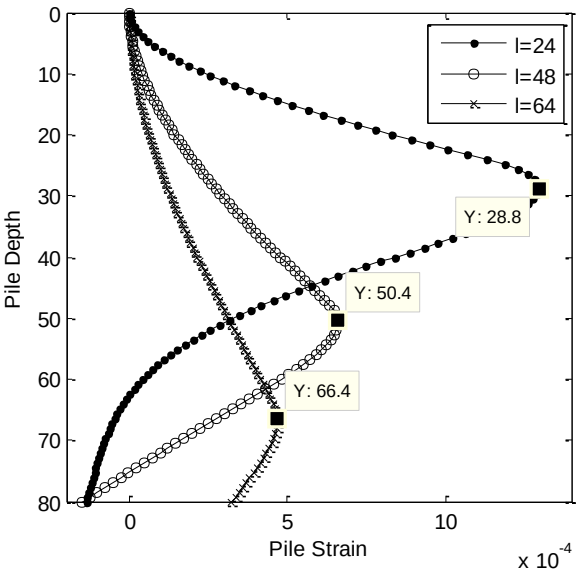

Figure 5-14. First modal strain profile

5.3.3 Scour monitoring based on modal strain profile

The modal information such as natural frequency and mode shape is easy to obtain from the time history data recorded from dynamic tests, which makes it attractive for damage and scour detection. Similar to the moment profile method, a strategy based on the modal strain (curvature) profile was also proposed in the present study. As shown in Figure 5-14, the modal strain extracted from the first modal shape is similar to the bending moment profile. The detected scour based on this strategy would be 8.78m (28.8ft), 15.36m (50.4ft) and 20.24m (66.4ft), compared to the true scour depth 7.32m (24ft), 14.63m (48ft), and 19.51m (64ft), respectively. Same as the bending moment case, the detected turning point of strains is typically lower than the true soil (scour) line because the soil provides an elastic (not rigid) support to the pile. Since the modal information is related to the physical property of the structure, it should be more applicable and practical than the bending moment from static loading.

5.4 Laboratory test

The present study developed a scour monitoring system using Fiber Optic Sensors (FOSs) that have wide applications in long-term monitoring of structures, especially in harsh environments. The major benefits of choosing FOSs for scour applications are: good corrosion-

resistance and long-term stability that make it possible to be embedded in soil and submerged in water; distributed sensing and multiplexing capabilities that make it possible to install a series of sensors along a single cable to collection information along the depth of the foundation; small size and light weight with little disturbance to the structure and soil; immunity to electromagnetic/radio frequency interference, etc.

Laboratory tests were conducted to verify the structural behavior under static and dynamic loadings and the feasibility of the proposed motoring methods. A pipe made of glass fiber reinforced polymer (GFRP) buried in sand was used to simulate the pile structure in soil, which is schematically depicted in Figure 5-15. A fiber reinforced polymer (FRP) bar attached with FBG sensors was mounted on the GFRP pipe at three positions, 0.0m, 0.4m and 0.8m, to measure the response of water impact. Both the pipe and the bar are fixed on a steel plate at the bottom. To simulate the water flow action, a shaking table was used to exert the stroke to the water tank sitting on the table. The water in the real river is in one direction, but it is back and forth in the tank. In order to reduce the drag force of water, the specimen was put close to one side in the tank. Five sensors were deployed both on the GFRP pipe and the FRP bar in an interval of 0.2m, namely, at the position of 0.0m, 0.2m, 0.4m, 0.6m, and 0.8m. For tests in water, the specimen was partially buried in a sand container and then submerged in the water tank. The heights of water and sand are adjustable as needed. Figure 5-15 shows an example that the bottom 0.4m is in the sand and the top 0.4m is in the water. A velocimeter was also used to measure the water velocity. Figure 5-16 shows the test specimen and layout. The property of the GFRP pipe is: outer diameter=11.4cm (4.5in), inner diameter=10.2cm (4in) and the axial Young's modulus obtained through the material test is 5.4GPa. The frequency filter is 250Hz.

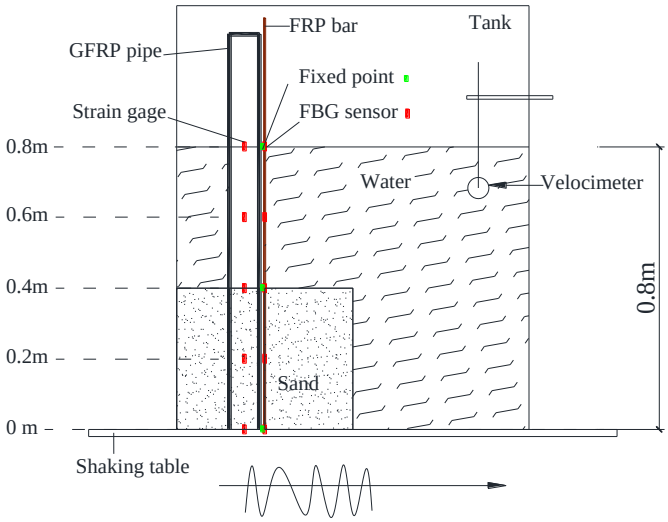

Figure 5-15. Schematic drawing of test design

Figure 5-16. Test specimen and layout on shaking table

Three monitoring mechanisms were tested. The first one is to detect the scour occurrence through the frequency change by clicking the GFRP pipe. The second one is the bending moment mechanism due to the static loading or the water flow as shown in Figure 5-17(a). Herein a force was applied on the top of the pipe to produce the bending moment. The third one is the high frequency response of the FBG sensors to water flow or debris impact as shown in Figure 5-17(b). A hanging weight was used to simulate the debris in river water, and the sensors on the FRP bar was specially designed for this mechanism.

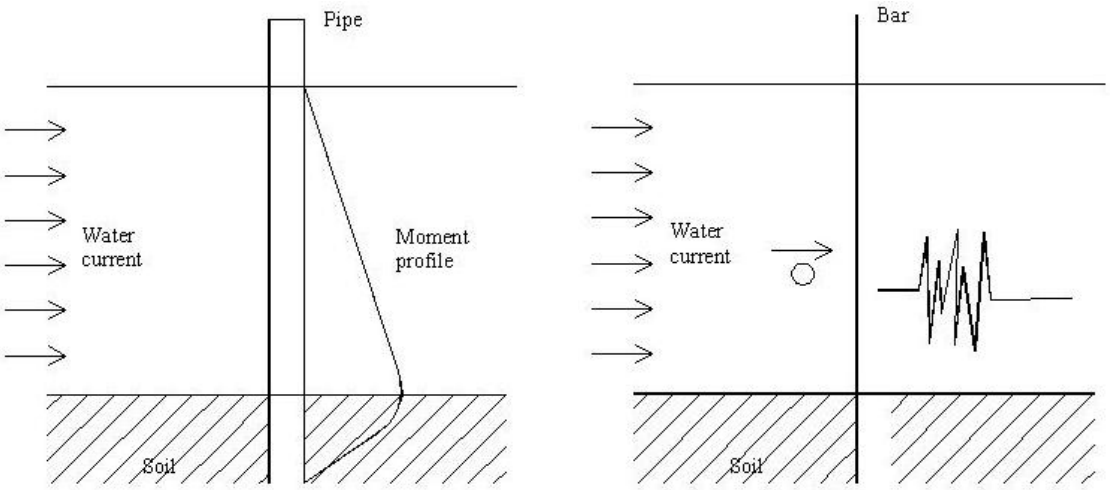

(a) Bending moment mechanism (b) High frequency signal from the debris

Figure 5-17. Monitoring mechanisms to be tested

5.4.1 Detection of frequency change

The GFRP pipe was first put on the ground without sand and clicked on the top, and was then buried in the sand with different heights, 0.2m, 0.4m and 0.6m. The time histories of strain response are transferred into the frequency domain using Fast Fourier Transform (FFT), as shown in Figure 5-18. The first frequencies of the four cases are 34.85Hz, 35.25Hz, 38.30Hz and 42.00Hz, respectively. Therefore, it confirms that the fundamental frequency of the structure decreases as the reduction of sand height, which indicates a scour activity.

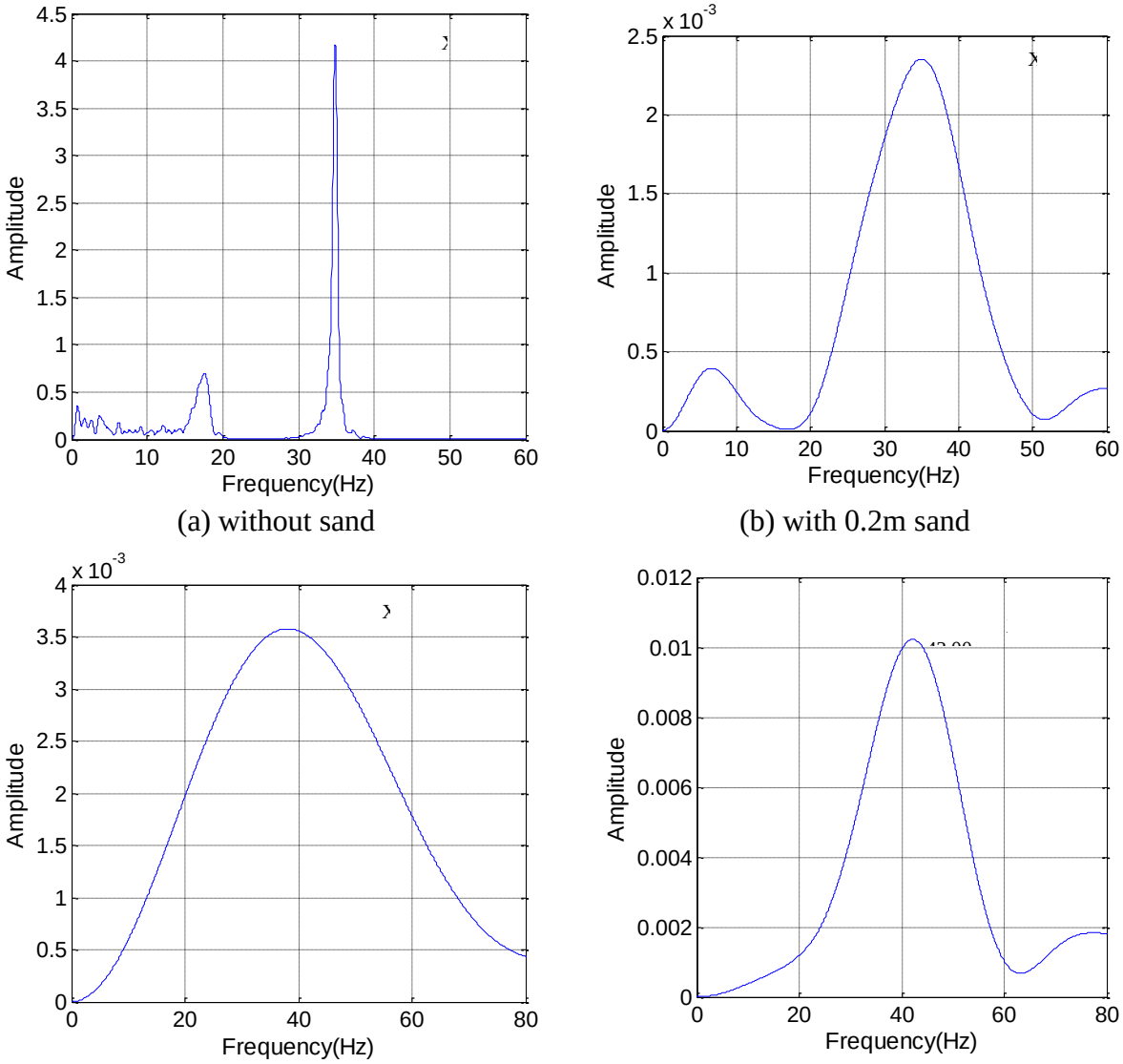

(a) without sand

(b) with 0.2m sand

(c) with 0.4 sand

(d) with 0.6m sand

Figure 5-18. FFT of strain response

5.4.2 Detection of moment/strain profile change

As observed earlier in the numerical simulation, the location of the maximum moment in the pile changes with the scour depth. In this section, tests of the GFRP pipe under different supporting conditions were conducted: without sand and with different heights of sand. A lateral force was applied intermittently on the top of the GFRP pipe to generate the bending moment in the pipe, and the time history of the strain response at different locations was recorded by the five sensors.

Without sand: The GFRP pipe was on the ground without any sand around and six runs were conducted. The strain responses of the five sensors of the first run are shown in Figure 5-19. For each run, the strain value of the five sensors at a specific time was extracted to demonstrate the strain distribution along the pipe length. Figure 5-20 is the strain value along the pile length at the five peak times shown in Figure 5-19. Those values are then normalized based on the ratio to the strain of the bottom sensor, namely, the strain value of the sensor at the position of 0.0m is set to be 1, as shown in Figure 5-21. The average of the normalized strain value at each run is then summarized in Figure 5-22. It can be found that the stain distribution is nearly linear.

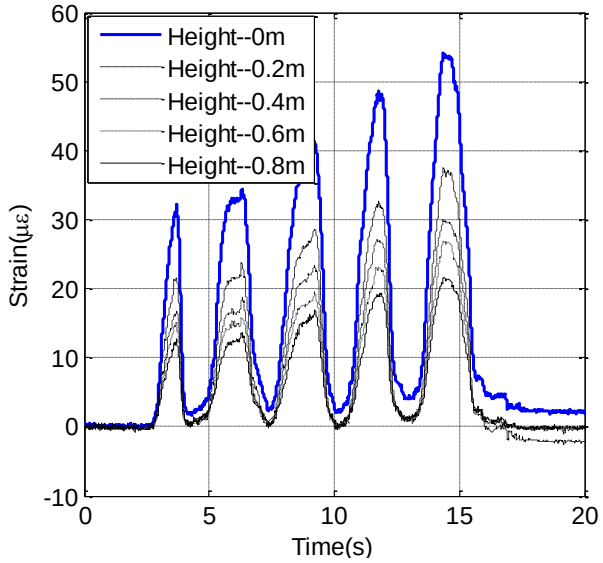

Figure 5-19. Strain response of the pipe without sand

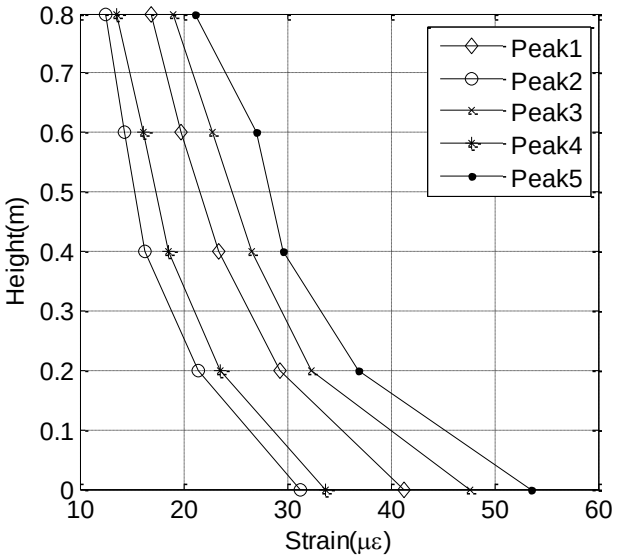

Figure 5-20. Strain distribution of 1st run

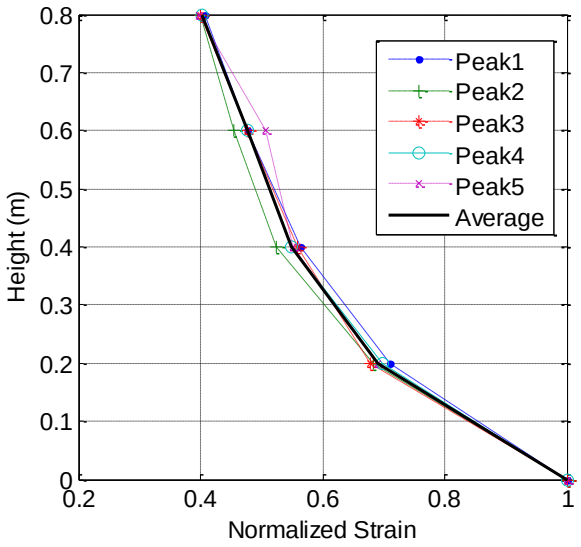

Figure 5-21. Normalized strain distribution of 1st run

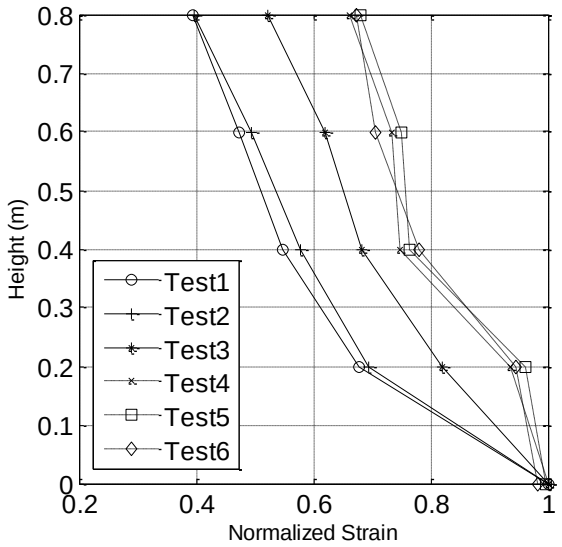

Figure 5-22. Normalized strain distribution of 6 runs

With sand of 0.2m high and 0.4m high: The GFRP pipe was buried in the sand with a height of 0.2m and 0.4m, respectively. With the same procedure, the normalized strain distributions of all the three runs are summarized in Figure 5-23 and Figure 5-24. The maximum strain in Figure 5-23 is at the position of 0.2m and that in Figure 5-24 is at the position of 0.4m, which is equal to the sand height of each case and indicates the scour depth.

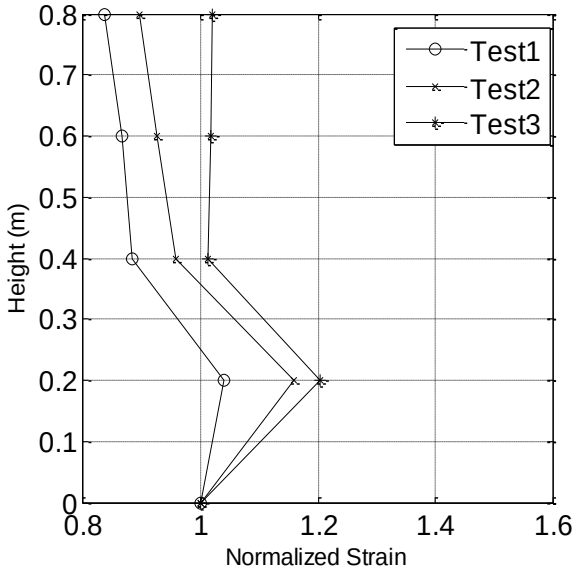

Figure 5-23. Normalized strain distribution of pipe with 0.2m sand

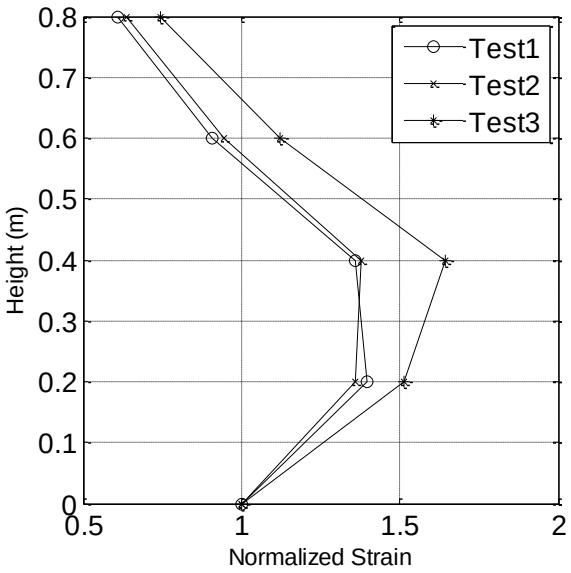

Figure 5-24. Normalized strain distribution of pipe with 0.4m sand

5.4.3 Water current test on the shaking table

In this test, the specimen was put into the water tank on the shaking table to simulate the water flow action, and hanging weights were used to simulate the debris in the river water. The GFRP pipe with the FRP bar was buried in different heights of sand. In the first case, the sand height was 0.4m and one hanging weight was at the position of 0.6m. In the second case, the sand height was 0.2m and two hanging weights were arranged at the position of 0.2m and 0.6m, respectively. The water height was 0.8m and the speed of the shaking table was set to be 0.1m/s, 0.25m/s and 0.5m/s.

The time histories of strains at the speed of 0.5m/s are shown in Figure 5-25. Figure 5-25(a) is the strain response from sensors on the FRP bar and Figure 5-25(b) is that from sensors attached on the GFRP pipe. It is observed that the response of the FRP bar is much stronger than that of the GFRP pipe, especially at the position of 0.6m where the hanging weight is located. Besides, the curves of both cases look totally different. The one in Figure 5-25(a) for height 0.6m looks like an impulse signal and is very obvious to be distinguished with others, which is due to the discontinuously impact of the hanging weight.

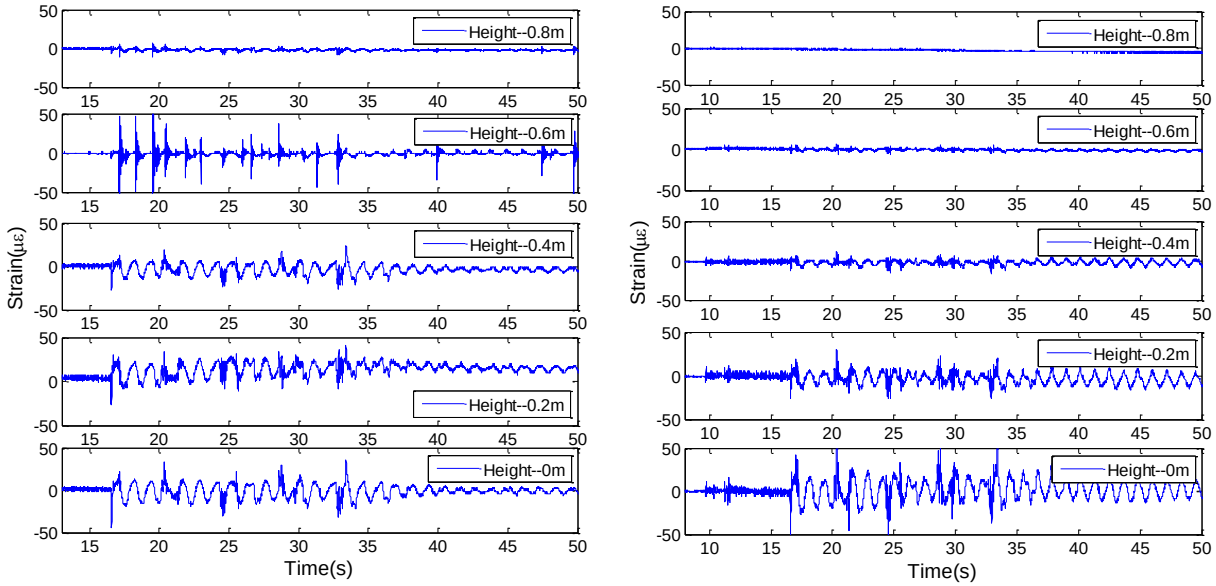

(a) FRP bar (b) GFRP pipe

Figure 5-25. Strain response with 0.4m sand

The same observation can be seen from the results of the second case with 0.2m sand as shown in Figure 5-26. Besides the position of 0.6m, Figure 5-26(a) reveals that the impulse-like signal appears at the position of 0.2m as well. From case 1 to case 2, the sand height reduces from 0.4m to 0.2m, which exposes the sensor and the hanging weight at the position of 0.2m. It indicates that as the soil is scoured, the sensor used to be buried in the soil is exposed to the water, and begins to respond recognizably differently due to the water current and debris impact. It is a good sign for scour detection.

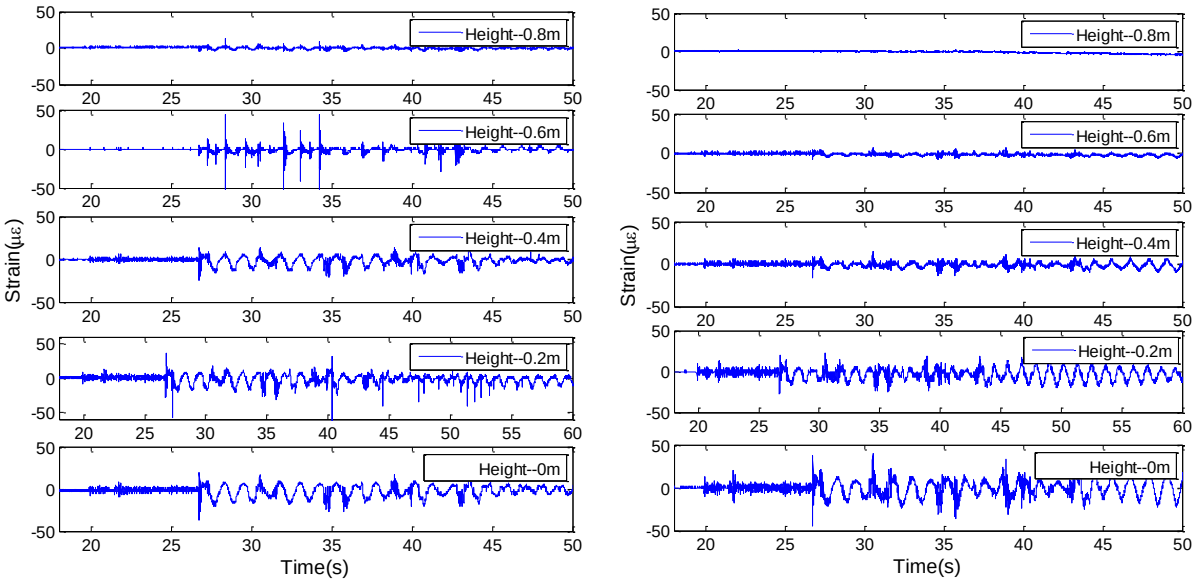

(a) FRP bar (b) GFRP pipe

Figure 5-26. Strain response with 0.2m sand

With the same procedure as described above, the strain distribution of the pipe at a given time was obtained by extracting from the time-history results of the five sensors, as shown in Figure 5-27, with a sand height of 0.4m and water speed of 0.25m/s. The maximum strain is at the position of 0.2m, which is lower than the sand height. The possible reason could be that the elastic coefficient of sand is not constant but linearly distributed along the depth, which means that the stiffness of the top sand is very small. Moreover, the sand saturated in water weakens its supporting ability and the water flow drags the top sand and makes it loose. Therefore, the identified scour depth is not exactly the same as the actual scour depth.

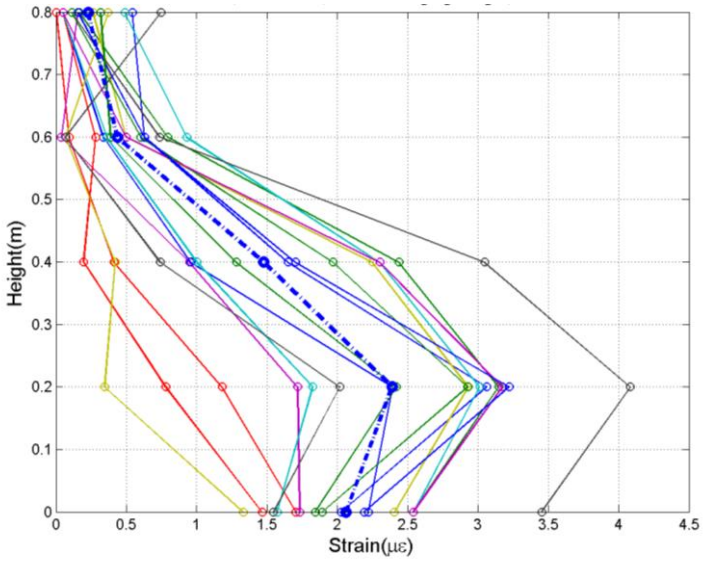

Figure 5-27. Strain distribution with 0.4m sand, v=0.25m/s

5.5 Conclusions

The present study mainly focused on the static and dynamic response of a single pile to scour effects. Based on observations from the theoretical and parametric analyses, the present study proposed three possible methods for detecting and monitoring bridge scour and developed a monitoring system using fiber optic sensors that had been verified in the laboratory. The following conclusions can be drawn:

(1) For any position of the pile, if it is buried deeply in soil, its bending moment is not significant. Only if the scour depth approaches to that position, the moment becomes significant and increases quickly to its maximum. Furthermore, the location of the maximum moment in the pile is close to the interface between water and soil, which can be used for detecting the scour depth.

(2) The pile's natural frequency decreases as the scour ratio increases, especially for the fundamental frequency of the pile, which benefits the scour monitoring.

(3) The bending test of the GFRP pipe buried in sand with different heights verifies the numerical observations, that is, the position of the maximum moment in the pile is close to the interface of sand and water. It also confirms the feasibility of the scour monitoring method based on the bending moment profile.

(4) The water flow test on the shaking table verifies the scour monitoring method based on the high frequency signal from the debris in the river water. As the sand level is reduced, the sensor used to be buried in the soil is exposed to the water, and it begins to respond recognizably differently due to the water flow and debris impact. It is a good sign for scour detection.

(5) The scour monitoring method based on the moment profile caused by the water flow impact is not as accurately verified. The possible reason is that the elastic coefficient of sand is not constant but linearly distributed along the depth, which means the stiffness of the top sand is very small. Moreover, the sand saturated in water weakens its supporting ability and the water flow drags the top sand and makes it loose. Therefore, the identified scour depth is not exactly the same as the actual scour depth.

5.6 References

Breusers, H. N. C., Nicollet, G., and Shen, H. W. (1977). "Local scour around cylindrical piers." Journal of Hydraulic Research, 15(3), 211-252.

Coskun, I. (2003). "The response of a finite beam on a tensionless Pasternak foundation subjected to a harmonic load." European Journal of Mechanics/Solids, 22, 151-161.

Clough, R., and Penzien, J. (2003). "Dynamics of Structures." Computer and Structures, Inc.

Deng, L., and Cai, C. S. (2007). "Applications of fiber optic sensors in civil engineering." Structural Engineering and Mechanics, 25(5), 577-596.

Deng, L., and Cai, C. S. (2010). "Bridge scour: prediction, modeling, monitoring, and countermeasures--review." Practice Periodical on Structural Design and Construction, ASCE, Vol. 15, No. 2, pp. 125–134.

Ding, Z. (1993). "A general solution to vibrations of beams on variable Winkler elastic foundation." Computer & Structures, Vol.47, No.1, 83-90.

Foti, S., and Sabia, D. (2011). "Influence of foundation scour on the dynamic response of an existing bridge." Journal of Bridge Engineering, 16, 295-304.

Han, Z. F., Ye, A. J., and Fan, L. C. (2010). "Effects of riverbed scour on seismic performance of high-rise pile cap foundation." Earthquake engineering and engineering vibration, Vol.9, No.4, 533-543.

Heza, Y. B. M., Soliman, A. M., and Saleh, S. A. (2007). "Prediction of the scour hole geometry around exposed bridge circular-pile foundation." Journal of Engineering and Applied Science, 54(4), 375-392.

Kassem, A., Salaheldin, T. M., Imran, J., and Chaudhry, M. H. (2003). "Numerical modeling of scour around artificial rock island of Cooper River Bridge." Transportation Research Records 1851, 45-50.

Lagasse, P. F., and Richardson, E. V. (2001). "ASCE Compendium of Stream Stability and Bridge Scour Papers." Journal of Hydraulic Engineering, 12797: 531-533.

Lagasse, P. F., Thompson, P. L., and Sabol, S. A. (1995). "Guarding Against Scour." Civil Engineering Magazine, 65(6), 56–59.

Laursen, E. M., and Toch, A. (1956). "Scour around bridge piers and abutments." Bullentin No.4, Iowa Highway Research Board, Ames, Iowa.

Lee, T. L., Jeng, D. S., Zhang, G. H., and Hong, J. H. (2007). "Neural network modeling for estimation of scour depth around bridge piers." Journal of Hydrodynamics, 19(3), 378-386.

Lim, S. Y. (1997). "Equilibrium clear-water scour around an abutment." Journal of Hydraulic Engineering, 123(3), 237-243.

Lin, C., Bennett, C., Han, J., Parsons, R.L. (2010). "Scour effects on the response of laterally loaded piles considering stress history of sand." Computers and Geotechnics, 37, 1008-1014.

Lin, Y. B., Chen, J. C., Chang, K. C., Chern, J. C., and Lai, J. S. (2005). "Real-time monitoring of local scour by using fiber Bragg grating sensors." Smart Materials and Structures, 14(4), 664-670.

Lu, J. Y., Hong, J. H., Su, C. C., Wang, C. Y., and Lai, J. S. (2008). "Field measurements and simulation of bridge scour depth variation during floods." Journal of Hydraulic Engineering, 134(6), 810-821.

Melville, B. W., and Raudkivi, A. J. (1977). "Flow characteristics in local scour at bridge piers." Journal of Hydraulic Research, 15(4), 373-380.

Melville, B. W., and Sutherland, A. J. (1988). "Design method for local scour at bridge piers." Journal of Hydraulic Engineering, 114(10), 1210-1226.

Mohammad, Z. K., Beheshti, A. A., and Behzad, A. A. (2009). "Estimation of current-induced scour depth around pile groups using neural network and adaptive neuro-fuzzy inference system." Applied Soft Computing, 9, 746-755.

Rytter, A. (1993). "Vibration based inspection of civil engineering structures." Ph. D. Dissertation, Department of Building Technology and Structural Engineering, Aalborg University, Denmark.

Sheppard, D. M., and William, M. Jr. (2006). "Live-bed local pier scour experiments." Journal of Hydraulic Engineering, 132(7), 635-642.

Shirhole, A. M., and Holt, R. C. (1991), "Planning for a comprehensive bridge safety program." Transportation Research Record 1290, Transportation Research Board, National Research Council, Washington, D.C., 1, 39-50.

Umbrell, E. R., Young, G. K., Stein, S. M., and Jones, J. S. (1998). "Clear-water contraction scour under bridges in pressure flow." Journal of Hydraulic Engineering, 124(2), 236-240.

Young, G. K., Dou, X., Saffarinia, K., and Jones, J. S. (1998). "Testing abutment scour model." Proceedings of the 1998 International Water Resources Engineering Conference, Vol.1, 180-185. Memphis, TN, USA.

CHAPTER 6. INSTRUMENTATION DESIGN FOR BRIDGE SCOUR MONITORING USING FIBER BRAGG GRATING SENSORS

6.1 Introduction

Bridge scour is one of the main causes of bridge failures. According to a study by Shirhole and Holt (1991), in the past 30 years more than 1,000 bridges collapsed in the United States, and about 60% failures were related to the scour of bridge foundations. Bridge scour has been identified to be the most common cause of highway bridge failures in the United States (Kattell and Eriksson 1998). Actually, according to a study by the Transportation Research Board in 1997, there were 488,750 bridges over streams and rivers in the United States, and the annual cost for scour-related bridge failures was estimated at $30 million (Lagasse et al. 1997).

Technically speaking, bridge scour is the result of the erosive action of flowing water, which excavates and carries away materials (mainly soils and gravels) from around the piers and abutments of bridges. There are generally three types of scours that affect the performance and safety of bridges, namely, local scour, contraction scour, and degradational scour (Parker et al. 1997). Among them, the local scour is the most critical in scour-related safety issues of bridges; it is generally caused by the interference of the structures with river flow, and it is characterized by the formation of a scour hole near bridge piers or abutments. A great deal of time, money and efforts has been dedicated to the scour detection and monitoring, and instrumentation design in order to obtain more accurate measurements. However, it is still not easy to accurately measure and monitor in real time the depth variations of scour at piers or abutments, especially in flooding environments.

Many methodologies and instrumentations have been proposed for measuring and monitoring the local scour depth (variations) near bridge piers or abutments, such as time-domain reflectometry (TDR), sonar and radar, sliding magnetic collar (SMC), and piezoelectric sensors. However, most of these available techniques have their drawbacks, which could limit the practical applications. For instance, the TDR technique is operated by sending an electromagnetic pulse and coupling it to a transmission line or cable with a fixed velocity (Dowding and Pierce 1994; Yankielun and Zabilansky 1999; Yu and Zabilansky 2006; Yu and Yu 2007). The response signals vary if there is any change in the current or potential. However, since the cable as a transmission line is often hundreds of meters in length, the pulse during the transmission stands a good chance to negatively attenuate and disperse the TDR signals. The electromagnetic environment can also affect the accuracy of the results. These drawbacks could significantly reduce the ability to detect and monitor the subtle scour variations if using the TDR technique.

Sonar and radar are other two familiar techniques to detect and monitor bridge scour (Mason and Shepard 1994; Millard et al. 1998; Cuevas et al. 2002; De Falco and Mele 2002; Park et al. 2004; Hunt 2005). Both of them are easy and convenient to apply in the field; however, the monitoring results are difficult to interpret, especially when the flowing water contains high concentration sediments, debris or rocks in a flooded river. The noises caused by

the turbidity of the flow also make the corresponding systems unreliable for the real-time monitoring of the scouring processes. Therefore, radar and sonar are usually good for applications after flooding, and the measured data of the scour depth can only indicate the final status of the degradation/aggregation surrounding the bridge piers or abutments. The maximum scour depth during floods generally occurring near the peak flood discharge, however, cannot be detected and monitored under these techniques, which should be the most significant concern. Lu et al. (2008) used a sliding magnetic collar (SMC) and a steel rod to monitor the bridge scour during floods. The lower tip of the steel rod was initially placed slightly below the riverbed in the main channel. When scour occurs, the steel road will drop as the surface of the riverbed drops. The scour depth is determined based on the total lowering distance of the steel rod. The major disadvantage of this instrument, similar to the sonar and radar, is that it cannot detect the refilling process of the scour to correctly determine the maximum scour depth. Besides, piezoelectric sensors, consisting of a series of spatially separated piezo films, can be also found in the scour application. It provides incremental-spatial resolution to track the entire scour cycle (Lagasse et al. 1997; Baglio et al. 2000). However, this is a delicate set-up and it is susceptible to being damaged by muddy waters and debris in the flooding period.

Based on this literature review, developing a real-time, reliable and robust system is very desirable for a local scour monitoring, which also needs to be easily installed in a riverbed near the bridge piers or abutments and collects the data safely. To this end, an innovative scour monitoring system including the instrumentation design is proposed using fiber Bragg grating (FBG) sensors. In this scour monitoring system, the application of FBG sensors can make the monitoring flexible, stable, and durable in harsh environments with the advantages of lightweight, highly temperature and radiation tolerant, and especially immunity from electromagnetic interference. Based on the wavelength response and multiplexing capability, FBG sensors can be easily multiplexed in a series of arrays along a single optical fiber to reduce the possible attenuation during the signal transmission in a long cable length. In contrast to other sensor networks, the proposed design can provide a real-time monitoring for the entire scouring process to correctly observe the maximum scour depth during floods. A good protection measure is also provided to prevent the monitoring system from being damaged by muddy waters and debris in the flooding period. Finally a laboratory test demonstrates that the proposed scour monitoring system using FBG sensors works well and its advantages over other monitoring systems are obvious.

6.2 Fiber bragg grating sensor

Fiber Bragg gratings are made by laterally exposing the core of a single-mode fiber to a periodic pattern of intense ultraviolet light (Casas and Cruz 2003; Deng and Cai 2007). The exposure produces a permanent increase in the refractive index of the fiber's core, creating a fixed index modulation according to the exposure pattern. This fixed index modulation is called a grating. At each periodic refraction change, a small amount of light is reflected. All the reflected light signals combine coherently to one large reflection at a particular wavelength when the grating period is approximately half the input light's wavelength. This is referred to as the Bragg condition, and the wavelength at which this reflection occurs is called the Bragg

wavelength. Light signals at wavelengths other than the Bragg wavelength, which are not phase matched, are essentially transparent or transmitted. The work principle of FBG sensors is shown in Figure 6-1.

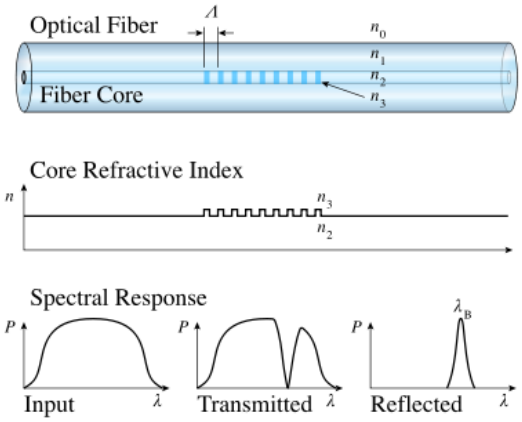

Figure 6-1. Work principle of FBG sensors

The Bragg wavelength λ_B depends both on the physical characteristics of the fiber and geometrical characteristics of the grating:

$$\lambda_B = 2n_e\Lambda \tag{6-1}$$

where n_e = effective refractive index of the grating in the fiber core; and Λ = grating period.

Both the effective refractive index and grating period vary with the change in strain $\Delta\varepsilon$, temperature change ΔT, and pressure change ΔP, imposed on the fiber. An applied strain and pressure will shift the Bragg wavelength through expansion or contraction of the grating periodicity and through the photo elastic effect. Temperature affects the Bragg wavelength through thermal expansion and contraction of the grating periodicity and through thermal dependence of the refractive index. If only the dominant linear effects of these three factors on FBG sensors are considered, neglecting higher-order cross-sensitivities, the amount of Bragg wavelength shift can be given by (Kersey 1997):

$$\Delta\lambda_B / \lambda_B = K_\varepsilon\Delta\varepsilon + K_T\Delta T + K_P\Delta P \tag{6-2}$$

where K_ε, K_T, and K_P= respective wavelength sensitivity coefficients for strain, temperature, and pressure for FBG sensors, respectively, which are further given by:

$$K_\varepsilon = \{1-0.5n_e[\rho_{12}-\nu(\rho_{11}-\rho_{12})]\}\lambda_B \tag{6-3a}$$

$$K_T = (1+\xi)\lambda_B \tag{6-3b}$$

$$K_P = [-(1-2\nu)/E + n_e^2(1-2\nu)(2\rho_{12}+\rho_{11})/2/E]\lambda_B \tag{6-3c}$$

where ρ_{11} and ρ_{12} = components of the fiber optic strain tensor; ν = Poisson's ratio; ξ = thermo-optic coefficient; and E = Young's modulus.

In Equation (6-2), even if assuming the pressure unchanged ($\Delta P = 0$), temperature and strain still cannot be measured simultaneously with one single grating since only one sensing

parameter, wavelength shift, is required in the FBG sensor application. To separate the strain signal from the temperature signal, different compensation methods of temperature effects have been reported in the literature (Xu et al. 1995; Idriss et al. 1998; Miridonov et al. 1999; Tennyson et al. 2000). Practically, with a matrix inversion technique, most of the applications utilize two superimposed FBG sensors written at two different wavelengths to decouple the strain and temperature (Xu et al. 1995; Idriss et al. 1998; Miridonov et al. 1999; Tennyson et al. 2000).

Therefore, fiber Bragg gratings, i.e., FBG sensors, can be used as direct sensing elements for strain and temperature. Based on the work principle introduced above applying FBG sensors to a scour monitoring system in the present study can give such advantages as below:

(1). High resolution, dynamics, and accuracy. The resolution of FBG sensors, the capability of detecting a very small variation of the measured quantity, can be of 0.1 parts per million (ppm), resulting in 0.1με of minimum measurable deformation. The dynamics of FBG sensors, the capability to measure a given quantity in a wide variation range with a specified resolution, allows length variations of over 10000 ppm, which makes a maximum measurable deformation over ±10000 με. The accuracy of FBG sensors, the maximum mismatch between the measured and the real value of a given quantity, is about 2 ppm, i.e., ±2 με. These performances make FBG sensors sufficiently sensitive to the pressure from flowing water/flood impact force.

(2). Immunity to electromagnetic noise. This is an intrinsic characteristic of FBG sensors due to the material (glass) they are made of. Being the glass, a dielectric material, electromagnetic fields cannot induce electric currents into the fiber optics, nor modify the wavelength or the intensity of the optical signal. For this reason FBG sensors, compared to some traditional techniques such as TDR, are very suitable for installation in harsh environments such as flooding rivers.

(3). Long term stability. Durability and stability is another important characteristic of FBG sensors. They can work for years without influence of negative effects due to aging, corrosion, and action of atmospheric agents that in general contribute to degrade the conventional sensors. This feature is especially important when applying FBG sensors in a sensing system of scour monitoring which usually requires a long term or permanent installation lasting for many years.

(4). Long distance installation. Due to the very low attenuation of fiber optics, FBG sensors can be installed at a distance of the order of tens of km far from the interrogation system via fiber optic cables. For this reason it is possible to create a scour monitoring system with a reliable connection requirement of a very long distance.

(5). Good physical performance. The small size and light weight of FBG sensors including fiber connection is a very useful feature when there is a very small space for the installation or in those cases where traditional sensors might load the structure. This makes FBG sensors an excellent choice in both surface-mounted and embedded sensing applications.

(6). Multiplexing capability. FBG sensors are highly attractive also because of their multiplexing capability in a distributive sensing network. They can be easily multiplexed in a series of arrays along a single optical fiber. For scour monitoring, it is a valuable and practical feature to create multiple sensing points in different depths using only one cable.

All the features of FBG sensors introduced above are important and will be applied in the following proposed scour monitoring system, which surely are the fundamental knowledge of this new design and make this new design more practical and effective over other scour monitoring systems.

6.3 Monitoring system and instrumentation design

Based on the discussions above, FBG sensors are identified as very useful and attractive devices to measure scour depths for the scour monitoring over other methods. Although FBG sensors have already demonstrated their advantages and applicability in many researches, their application in scour monitoring is actually a very new attempt. How to design an efficient and reliable scour monitoring system and instrumentation with FBG sensors is still a significant issue in the practical application. In addition, FBG sensors cannot be applied directly in the field because, after certain experimental evaluations, they are found to be unable to withstand the conditions encountered in floods due to their brittleness (Lin et al. 2005). The present study is to design an innovative monitoring system not only to fully exploit all the advantages of FBG sensors in the scour monitoring but also to protect FBG sensors in the field.

6.3.1 Monitoring system designs

To this end, three designs of the scour monitoring system using FBG sensors are proposed. The recommended design will be given after a comparison.

(1) Design 1

In this design, FBG sensors are arrayed at a certain interval along a single optical fiber in series on a steel bar (Details in Figure 6-2). This steel bar is supported as a continuous beam using fixed joints inside a steel tube which is a hermetic space (B-B in Figure 6-2). Each FBG sensor in this system is covered by a waterproof rubber seal like a button, which goes through the steel tube from a hole (A-A and B-B in Figure 6-2). The detailed sketch of Design 1 is shown in Figure 6-2.

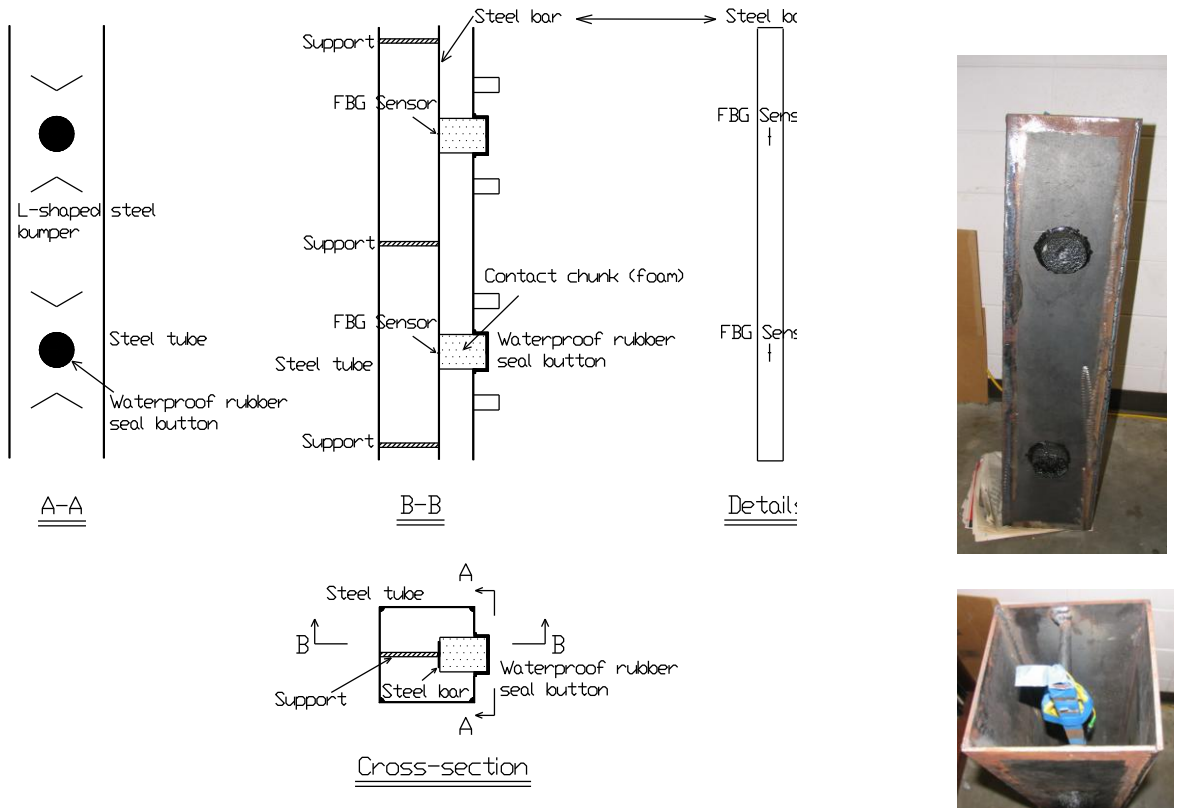

Figure 6-2. Detailed sketch of Design 1

Based on this design, when the scour occurs FBG sensors should emerge from the riverbed where they used to be buried in the soils. There are two phenomena that can be sensed by FBG sensors, the flowing water pressures and flowing water impact forces. Specifically speaking, the flowing water pressures, through the waterproof rubber seal, can bend/deform the steel bar (dashed line in Figure 6-3) and this bending can be sensed as strain variations by the FBG sensors glued on the steel bar. The flowing water impact forces toward the sensors can be also directly sensed by FBG sensors. Both of the sensed phenomena are regarded as the significant signs to indicate the successful detection and monitoring of scour. Along with the development of scour, more and more FBG sensors emerge from the riverbed. Depending on the position of the emerging FBG sensors, it is easy to notice where the scour develops and the whole process of scour can also be monitored and recorded in real time. In other words, both the actual maximum scour depth and deposition process (soil backfilling) can be clearly observed in addition to the final scour depth after floods. The waterproof rubber seal including an L-shaped steel bumper should be able to prevent damages to FBG sensors in case of a flood flowing at an excessive velocity beyond the protection criterion, or if debris in the flow strikes with excessive impact forces. The monitoring principle of this design is shown in Figure 6-3.

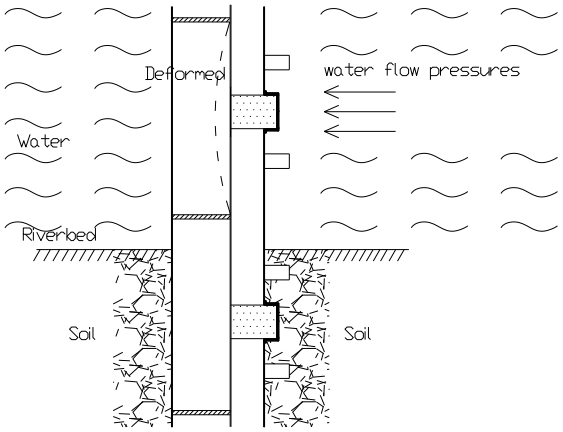

Figure 6-3. Monitoring principle of Design 1

However, this design has a few problems when it comes to practical applications. One of them is the influence from the hydrostatic pressures in the water or rivers, which may make the waterproof rubber seal buttons not function as intended. Due to a tube design which is a hermetic space, the hydrostatic pressures applying on FBG sensors on the steel bar through the buttons are actually very significant especially near the bottom of rivers. The steel bar or other structure components not only sustain the flowing water pressures and flowing water impact forces but also the hydrostatic pressures which may be much higher than the former. However, as a matter of fact, the hydrostatic pressures are nothing but negative for the instrumentation design, which could make the steel bar unnecessarily strong (high thickness or large width) and also make the buttons relatively insensitive to the external forces.

For instance, if the highest velocity of flowing water (usually in floods) is assumed as 3.5m/s and the cross-section area of waterproof rubber seal is $0.005m^2$ (radius=0.04m), the flowing water force acting on a waterproof rubber seal or an FBG sensor can be calculated as about 300N based on the following equation:

$$F_D = C_D A_s \rho \frac{V^2}{2} \tag{6-4}$$

where F_D = flowing water force acting on a waterproof rubber seal or an FBG sensor; C_D = coefficient representing the pressure and friction effects, which is related to the Reynolds number, herein is about 1.0 based on the shape of waterproof rubber seal and Reynolds number; A_s = cross-section area of waterproof rubber seal; ρ = water density; and V = flowing water velocity.

Based on the strength design, this 300N of flowing water force requires 0.04m for the width of steel bar and 0.005m for its thickness. However, if assuming 4m river depth after scour, 0.5m interval between two sensors, and still the same cross-section area of waterproof rubber seal, the hydrostatic pressures only results in a force that requires at least another 0.04m increase for the width of steel bar and another 0.005m increase for its thickness. This is obviously unnecessary and uneconomical. In addition, the doubled thickness obviously can weaken the mechanical response (strains) of the steel bar, which may reduce the sensing sensitivity of FBG sensors for scour monitoring.

(2) Design 2

Similar to Design 1, FBG sensors in Design 2 are also arrayed at a certain interval along a single optical fiber in series on a steel bar (A-A and B-B in Figure 6-4). However, there are two major differences in Design 2. Firstly, in order to solve the hydrostatic pressure problem, two channel beams are used to form a hollow structure where the flowing water can pass through the tube (Cross-section in Figure 6-4). By doing this, the hydrostatic pressures on the monitoring system, especially on the steel bar, can be totally ignored because it is self-balanced. Secondly, the steel bar is changed from a supported continuous beam with two fixed joints to a cantilever beam, which is more sensitive to the flowing water pressures and impact forces. Steel protection sticks are added on the channel beams to prevent direct damages to FBG sensors if debris in the flow strikes with excessive impact forces (A-A in Figure 6-4). The detailed sketch of Design 2 is shown in Figure 6-4.

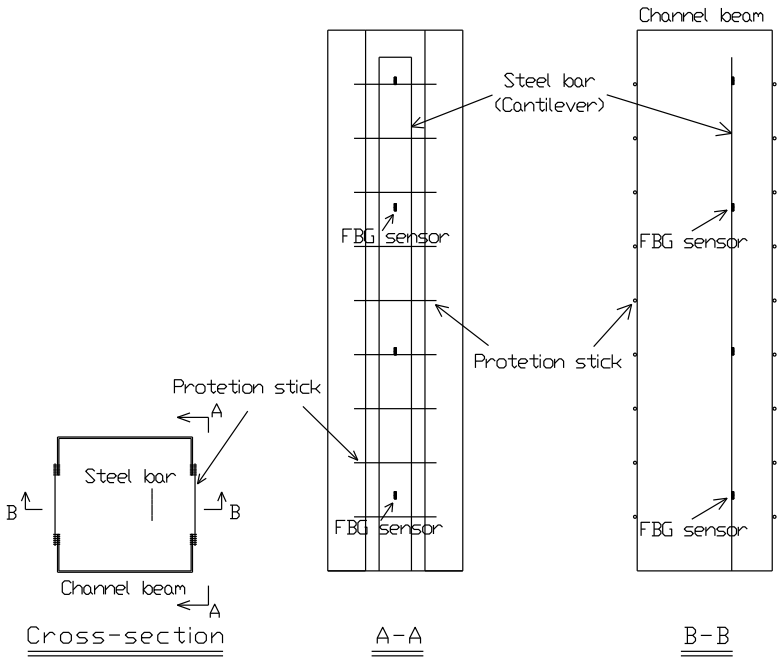

Figure 6-4. Detailed sketch of Design 2 segment

Similar to Design 1, the scour monitoring based on this design is also conducted by sensing the same flow information from the emerging FBG sensors. Along with the scour development, FBG sensors emerge from the riverbed one after the other from the top to bottom of the steel bar. Considering the steel bar as a cantilever, the later emerging FBG sensors, more towards the bottom of the cantilever beam, obviously can sense more response from the flowing water pressures and impact forces (dashed line, i.e., deformed steel bar, in Figure 6-5). This not only shows where the scour develops but also can be regarded as an increasing alert along with the constantly developing scour. Figure 6-6 gives a schematic drawing for different responses of every FBG sensors when the riverbed locally drops due to the scour development (in the ideal

condition). It is easy to understand that the whole process of scour (the actual maximum scour depth and deposition process) can be also monitored and recorded by this design.

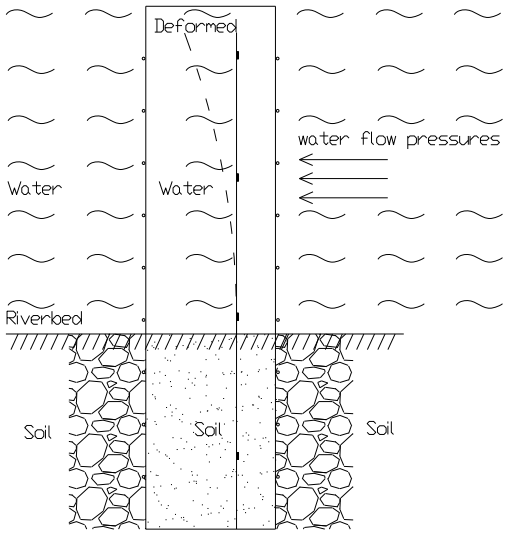

Figure 6-5. Monitoring principle of Design 2

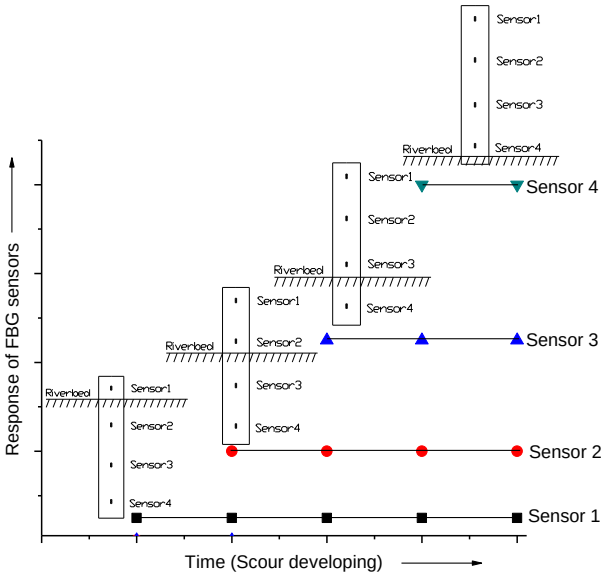

Figure 6-6. Schematic description for the response of each FBG sensor

However, after the preliminary test in the laboratory, it is found that the protection sticks could stop the soil in the hollowed tube from being flowed away; as a result FBG sensor will not function as intended. This would cause a significant influence to the monitoring accuracy on the entire scour process. If simply removing the protection sticks, FBG sensors should be easily damaged in flooding environments.

(3) Design 3 (recommended)

The main monitoring principle and system design in Design 2 are still applicable in Design 3. However, much attention is paid here to the issue that how to assure the soil level inside the tube is exactly the same as the riverbed level outside the tube. To this end, the steel bar is moved near to the open side of the tube in order to make FBG sensors as close as possibly to the soil outside the tube which represents the real riverbed level (B-B and C-C in Figure 6-7). There are no protection sticks in this design any more. Instead, a protection system is directly used on the surface of FBG sensors on the steel bar. Herein, epoxy resin is used as a sensor protection to fulfill the groove formed by two pieces of steel angles attached on the steel bar (Figure 6-8). By doing this, FBG sensors can be entirely covered by epoxy resin to prevent direct damages to FBG sensors from the debris in flowing water. The two steel angles themselves can also stop the direct hit to FBG sensors from the debris.

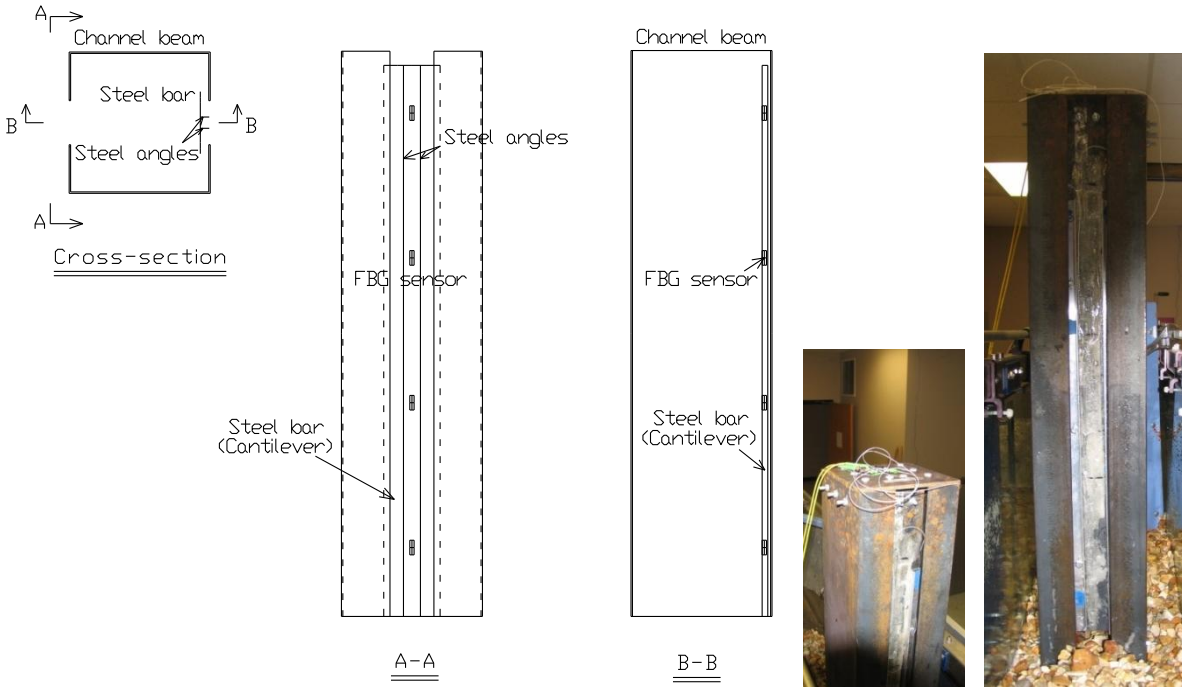

Figure 6-7. Detailed sketch of Design 3

Same as previous designs, the scour monitoring based on this design is conducted by sensing the flowing water information from the emerging FBG sensors. As discussed in Design 2, a cantilever design of the steel bar can reserve all the advantages introduced earlier. The whole process of scour (the actual maximum scour depth and deposition process) can be monitored and recorded in real time under a reliable sensor protection system by this design. The monitoring principle of this design is shown in Figure 6-9.

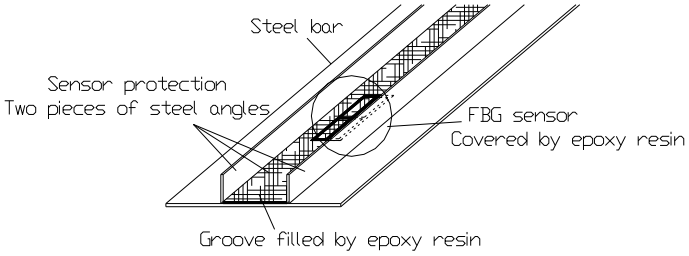

Figure 6-8. Design of sensor protection system

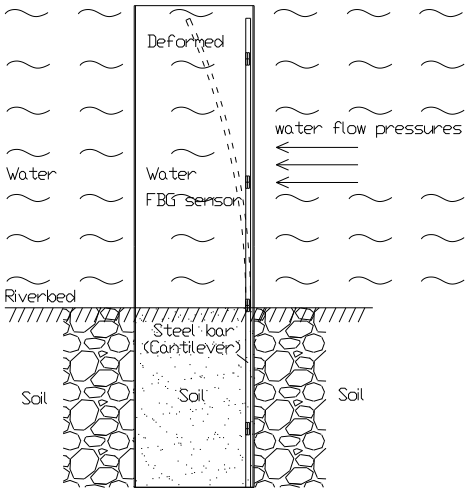

Figure 6-9. Monitoring principle of Design 3

6.3.2 Comparison and recommendation

Table 6-1 shows the comparison results among the three scour monitoring designs introduced earlier. As can be seen from the comparison in Table 6-1, Design 3 has many advantages over the other two designs especially from the viewpoints of sensing sensitivity, sensing accuracy, and sensor protection system. In the present study, Design 3 is highly recommended for the scour monitoring using FBG sensors and verified in a laboratory test.

Table 6-1. Comparison results

Designs	Eliminating unnecessary hydrostatic pressures	Sensing sensitivity for flowing water	Sensing accuracy for riverbed level	Showing increasing alert when scour develops	Monitoring whole process of scour	Protecting FBG sensors
Design 1	NO	NO	YES	NO	YES	YES
Design 2	YES	YES	NO	YES	YES	NO
Design 3	YES	YES	YES	YES	YES	YES

6.4 Experimental setup

6.4.1 Instrumentation manufacture

Usually at least 4m depth below riverbed needs to be monitored for the purpose of scour detection. It is inconvenient to build the instrument with the whole depth/length all at once. In the present study, the proposed instrument is manufactured as several 1m-depth-segments. Each segment has a complete scour monitoring system with FBG sensors introduced in Design 3. Each segment is assembled by several steel components using screws (which are more flexible than using weld) (Figure 6-10). Through connecting every segment in field, the monitoring instrument with any required depth/length can be easily installed for a specific bridge (Figure 6-10).

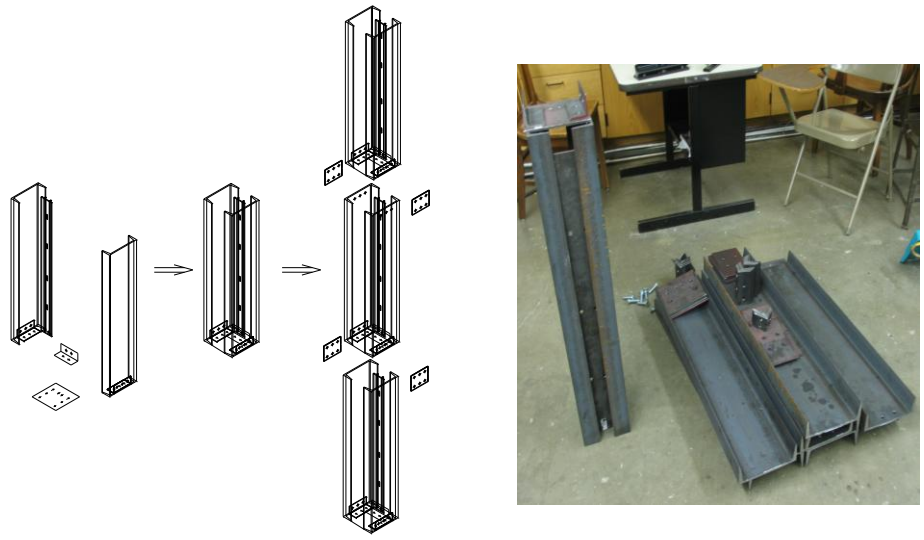

Figure 6-10. Instrumentation assembling

Based on the recommended design of Design 3, installation of FBG sensors and building their protection system is another important process in the instrumentation manufacture. Figure 6-11 demonstrates this process in details. Herein, FBG sensors are manufactured by T&S Communication. Ltd (Bandwith@3dB: <0.3, Min. SLSR: > 15dB, Min. Reflectivity: >90%) and an arc fusion splicer (FSM-50S) manufactured by Fujikura Ltd are used to connect FBG sensors in series with connection protection.

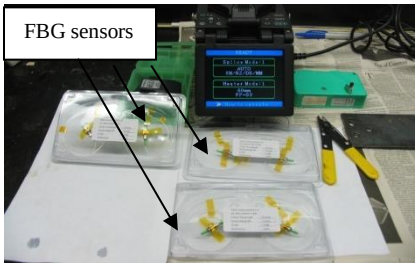

Step1 Sensor preparation

Step 2 Sensor connection

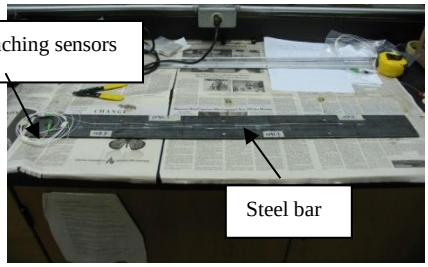

Step 3 Sensor attachment (on steel bar)

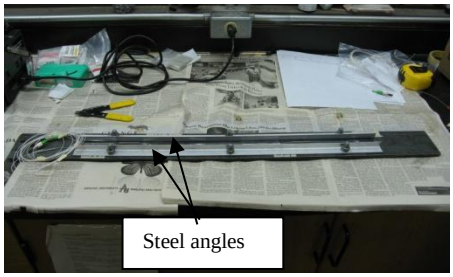

Step 4 Sensor protection (steel angles)

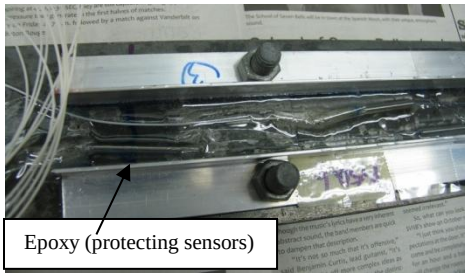

Step 5 Sensor protection (epoxy)

Figure 6-11. Installation of FBG sensors and their protection system

6.4.2 Experiment design

The experiments are conducted in a 10 m-long, 0.4 m-wide and 0.65 m-deep flume with glass sidewalls at Louisiana State University, which is shown in the left hand of Figure 6-12. The scour monitoring instrument is placed in the middle of the flume paved by sands and gravels with "riverbed" elevation of around 0.5m. The prescribed discharge and its corresponding depth for each experimental case are controlled by adjusting the inlet valve and tailgate in the flume. Three sensors, each sensor with a desired wavelength, are mounted on the surface of a cantilevered steel bar and arranged in series along one single optical fiber. These three sensors, namely sensors 1, 2, and 3, are mounted at 55.5cm, 30.5cm, and 5.5cm away from the bottom of the cantilevered steel bar partially submerged with the largest flowing water level of 60cm in the experiment, see the right hand of Figure 6-12. The scour at riverbed can be simulated by washing away the sands and gravels through the flowing water in this experiment setup. There are three runs, namely cases 1, 2, and 3, with different flowing water velocities and different discharge processes in this experiment. When the running water flows towards the cantilevered steel bar in these cases, a deformation strain is generated by the bending moments and flowing water impact forces. If FBG sensors are buried below the riverbed surface, there is no or small response for FBG sensors. Once FBG sensors emerge from the riverbed due to the developing scour, the

scour depth can be directly detected from the sensor responses, the corresponding varying wavelengths, and the sensor positions.

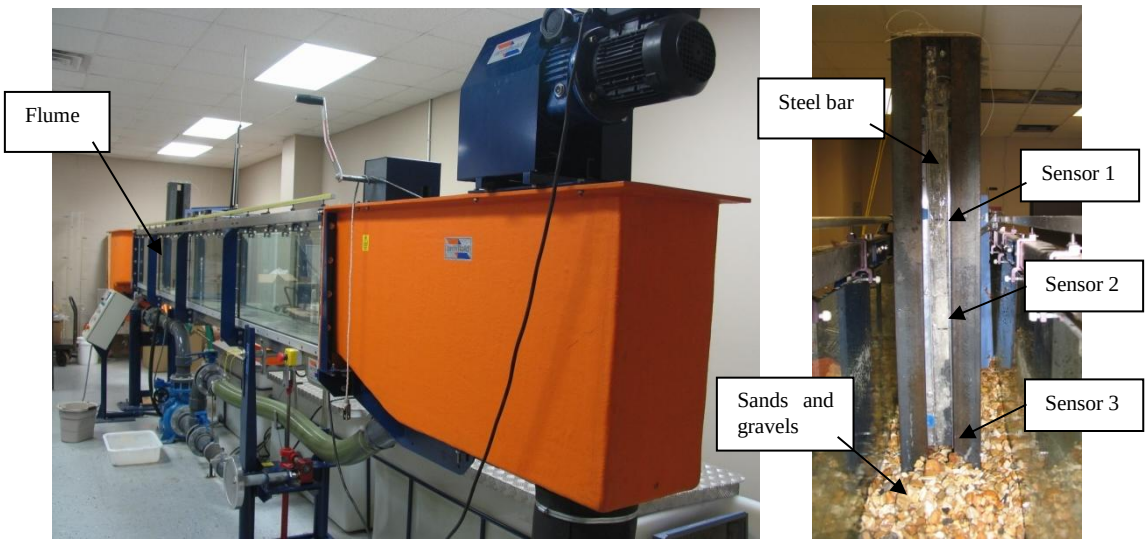

Figure 6-12. Water flume and experimental setup

6.5 Experimental results and data analysis

As mentioned earlier, there are three runs, namely cases 1, 2, and 3, with different flowing water velocities and different discharge processes in this experiment. In all cases, the temperature influence to FBG sensors is ignored.

6.5.1 Experimental results and data analysis for case 1

In this case, the flowing water velocity is around 0.65 m/s, half limit discharge velocity of this flume. From the experimental results of case 1 (Figure 6-13), the local scour depth can be observed directly from the different responses of FBG sensors. Since sensor 1 has exposed to water flow, it picks up information due to flow water pressure and impact and the measurement is relatively constant. As the running water eroding the sands and gravels, as presented in Figure 6-13, sensor 2 finally emerges from the riverbed at the time of 60s and the corresponding wavelength shift increases very quickly thereafter. Later on until sensor 2 totally comes out at the time of 65s, its wavelength shift becomes relatively stable again, but clearly greater than before. Among these FBG sensors, sensor 2 shows the largest wavelength shift, representing the largest bending moment in the steel bar, since only sensor 2 emerges from the riverbed surface. Accordingly it can be seen that scour has already developed to the location of sensor 2. Since only half limit discharge velocity of this flume is applied in this case, sensor 3 does not emerge from the riverbed surface and it only takes reading due to temperature variations and noises. During the experiment, sin-wave-like noises are also detected and possibly induced by the vibration of the cantilevered steel bar. This vibration may be correlated with the motions of sands, gravels (transported particles), and flowing water (fluid turbulence), especially at the emerging

stage of the sensor. It can be concluded that by identifying the emerging sensor locations, the specific scour depth can be successfully monitored.

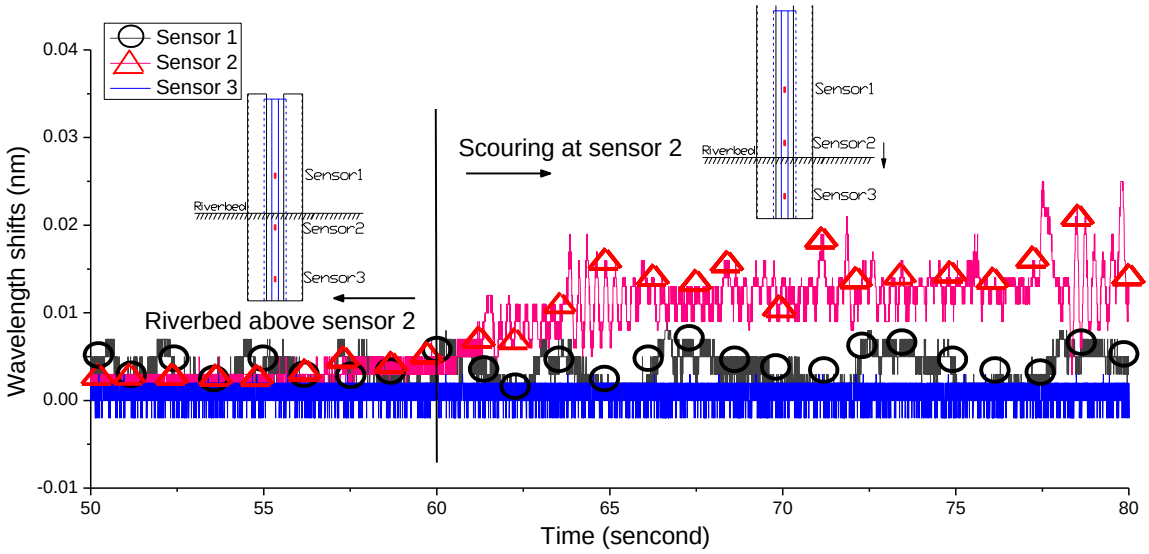

Figure 6-13. Experimental results of case 1

6.5.2 Experimental results and data analysis for case 2

Considering different flowing water velocities, a full discharge velocity of this flume is applied, which is around 1.3 m/s, in case 2. From the experimental results of case 2 (Figure 6-14), the process of increase of local scour depth can be observed from an in-sequence response of more than one FBG sensors. As case 2 experiment starts, the given constant discharge is released at the upstream end of the flume. When the running water arrives and makes contact with the cantilevered steel bar sensor 1 responds firstly, as shown in Figure 6-14. When sensor 2 starts to emerge from the riverbed at the time of 20s, it is obvious that the reading of the wavelength shift changes significantly until it totally emerges. After the time of 30s, the reading of sensor 2 is approximately constant because the water level already remains constant. The variation of the reading may be attributed to the presence of particle motion of sands and gravels and fluid turbulence induced by the flow velocity field. At this time, almost no reading is obtained from sensor 3 because it is still buried in the soil under the riverbed.

With sands and gravels continuously washed away (in this case, the flowing water velocity is much higher than in case 1), as illustrated in Figure 6-14, sensor 3 begins to emerge by the running water in the scouring process at the time of 40s, 20s later than the sensor 2 emerging. Due to sensor 3's location at the bottom of the tube, the corresponding bending of the steel bar caused by running water should be larger than other positions. Accordingly, the response of sensor 3 is obviously much greater than the other sensors. Then, during a very short period (about 10s), the highest wavelength shift of sensor 3 is reached and later on keeps constant after the time of 50s. This shows the scour has already developed to the bottom position of the tube, which also successfully reveals the scour depth from the sensor reading. Thereafter,

the readings from all the sensors remain constant, with some sin-wave-like noises, until the end of experiment. It can be concluded that by the proposed instrumentation design the scour development can be successfully monitored in real time.

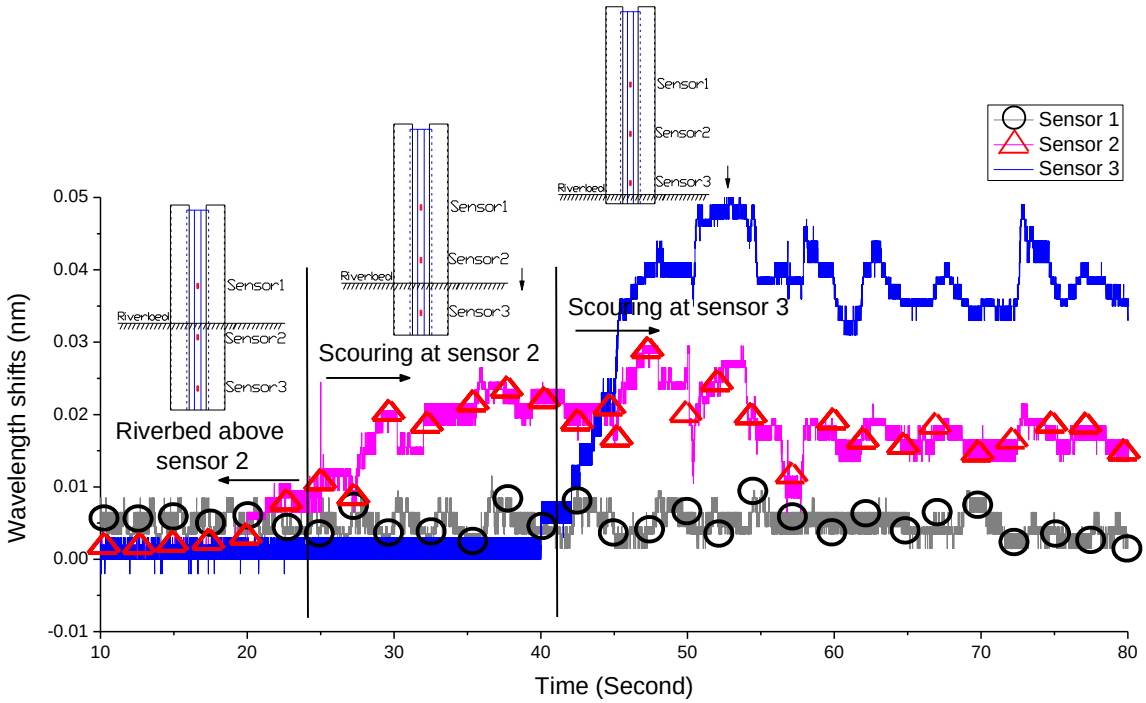

Figure 6-14. Experimental results of case 2

6.5.3 Experimental results and data analysis for case 3

To investigate the processes of both scour and deposition on the riverbed, the experimental test of case 3 is conducted. In case 3, only the result from sensor 2 is shown in Figure 6-15 for a clear demonstration. With the same experimental setup as previous cases, sensor 2 is buried under the riverbed at the beginning of the experiment. The experiment starts by releasing the given discharge from the upstream end of the flume. As the running water level rises gradually, the washed-away sands and gravels indicate that the scour is developing. After the time of 25s in Figure 6-15, sensor 2 emerges and senses the bending strain which is generated by the flowing water acting on the cantilevered steel bar. This developing scour is directly reflected by the wavelength shifts of sensor 2 and lasts until the time of 50s. After the time of 50s, scour stops temporarily. Then, sensor 2 is buried again by the refilled sands and gravels and the reading of sensor 2 consequently decreases and remains in low values until the time of 70s. To stimulate this deposition (refilling) process, extra sands and gravels are poured directly near the steel tube (i.e., the scour monitoring instrument) after the time of 50s and meanwhile the discharge velocity decreases to keep the deposition status. After the time of 70s, the refilling process ends and scour develops again. During this period, the discharge velocity goes up and the running water begins to re-erode the riverbed. As a result, the sensor 2 emerges again from the riverbed and the reading of sensor 2 increases again which is similar to the initial increasing.

It is clear to see that the refilling process can be entirely monitored using this proposed instrumentation design and the deposition height can be also determined by the emerging sensor positions.

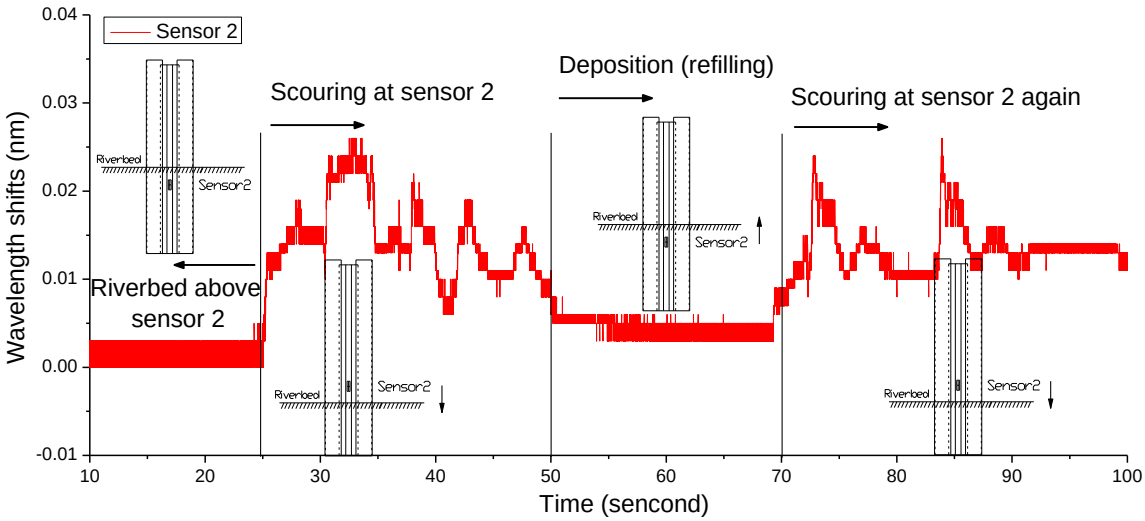

Figure 6-15. Experimental results of case 3

Based on the three cases of experiments, apparently, the proposed scour monitoring system using FBG sensors is capable of measuring the maximum scour depth and the whole process of scour development including soil deposition. Using the same monitoring principle, the deposition height can be also detected and monitored.

6.6 Conclusion

In order to measure and monitor scour depth variations in real time including deposition (refilling) process, three designs for a scour monitoring system using FBG sensors are discussed in the present study. Based on a comparative study, the third one is highly recommended and its manufacture for developing a real instrument is also introduced, which can fully utilize all the advantages of FBG sensors in a scour monitoring. The basic idea of the recommended scour monitoring system is to sense the scour depth variations and deposition process by identifying the locations of emerging FBG sensors from the riverbed. A reliable sensor protection system is meanwhile designed for FBG sensors in harsh environments, especially in floods. Finally, a verification test using a flume is carried out in the laboratory and three experimental runs are conducted to demonstrate the capability of FBG sensors and applicability of the recommended scour monitoring system and instrumentation. It can be concluded that the recommended scour monitoring system using FBG sensors is capable of measuring the maximum scour depth, entire process of scour development, and deposition height due to the refilling process. The advantages over other conventional scour monitoring systems are proven to be obvious. It should be noted that the purpose of the entire instrumentation design is not only just for the bridge scour monitoring using FBG sensors, but also for applying FBG sensors more effective and efficient in

other harsh environments. A field bridge has been selected in the State of Louisiana and the long term stability for this scour monitoring system will be further conducted.

Acknowledgement

The investigators are thankful to Federal Highway Administration and Louisiana Transportation Research Center (LTRC) for funding this project. The contents presented reflect only the views of the writers who are responsible for the facts and the accuracy of the data presented herein. We would like to also express thankfulness to those who provided help during the development of these initial tasks of this research program. Special thanks go to the project manager Mr. Walid Alaywan, La DOTD.

6.7 References

Baglio, S., Faraci, C., Foti, E., and Musumeci, R. (2000). "Stereo vision for noninvasive dynamic measurements of the scour process around a circular cylinder in an oscillating flow." OCEANS 2000 MTS/IEEE Conference and Exhibition vol 2, 987-992.

Cuevas, K. J., Buchanan, M. V., and Moss, D. (2002) "Utilizing side scan sonar as an artificial reef management tool." OCEANS'02 MTS/IEEE vol 1, 136-140.

Casas, J. R., and Cruz, P. J. S. (2003). "Fiber optic sensors for bridge monitoring." Journal of Bridge Engineering, 8(6), 362-373.

Deng, L., and Cai, C. S. (2007). "Applications of fiber optic sensors in civil engineering." Structural Engineering & Mechanics, 25(5), 577-596.

De Falco, F. and Mele, R. (2002). "The monitoring of bridges for scour by sonar and sedimetri." NDT & E International, 35(2), 117-123.

Dowding, C. H. and Pierce, C. E. (1994). "Use of time domain reflectometer to detect bridge scour and monitor pier movement." Proc. Symp. and Workshop on Time Domain Reflectometry in Envir., Infrastruct. and Mining Application, 579-587.

Hunt, B. E. (2005). "Scour monitoring programs for bridge health." Proceedings of 6th International Bridge Engineering Conference: Reliability, Security, and Sustainability in Bridge Engineering, Transportation Research Board, Boston, Massachusetts, 531-536.

Idriss, R.L., Kodindouma, M.B., Kersey, A.D. and Davis, M.A. (1998). "Multiplexed Bragg grating optical fiber sensors for damage evaluation in highway bridges."Smart Materials and Structures, 7(2), 209-216.

Kattell, J., and Eriksson, M. (1998). "Bridge Scour Evaluation: Screening, Analysis, and Countermeasures." Pub. Rep. No. 9877, USDA Forest Service, Washington, D.C.

Kersey, A. D., Davis, M. A., and Patrick, H. J. (1997). "Fiber Grating Sensor." Journal of Lightwave Technology, 15(8), 1442-1463.

Lu, J.-Y., Hong, J.-H., Su, C.-C., Wang, C.-Y., and Lai, J.-S. (2008). "Field measurements and simulation of bridge scour depth variation during floods." Journal of Hydraulic Engineering, 134(6), 810-821.

Lin, Y. B., Chen, J. C., Chang, K. C., Chern, J. C., and Lai, J. S. (2005). "Real-time monitoring of local scour by using fiber Bragg grating sensors." Smart Materials and Structures, 14(4), 664–670.

Lagasse, P. F., Richardson, E. V., Schall, J. D., and Price, G. R. (1997). "Instrumentation for measuring scour at bridge piers and abutments." National Cooperative Highway Research Program (NCHRP) Report No. 396, Transportation Research Board, Washington, D.C.

Mason, R. R. and Shepard, D. M. (1994). "Field performance of an acoustic scour-depth monitoring system." Proc. Fundamentals and Advancements in Hydr. Measurements and Experimentation, ASCE, 366-375.

Miridonov, S. V., Shlyagin, M. G., and Tentori-Santa-Cruz, D. (1999). "Digital demodulation of a twin-grating fiber optic sensor." Fiber Optic and Laser Sensors and Applications; Including Distributed and Multiplexed Fiber Optic Sensors VII, Proceedings SPIE, 3541, 33-40.

Millard, S. G., Bungey, J. H., Thomas, C., Soutsos, M. N., Shaw, M. R., and Patterson, A. (1998). "Assessing bridge pier scour by radar." NDT & E International, 31(4), 251-258.

Park, I., Lee, J., and Cho, W. (2004). "Assessment of bridge scour and riverbed variation by a ground penetrating radar." Proceedings of 10th International Conference on Ground Penetrating Radar, GPR 2004, Delft, Netherlands, 411-414.

Parker, G. W., Bratton, L., and Armstrong, D. S. (1997). "Stream stability and scour assessments at bridges in Massachusetts." U.S. Geological Survey Open File Report No. 97-588 (CD-ROM), Massachusetts Highway Dept. Bridge Section, Marlborough, Mass., 53.

Shirhole, A. M., and Holt, R. C. (1991). "Planning for a comprehensive bridge safety program." Transportation Research Record No. 1290, Transportation Research Board, National Research Council, Washington, D.C.

Tennyson, R.C., Coroy, T., Duck, G., Manuelpillai, G., Mulvihill, P., Cooper, David J.F., Smith, P.W.E., Mufti, A.A. and Jalali, S.J. (2000). "Fiber optic sensors in civil engineering structures."Canadian Journal of Civil Engineering., 27(5), 880-889.

Xu, M. G., Dong, L., Reekie, L., Tucknott, J. A., and Cruz, J. L. (1995). "Temperature-independent strain sensor using a chirped Bragg grating in a tapered optical fiber." Electronics Letters, 31(10), 823-825.

Yu, X., and Yu, X. (2007). “Algorithm for time domain reflectometry bridge scour measurement system.” Proceedings of 7th International Symposium on Field Measurements in Geomechanics (FMGM), Boston, Massachusetts, 1-10.

Yu, X., and Zabilansky, L. J. (2006). “Time domain reflectometry for automatic bridge scour monitoring.” Proceedings of Sessions of GeoShanghai (Geotechnical Special Publication), Shanghai, China, 149, 152-159.

Yankielun, N. E. and Zabilansky, L. (1999). “Laboratory investigation of time-domain reflectometry system for monitoring bridge scour.” Journal of Hydraulic Engineering, 125(12), 1279-1284.

CHAPTER 7. SCOUR EFFECT ON BRIDGE AND VEHICLE RESPONSE UNDER BRIDGE-VEHICLE-WAVE INTERACTION

7.1 Introduction

Bridge scour is a significant issue in the United States. In the last 30 years, more than 1,000 bridges have collapsed and approximately 60% failures of them are related to the foundation scour (Shirhole and Holt 1991, Lagasse and Richardson 2001). On-going screening and evaluation of the vulnerability of the nation's highway bridges to scour by different state Departments of Transportation have identified more than 18,000 bridges that are considered as scour-critical and in need of repair or replacement. Furthermore, more than 100,000 bridges over water in the United States have "unknown foundations" (Lagasse et al. 1995), which means that their vulnerability to scour cannot be calculated by normal hydraulic and geotechnical analysis procedures. Therefore, there is an urgent need for innovative, effective, and economical techniques to detect and monitor the foundation scour.

Bridge scour is a very complicated process that involves the interaction between the flow, the erodible riverbed, and the bridge pier or abutment. Deng and Cai (2010) presented a comprehensive review on approaches for modeling and predicting bridge scour. In the past few decades, the previous research mainly focused on studying the scour mechanism by developing numerical models (Melville and Raudkivi 1977; Young et al. 1998; Kassem et al. 2003) as well as laboratory models (Umbrell et al. 1998; Sheppard and William 2006). Based on these studies, different methods to predict bridge scour using the available information prior to or during flood events were proposed including empirical equations (Laursen and Toch 1956; Breusers et al. 1977; Melville and Sutherland 1988; Lim 1997; Heza et al. 2007), and neural network method (Lee et al. 2007; Mohammad et al. 2009) to establish a relationship between the scour depth and various factors.

A more direct approach is to investigate the scour consequences, i.e., the structural response and feature changes of the bridge due to scour. However, till now few studies have been carried out on this topic. Zhang et al. (2005) using HHT-based approach on acceleration recordings from controlled field vibration test of piles in intact, minor-, and severe-damage states singled out some natural frequencies of the structure. Samizo et al. (2007) proposed a method to define the natural frequencies of bridges using long-term microtremor measurements made on existing bridge piers, and concluded that the natural frequencies of bridge piers decline with decreasing foundation depth during scour. Ruocci and co-workers (2009, 2010 and 2011) built a scaled experimental model of a two-span masonry arch bridge to investigate the effect of the central pile settlement due to riverbank erosion and to identify the most damage sensitive structural symptoms of pier erosion. Han et al. (2010) studied the influence of scour on the seismic performance of foundations through several elasto-plastic static pushover analyses. Lin et al. (2010) studied scour effects on the response of laterally loaded piles considering the stress history of the remaining sand. Foti and Sabia (2011) performed numerical simulations to assess the sensibility of the overall dynamic response of the system to the foundation scour. Loh et al.

(2011) constructed an experiment in the hydraulic lab to study the scour-depth variation in relating to the dynamic features of the bridge structure during scouring process.

The present study aims to investigate the scour effect on the response of bridge substructure, superstructure and even the vehicle traveling on the bridge. The soil and scour model are developed, and the scour effect on a single pile and a pile group is analyzed first. As one of the major loads, the water current and wave loads are calculated for each bent based on the Morison equation. The interaction between the bridge, vehicle and water are then analyzed to obtain the responses and study the scour effect.

7.2 Vehicle-bridge-wave interaction

7.2.1 Equation of motion

The model of vehicles used as response receivers is considered as a SDOF vehicle model, while vehicles of the traffic flow serving as random excitation, are modeled as a combination of several rigid bodies connected with several axle mass blocks, springs, and damping devices (Cai and Chen 2004). The suspension systems and elasticity of tires are idealized as liner elastic spring elements and dashpots. The bridge deck and the moving tires are assumed to be point-contact. The axle number may vary from two to five. In the present study, a two-axle vehicle model (Shi 2006 and Deng 2009) is used to establish the equation of motion of the vehicle as well as the vehicle-bridge coupling equations in the following sections. The equation of motion for a bridge and vehicle with discretized finite elements can be written as follows:

$$\begin{aligned} [M_b]\{\ddot{d}_b\}+[C_b]\{\dot{d}_b\}+[K_b]\{d_b\} &= \{F_b{}^c\}+\{F_b{}^w\} \quad (a) \\ [M_v]\{\ddot{d}_v\}+[C_v]\{\dot{d}_v\}+[K_v]\{d_v\} &= \{F_v{}^c\}+\{F_G{}^G\} \quad (b) \end{aligned} \tag{7-1}$$

where $[M_b]$, $[C_b]$, and $[K_b]$ are the mass, damping, and stiffness matrices of the bridge, respectively; $\{d_b\}$ is the displacement vectors for all DOFs of the bridge, respectively; $\{\dot{d}_b\}$ and $\{\ddot{d}_b\}$ are the first and second derivative of $\{d_b\}$ with respect to time, respectively; The terms with *v* as the subscript is for vehicles. $\{F_b{}^c\}$ and $\{F_v{}^c\}$ are contact force between vehicle and bridge; $\{F_G{}^G\}$ is the self-weight of vehicles; and $\{F_b{}^w\}$ is the wave force on the bridge foundation.

Road Surface Condition

The road surface condition is an important factor that affects the dynamic responses of both the bridge and vehicles. A road surface profile is usually assumed to be a zero-mean stationary Gaussian random process and can be generated through an inverse Fourier transformation based on a power spectral density (PSD) function (Dodds and Robson 1973) as:

$$r(X)=\sum_{k=1}^{N}\sqrt{2\varphi(n_k)\Delta n}\cos(2\pi n_k X+\theta_k) \tag{7-2}$$

where θ_k is the random phase angle uniformly distributed from 0 to 2π; $\varphi()$ is the PSD function (m^3/cycle) for the road surface elevation; and n_k is the wave number (cycle/m). In this study, the following PSD function (Huang and Wang 1992) has been used:

$$\varphi(n) = \varphi(n_0)(\frac{n}{n_0})^{-2} \qquad (n_1 < n < n_2) \tag{7-3}$$

where n is the spatial frequency (cycle/m); n_0 is the discontinuity frequency of $1/2\pi$ (cycle/m); $\varphi(n_0)$ is the roughness coefficient (m^3/cycle) whose value is chosen depending on the road condition; and n_1 and n_2 are the lower and upper cut-off frequencies.

7.2.2 Wave force

Wave forces can be separated into four categories (FEMA 2011):

- Non-breaking waves: can usually be computed as hydrostatic forces against walls and hydrodynamic forces against piles.
- Breaking waves: short duration but large magnitude forces against walls and piles.
- Broken waves: similar to hydrodynamic forces caused by flowing or surging water.
- Uplift: often caused by wave runup, deflection, or peaking against the underside of horizontal surfaces.

Though the forces from breaking waves of these four categories are the largest ones and produce the most severe loads (Irschik and Sparboom 2004), forces from non-breaking waves dominate in the river with small waves. Therefore, non-breaking waves are the main concern in the present study. The force exerted by non-breaking surface waves on a body such as a pile in an unsteady viscous flow can be determined using the Morrison's Equation (Morison et al. 1950), which is made up of two components, namely: an inertia force in phase with the local flow acceleration and a drag force proportional to the square of the instantaneous flow velocity. The Morison's equation is valid for cylinders with ratios of diameter to wave length being less that 0.15. In an oscillatory flow with a flow velocity $U(t)$, the Morison equation gives the inline force parallel to the flow direction (Sumer et al. 2006):

$$F = F_I + F_D = \rho C_M V\dot{U} + \frac{1}{2}\rho C_D AU|U| \tag{7-4}$$

where F_I is the inertia force and F_D is the drag force. U and $\dot{U}$ are the flow velocity and acceleration, respectively. ρ, A and V are the flow density, the cross-sectional area of the pile perpendicular to the flow direction and the volume of the pile, respectively. C_M and C_D are the inertia and drag coefficient, respectively, which depend in general on the Keulegan–Carpenter (KC) number, Reynolds number, and surface roughness.

For instant for a circular cylinder with a diameter D in oscillatory flow, the area per unit cylinder length is A=D and the volume per unit length is $V = \frac{\pi}{4} D^2$. Thus, the total wave force per unit cylinder length is,

$$F = \rho C_m \frac{\pi}{4} D^2 \dot{U} + \frac{1}{2} \rho C_d D U |U| \tag{7-5}$$

Thus, the total force acting on the pile is obtained by integrating Equation (7-5) from the water bottom level, -d, to the wave elevation η, such that,

$$F_{total} = \int_{-d}^{\eta} \left(\rho C_m \frac{\pi}{4} D^2 \dot{U} \right) dz + \int_{-d}^{\eta} \left(\frac{1}{2} \rho C_d D U |U| \right) dz \tag{7-6}$$

Similarly, the total bending moment resulting from the wave force on the pile bottom can be derived as,

$$M_{total} = \int_{-d}^{\eta} F z dz = \int_{-d}^{\eta} \left(\rho C_m \frac{\pi}{4} D^2 \dot{U} \right) z dz + \int_{-d}^{\eta} \left(\frac{1}{2} \rho C_d D U |U| \right) z dz \tag{7-7}$$

Subsequently, the acting position of the total wave force on the pile can be obtained through dividing the moment by the total force.

7.2.3 Assemble of the vehicle-bridge-wave system

In terms of finite element method and point-contact assumption, the interaction forces between the vehicle and the bridge deck may not apply at element nodes of the bridge as the vehicle passes over it. Therefore, the interaction forces in Equation (7-1), $\{F_b^c\}$ and $\{F_v^c\}$, need to be transformed into equivalent nodal forces $\{F_b^{cN}\}$ in the finite element analysis. This can be done using the virtual work principle, which can be expressed as:

$$\{d_{b\_nodal}\}^T \{F_b^{cN}\} = \{d_{b\_contact}\}^T \{F_b^c\} = ([N_b]\{d_{b\_nodal}\})^T \{F_b^c\} = \{d_{b\_nodal}\}^T ([N_b]^T \{F_b^c\}) \tag{7-8}$$

$$\{F_b^{cN}\} = [N_b]^T \{F_b^c\} \tag{7-9}$$

where $\{d_{b\_nodal}\}$ is the displacements for bridge nodes of the element in contact; $\{d_{b\_contact}\}$ is the displacement of the bridge-vehicle contact point; and $[N_b]$ is the shape function of bridge element in contact.

Similarly, the total wave force on the foundation, $\{F_b^w\}$, is distributed on the nodes around the acting point using the virtual work principle:

$$\{F_b^{wN}\} = [N_b^w]^T \{F_b^w\} \tag{7-10}$$

where $\{F_b^{wN}\}$ is equivalent nodal forces on bridge foundation; and $[N_b^w]$ is the shape function.

Finally, the equation of motion of the VBC system can be assembled and rewritten in the matrix form as below (Shi 2006 and Deng 2009):

$$\begin{bmatrix} M_b & \\ & M_v^N \end{bmatrix}\begin{Bmatrix} \ddot{d}_b \\ \ddot{d}_v \end{Bmatrix}+\begin{bmatrix} C_b+C_{b-b} & -C_{b-v} \\ -C_{v-b} & C_v^N \end{bmatrix}\begin{Bmatrix} \dot{d}_b \\ \dot{d}_v \end{Bmatrix}+\begin{bmatrix} K_b+K_{b-vb}+K_{b-cb} & -K_{b-v} \\ -K_{v-b}-K_{v-cb} & K_v^N \end{bmatrix}\begin{Bmatrix} d_b \\ d_v \end{Bmatrix}=\begin{Bmatrix} -F_{b-r}-F_{b-cr}-F_{b-w} \\ F_{v-r}+F_{v-cr}-F_G^N \end{Bmatrix} \tag{7-11}$$

The additional terms $C_{b-b}, C_{b-v}, C_{v-b}, K_{b-vb}, K_{b-cb}, K_{b-v}, K_{v-b}, K_{v-cb}, F_{b-r}, F_{b-cr}, F_{v-r}$, and F_{v-cr} in Equation (7-11) are due to coupling effect between the bridge and vehicles. When a vehicle travels on the bridge, the position of the contact point changes with time, which means the road roughness $r(x)$ at the contact point and the shape function are both time-dependent terms, indicating that all the additional terms in Equation (7-11) are time-dependent terms. With the modal superposition technique, Equation (7-11) can be further rewritten as follows:

$$\begin{bmatrix} I & \\ & M_v \end{bmatrix}\begin{Bmatrix} \ddot{\xi}_b \\ \ddot{d}_v \end{Bmatrix}+\begin{bmatrix} 2\omega_i\eta_i I+\Phi_b{}^T C_{b-b}\Phi_b & -\Phi_b{}^T C_{b-v} \\ -C_{v-b}\Phi_b & C_v^N \end{bmatrix}\begin{Bmatrix} \dot{\xi}_b \\ \dot{d}_v \end{Bmatrix} \tag{7-12}$$
$$+\begin{bmatrix} \omega_i{}^2 I+\Phi_b{}^T(K_{b-vb}+K_{b-cb})\Phi_b & -\Phi_b{}^T K_{b-v} \\ -(K_{v-b}+K_{v-cb})\Phi_b & K_v^N \end{bmatrix}\begin{Bmatrix} \xi_b \\ d_v \end{Bmatrix}=\begin{Bmatrix} -\Phi_b{}^T(F_{b-r}+F_{b-cr}+F_{b-w}) \\ F_{v-r}+F_{v-cr}-F_G^N \end{Bmatrix}$$

where the vehicle-bridge coupled system contains only the modal properties of the bridge and the physical parameters of the vehicles.

7.3 Bridge information

7.3.1 Superstructure

The bridge is located in LaSalle Parish, Louisiana across Little River and carries the westbound and eastbound lanes of LA 8. The bridge was built in 1981 with a length of 562'-1 ¼" (171.330m), as shown in Figure 7-1. It consists of two 4-span units (4×70ft (21.336m)) that each contains a reinforced concrete deck and continuous Type III precast prestressed girders supported by concrete pile bents with a reinforced concrete bent cap. The clear roadway width is 40ft (12.192m). The bents are constructed perpendicular to the roadway centerline.

Figure 7-1. Bridge layout

The bridge includes two types of bents: Bent type I (bent 2, 4, 5, 7 and 8) consists of five 24"-square precast prestressed concrete piles; Bent type II (bent 3 and 6) are double row bents with six 24"-square concrete piles, as shown in Figure 7-2. The outside piles of Bent type I are inclined with a slop of 1.5/12, and that of Bent type II are inclined in both longitudinal and lateral direction with the same slop.

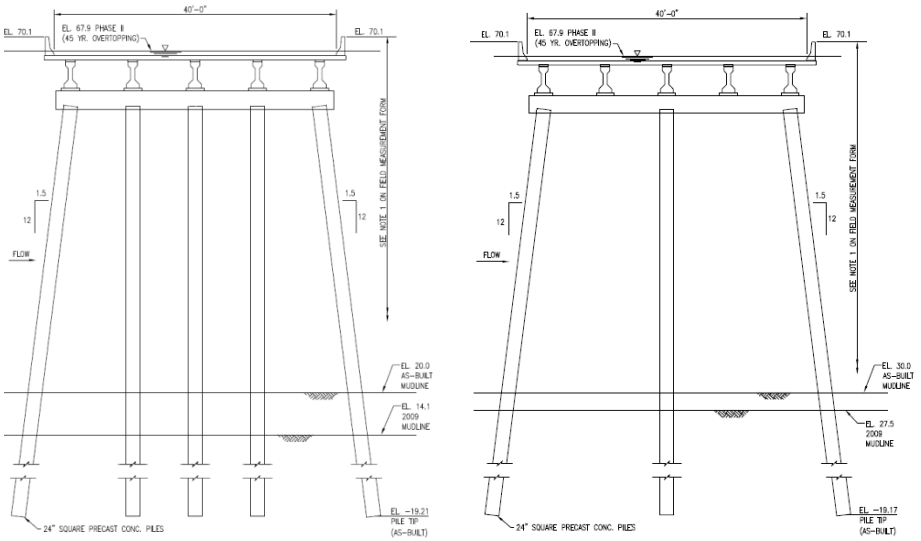

(a) Bent type I (b) Bent type II

Figure 7-2. Bent types

7.3.2 Soil properties

Based on the boring information at the bridge site, the 18 layers of soil numbered from the top to the bottom can be treated as four categories: the cohesionless sand (layer 1~4), cohesive clay 1 (layer 5~8), cohesive clay2 (layer 9~15) and cohesionless sand (layer 16~18). The lowest elevation of the pile is in the third category. Therefore, only the top three soil categories are considered for the bridge and are named as soil layer 1 (original layer 1~4), layer 2 (original layer 5~8), and layer 3 (original layer 9~15). The soil parameters of each layer are listed in Table 7-1.

7.3.3 Foundation scour history

The Little River in the vicinity of the bridge site is classified as a perennial, meandering river of medium size (10-500ft) (LADOTD 2010). The streambed material is primarily silt and gravel. The channel is substantially contracted at the bridge site. The flow area at the bridge section is reduced to 59% of the approach section flow area, and the channel section width at the bridge site is narrowed to 72% of the approach channel width. This contraction causes increased stream velocities at flood stages and results in high rates of scour. The flow capacity of the bridge section at the high water elevation of 61.0ft is close to the 10 year flow event (61,585 cfs). The estimated overtopping flow has an approximate frequency of 45 years, and the hydraulic data for the 45 year overtopping flood event is used in the present study.

Table 7-1. Soil parameters

Soil layer		Layer 1	Layer 2	Layer 3
Soil type Soil lateral model		Cohesionless Sand (Reese)	Cohesive Clay (Stiff<Water)	Cohesive Clay (Stiff<Water)
Soil depth	(ft)	36	20	56
Total unit weight	γ(pcf)	115	120	120
Undrained shear strength	Cu(psf)	-	2000	3000
Internal friction angle	φ(degrees)	25	-	-
Major principal strain@50%	ε50	-	0.007	0.005
Poisson's ratio	ν	0.35	0.45	0.45
Subgrade modulus	K (pci)	25	266	399
Young's modulus	E(ksi)	0.4	3	4.7
Shear modulus	G (ksi)	0.2	1	1.6

The ground lines of the bridge at different stages: as-built, site visit in year 2000, site visit in year 2009 (current) and the predicted 100 year ground elevation are listed in Table 7-2. The mudline information shows that Bent 2 (on the inner side of the channel) and Bent 7 (on the outer side of the channel bend) have experienced the most of the net degradation, approximately 14.5ft (4.42m) and 15.3ft (4.66m) in 30 years, respectively. Figure 7-3 shows the ground line changing with time.

Table 7-2. Bridge bent information

Bent No.	Station (ft)	As-built ground Elev. 1979	Ground Elev. 2000	Current Ground Elev. 2009	Mudline Change (ft)	Predicted 100 year scour Elev.	Pile Length (ft)
1	163+15.0	63	62.7	57.5	5.5	62.7	45
2	163+75.0	55	43.6	40.5	14.5	28.5	60
3	164+45.0	30	28.7	22.5	7.5	2.7	80
4	165+15.0	19	16.7	13.3	5.7	-9.3	80
5	165+85.0	20	18.3	14.1	5.9	-7.7	80
6	166+55.0	30	31.8	27.5	2.5	5.8	80
7	167+25.0	56	50.7	40.7	15.3	35.9	80
8	167+95.0	56	57.2	52.5	3.5	49.5	55
9	168+55.0	63	63	58.5	4.5	63	45

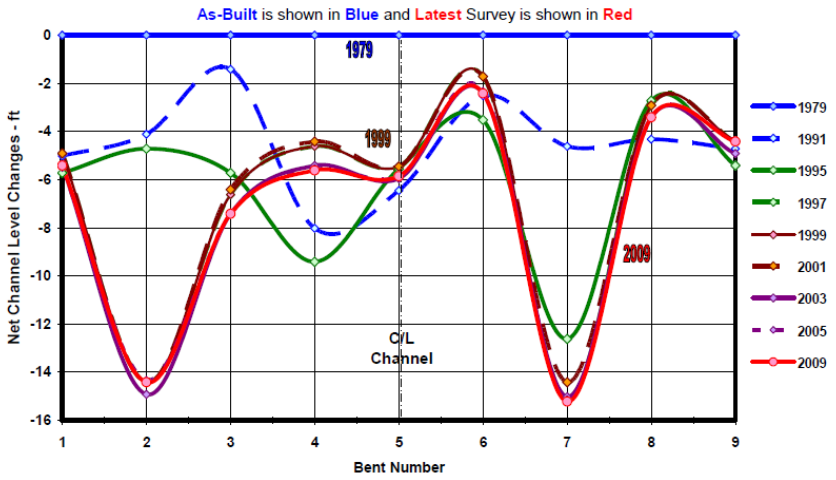

Figure 7-3. Ground line changing with time.

7.4 Scour models and wave loads

7.4.1 Soil model

The soil resistance to the pile movement is modeled using *p-y* curves and t-z curves for lateral and axial loading, respectively (Mostafa and El Naggar 2004). The purpose of the present study is to evaluate scour effect on the lateral capacity of the foundation, thus, only the *p-y* curves is used here. The lateral soil resistance-deflection (p-y) relationships are nonlinear and calculated based on the API (1993) design guidelines for fixed offshore platforms. The *p-y* curves for sand in the absence of more definitive information may be approximated at any specific depth H, by the following expression:

$$P = Ap_u \tanh\left[\frac{kH}{Ap_u} y\right] \tag{7-13}$$

where, A is the factor to account for cyclic or static loading condition; p_u is ultimate bearing capacity at depth H; k is the initial modulus of subgrade reaction and is the function of angle of internal friction, ϕ'. The *p-y* curve is a continuous hyperbolic tangent curve.

The *p-y* curves for soft and stiff clay are also non-linear and need to be calculated by numerical ways. In the present study, the *p-y* curves were computed using the program COM624P (Reese and Wang, 1993) that models a single foundation under lateral loads. COM624P divides the member into a maximum of 300 segments, imposes the loading conditions at the top of the pile and solves the differential equation by the finite differences method for the displacements along the pile. Since the soil is considered non-linear, an iterative approach is taken where the soil modulus is varied. The *p-y* curves are then input into the ANSYS program as the real constants the Combin39 nonlinear spring element to simulate the soil.

As discussed earlier, three layers of soil are considered for the bridge: layer 1 (sand), layer 2 (clay 1) and layer 3 (clay 2). Figure 7-4 (a) ~ (c) show the *p-y* curves of soil in different layers. As for the sand, the *p-y* curve is almost linear in the beginning and the force becomes constant over a certain deflection, while for the clay the force decreases after the soil has a deflection of around 0.5in and becomes a very small value over a certain limit.

It is noted that the force obtained from COM624P is the force per unit length, which should be multiplied by the length of each divided segment to become the real constant of the Combin39 element in ANSYS. Figure 7-4 (d) demonstrates the stiffness (slop of *p-y* curve) of Combin39 elements for soil layer 1 at Bent 6. As listed in Table 7-2, the ground line of Bent 6 in 1979 is 360" and 330" in 2000. The figure shows the linear change of soil stiffness along the pile depth and the stiffness difference due to the 30" scour depth from year 1979 to 2000.

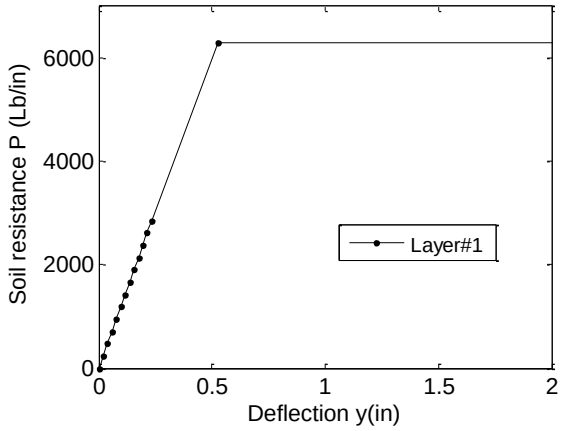

(a) p-y curve of soil layer 1

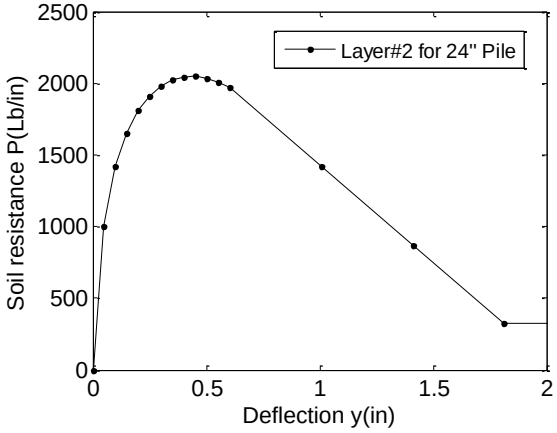

(b) p-y curve of soil layer 2 for 24" pile

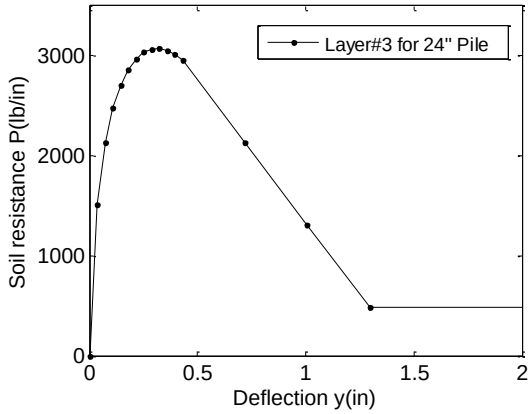

(c) p-y curve of soil layer 3 for 24'' pile

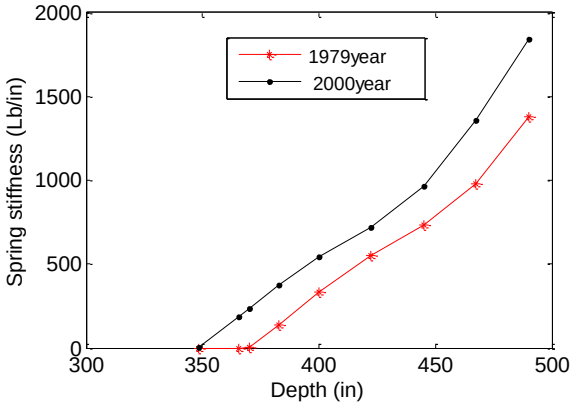

(d) element stiffness for soil layer 1 at Bent6

Figure 7-4. Soil p-y curves

7.4.2 Scour model

The main scour around a pile consists of the local scour and general scour (Xanthakos 1995). The general scour refers to the change of riverbed level and the local scour is due to higher flow velocities and formation of vortices around the pile. Due to the complexity of the local scour and the uncertainty of the empirical formula for calculating the local scour depth, the present study only considers the scour caused by the ground change and assumes that all piles at the same bent have the same scour depth. Therefore, the scour effect is studied based on the change of the scour depth.

Since the soil around the pile is simulated as the Combin39 spring element, the effects of foundation scour are then modeled by removing spring elements. However, after being exposed to the water the stiffness of the underneath soil changes due to stress release after the top soil is scoured. Therefore, the scour process cannot be modeled by simply removing several spring elements. Instead, the present study recalculated the *p-y* curves based on the new ground level.

7.4.3 Wave loads

The Equation (5) ~ (7) are for calculating wave loads on the vertical cylinder. The piles in this study are inclined square piles including two types: inclined in the wave plane such as bents 2~4 and out of the wave plane such as bents 3 and 6.

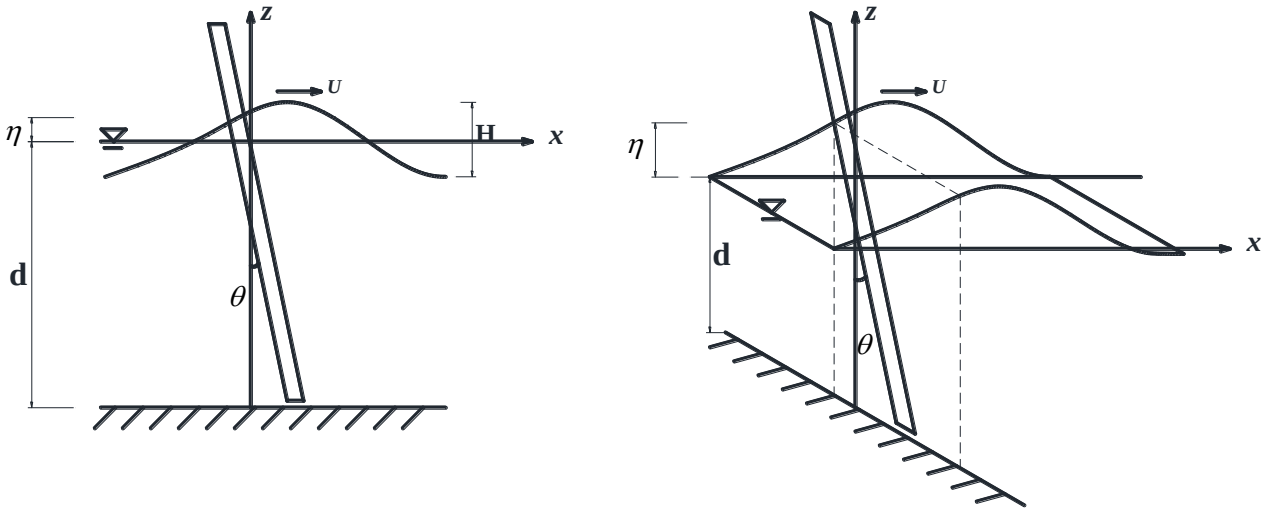

(a) pile in the wave plane (b) pile perpendicular to the wave plane

Figure 7-5. Wave-current force on an inclined square pile

For a square pile with a diameter D and a length d in water is at an angle ɵ within an unsteady inflow. Besides the wave, the flow itself can result in drag force as well. Herein, both the flow and wave loads are considered. The inflow velocity is U_f, and the horizontal and vertical

velocity of the wave is U_x and U_z, respectively. Decompose the velocity into two components: normal to the pile and tangential to the pile. The Morison's equation with respect to the inclined square pile can be expressed in a vector form as (Yao 2009),

$$\vec{F} = \frac{1}{2}\rho C_D D\left|\vec{U}_n\right|\vec{U}_n + \rho C_M D^2 \frac{\partial \vec{U}_n}{\partial t} \tag{7-14}$$

where $\vec{F}$ is the wave force on the inclined pile at the depth z; $\vec{U}_n$ and $\frac{\partial \vec{U}_n}{\partial t}$ are the inflow velocity and acceleration normal to the pile, respectively; $\left|\vec{U}_n\right|$ is the module of $\vec{U}_n$; and C_D and C_M are the drag coefficient and inertia coefficient, respectively. According to the AASHTO (2008), $C_D = 1.4$ for square pile and $C_M = 2.0$.

The three components of the force (F_x, F_y and F_z) are given as a function of velocity components (U_{nx}, U_{ny} and U_{nz}) and acceleration (a_{nx}, a_{ny} and a_{nz}) as,

$$\begin{Bmatrix} F_x \\ F_y \\ F_z \end{Bmatrix} = \frac{1}{2}\rho C_D D\left|U_n\right|\begin{Bmatrix} U_{nx} \\ U_{ny} \\ U_{nz} \end{Bmatrix} + \rho C_M D^2 \begin{Bmatrix} a_{nx} \\ a_{ny} \\ a_{nz} \end{Bmatrix} \tag{7-15}$$

And the normal velocity can be calculated from the coordinate transformation such that,

$$\begin{Bmatrix} U_{nx} \\ U_{ny} \\ U_{nz} \end{Bmatrix} = \begin{bmatrix} 1-C_x^2 & -C_xC_y & -C_xC_z \\ -C_xC_y & 1-C_y^2 & -C_yC_z \\ -C_xC_z & -C_yC_z & 1-C_z^2 \end{bmatrix} \begin{Bmatrix} U_f + U_x \\ U_y \\ U_z \end{Bmatrix} \tag{7-16}$$

$$\left|U_n\right| = \sqrt{(U_f + U_x)^2 + U_y^2 + U_z^2} \tag{7-17}$$

where $C_x = \cos\theta_x$, $C_y = \cos\theta_y$ and $C_z = \cos\theta_z$ are the cosine functions of pile angles to each coordinate. U_x, U_y and U_z are the wave velocity in each direction. The same transformation is applied to acceleration. With the assumption of the linear wave theory, for an incoming wave with an elevation $\eta(x,t) = \frac{H}{2}\cos(kx - \omega t)$, the velocity and acceleration of the wave are ($U_y = 0$),

$$U_x = \frac{H\omega}{2}\frac{\cosh k(z+d)}{\sinh kH}\sin(kx - \omega t) \tag{18a}$$

$$a_x = \frac{\partial U_x}{\partial t} = \frac{H\omega^2}{2}\frac{\cosh k(z+d)}{\sinh kd}\sin(kx - \omega t) \tag{18b}$$

$$U_z = \frac{H\omega}{2}\frac{\sinh k(z+d)}{\sinh kd}\sin(kx - \omega t) \tag{18c}$$

$$a_z = \frac{\partial U_z}{\partial t} = -\frac{H\omega^2}{2}\frac{\sinh k(z+d)}{\sinh kd}\cos(kx - \omega t) \tag{7-18d}$$

where $\omega^2 = gk\tanh(kd)$.

By substituting the above equations into Equation (7-15), the water force per length in the flow direction can be derived as,

$$F_x = \frac{1}{2}\rho C_D D|U_n|U_{nx} + \rho C_M D^2 a_{nx} \tag{7-19}$$

As the pile is inclined to the water flow, at any time instant the phase of the velocity and acceleration is not the same at different positions along the pile length. Therefore, the total force cannot be obtained by simply integrating along the pile length. Instead, the numerical integrating is applied, i.e. the pile is divided into segments and all forces at each segment are then summarized as the total force.

$$F_{Tx} = \sum_{i=1}^{N} F_x(x_i, z_i, t) \bullet \Delta L_i \tag{7-20}$$

where N is the segment number, x_i and z_i are the coordinates of the i-th segment center; and ΔL_i is the i-th segment length.

Take a pile of bent 7 as an example. The pile length in water, d= 4.383m, was divided into segments with 0.1m long and the wave force on each segment is shown in Figure 7-6(a) with duration of 10s. Due to water viscosity, the water force decreases with the depth. We can see the wave force on the top part of the pile changing periodically from maximum (about 4500N) to minimum (about 500 N). Figure 7-6(b) shows the total wave force acting on the pile along versus time.

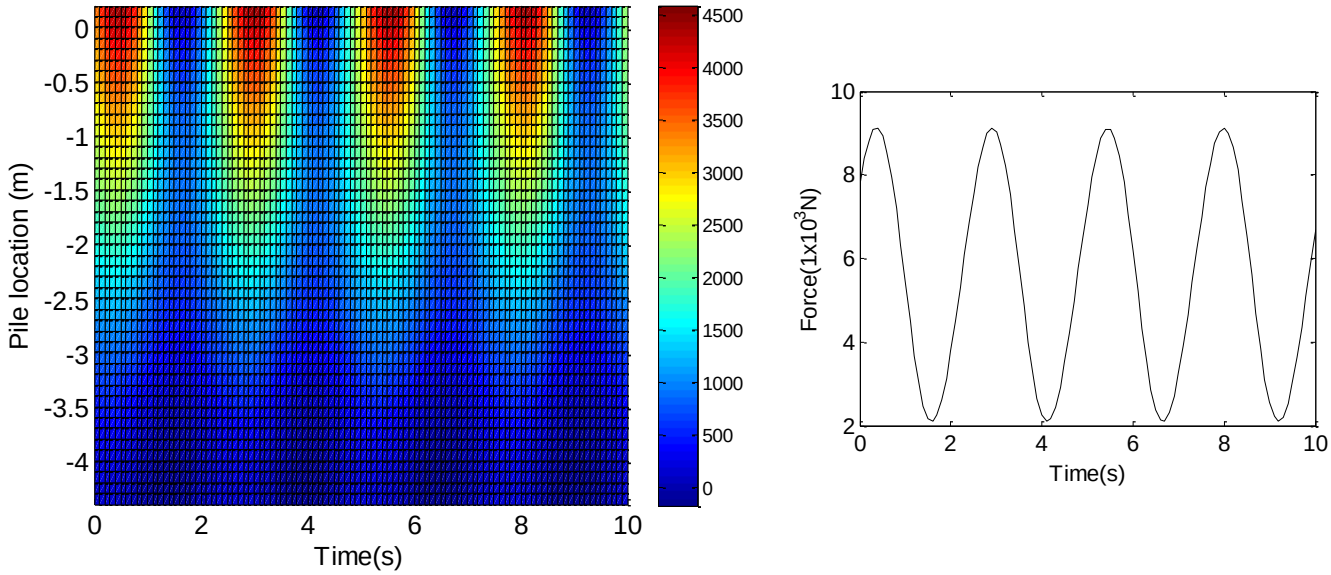

(a) force distribution along the pile (b) total horizontal force

Figure 7-6. Wave force of a pile in bent7

7.5 Response of a single pile and bent

In a simply supported bridge, the longitudinal direction of one end of the superstructure is not restricted, which means the foundation top is free to move. It is the same for some foundations of continuous bridges. It implies that some piles in a simple or continuous bridge work similar to an independent pile. Therefore, the scour effect on a single pile and a bent was investigated first. As the scour varies in different bents, three typical situations were considered:

- A pile of bent 7 with scour only in soil layer 1;
- A pile of bent 4 with scour only in soil layer 2 and 3;
- A pile of bent 6 with scour including both degradation and aggradation in soil 1 and 2.

Four stages of scour levels were considered for comparison: the intact state (as-built in 1979), site visit in 2000, site visit in 2009 and the predicted 100 year. Meanwhile, three types of loading were analyzed, i.e. static loading on the pile top, free vibration, and wave force loading.

7.5.1 Response of a single pile

The pile top of the middle bents such as bents 2~4 and bents 6~8, is connected with the superstructure in the lateral (z) direction but is almost free in the longitudinal (x) direction. The lateral displacement of the pile top is restricted to consider the superstructure effect, but the pile top is free to move in the x direction and free to rotate.

Static results

A pile of bent 7 was analyzed with a horizontal force applying near the pile top in both x and z directions, and the result is shown in Figure 7-7 including displacement, rotation and strain along the pile depth. The dash-dot line in the figure marks the scour depth of the four stages. As for the x direction, the pile response increases with the scour depth and the strain maximum point is close to the scour depth, which is consistent with results of a single pile with free end in the top in the reference (Kong et al. 2013). As the z displacement of the top is restricted, the response becomes smaller. The maximum value in the rotation and strain profile can both reflect the scour depth.

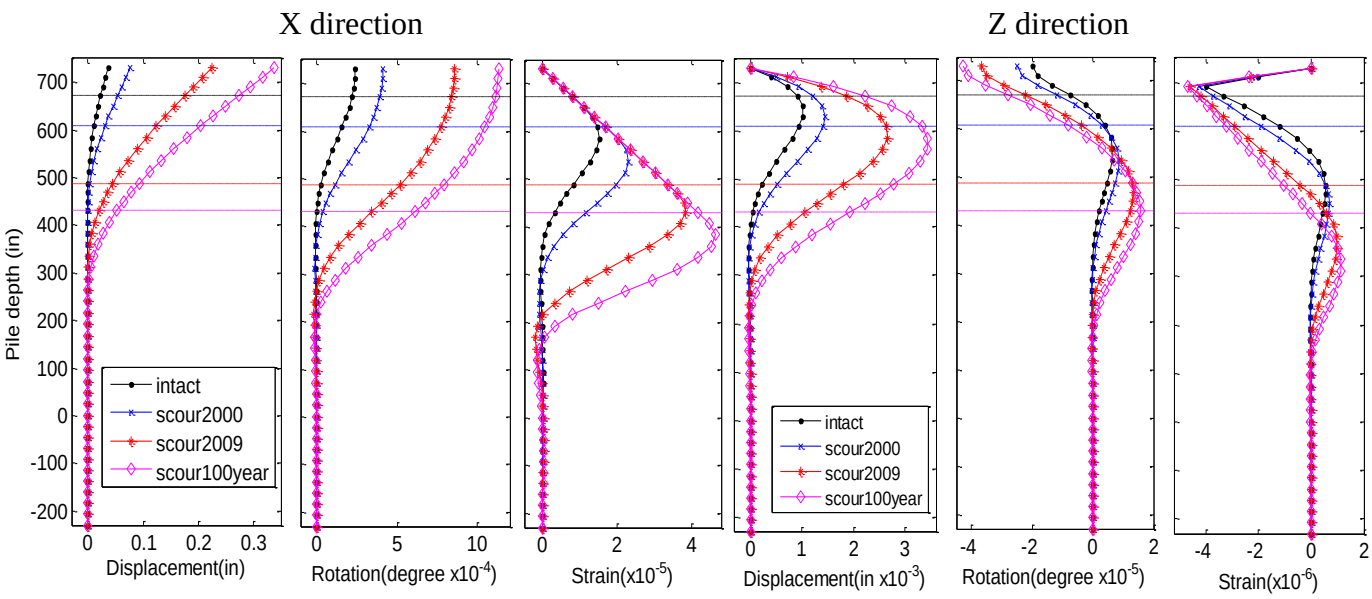

Figure 7-7. Static results of a pile in bent 7
(– - – the scour depth from top to bottom is intact, scour2000, scour 2009 and scour100year)

The results of other two cases, bent 4 and 6 were shown in Figure 7-8. The slop of profiles is much larger than that of Figure 7-7 because the scour involves soil layer 2 and 3 that have higher stiffness than layer 1. The maximum value of strain profile is closer to the scour depth when the scour depth becomes larger.

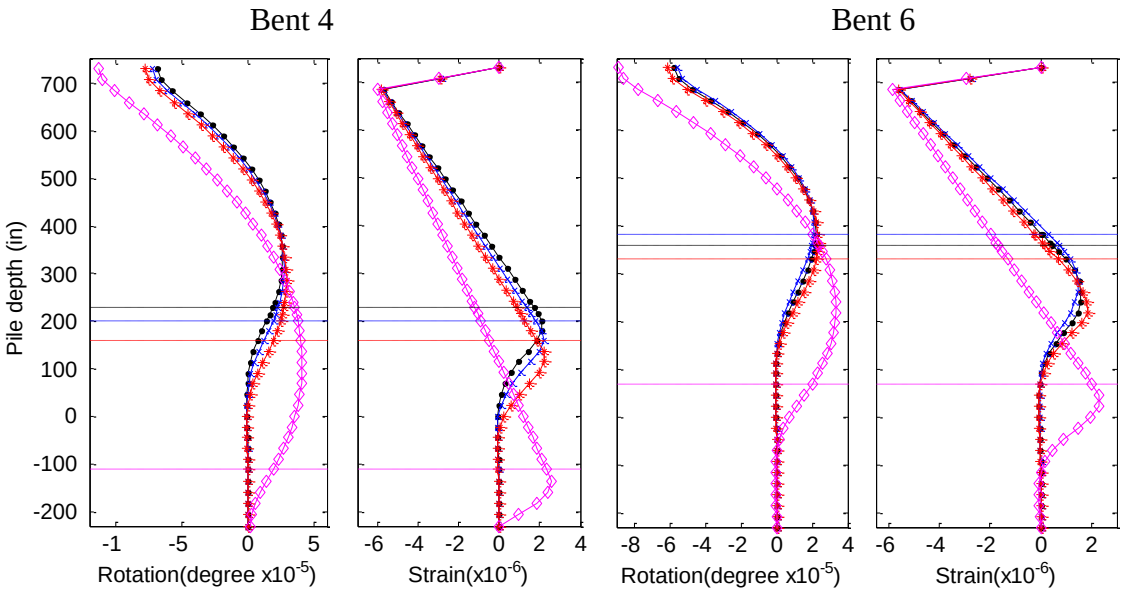

Figure 7-8. Static results of a pile in bent 4&6

Modal results

The free vibration of the pile with different scour depths was analyzed to study the scour effect on the dynamic characteristic of the pile. Table 7-3 lists the first ten frequencies of a pile in bent 7. As can be seen, the second frequency of the intact pile and the pile with scour in 2000 is equal to the fourth frequency of the other two cases. This frequency is not related to the scour damage. It indicates that the mode sequence is changed due to occurrence of scour in different depth. All the modes are reorganized based on the same modal shapes as listed in Table 7-4. It can be clearly seen that the scour has significant effect on the first two bending modes. Even though the pile top is restricted in z direction, the effect is still significant. It also indicates that the scour effect is mainly on the low frequency of the pile (Kong et al. 2013).

Table 7-3. Frequency results of a single pile (Hz)

No.	Intact	Scour2000	Scour2009	Scour100year
1	9.780	6.033	3.004	2.293
2	**18.586**	**18.586**	11.657	9.209
3	25.471	19.724	15.676	12.634
4	29.421	24.428	**18.586**	**18.586**
5	30.678	30.678	28.375	24.881
6	39.554	35.718	30.678	29.101
7	42.264	38.720	32.165	30.678
8	51.356	48.829	44.267	42.449
9	54.852	52.685	48.907	47.327
10	55.783	55.783	55.783	55.783

Table 7-4. Reorganized frequency results

Modes	Intact	Scour2000		Scour2009		Scour100year	
	F	F	Ratio (%)	F	Ratio (%)	F	Ratio (%)
1st x-bending	9.780	6.033	38.3	3.004	69.3	2.293	76.6
1st z-bending	25.471	19.724	22.6	11.657	54.2	9.209	63.8
2nd x-bending	29.421	24.428	17.0	15.676	46.7	12.634	57.1
2nd z-bending	39.554	35.718	9.7	28.375	28.3	24.881	37.1
3rd x-bending	42.264	38.720	8.4	32.165	23.9	29.101	31.1
3rd z-bending	51.356	48.829	4.9	44.267	13.8	42.449	17.3
4th x-bending	54.852	52.685	4.0	48.907	10.8	47.327	13.7

7.5.2 Response of a pile group

Since the bent 7 has the largest mudline change, it was selected and analyzed to study the scour effect on a pile group. The natural frequency of bent 7 under different scour depths was analyzed first and listed in Table 7-5 with the reorganized result. Although the five piles are combined together with a cap, the scour effect on the z direction is still significant.

Table 7-5. Frequency results of a pile group

Mode	Intact	Scour2000		Scour2009		Scour100year	
	F(Hz)	F(Hz)	Ratio (%)	F(Hz)	Ratio (%)	F(Hz)	Ratio (%)
X-bending	4.558	3.032	33.5	1.694	62.8	1.350	70.4
Z-bending	4.930	3.539	28.2	2.425	50.8	2.166	56.1
Pile deform	24.559	19.134	22.1	11.417	53.5	9.039	63.2
Pile deform	24.572	19.394	21.1	11.481	53.3	9.070	63.1

As for wave loads on a pile group, there are two ways to calculate (Liu et al. 2007; Crowley 2008): the first method is to multiply the wave force of a single pile with the pile numbers in the group; and the second method is to calculate separately the wave force of each pile in the group and multiply a reduction coefficient. As for the first method, the calculated total force is generally larger than the real value because of the phase difference of the waves passing through the different piles in the group and the group effects. With respect to the pile groups of the investigated bridge, the pile layout makes the wave force on each pile greatly different and the spacing of each pile is larger than 2.5 times of pile diameter. Thus, the wave force on the pile group is calculated separately for each pile in the group. Figure 7-9 shows the total force acting on each pile of bent 5. Piles 1 and 5 are the outside inclined piles and piles 2~4 are the middle vertical piles. As shown in the figure, the amplitude of piles 2~3 is the same, but the phase is different. The force on the inclined piles is smaller than that on the vertical piles due to the angle effect.

Applying the above wave loads on the bent 7, the time history of the bent response can be obtained. Figure 7-10 shows the displacement and acceleration of the bent top. The first six second is the response under wave loads and the next two second is the free vibration of the bent after the wave load is removed. Figure 7-11 presents the Fast Fourier Transform (FFT) of the above response. The first frequency is faintly visible from the FFT of the displacement response, while the first two frequencies can be clearly identified from the FFT of the acceleration response. Compared with the FE result shown in Table 7-5, the frequencies extracted here, which is the first and second bending mode in z direction, is very close to the FE result. It indicates that the frequency of the bent can be extracted from the dynamic response under wave loads, which could then be used to detect scour damage.

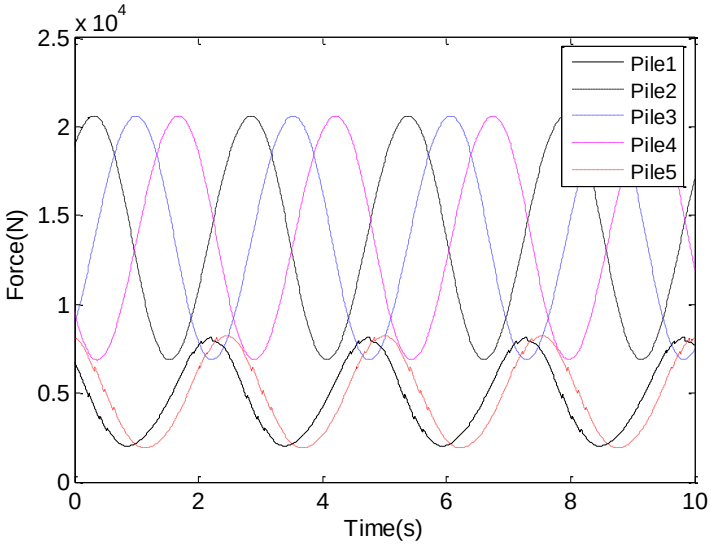

Figure 7-9. Total force on piles of bent 7

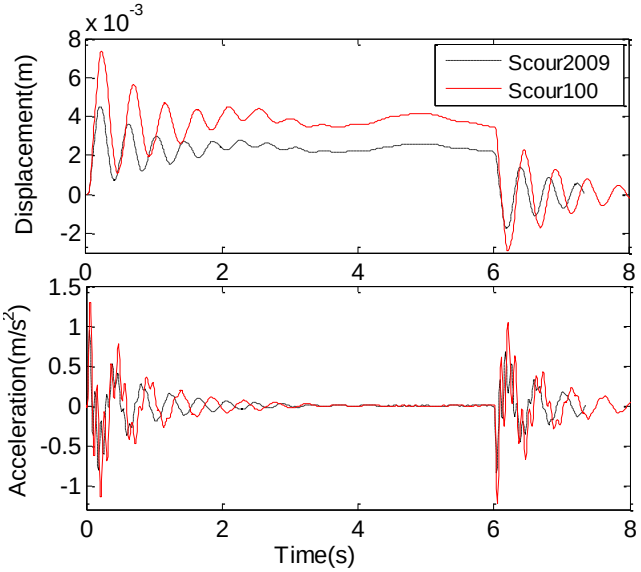

Figure 7-10. Response of pile top

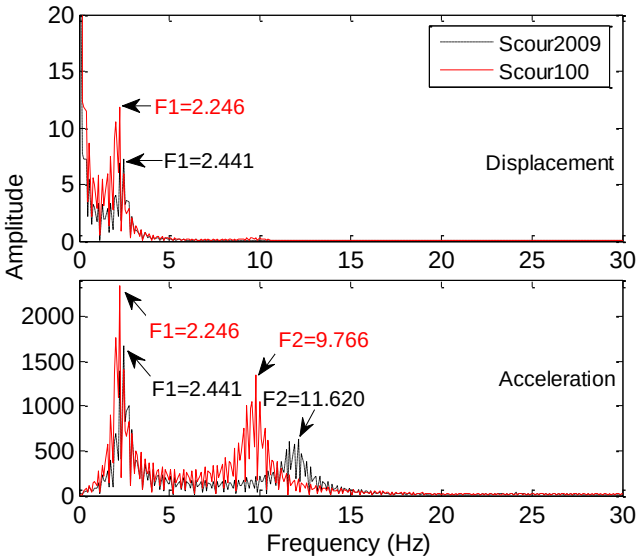

Figure 7-11. FFT of pile response

7.6 Bridge and vehicle responses

The water current and wave load is the major force for the foundation. Under the wave loading, the foundation scour would affect the bridge response and consequently affect the response of the vehicle traveling on it. In this section, both bridge and vehicle responses were investigated to study the applicability for detecting foundation scour.

7.6.1 Bridge-vehicle-wave model

Bridge model

The FE model of bridge was created in program ANSYS as shown in Figure 7-12. The bridge deck was modeled as shell elements, the girder, diaphragm and pile were modeled using beam elements. The bent cap was solid elements to better connect the girder and the pile. The girder was simply supported on the bent cap in both longitudinal (x) and lateral (z) directions as shown in the left corner of Figure 7-12 , i.e. the end bents, bents 1 and 9, have the same displacement with the girder in x direction, and for each bent it has the same displacement with only one end girder the in z direction. The displacement in y direction of all contact points was coupled. The soil was modeled as Combin39 nonlinear spring elements and the scour was modeled by removing spring elements and recalculating the stiffness as discussed earlier. The right corner of Figure 7-12 shows the real shape of the structure by displaying the section of each element.

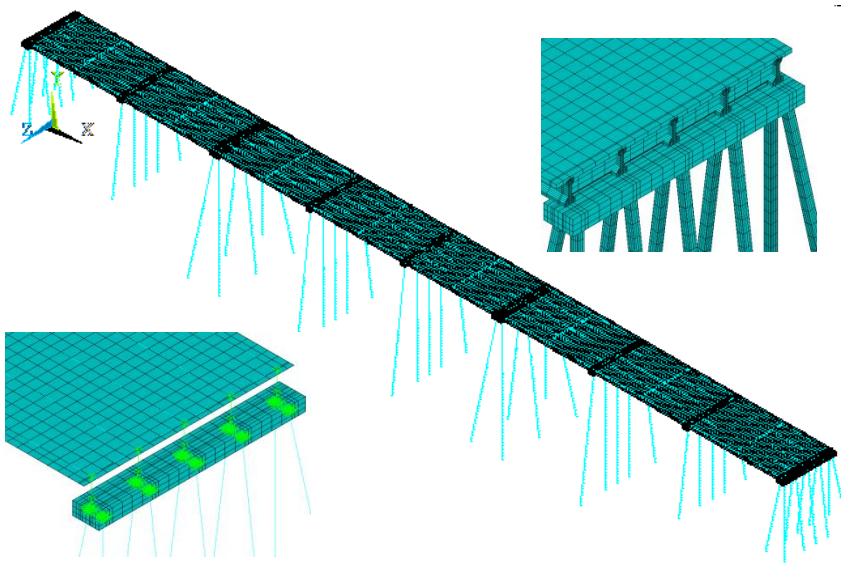

Figure 7-12. Bridge FE model

Vehicle model

A test vehicle proposed in Chapter 4 was used, which is a tractor-trailer system. The tractor model is based on a dump truck with a single front axle and a two-axle group for the rear (Figure 7-13). The static loads for the first, second, and third axle of this truck are 80.0 kN, 95.6 kN, and 95.6 kN, respectively. The distance between the front axle and the center of the two rear axles is 6.25 m, and the distance between the two rear axles is 1.2 m. This 3-axle truck was simulated as a 2-axle model by compressing the rear two axles into one axle as shown in Figure 7-14 (Shi 2006). The two following trailers each modeled as a SDOF vehicle model are connected behind the truck model.

Figure 7-13. Dump truck used in bridge testing

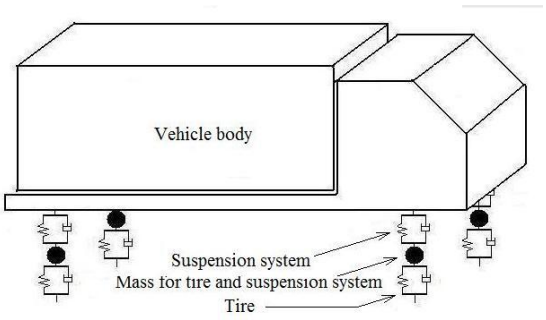

Figure 7-14. Model 1 for the test vehicle

Wave load

The method for calculating the wave force on a pile group as discussed earlier was used to calculate the wave load on each bent of the bridge. The bent property and scour information were listed in Table 7-2. Herein, only two stages of scour situation were considered, the intact (as-built 1979) and the scour 2009 (current stage). The water wave and current parameters in the river were based on the in-situ data, as listed in Table 7-6. The waver surface elevation of 55.08ft was used instead of the overtopping elevation of 67.90ft in 45 years frequency because the wave load caused by the 55.08ft elevation is larger than that of 67.90ft based on comparison. During the overtopping flood, the piles were far under the surface wave and subjected to small force from the wave, while the bridge deck is more dangerous. The wave height and length were assumed as 0.6m and 10m, respectively.

Table 7-6. Hydraulic data

	Bent 2	Bent5	Bent6	Bent8
Stream velocity(f/s)	4.0	6.0	9.3	5.0
Water surface elevation (ft)	55.08	55.08	55.08	55.08
Bottom of cap elevation (ft)	60.08	60.08	60.08	60.08

7.6.2 Results of bridge free vibration

The natural frequency of the bridge was analyzed first to study the change of bridge dynamic characteristic due to scour effect. The results of the four cases are listed in Table 7-7. Due to the non-composite connection between the girder and the bent cap, some modes are related to the vibration of the bent itself. As can be seen, the ratio of natural frequency change that relates to the bent vibration and the entire bridge vibration is very large, such as the mode of bent3-x-bending and the third z-bending and the torsion.

7.6.3 Bridge response under wave loads

By applying the wave loads on the foundation, the dynamic response of the bridge superstructure and foundation can be obtained. The acceleration time histories on the top of bent 4, bent 6 and bent 7 under cases of intact and scour 2009 are shown in Figure 7-15. The inertia

force of the wave dominates the beginning part of the acceleration response, while the later part is mainly the drag force that has little change due to the transit effects of wave loads. Figure 7-16 shows the FFT of the above time history. As discussed earlier, the occurrence of scour changes the mode sequence of the structure and makes higher mode move forward. In the case of scour 2009 in the figure, more frequencies become visible after scour happened.

Table 7-7. Frequency results of bridge

Modes	Intact	Scour2000		Scour2009		Scour100year	
	F(Hz)	F(Hz)	Ratio (%)	F(Hz)	Ratio (%)	F(Hz)	Ratio (%)
Bent4-x-bending	0.830	0.766	7.7	0.687	17.2	0.385	53.6
Bent5-x-bending	0.857	0.810	5.5	0.706	17.7	0.399	53.4
1st Z-bending	0.936	0.871	6.9	0.812	13.3	0.751	19.8
2nd Z-bending	1.976	1.836	7.1	1.676	15.2	1.006	49.1
3rd Z-bending	2.319	1.969	15.1	1.694	27.0	1.350	41.8
Bent3-x-bending	3.462	2.288	33.9	1.762	49.1	1.702	50.8
Bent6-x-bending	3.462	3.032	12.4	2.157	37.7	2.081	39.9
Torsion	4.160	3.432	17.5	3.349	19.5	2.288	45.0
Bent2-x-bending	4.200	3.507	16.5	3.408	18.8	2.289	45.5
Bent7-x-bending	4.558	4.137	9.2	3.460	24.1	2.293	49.7
Bent8-x-bending	4.569	5.026	10.0	4.086	10.6	2.302	49.6
Deck-bending	5.080	5.034	0.9	4.435	12.7	2.323	54.3
Deck-bending	5.124	5.036	1.7	4.440	13.3	2.323	54.7

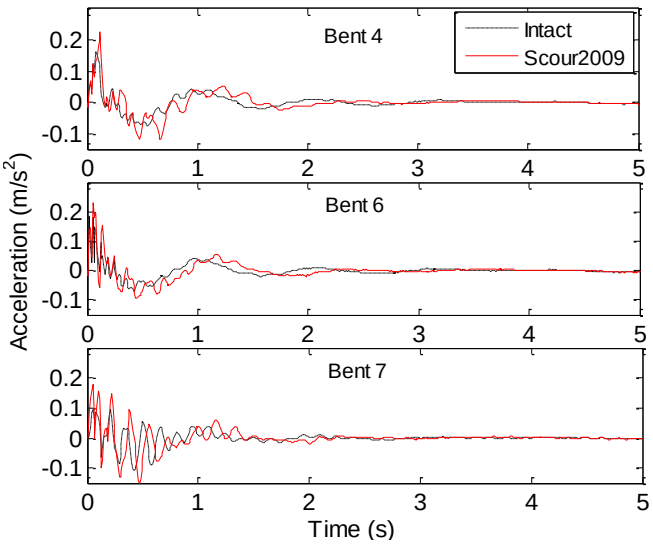

Figure 7-15. Response of bent top

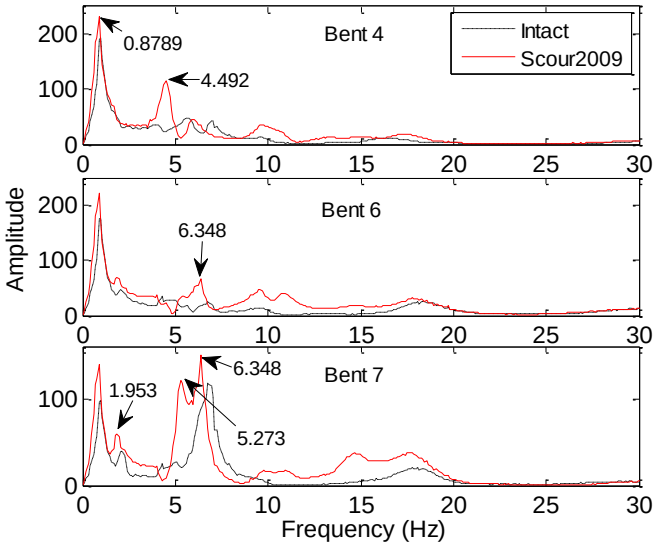

Figure 7-16. FFT of bent response

The acceleration time history of the bridge deck was also obtained. Three locations were selected for demonstration: a deck point on the top of bent 3, a point in the middle of the fourth span and a deck point on the top of bent 7, that is, node 43101, 44009 and 34655 as shown in Figure 7-17. Here only the FFT result is displayed. The FFT of node 34655 is almost the same as the one of bent 7 in Figure 7-16, which indicates that the superstructure response has the potential to be used for scour detection of foundation.

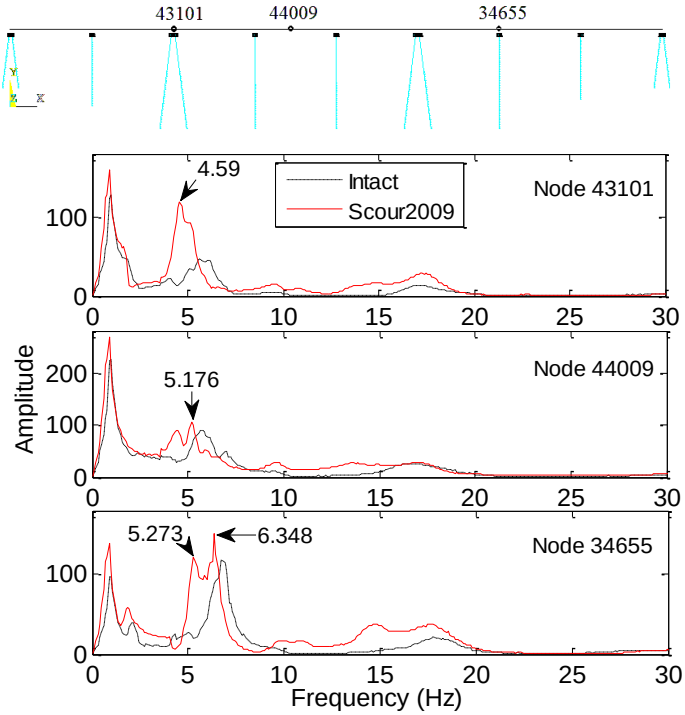

Figure 7-17. FFT of bridge deck response

7.6.4 Vehicle response under wave loads

In the case with wave loads on the foundation and vehicles traveling on the bridge, the dynamic response of the vehicle was obtained. As shown in Figure 7-18(a), the acceleration time history of the first trailer under cases of Intact and Scour2009 are displayed. The methodology discussed in Chapter 4 was used to generate the residual response of the two trailers and the FFT results are shown in Figure 7-18(b). The first recognized frequencies for Scour2009 and Intact cases are 0.879 Hz and 1.074 Hz, respectively. As can be seen in Table 7-7, those frequencies are related to the first z-bending mode (0.812 and 0.936 Hz based on free vibration analysis in the table), which indicates the frequency change due to scour damages. Thus, the vehicle response can be potentially used to detect foundation scour damages.

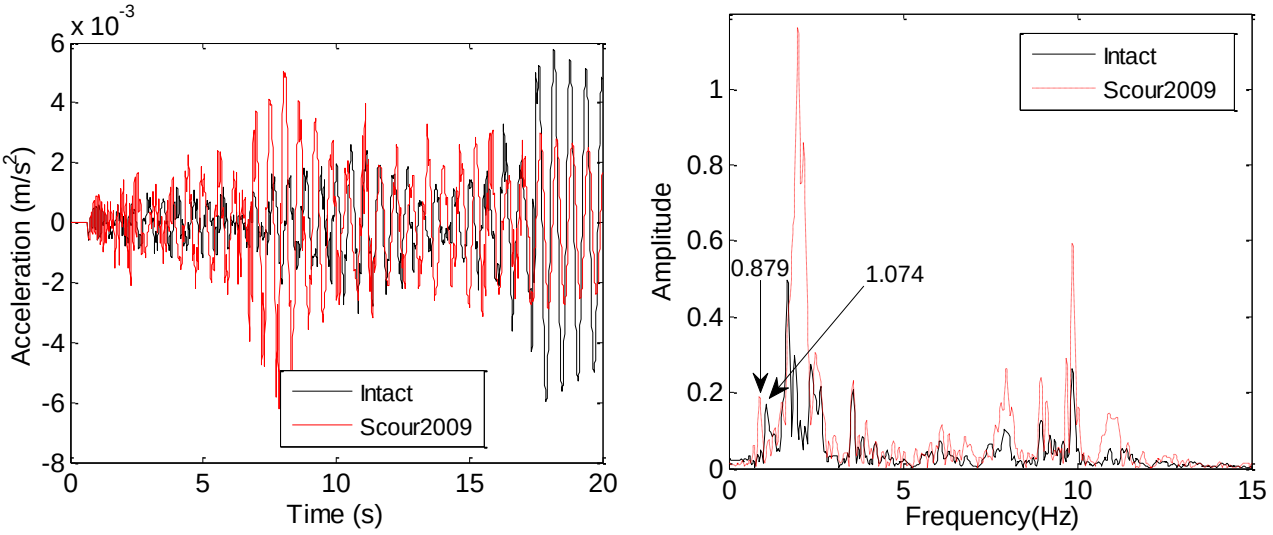

(a) Accelerations of trailer 1 (b) FFT of vehicle residual response

Figure 7-18. Vehicle response without wave loads

7.7 Conclusions

The present study investigated the scour effect on the bridge and vehicle responses by creating soil and scour models and calculating wave and current loads on the piles. Based on the response of a single pile, a pile group, the entire bridge and the vehicle, some conclusions can be obtained as follows:

(1) The static result of a single pile is consistent with the previous work of the study, i.e. the maximum value in the rotation and strain profile can roughly reflect the scour depth. With respect to the natural frequency, the mode sequence is changed due to occurrence of scour in different depths. For the modes with the same mode shape, the scour has significant effect on the low frequency of the pile.

(2) The response of the pile group under wave loads were obtained and transferred to the frequency domain. The first two frequencies can clearly be recognized in the frequency spectra of accelerations, and is very close to the true value. The extracted frequency can then be used to detect scour damage.

(3) The scour effect on the entire bridge was analyzed under wave loads, and both the response of the bridge deck and the bent top were obtained. The frequency related to each bent can be extracted from the response of that bent. The occurrence of scour allows more frequencies visible after scour has happened. The frequency spectra extracted from the deck point near the support is very close to that of the foundation, which indicates the superstructure response has the potential to be used for scour detection of foundation.

7.8 References

American Association of State Highway and Transportation Officials (AASHTO). (2008). "Final draft: Guide specifications for bridges vulnerable to coastal storms (BVCS-1)." Washington, DC.

American Petroleum Institute (API). (1993). ''Recommended practice for planning, designing, and constructing fixed offshore platforms—Working stress design.'' 20th Ed., API RP2A-WSD, Washington, D.C.

Breusers, H. N. C., Nicollet, G., and Shen, H. W. (1977). "Local scour around cylindrical piers." Journal of Hydraulic Research, 15(3), 211-252.

Crowley, R. (2008). "Drag forces on pile groups." Master thesis, University of Florida.

Deng, L., and Cai, C. S. (2007). "Applications of fiber optic sensors in civil engineering." Structural Engineering and Mechanics, 25(5), 577-596.

Deng, L., and Cai, C. S. (2010). "Bridge scour: prediction, modeling, monitoring, and countermeasures--review." Practice Periodical on Structural Design and Construction, ASCE, Vol. 15, No. 2, pp. 125–134.

El Naggar, M. H., Bentley, K. (2000). "Dynamic analysis for laterally loaded piles and dynamic p–y curves." Canadian Geotechnical Journal, 2000, 37(6): 1166-1183.

Federal Emergency Management Agency (FEMA). (2011). "Coastal Construction Manual, Principles and Practices of Planning, Siting, Designing, Constructing, and Maintaining Residential Buildings in Coastal Areas (Fourth Edition)." Volume II, August 2011.

Foti, S., and Sabia, D. (2011). "Influence of foundation scour on the dynamic response of an existing bridge." Journal of Bridge Engineering, 16, 295-304.

Han, Z. F., Ye, A. J., and Fan, L. C. (2010). "Effects of riverbed scour on seismic performance of high-rise pile cap foundation." Earthquake engineering and engineering vibration, Vol.9, No.4, 533-543.

Kassem, A., Salaheldin, T. M., Imran, J., and Chaudhry, M. H. (2003). "Numerical modeling of scour around artificial rock island of Cooper River Bridge." Transportation Research Records 1851, 45-50.

Kong, X., Cai, C. S., Hou, S. (2013). "Scour effect on a single pile and development of corresponding scour monitoring methods." Smart Materials and Structures, 22(5), 055011, doi:10.1088/0964-1726/22/5/055011.

Irschik, K., Sparboom, U. (2004). "Breaking wave loads on a slender pile in shallow water." Proc. 29th int. Conf. Coastal Eng. (ICCE 2004), ASCE, Lisbon.

Lagasse, P. F., and Richardson, E. V. (2001). "ASCE Compendium of Stream Stability and Bridge Scour Papers." Journal of Hydraulic Engineering, 12797: 531-533.

Lagasse, P. F., Thompson, P. L., and Sabol, S. A. (1995). "Guarding Against Scour." Civil Engineering Magazine, 65(6), 56–59.

Laursen, E. M., and Toch, A. (1956). "Scour around bridge piers and abutments." Bullentin No.4, Iowa Highway Research Board, Ames, Iowa.

Lee, T. L., Jeng, D. S., Zhang, G. H., and Hong, J. H. (2007). "Neural network modeling for estimation of scour depth around bridge piers." Journal of Hydrodynamics, 19(3), 378-386.

Lim, S. Y. (1997). "Equilibrium clear-water scour around an abutment." Journal of Hydraulic Engineering, 123(3), 237-243.

Lin, C., Bennett, C., Han, J., Parsons, R.L. (2010). "Scour effects on the response of laterally loaded piles considering stress history of sand." Computers and Geotechnics, 37, 1008-1014.

Lin, Y. B., Chen, J. C., Chang, K. C., Chern, J. C., and Lai, J. S. (2005). "Real-time monitoring of local scour by using fiber Bragg grating sensors." Smart Materials and Structures, 14(4), 664-670.

Liu, S. X., Li, Y. C., Li, G. W. (2007). "Wave current forces on the pile group of base foundation for the East Sea Bridge, China." J. of Hydrodynamics, 19 (6), 661-670.

Loh, C.H., Wu, F.M., Chao, S.H. (2011b). "In situ structural health monitoring for bridges under ambient stimulus: effect of scouring." The Engineering Mechanics Institute 2011 Conference, June 2-4, Boston, USA.

Louisiana Department of Transportation and Development (LADOTD). (2010) "Phase III stability analysis draft report." State Project Number: 700-99-0461, Louisiana.

Lu, J. Y., Hong, J. H., Su, C. C., Wang, C. Y., and Lai, J. S. (2008). "Field measurements and simulation of bridge scour depth variation during floods." Journal of Hydraulic Engineering, 134(6), 810-821.

Melville, B. W., and Raudkivi, A. J. (1977). "Flow characteristics in local scour at bridge piers." Journal of Hydraulic Research, 15(4), 373-380.

Melville, B. W., and Sutherland, A. J. (1988). "Design method for local scour at bridge piers." Journal of Hydraulic Engineering, 114(10), 1210-1226.

Morison, J. R., O'Brien, M. P., Johnson, J. W., Schaaf, S. A. (1950). "The force exerted by surface waves on piles." Petroleum Transactions (American Institute of Mining Engineers) 189: 149–154.

Mostafa, Y. E., El Naggar, M. H. (2004). "Response of fixed offshore platforms to wave and current loading including soil-structure interaction." Soil Dynamics and Earthquake Engineering, 24, 357-368.

Mostafa, Y. E., El Naggar, M. H. (2004). "Response of fixed offshore platforms to wave and current loading including soil-structure interaction." Soil Dynamics and Earthquake Engineering, 24, 357-368.

Mohammad, Z. K., Beheshti, A. A., and Behzad, A. A. (2009). "Estimation of current-induced scour depth around pile groups using neural network and adaptive neuro-fuzzy inference system." Applied Soft Computing, 9, 746-755.

Reese, L. C., and Wang, S. T. (1993). "COM624P—Laterall loaded pile analysis program for the microcomputer." FHWA-SA-91-048, Federal Highway Administration, Dept. of Transport, Washington, D.C.

Ruocci, G., Ceravolo, R., and De Stefano, A. (2009). "Modal identification of an experimental model of masonry arch bridge." Key Engineering Materials, Vol.413-414, 707–714.

Ruocci, G. (2010). "Application of the SHM methodologies to the protection of masonry arch bridges from scour." PhD Thesis, Department of Structural and Geotechnical Engineering, Politecnico di Torino, Italy.

Ruocci, G., Quattrone, A., and De Stefano, A. (2011). "Multi-domain feature selection aimed at the damage detection of historical bridges." The 9th International Conference on Damage Assessment of Structures (DAMAS 2011), Journal of Physics: Conference Series 305 (2011) 012106.

Rytter, A. (1993). "Vibration based inspection of civil engineering structures." Ph. D. Dissertation, Department of Building Technology and Structural Engineering, Aalborg University, Denmark.

Sumer, B. M., Fredsøe, J. (2006). "Hydrodynamics around cylindrical structures, Advanced Series on Ocean Engineering, 26 (revised ed.)." World Scientific, ISBN 981-270-039-0.

Samizo, M., Watanabe, S., Fuchiwaki, A., Sugiyama, T. (2007). "Evaluation of the structural integrity of bridge pier foundations using microtremors in flood conditions." QR of RTRI, Vol. 48, No.3, 153-157.

Sheppard, D. M., and William, M. Jr. (2006). "Live-bed local pier scour experiments." Journal of Hydraulic Engineering, 132(7), 635-642.

Shirhole, A. M., and Holt, R. C. (1991), "Planning for a comprehensive bridge safety program." Transportation Research Record 1290, Transportation Research Board, National Research Council, Washington, D.C., 1, 39-50.

Umbrell, E. R., Young, G. K., Stein, S. M., and Jones, J. S. (1998). "Clear-water contraction scour under bridges in pressure flow." Journal of Hydraulic Engineering, 124(2), 236-240.

Yao, W. Y. (2009). "An engineering approach for computation of wave loads on pile-slab structures." Master thesis, Shanghai Jiao Tong University, China.

Young, G. K., Dou, X., Saffarinia, K., and Jones, J. S. (1998). "Testing abutment scour model." Proceedings of the 1998 International Water Resources Engineering Conference, Vol.1, 180-185. Memphis, TN, USA.

Zhang, R. R., King, R., Olson, L. Xu, Y. L. (2005). "Dynamic response of the Trinity River Relief Bridge to controlled pile damage: modeling and experimental data analysis comparing Fourier and Hilbert-Huang techniques." J. of Sound and Vibration, 285, 1049-1070.

CHAPTER 8. CONCLUSIONS AND RECOMMENDATIONS

In this dissertation, a framework of vibration-based damage detection was developed and a combined optimization method was proposed. In the vehicle-bridge coupled system, a new method using the transmissibility of vehicle and bridge responses was developed to detect damages of the bridge. In order to make use of the vehicle response, a tractor-trailer test system was designed to obtain reliable responses and extract bridge modal properties from the dynamic response of moving vehicles. The above method was then applied to detect bridge scour damage. The scour effect on a single pile was studied and methods were proposed and applied to monitor the bridge scour using fiber bragg grating sensors. With the objective to detect scour damage from the bridge response and/or vehicles, the scour effect on the response of the entire bridge and even the traveling vehicle was also investigated under the bridge-vehicle-wave interaction. The contribution and conclusions of the dissertation can be summarized into three parts as follows.

8.1 Framework of vibration-based damage detection (Chapter 2)

Vibration-based damage detection methods are especially pervasive as the global damage identification technique. This study developed a framework for damage identification in different levels and proposed an optimization method. The following conclusions are drawn:

- The framework gave a guideline about the three crucial steps for damage detection: (1) selecting parameters and objective features, (2) building a reasonable structural model, and (3) adopting optimization techniques to solve the problem.

- A comparative analysis on a numerical beam with three damage scenarios was conducted to study the following aspects: the selection of parameters and determination of its initial values and boundaries, the construction of sensitive objective functions, the creation of structural models, and the performance of different optimization techniques.

- The proposed optimization method that combines the Genetic Algorithm (GA) and the First Order (FO) method shows the capability of finding a good solution using any initial values. It can also converge very fast with very few generations.

- The methodology was demonstrated on a simplified model of a bridge with scour history.

8.2 Damage detection based on dynamic response of VBC system (Chapter 3~4)

The research of damage detection in the frequency domain is prosperous such as methods based on modal data, transfer function or frequency response function (FRF) and transmissibility. Nevertheless, the measurement of FRF and transmissibility requires external harmonic forces as the input. In the present study, the transmissibility of the vehicle-bridge coupled (VBC) system is used for damage detection since the transmissibility is a local quantity

with a high sensitivity and a vehicle in the VBC system can serve as both a force exciter and a response receiver. The following conclusions are drawn:

- The transmissibility extracted from the bridge-only system was investigated first and it had very stable and effective results, thought it requires external excitation forces. As for the transmissibility extracted from the VBC system, six transmissibility damage indexes (TDIs) were compared and two TDIs were found to have better results. Moreover, it is found that the low frequency part of the vehicle transmissibility is useful.

- The parametric study on the effect of measurement numbers, surface roughness, vehicle speed, and vehicle numbers shows: The roughness level and the vehicle speed have very small effects on the TDI of bridge response but significant effect on the TDI of vehicle response, especially for small damage. It suggests a moderate vehicle speed for field testing. The result with random traffic flow is much better than that with the regular traffic flow.

- The proposed Method I uses the first vehicle standing at a fixed position as reference and the second vehicle moving step by step to record responses at positions along the bridge. The modal information such as natural frequencies and mode shape squares are successfully extracted from the transmissibility of vehicle response. Nevertheless, the result is affected by the position of the reference vehicle. The reference vehicle should avoid putting at the position (or node) with zero amplitude in each mode shape, especially for the first few modes that greatly affect the measuring result.

- The Method II uses two vehicles that are at a constant distance. They stop at the designated position and move to the next position in the same pace after the signals are recorded. The result is slightly worse than that of Method I. The distance between those two vehicles is an important factor.

The transmissibility and dynamic response of the vehicle are measured in the condition that both vehicles stopped at the designated position with vertical vibration only. As the vehicle response carries the vibration information of the bridge, the present study proposed a testing vehicle consisting of a tractor and two following trailers to extract bridge modal properties from the residual vehicle response. Conclusions can be drawn as follows:

- The proposed method that extracts bridge modal properties from the residual response of two trailers is more effective than that from the individual trailer or from the residual spectrum of the two trailers reported in the literature. In the case when the bridge is sufficiently excited by other ongoing traffic vehicles, the proposed method works even better.

- The effect of the trailer mass and stiffness, the spacing between the two trailers and the traveling speed were investigated. The results indicate that a sufficient contact between the vehicle and bridge to avoid separation should be maintained for better results. Similarly, it

is recommended that the spacing of the two test trailers should be less than 5.0m and a speed of 5~10m/s is suggested in the studied example.

- The proposed method was applied on the field bridge. Two types of test vehicle models were proposed. For vehicle model I using an independent SDOF vehicle to simulate the trailer, the bridge frequencies can be easily extracted.

- The two trailers of vehicle model II are simulated with the rear two axles of a modified 5-axle vehicle model. Both the residual response of two wheels of the same trailer and that of wheels of the two trailers were considered but cannot lead to good results.

8.3 Bridge scour effect and monitoring (Chapter 5~7)

The present study mainly focused on the static and dynamic response of a single pile to scour effects. Based on observations from the theoretical and parametric analyses, in the present study three possible methods were proposed to detect and monitor bridge scour and a monitoring system was developed using fiber optic sensors that had been verified in the laboratory. The following conclusions can be drawn:

- For any position of the pile, if it is buried deeply in soil, its bending moment is not significant. Only if the scour depth approaches to that position, the moment becomes significant and increases quickly to its maximum. Furthermore, the location of the maximum moment in the pile is close to the interface between water and soil, which can be used for detecting the scour depth. The bending test of the GFRP pipe buried in sand with different heights verifies the numerical observations and confirms the feasibility of the scour monitoring method based on the bending moment profile.

- The pile's natural frequency decreases as the scour ratio increases, especially for the fundamental frequency of the pile, which benefits the scour monitoring. The water flow test on the shaking table verifies the scour monitoring method based on the high frequency signal from the debris hitting or flow impact in the river water. As the sand level is reduced, the sensor used to be buried in the soil is exposed to the water, and it begins to respond recognizably differently due to the water flow and debris impact. It is a good sign for scour detection.

- The scour monitoring method based on the moment profile caused by the water flow impact is not as accurately verified. The possible reason is that the elastic coefficient of sand is not constant but linearly distributed along the depth, which suggests a small stiffness of the top sand. Moreover, the sand saturated in water weakens its supporting ability and the water flow drags the top sand and makes it loose. Therefore, the identified scour depth is not exactly the same as the actual scour depth.

The scour detection method based on a single pile was applied on a field bridge. Three designs for a scour monitoring system using FBG sensors to measure and monitor scour depth

variations in real-time including deposition (refilling) process were discussed and the third one is highly recommended based on a comparative study. The basic idea of the recommended scour monitoring system is to sense the scour depth variations and deposition process by identifying the locations of emerging FBG sensors from the riverbed. A reliable sensor protection system is meanwhile designed for FBG sensors in harsh environments, especially in floods.

A verification test using a flume was carried out in the laboratory to demonstrate the capability of FBG sensors and applicability of the recommended scour monitoring system and instrumentation. Based on the laboratory test, the recommended system is capable of measuring the maximum scour depth, entire process of scour development, and deposition height due to the refilling process. The advantages over other conventional scour monitoring systems are proven to be obvious. It should be noted that the purpose of the entire instrumentation design is not only just for the bridge scour monitoring using FBG sensors, but also for applying FBG sensors more effectively and efficiently in other harsh environments. A field bridge has been selected in the State of Louisiana and the long term stability for this scour monitoring system will be further investigated.

Due to the advantages of vibration-based damage detection methods and with the objective of detecting scour damage from the responses of bridge and vehicle, the scour effect on the bridge and vehicle responses was investigated. The responses of a single pile, a pile group, the entire bridge and the vehicle under static loading, free vibration, and wave loading were studied, and the following conclusions are drawn:

- The static result of a single pile is consistent with the previous work of the study, i.e. the maximum value in the rotation and the strain profile can roughly reflect the scour depth. With respect to the natural frequency, the mode sequence is changed due to the occurrence of scour in different depths. For the modes with the same mode shape, the scour has significant effect on the low frequency of the pile.

- The response of the pile group under wave loads were obtained and transferred to the frequency domain. The first two frequencies can clearly be recognized in the frequency spectra of accelerations, and is very close to the true value. The extracted frequency can then be used to detect scour damage.

- The scour effect on the entire bridge was analyzed under wave loads, both the response of the bridge deck and the bent top were obtained. The frequency related to each bent can be extracted from the response of that bent. The occurrence of scour allows more frequencies to become more visible after scour has happened. The frequency spectra extracted from the deck point near the support is very close to that of the foundation, which indicates the superstructure response has the potential to be used for scour detection of foundation.

8.4 Recommendations

The writer believes that the following issues deserve further research:

- The feasibility of using the transmissibility obtained from two "static" vehicles to extract bridge frequencies and mode shapes has been studied. A methodology of using the transmissibility to detect damage location and severity in bridge is deserved to be developed.

- In the time-frequency analysis using the STFT, the window that is fixed-sized cannot assure a high resolution for high frequencies. It is necessary to use an adaptive STFT or introduce other time-frequency method. Furthermore, a better vehicle model is needed to simulate the two trailers of the tractor-trailer system and the noise effect should be taken into consideration to further study this method. Meanwhile, the case study in the present study does not have the measured vehicle response and a field test is highly recommended to verify this method.

- The wave force calculated from the empirical Morison equation is not accurate since it only considers the inertia and drag force. The CFD analysis is necessary to simulate the water current and wave around the piles and obtain the more accurate water force on the piles, though water force is used here only to excite bridge vibrations and the accuracy is not a major concern.

- The excitation of water force is mainly in the lateral direction, i.e., the lateral response of the vehicle will be excited and should be considered. Therefore, the future work should study the lateral response of the vehicle under the wave force by considering the lateral contact between the vehicle and the bridge.

- A field bridge has been selected to apply the recommended design for the bridge scour monitoring system using FBG sensors. It is a good opportunity to verify the system in field. A further study is necessary to assure reliable results.

VITA

Mr. Xuan Kong was born in 1985 in Jiangxi Province, P.R. China. He received his Bachelor of Science degree from the Department of Civil Engineering at Huazhong University of Science and Technology, P.R. China, in June 2006 and his Master of Science degree from the Department of Bridge Engineering at Tongji University, China, in June 2009.

Mr. Kong has worked as a Graduate Research Assistant at Louisiana State University since August 2009. He has been involved in research in several areas, such as structure dynamics, FE analysis, optimization techniques, bridge and vehicle coupled analysis, fiber optical sensor, model updating and damage detection, and health monitoring on bridge scour. He has more than 10 publications, listed as follows:

Journal papers

1. **Kong, X.,** Cai, C. S. (2013). "Framework of vibration-based damage identification and an improved optimization method." Engineering Structures, (to be submitted).

2. **Kong, X.,** Cai, C. S. (2013). "Damage detection based on transmissibility of vehicle and bridge coupled system." Journal of Sound and Vibration, (to be submitted).

3. **Kong, X.,** Cai, C. S. (2013). "Extracting bridge modal properties from dynamic responses of moving vehicles." Journal of Sound and Vibration, (to be submitted).

4. **Kong, X.,** Cai, C. S. (2013). "Scour effect on bridge and vehicle response under bridge-vehicle-wave interaction." Smart Materials and Structures, (to be submitted).

5. **Kong, X.,** Cai, C. S., Hou, S. (2013). "Scour effect on a single pile and development of corresponding scour monitoring methods." Smart Materials and Structures, 22(5), 055011, doi:10.1088/0964-1726/22/5/055011

6. Xiong, W., Cai, C. S., **Kong, X.** (2012). "Instrumentation design for bridge scour monitoring using fiber bragg grating sensors." Applied Optics, Vol. 51, No. 5, 547-557.

7. **Kong, X.,** Wu, D. J., Cai, C. S., Liu, Y. Q. (2012). "New strategy of substructure method to model long-span hybrid cable-stayed bridges under vehicle-induced vibration." Engineering Structures 34, 421–435.

8. **Kong, X.,** Wu, D. J., Jian, F. L. (2009). "Analysis on vertical crack of highway concrete slab of highway-railway combined bridge." J. of Railway Standard Design (in Chinese).

Proceedings and Conference Papers:

9. **Kong, X.,** Cai, C. S. (2013). "Numerical study on transmissibility in VBC system and

application for damage identification." EMI 2013, Aug. 4-7, 2013, Northwestern University, Evanston, IL.

10. **Kong, X.,** Cai, C. S., Hou, S. (2013). "Development of scour monitoring methods based on scour effect analysis." 9th International Workshop on Structural Health Monitoring, Sept. 10-12, Stanford University, CA.

11. **Kong, X.,** Cai, C. S, Xiong, W. (2012). "Instrumentation design for bridge scour monitoring using fiber bragg grating sensors." EMI/PMC 2012, June 18-20, 2012, University of Notre Dame, IN, USA.

12. **Kong, X.,** Cai, C. S. (2011). "Fast damage detection of bridge structures from dynamic response of a passing vehicle." 2011 Engineering Mechanics Institute Conference (EMI2011), June 2-4, 2011, Boston.

13. **Kong, X.,** Wu, D. J., Cai. C. S. (2010). "Application of substructure method to vehicle-induced dynamic response of long-span hybrid cable-stayed bridge." ISLPBS, June 27-29, 2010, Changsha, China.

14. He, J., Liu, R., **Kong, X.,** Liu, Y. Q., Chen, A. R., YODA, T. (2009). "Model tests and simulation analysis on steel-concrete joint part of hybrid cable-stayed bridge." The 10th Conference on Structural Safety and Reliability, Sept.13-17, Japan.

15. **Kong, X.,** Wu, D. J. (2008). "Reason analysis on concrete crack of highway deck of Nanjing Yangtze River Bridge." The 6th National Civil Engineering Forum for Graduate Students, Nov.22-23, 2008, Beijing, China.